Measurement of Electrostatic Dipoles and Net Charge on Air Dispersed Particles

---

A thesis submitted in fulfilment of the requirements

for the degree of Doctor of Philosophy

in Chemical and Process Engineering

at the University of Canterbury

Payel Bagga

May 2009

Abstract

Dipoles are expected to often dramatically enhance the mutual collision rate of diffusing particles (above the effects of Brownian or turbulent motion). However, this spreading awareness of the possible influence of discrete dipoles on particles is still based largely on theory, and some qualitative experience of particle behaviour from microgravity experiments. Individual particle dipoles have not yet been definitely isolated in experiments, nor measured in practical situations. In this project, it was intended to measure, for the first time, distributions of dipole strength (as well as net charge and particle size) on particulates dispersed into air by typical industrial and pharmaceutical processing methods.

The instruments designed to do this were built around a sampling head which allowed examination of a flow of dust dispersed into an air stream. During dispersal, the particles suffered tribocharging by mutual separation and collision on walls. Examination of the particles involved recording the path of particles as they moved through a non-uniform electric field around a central electrode, which was supplied with high voltage. Particles were attracted towards the central electrode (of 0.5 mm diameter in this study) if they contained dipoles, independent of the polarity of the field or their net charge. Particles to be examined were illuminated by a laser sheet as they moved past, and a high speed video captured their trajectories (over a field of view of around 5 mm).

The equation of motion of a particle which involved the forces of both particle net charge and dipole strength was applied to the particle path to evaluate both these parameters. The particle trajectories were modelled, and checked against the observed experimental trajectories. The voltage applied to the probe varied from 4 kV to 18 kV but for most of the runs 6 kV voltage was used. The electric field around the probe tip was assumed to be same as that for a spherical electrode of the same size as the probe. The flow field axially towards and around the probe tip was calculated using the Stokes creeping flow equations around a sphere. The calculated electric and flow fields were checked against COMSOL Multiphysics models applied to actual geometries and flow regimes.

The rotation dynamics of the particles was also considered important in the technique, requiring possibly extra knowledge of the initial direction of the dipole. The flow was led through a lateral field between two plates in order to orient the direction of any dipoles in the direction of the lateral field. The expected orientation of dipoles coming out of the plates was used as an initial guess of their orientation for modelling the rotation of the dipoles when they entered the probe field. Misalignment after leaving the plate field and before entering the probe field was also considered, and was found to be important due to vortices characterised by smoke and particle studies. However, the trajectory modelling revealed that the particles studied quickly rotated into alignment with the probe field, providing maximum attractive force to the probe, and so the values of net charge and dipole strength obtained did not depend on the initial orientation.

Estimated errors of particle position and diameter used in all the calculation steps were judged to be well within a basic image error limit of ±1 pixel. Some particle trajectories showed unexplainable shapes which was traced to the influence of large mixing eddies around the gas/particle jet. A check for corona discharge at the probe tip was made both at the beginning and at the end of the sampling experiments. No corona was detected initially (up to 18 kV), but a discharge could be observed at voltages close to 7 kV in the later checks.

Particles of acrylic, glass bubbles, whole milk and fertiliser powder were sampled and net charges and dipole charges were estimated. The sampled particles overall had net charge and dipole charge in the range of 10^{-15} C to 10^{-12} C on individual particles with diameters 20 μm -130 μm. Dipoles were more evident (more easily measured) for glass bubbles but the presence of dipoles on other particle samples was found and could not be completely ruled out for many of them. The analysis procedure is presently time consuming but can be automated so it is recommended in the future that it should be automated. The work can be extended into industrial situations by sampling moving dust suspensions, e.g. fluid bed overflows and pneumatically conveyed outflows, useful in the dairy and fertilizer industries.

Acknowledgements

I would like to express my earnest thanks to my supervisor, Associate Professor John Abrahamson, for his support, vision and patience throughout this research work. His guidance helped to shape me into an independent researcher and develop skills that will help me in advancing to my career goals. His support and warmth through the ups and downs of the PhD kept me going. John's in-depth knowledge and detailed thinking always amazed me. Working under his supervision was a great learning experience.

I would also like to thank my co-supervisor, Dr. John Marshall, for his support and guidance throughout this research. His critical thinking and constructive remarks particularly with the conference papers were always a great help and improvement.

I would like to acknowledge the CAPE technical staff of Peter Jones, Tim Moore, Trevor Berry, Bob Gordon, and Tony Allen. I thank them all for their support showed in designing, modifying and improving the experimental setup. Special thanks to Julian Phillips for designing the laser setup used in the experiments.

Finally I would also like to thank my family members for their incessant support and motivation without which reaching here was not possible.

TABLE OF CONTENTS

APPENDICES

Nomenclature

Abbreviations

Abbreviation	Explanation
AC	Alternating current
AFM	Atomic force microscopy
CCD	Charge coupled device
CMOS	Complimentary metal-oxide semiconductor
DC	Direct current
DEP	Dielectrophoretic force
FESEM	Field emission scanning electron microscope
ID	Internal diameter
LB	Langmuir-Blodgett
PDE	Partial differential equations
PMMA	Polmethylmethacrylate
PTFE	Polytetraflouroethylene
RANS	Reynolds-averaged Navier-Stokes
SEM	Scanning electron microscope
TTL	Transistor-transistor logic

Symbols

Symbol	Explanation
A	Constant which is a function of the gas, used in measuring field strength of onset of corona
a	Radius of the probe tip (inner electrode), m
a	Radius of the sphere, m
A_p	Projected area of the particle, m^2
B	Constant which is a function of the gas, used in measuring field strength of onset of corona
b	Tube inner radius (outer electrode), m
C_D	Drag coefficient
C_o	Constant in Abraham drag equation

C_p	Specific heat capacity at constant pressure, J/(kg.K)
d	Diameter, m
D	Particle diffusivity
D_p	Diameter of particle, m
E'	Field strength of onset of corona
e_o	Elementary charge, C
E_o	Electric field between the preselector plates ,V/m
E_r	Component of electric field E in r-direction
E_y	Component of electric field E in y-direction
E_z	Component of electric field E in z-direction
$\vec{E}$	Electric field, V/m
$\vec{F}_{dip}$	Dipole force
$\vec{F}_{ind}$	Induced dipole force
$\vec{F}_{image}$	Image force
$\vec{F}_{mono}$	Monopole force
F	Body force, N/m^3
$F_{d\ radial,}$	Drag force in radial direction (r-direction)
$F_{d,}$	Drag force
$F_{d,axial}$	Drag force in axial direction (z-direction)
$F_{el,}$	Electrostatic force
$F_{el,axial}$	Axial electrostatic force
$F_{el,radial}$	Radial electrostatic force
F_p	Force on a particle
G	Couple experienced by a rotating sphere
I	Identity operator
i	Turbulence intensity
J	Moment of inertia
k	Turbulent kinetic energy
k_B	Boltzmann constant, m^2kg/s^2K
L	Representative length
m	mass of the particle, kg
P	Dipole strength, Cm

p	Pressure, Pa
P_o	Absolute pressure, (measuring filed strength of onset of corona)
P_r	Component of vector P in r-direction
P_y	Component of vector P in y-direction
P_z	Component of vector P in z-direction
Q	Charge enclosed by the surface, C
q	Point charge, C
q	Heat flux vector, W/m^2
Q	Heat sources, W/m^3
q_{dip}	Dipole charge, C
q_{net}	Net charge, C
R_e	External radius of the shell, m
Re	Reynolds number
Re_p	Reynolds number of particle
r_{exp}	Experimental cylindrical radius, m
R_i	Internal radius of the shell, m
r_{model}	Theoretical cylindrical radius, m
r_O	Wire radius, m
R_p	Radius of the particle, m
r_{sph}	Spherical radius, m
S	Strain rate tensor
T	Absolute temperature, K
t_B	Characteristic time, s
t_{BC}	Modified characteristic time, s
T_o	Absolute temperature, used in measuring filed strength of onset of corona
$trace$	Sum of the elements on main diagonal of a matrix
U	Multiplication factor in equation for induced dipole force
u	Velocity vector, m/s
u'	Velocity fluctuations in x direction
u_∞	Approach velocity of the gas, m/s
u_a	Axial velocity, m/s
U_e	Energy barrier

U_g	Gas velocity, m/s
u_{gr}	Gas velocity in radial direction, m/s
u_{grsph}	r-component of the gas velocity
u_{gz}	Gas velocity in axial direction, m/s
$u_{g\theta}$	θ-component of gas velocity
$\bar{U}_m$	Mean velocity, m/s
U_o	Velocity at the nozzle exit, m/s
U_p	Particle velocity, m/s
u_{pr}	Particle velocity in radial direction, m/s
u_{pz}	Particle velocity in axial direction, m/s
U_{rel}	Relative velocity, m/s
u_θ	Angular velocity of the particle, radian/s
V	Voltage applied, Volts
v'	Velocity fluctuations in y direction
V_c	Contact potential difference, V
w'	Velocity fluctuations in z direction
x	Mean particle separation
x_c	Capture distance, m
x_c	Radius of particle, m
z	Axial distance, m
z_o	Critical distance, m
δ_o	Boundary layer thickness
δ^t	Relative air density, kg/m^3
$\Delta\theta(t)$	One dimensional angular displacement, radians
ε_e	Permittivity of the medium outside the sphere, F/m
ε_i	Permittivity of the medium inside the sphere, F/m
ε_o	Permittivity of vacuum, F/m
ε_r	Permittivity of the grain *relative* to that of a vacuum
η	Dynamic viscosity, Pa s
η_{air}	Viscosity of air, Pa s
η_r	Eddy (turbulent) viscosity
θ_d	Angle of drag force, radians
θ_p	Angles of particle velocity, radians

θ_r	Angle vector P makes with r-axis, radians
θ_{stk}	Angle of the particle relative to the downstream direction of the gas flow, radians
θ_T	Dipole-to-field angle, radians
θ_u	Angles of gas velocity, radians
θ_y	Angle vector P makes with y-axis, radians
θ_z	Angle vector P makes with z-axis, radians
κ	Coulomb's constant
λ	Dimensionless dipole strength
μ	Refractive index
ρ_a	Apparent density, kg/m^3
ρ_{air}	Density of air, kg/m^3
ρ_s	Bulk density, kg/m^3
σ	Surface charge density, C/m^2
σ_H	Maximum surface charge density for small spheres, C/m^2
τ	Viscous stress tensor, Pa
Φ	Work function, eV
Φ	Volume fraction
Φ	Scalar quantity of flow
Φ'	Fluctuating value part of flow quantity
$\bar{\phi}$	Average value part of flow quantity
$\tilde{u}$	Constant approach velocity of gas, m/s
$\tilde{v}$	Tangential eddy velocity, m/s
Θ	Rotational diffusion coefficient
ψ	Electric flux, V m
ω	Dissipation per unit turbulent kinetic energy
$\Omega(t)$	Mean squared angular displacement
$\sum SS$	Sum of errors squared

1. Introduction

Powders and other particulate solids are widely used as raw materials, intermediates, or final products with the interparticle forces contributing to the properties of powders. The electrical charging of the particle surfaces during their handling in air leads to various phenomena. Accurate knowledge of both the particle charging process and the electrostatic forces allows the control of electrostatic phenomena, which is particularly important for fine powders since the electrostatic forces may often exceed gravity or inertial forces.

Some of the applications and situations demanding this knowledge are listed by Mazumder et al. (2006) and include:

(a) generation and deposition of unipolarly charged dry powder without the presence of ions or excessive ozone,
(b) control of tribocharging processes for consistent and reliable charging,
(c) thin film(< 25 μm) powder coating and powder coating on insulative surfaces,
(d) fluidisation and dispersion of fine powders,
(e) mitigation of Mars dust,
(f) effect of particle charge on the lung deposition of inhaled medical aerosols,
(g) nanoparticle deposition and
(h) plasma/corona discharge processes.

An electric dipole consists of two charges of the same magnitude but opposite in polarity, separated by a small distance (Cross, 1987). If the charge is q and the separation is a, then the dipole moment is defined as qa. When a dipole is placed in a uniform electric field there is no net translational force on it, because the two charges experience equal and opposite forces, but there is a rotational force and the dipole will align in the direction of the electric field. If a dipole is placed in a non-uniform field it experiences a translational force as well as a couple.

1.1 Dipole Generation and Effects

1.1.1 Tribocharging (Electric dipoles on dust particles)

There are a number of mechanisms for charging particles. They are usually charged by ions arising from corona discharge or by contact with another material i.e. tribocharging. Tribocharging is the most frequently occurring phenomena for charging materials. It occurs through two mechanisms, contact charging and friction charging. In both cases the mechanical processes involved are sliding, rolling, impact, and separation of surfaces or deformation leading to charge distribution at stress points. When two insulating materials come into contact then on separation charges transfer from one to the other. The surfaces of both contacting surfaces acquire a net electric charge, with one becoming negative and other positive. The amount of triboelectric charge exchanged between two contacting surfaces depends upon their relative speed, the difference in work function, and on the pressure between the surfaces in contact (Hogue et al., 2006). As the pressure increases, the area or the number of contact points increases. The surface charge density achieved by this process can be very high. Most frictionally charged surfaces have both positively and negatively charged areas, but one polarity predominates, determining the net charge of the surface (Cross, 1987).

Proposed Dipole Theory

Generally particle electrostatic behaviour has been explained on the basis of net charge and induced dipoles. Abrahamson and Marshall (2002) proposed a dipole theory which supports the existence of "permanent electric dipoles" on dielectric particles. According to this theory on dispersion of a heap of particles the contacting surfaces separate and charge is transferred leaving some with only positive surface charge, some with negative and the remainder with both on different parts of their surface (with or without net charge) leading to dipoles or perhaps even higher order polarity. Experimental observations by Marshall (2000) concluded that in a dust aggregating environment, dipole forces are expected to *grow* as the particles aggregate rather than *cancel* as tends to happen with systems dominated by net charge. As an extreme size example of this, Wang et al. (2005) explained the particle

aggregation rates necessary to allow planets to form on the basis of the Abrahamson/Marshall dipole theory.

1.1.2 Electric Dipoles on Nanoparticles

Nanoparticles are often produced by condensation of vaporised materials. For nanometer-sized particles tribocharging is not generally possible before aggregation. However extended nanoparticle chains as long as those of magnetic dipoles (Aleksandrov et. al 1982), e.g., chains of nanospheres from an electrical discharge (Abrahamson and Dinniss, 2000) have been observed in various studies. It is known that the oxidation process of metals creates local fixed charges of both signs, and hence permanent dipoles on nanoparticles are a logical outcome of this (Abrahamson and Marshall, 2002). If the material forming a nanoparticle is reactive to the gaseous environment, like silicon nanoparticles formed from silicon vapour condensed within air, an oxide layer is formed around the particles. Several surface charges are deposited at different places on each nanoparticle leading to the formation of both net charge and an electrical dipole on each particle (Abrahamson, 2008). Spectroscopic evidence indicates strong thermally stable electrical dipoles on <10 nm metal clusters wrapped in an oxidic coating (Schemeisser, 1999).

1.1.3 Other Methods

A particle will have a net dipole, if its core is very asymmetric or has some other asymmetric history. Water molecules have no net polarization due to perfect balance of molecular dipoles. But an icy particle with no initial net dipole can fragment on collision or simply depolarize on one side, creating a net dipole (Wang et al., 2005).

1.1.4 Effects of Dipoles

The dipole-dipole interaction causes faster aggregation and higher resistance to shattering of an aggregate (Marshall and Cuzzi, 2001). An aggregate formed of dipoles is expected to develop a larger dipole and hence provide a net long range attractive force (Marshall et al., 2005). This long range attractive force can affect

deposition of particles, e.g., pharmaceutical powders in respiratory tracts, their flow behaviour, e.g., in flow through pipes or fluidisation etc.

1.2 Objectives

The dipole strength on particles has been measured only once and that also in special circumstances (Hays and Wayman, 1989). There has been no direct measurement of dipoles on individual dust particles. This study was a first attempt to do this, and the new information is expected to open up new insights for the behaviour of solid particles, both in nature (e.g. cosmology) and in industry.

The main objective of this study was to establish a technique for measurement of distributions of net charge and dipole strength for powders on dispersion in air. Equipment was designed to do this constituting a pulsing laser driven as a multi-flash, high-speed video camera and a high voltage AC supply. These three units were synchronised in order to image the trajectories of air suspended particles on a single frame or in some cases consecutive frames. The mostly spherical dielectric particles studied were subjected to a non-uniform electric field around a probe and then their recorded trajectories were followed for analysis. The image analysis software used for this purpose was Sigma scan Pro 5.

The second objective was to model the particle behaviour under electrostatic forces. The trajectories were modelled theoretically for position and orientation using the particle momentum conservation equations for both translational and rotational motion. The integrated positions from the translational momentum equation were fitted to the experimental trajectories by adjustment of net charge and dipole strength. The flow field and electric field were also modelled around the probe.

A third objective was to understand the tribocharging of particles, and consequently the aggregation behaviour of many particle systems.

1.3 Importance of Non-Uniform Field

In an inhomogeneous electric field set up between a small electrode and a surrounding larger one, monopoles can be attracted or repelled from the central electrode, but any dipoles are always attracted towards a higher field (in this case towards the inner electrode), once they have aligned themselves. In this study a simple wire probe immersed in the suspension flow to be studied was chosen as the most convenient way to generate a non-uniform field. Application of high voltage to this probe provided a nearly spherical field around and in front of the tip of the probe. It was expected that dipole forces will dominate over the monopole forces closer to the tip of the probe. The voltage was reversed in polarity frequently during a run, to allow a symmetrical treatment of both positive and negative particles while flows and velocities remain constant (reducing possible distribution bias), and also to provide additional checks on the trajectory analysis when a polarity switch occurred during a trajectory. One expects that the charge parameters of a particle will remain constant before and after such switches. For most runs the direction of any dipoles was preset before particles moved close to the probe, by subjecting them to a constant transverse field via two plates. Also this field removed some particles with higher net-charge, to allow easier analysis of the dipoles present.

1.4 Programme and Outline of Thesis

Chapter 2 presents a literature review on the measurement of particle charge and mechanisms of charging. It also includes a brief description of the analogy between magnetic and electric dipoles. This is followed by a review on dipoles in the context of geophysical applications and pharmaceuticals. Fluid dynamics involved in the process of measurements described in this thesis has been discussed at the end.

Chapter 3 focuses on design of various parts of the experimental set up. It also includes the details of particle samples analysed.

Chapter 4 and 5 describes in detail the forces assumed and equations involved in modelling the trajectories of particles. Chapter 5 presents the modelling of the flow

field and electric field close to the probe tip using the COMSOL Multiphysics 3.4 software.

Chapter 6 explains the problems encountered at the initial stage of the experiments during particle imaging etc. It also includes a stepwise procedure to measure net charge and dipole by fitting the theoretical model with experimental results.
Lastly it presents the details of image processing and extraction of data.

Finally Chapter 7 and 8 present the results and discussions. In Chapter 9 conclusions are drawn and recommendations given for further improvement of the technique.

2. Literature Survey

2.1 Measurement of Particle Charge

The presence of electric charge can be beneficial in various applications, as in dust control by electric precipitators, deposition of pharmaceutical powders, electrostatic coating, spraying, and xerography. It can also be hazardous since an excess charge buildup can cause problems such as causing segregation, unreliable flow, generating nuisance discharges and even causing dust explosions in applications such as gas-solid fluidized bed reactors and pneumatic transport lines. The measurement of electric charge on a particle is necessary to better control its behaviour. In a review by Brown (1997) two general types of methods of measurement of particle charge have been proposed, the first type "static" methods and the second "dynamic" methods. The *static* method involves direct measurement of absolute charge expressed as a number of electrons or quantity of electric charge in excess, or deficit of neutrality. A Faraday cage can be used for such static measurements based on charge transfer or induction. The dynamic methods infer charge from measuring electrical mobility which is the ability of a particle to move in an electric field and is given by the ratio of particle velocity at steady state to the field in which it moves. In dynamic methods particles are subjected to (high) electric field and the velocity reached by them is therefore related to their electric mobility. Each of the methods has its own advantages and complications.

The static charge is generally measured by transfer of charge to a capacitor and then measuring the voltage developed. The collection electrode may be a wire or can be coarse conducting grid on which particles leave charge by impact (Krupa and Jaworek, 1989). Apart from giving up its charge the particle can also be collected in a Faraday cup in which it induces an equal charge. The Faraday cup operation is based on Gauss's Law, which states that $Q = \psi$, where ψ is the electric flux. The flux from the charge on the particle produces an equal charge on the outside of the cup that can be measured by an electrometer as shown in Figure 2.1. The outside of the cup should

be shielded properly and insulation between the inner and outer containers of the cup must be extremely high.

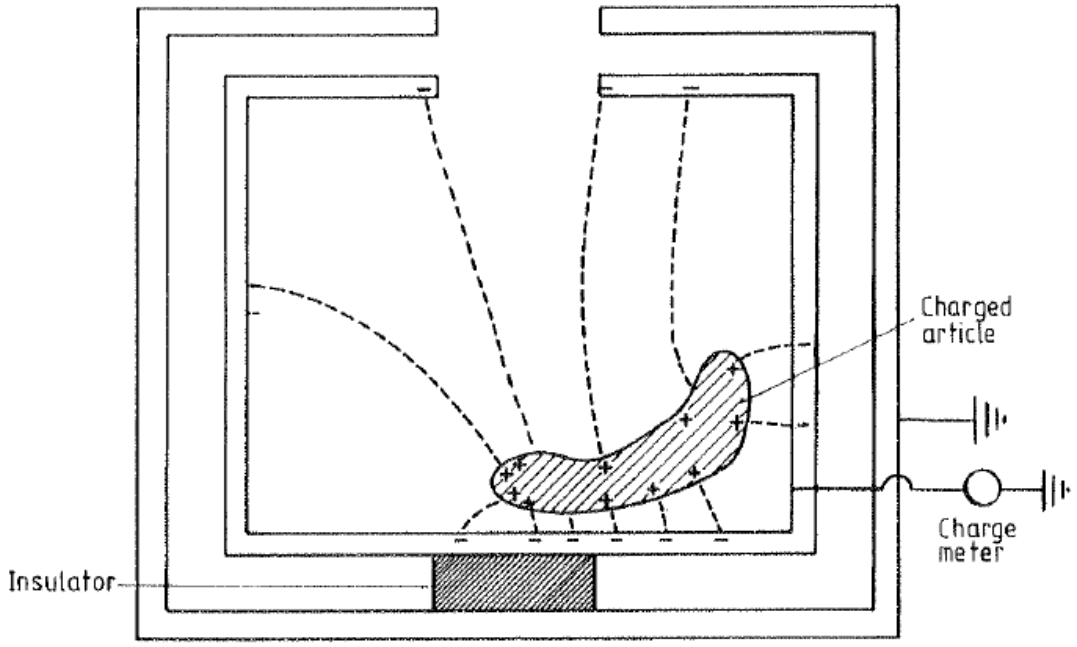

Figure 2.1: A Faraday cup (Cross, 1987).

The static methods of charge measurement have drawbacks that only the *mean* charge is measured and only charges much higher than that of a single electron can be detected. Measurement of the dynamic response of a particle in an electric field has more flexibility (Brown, 1997). Small particles carrying small charges can be classified (or measured) with dynamic analysis.

Millikan (1950) in his attempt to measure the charge on an electron used a one-dimensional equation of motion of a particle in a vertical electric field with gravity opposing the motion. This method has been used by different researchers by making various modifications for essentially measuring the charge of a single particle. Kunkel (1950) used electric field acting at right angles to gravity. The particle trajectories were recorded with a camera on photographic film using intermittent illumination to get trajectories as dotted lines. There was a problem of confining particles of interest to the focal plane of the system. The movement in a horizontal electric field of aerosol particles of size ranging from 4.5 - 40 nm was videotaped after enlarging them to about 1 μm in a visual square field of ~ 1 mm^2, with 0.1 mm depth of focus (Kousaka et al., 1981, 1983). The particles used were zinc chloride and dioctyl-sebacate and

they were enlarged by condensation of dibutyl-phthalate or dioctyl-phthalate vapor on them. It was assumed that in the enlarging process none of the particles were newly charged.

Rather than studying single particles at a time, devices have been developed in order to gather information about a population of particles yielding their size and charge distributions. Such devices are known as mobility analyzers and can work as either differential or cumulative analyzers. A number of such devices were reviewed by Knutson and Whitby (1975). A mobility analysis device can use any one of a number of geometries but the most common ones use parallel plates or concentric cylinders. It has been observed that neither the geometry of the device nor the form of flow field has a critical effect on the performance of mobility analyzers. Generally in a differential analyzer when the airflow and electric field are set, only particles within a limited range of electric mobility are selected for sampling. Emets et al. (1990) analyzed particles using an optical scattering particle counter for size-selecting. The electric field was periodically reversed so that particles with charges of either sign could be counted separately. The device allowed analysis of particles ranging from 0.3 to 10 μm in diameter with charge ranging from unity to 10^5 elementary charges of both signs.

In a cumulative mobility analyzer, an aerosol passing through the device is subjected to the electric field, with a fraction of particles being captured on the plates, the fraction depending on the field applied and electrical mobility of the particles (Brown, 1997). Penny and Lynch (1957) passed an aerosol between parallel plates for measurement of particle mobility. A variable voltage was applied between the plates and a particle in the electric field experienced an electrostatic force proportional to the applied voltage. The collection efficiency on the plate was found to be linearly dependent on applied voltage over much of its range. Most of the cumulative mobility analyzers have been designed for submicron particle sizes and an increase in size will lead to very long collection electrodes due to lower electromobility of larger particles. Also if flow velocities are large the collecting electrodes need to be longer.

A modification in the technique of collection based on electromobility of particles was suggested by Coury and Clift (1984), Coury et al. (1991). They designed an

electrostatic charge classifier as shown in figure 2.2. Dust laden air was introduced through a slit across the width of a rectangular channel in between two flows of filtered gas at the same velocity. The gas then passed between two parallel plates between which the deflecting potential was applied. Then it entered a section of parallel collecting plates where it was exposed to negative corona leading to deposition on the earthed collecting plates.

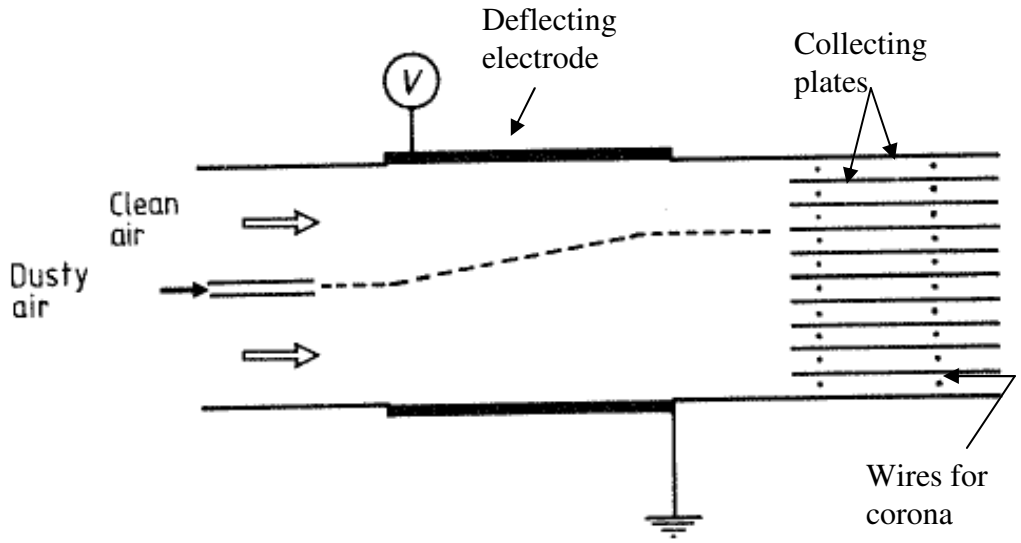

Figure 2.2: Measurement of particle charge (Coury and Clift, 1984).

The particles were classified by electromobility according to the plate on which they were deposited. This enabled shorter electrodes to be used and needed a single deflecting voltage instead of the range of different potentials used by Penny and Lynch (1957). Using this instrument, the measurement of charge distribution of gas-borne particles up to 15 microns in diameter could be made with high flow rates (up to 0.35 L/s with velocity through the collecting plates up to 1.2 m/s).

In both the static and dynamic methods the problems are (a) confining the particles to be analysed to the narrow focal plane of the system and (b) very long sampling times which involve tedious post-processing analysis. All methods originating from Millikan experiments are essentially single particle methods and considerable time needs to be spent studying each particle, hence only a small number of particles can be processed. Though the mobility analysis methods analyze populations of particles, error is introduced when there is a significant fraction of uncharged particles. Due to

turbulent diffusion (Re_{plates} ~ 20,000) such particles would blur the discrimination. This can be misleading in mass and charge measurements because the assessment of these parameters is made on the basis of the fraction of particles collected on each of the collection plates.

Laser Doppler Velocimetry (LDV) was used by Mazumder et al. (1991) in order to measure both charge as well as size of individual particles. The diameter of the particle was determined from the delay of the phase of particle oscillations relative to the phase of an oscillatory acoustic field. The charge was calculated from the velocity and direction of particle drift in a superimposed steady electric field. This method also involves considerable time (below 100 particles per second) and showed difficulties in processing particles having high charges. Kulon et al. (2003) described using the technique of Phase Doppler Anemometry (PDV) as a further extension of LDV. This has a relatively high data rate of analyzed particles, usually greater than 1000 particles per second.

A "bipolar charge measurement" system was developed by Balachandran et al. (2003) which enabled measurement of both charge polarities of bipolar charged aerosols. The electric field acted perpendicular to the flow field. The setup shown in Figure 2.3 was an integrated bifurcator-precipitator with a front-end cylindrical arrangement consisting of two D shaped sections. Each section had three wire electrodes of 1mm diameter maintained at a constant high potential during the particle flow through the system. Depending on the applied voltage and its polarity the particles entering the field were attracted to the wires or deflected towards the outer cylinder where they were deposited. The amount of charge accumulated at the outer wall was measured with electrometer separately for each section. This system provides measurements for the particle size range between 1 and 10 μm and instead of net charge the measurement of bipolar charge fractions helps to better understand the electrostatic properties of the material. This could be useful for pharmaceutical powders where in inhalation therapy the particle charge can influence aerosol deposition in lungs (Balachandran et al., 2003).

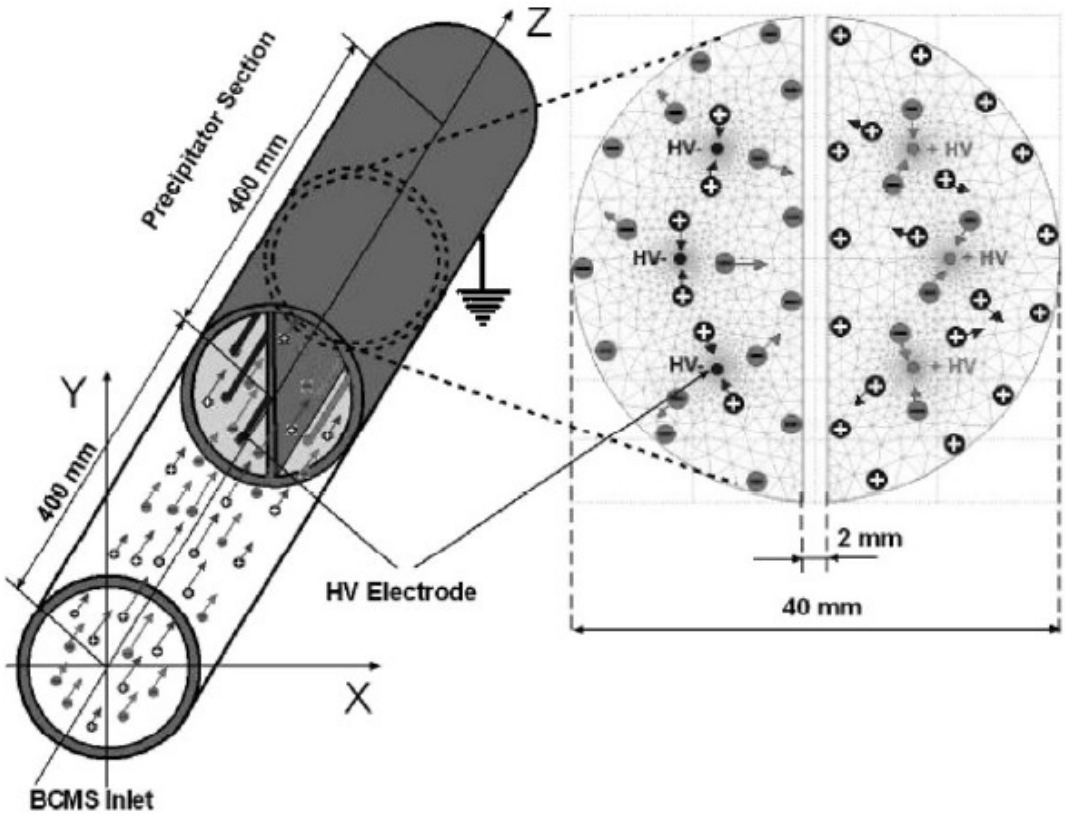

Figure 2.3: The basic geometry of bifurcator-precipitator (Balachandran et al., 2003).

Charge measurement in a fluidized bed is another common application. In fluidized bed reactors and transport lines insulator-insulator contact charging is often considered as the main cause of electrostatic charge generation and build up. Instruments using a Faraday cage cannot perform online monitoring of the specific charge distribution in a fluidised bed. Insertion of static probes leads to a disturbance in the flow, changing the local characteristics of the solids. Also deposition of particles on such a probe causes the electric potential to be lower than the true potential. Chen et al. (2003) used a suspended ball probe for measurement of the charge to mass ratio for gas-solids fluidized beds. A sensitive collision probe of diameter 3.2 mm was employed to explore induction and collision charge transfer by uniformly charged particles in the vicinity of a rising bubble, when the single bubble passed by the probe. The electric signals were recorded by an electrometer and interpreted to find net specific charge of fluidized particles. The experimental values were consistently lower than the maximum specific charge predicted using electric breakdown potential in air. This was attributed to low operating gas velocities used (Chen et al., 2003), limiting the buildup of charge intensities on particles and leakage of charges through walls of the bed. Another possibility discussed was that fluidized

beds might be charged in a bipolar manner due to wide size distributions, with fine and large particles attaining charges of opposite polarity. Therefore the specific charge for particles of specific size ranges could be significantly higher then the *net* specific charge (Astbury and Harper, 1999).

Charge measurements have also been made for a single particle impact on a target plane. Watanabe et al. (2006) have studied impact charge transfer for irregularly shaped pharmaceutical powders in the size range 500-600 μm on a stainless steel metal target using two Faraday cages. Due to the irregular shape of the particles the charge transfer greatly depended on the orientation of a particle just before impact and hence the contact area. It was observed that the impact charge increased with impact velocity. The equilibrium charge, defined as the initial charge on particle such that no net charge transfer occurs at impact, was independent of the impact velocity and impact angle. A need for recording the contact deformation with a high speed camera has been realized (Watanabe et al., 2006) in order to relate the mechanical properties to the charging behavior.

2.2 Mechanism of Charging

The charging of solids and liquids can take place in a number of ways. The major charging mechanisms can be categorised as (Cross, 1987):

1. Tribocharging
2. Corona charging
3. Charging by the capture of small particles
4. Induction charging
5. Double-layer charging

Most of the surfaces have both negatively and positively charged areas but one polarity predominates determining the net charge of the surface. When two insulating materials come in contact with each other or are rubbed together, the surfaces acquire a *net* electric charge. Each of the two surfaces is left with a net charge with one becoming negative and other positive. This contact or frictional charging, generally

known as tribocharging, is the most common surface charging mechanism. For charging surfaces in a more defined way a corona discharge is commonly used. A corona discharge is produced by applying a high voltage between two differently sized electrodes to produce a non-uniform electric field. One of the electrodes has a small radius of curvature and an electrical discharge occurs in a limited region near this electrode. An avalanche of electrons and ions of a single polarity is created which can charge any immersed surface such as that of a particle to a controlled limit.

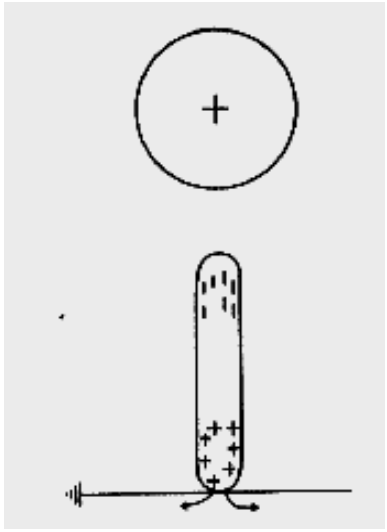

Figure 2.4: Induction charging of rod in the electric field between sphere and plane (Cross, 1987).

A particle may also become charged by the capture of smaller charged particles rather than ions (Cross, 1987). Materials which are electrically conducting can also be induction charged. A conductor becomes charged by contacting an earth provided an electric field is present (Figure 2.4). Another charging mechanism is double-layer charging. Liquids which are not perfectly pure contain some free ions. Under some circumstances these ions can be separated and the liquid acquires a net charge. Charge separation occurs on a microscopic scale at any interface with a liquid leading to the formation of a diffuse electrical layer. A double layer (Figure 2.5) is formed from two layers, the first of one polarity of charge held tightly to the interface and the other of opposite polarity attracted to the bound charge but held much more weakly.

This study concerns particles charged mainly by tribocharging which is discussed in detail in the following section.

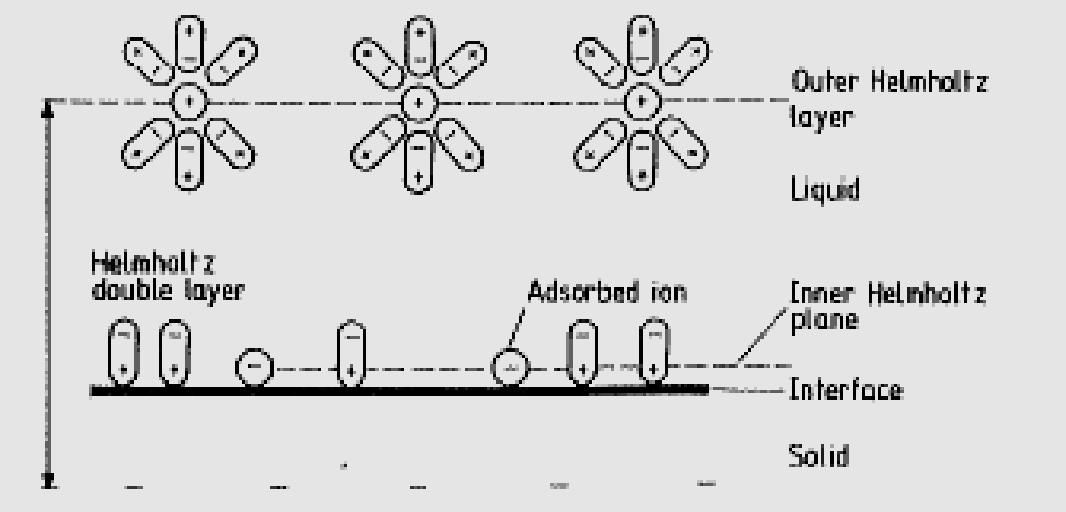

Figure 2.5: Schematic diagram of a solid-liquid interface (from Moore 1973) © John Wiley 1973.Reprinted by permission of John Wiley and Sons Inc. (Cross, 1987).

2.2.1 Tribocharging

Tribocharging can be studied under two different categories depending on whether there is a mere contact or rubbing between the two surfaces and these two are termed either ***contact charging*** or ***frictional charging***. Rather than a single contact generally charging occurs when two surfaces are rubbed together in air leading to frictional charging. The remainder of this section will introduce tribocharging in general, and will be followed by sections on contact charging and then frictional charging.

To understand the charge movement between two materials the energy of the electrons and ions at their surfaces is considered and the way they move both within and between the materials. Materials can be arranged in a table according to the direction of positive charge which is transferred, with every material charging positive against material below it in the table. This is known as the triboelectric series. The subject has three main divisions: electrification of metals by metals; of insulators by metals; and of insulators by insulators.

Metal-Metal Charging

The charge acquired by a metal when contacted by another metal is determined by the condition that, for equilibrium, the Fermi levels of the two metals must coincide. In metals the outer electrons are assumed to form a sea of electrons free to move

throughout the crystal lattice. The energy required to move an electron from the top of the distribution (Fermi level), out of the metal to infinity, is called the work function. The metal with a larger work function than that of the other charges negatively. A contact potential difference is built up between the metals equal to the difference in the work functions ϕ divided by the elementary charge

$$V_c = (\phi_B - \phi_A)/e_o \tag{2.1}$$

where e_o=1.602 x 10^{-19} C. Typical metal work functions are 4 to 5 eV and thus the work function differences are 0 to 1 eV. During the separation process of the surfaces, the capacitance between them decreases and thus the potential difference increases if the charge remains fixed (Harper, 1967). For sufficiently short distances, the increasing potential difference drives a tunnelling current in the direction to maintain a constant contact potential difference. The tunnelling current decreases with increasing distance and is effectively stopped at a critical distance z_o that is of the order of nanometres (Lowell, 1976).

Metal-Insulator Charging

At the absolute zero of temperature both crystalline insulators and semiconductors have a full valence band and an empty conduction band with each having different band gaps. The delocalised nature of an electron and the band structure of the electron energies are a consequence of the periodicity of the crystal. However most of the insulators are amorphous. In a real amorphous material there is still effectively a forbidden energy gap but for temperature above zero there will be some electrons with energies within that gap localised at one position in the material (Mott, 1968). Hence there is no completely forbidden gap in the insulators. Localised energy levels exist due to impurities, defects in crystal structure, and the presence of a surface. The contact potential between a metal and an insulator depends upon the energy states within the insulator band gap and the Fermi energy of the metal. Since numerous experiments (Cross and references therein) have found the amount of transferred contact charge to vary linearly with the metal work function, it is customary to assign an effective work function to insulators. Triboelectric series of the insulators have been constructed in this way.

Ionic Conduction in Solid Insulators

Ion conduction is observed in some crystalline insulators, in electrolytes, in many amorphous materials and in electrolytic layers on surfaces with adsorbed water. For ionic conduction in dielectric solids, ions will move by a thermally activated process. At a temperature T, the ion will have a probability P, of having enough energy to jump to an adjacent stable position, given by

$$P = A\,exp(U_e / k_B T) \tag{2.2}$$

where U_e is the energy barrier which must be overcome, T is the absolute temperature and k_B is the Boltzmann constant (Cross, 1987).

The electrification of insulators by metals and of insulators by insulators will be discussed in detail in the following sub-sections.

2.2.1.1 Metal-Insulator Contact Charging

The phenomenon of contact charging has a long history but is still little understood. Little progress has been made towards understanding contact charging of solids because of the lack of experimental reliability of the results. Experiments on contact charging have mostly been carried out in a vacuum to avoid charge loss by the air electrical breakdown when the surfaces separate. There are two main categories of present models of contact charging of insulators by metals. The first category includes those models that assume a thermodynamic equilibrium is achieved between the contacting surfaces. The second category of model assumes that equilibrium is not established during the time of contact and contact charging is due to electrons tunnelling into states at or near the surface of the insulator. The thermodynamic equilibrium model predicts a dependence of the contact charge density on the work function of the contacting metal. The non-equilibrium (tunnelling) model predicts contact charge density from surface states density or redistribution of electrons. Both these concepts and the progress made will be discussed in the following paragraphs.

The theory of metal-metal contact electrification is based on thermodynamic equilibrium. On contact between two metals electrons are exchanged between them so that they come into thermodynamic equilibrium. As the metals separate as explained earlier the electrons will tend to tunnel across the gap to maintain the thermodynamic equilibrium; that is to maintain the potential difference equal to the contact potential difference (Harper, 1967). Hence charge on the metals after separation will not be same as the charge when they are in atomic contact. The observed order of magnitude of the surface charge density σ for different insulators after contact with a metal surface is in the range $10^{-5} - 10^{-3}$ C/m^2 (Lowell, 1976).

There are a few elaborate reviews on the topic by Harper (1967), Lowell (1980) and Cross (1987). Most of the earlier experiments (Davies,1967,1969; Arridge ,1967) on charge transfer between metal and insulator showed a simple linear relationship between the charge transferred and the metal work function but later some non linear relationships and scatter was reported (Lowell, 1976). If the contact charge on the insulator depends on the metal work function, the mechanism of transfer can be attributed to the electron transfer and the amount of energy transferred is governed by the energy difference between the metal Fermi level and some energy level in the insulator which is difficult to define (Davies, 1969; Lowell and Rose-Innes, 1980). From the experiment carried out by Davies (1969) for contact charging of Nylon 66 by various metals it was observed that the insulator may charge positive or negative depending on the work function of the contacting metal. On this basis Lowell pointed out the possibility that the insulators contain empty states that can accept electrons from metal, as well as full ones that can donate electrons. The energy of both kinds of electron state must be close to Fermi energy of metals. For these states one possibility is that there are many same-energy electron states, but some of them are empty and some occupied. Alternatively the electron states may be distributed over a wide range of energy, with states below a certain energy being full and those above being empty.

When an insulator is repeatedly touched by a metal on the *same* spot, the charge transferred to insulators increases on each contact (Harper, 1967; Fabish et al., 1976). There are various other explanations for increase in charge by repeatedly touching insulator at the same place with same metal like total time of contact, different contact area, viscoelastic behaviour of polymers, thermodynamic equilibrium etc., but none is

fully able to explain the process. If the area previously contacted receives more charge on a second contact then thermodynamic equilibrium cannot have been established between the metal and the insulator, at least in a single contact (Lowell and Rose-Innes, 1980). Lowell's (1976) experimental results on polyethylene, PTFE and PET showed that multiple contacts were required to establish the previously observed linear relationship between charge transfer and work function. He proposed that the contact charge resides in the surface states or in the bulk states which are so close to surface that electrons may tunnel directly between them and the metal. This was the basis for the tunnelling model. During contact the electrons enter or leave only those states which were within 3 nm of the surface i.e. close enough to the interface. Bulk states were filled during multiple contacts in which charge was redistributed during, or after, each contact. He suggested that the successive contacts disturbed the microstructure of the polymer near the surface so that some of the filled traps moved away into the bulk and the empty states were brought closer. This mechanism could not work for hard insulators and hence would not account for charge accumulation in these materials.

Homewood and Roseinnes (1982) conducted experiments with hard crystalline insulators (diamond and corundum) using a solid gold sphere of 2 mm diameter as a metal contactor. The time of contact was kept equal to 5 s and the time between contacts varied from 9.5s to 114 s. The rate of build-up of charge on repeated contacts was faster for longer times between contacts. The mechanism of charge accumulation was thought to be due to slight electrical conductivity. On first contact the charge transferred was held close to the region of contact by attraction to its image charge. Between the contacts due to its self repulsion, the charge leaked from the point of contact because of slight conductivity and was replaced on the next contact thereby increasing the total charge on the insulator.

Generally all theories of electronic transfer assume a specific distribution of electron energy levels. Hays (1978) explained the linear relationship between the charge transferred and the work function on the basis of high density of the surface states. The bulk states close to the surface can communicate with a contacting metal either as electrons tunnel short distances into the insulator or to states associated with the surface. Fabish et al. (1976) investigated the distribution of electrons between the bulk

and the surface states in their study of the distribution of charge in polymers by measuring the surface potential. They concluded that low work function metals interacted mainly with the near bulk states whereas high work function metals filled mainly the surface states. The bulk states were filled to a depth of 4 μm below the surface while Lowell (1976) calculated the depth for an electron transfer from the surface to the bulk states for insulators only to be 2 nm.

In the tunnelling models the transferred contact charge cannot transfer beyond the tunnelling distance (penetration depth) below the surface of the insulator. Homewood (1984) found the depth of charge penetration for PMMA (polmethylmethacrylate) to be ~0.4 nm in support of the tunnelling model for charge transfer. They calculated a characteristic depth to which charge must be distributed into the bulk of the insulator to achieve thermodynamic equilibrium to be about 300 nm. It was concluded that the two types of models (equilibrium or tunnelling) can be distinguished by measuring the distance to which contact charge penetrates into the insulator.

Charge generation has also been studied by single impacts of particles with a target plane due to their simplicity leading to fundamental understanding. Matsuyama and Hideo (1995) studied contact electrification through impact charging generated by single collisions between spherical polymer particles (Teflon, Nylon, Polystyrene etc.) 3.2 mm in diameter and metal plates. They observed that the surface charge densities were smaller than expected from the properties of contacting surfaces (assuming a typical solid state work function difference of 1eV leads to results orders of magnitude larger than observed) but comparable to that by which the gaseous discharge in the atmosphere occurs (Pascoe's Law). Later they tested metal particles and proposed (Matsuyama and Yamamoto, 2006a) a charge relaxation model. The model predicts that both the polymer and the metal particles lose all initial charge and lose the charge generated at contact due to impact with a metal target by charge relaxation during the separation process. This charge relaxes during contact as the contact was assumed to be sufficiently long to cause gaseous discharge in atmospheric conditions.

Schein (1999) carried out "double blow-off" experiments with 10 micron toner particles in which the toner particles were blown onto a piece of metal and then blown

off. If the final particle charge on the particle was limited by air breakdown then it is determined by the particle's potential curve being tangent to Paschen's curve (Schein, 1998). It was found that the charge to mass ratio was much less than the equilibrium charge that such particles should carry if it was limited by air breakdown. Also if air breakdown limits the final charge then it is uniquely determined by the particle diameter and dielectric constant. Even then toner charge is highly variable among different toner-carrier mixes and even within a mix. Hence Schein concluded that toner charging was not limited by the gaseous breakdown. Later Matsuyama et al. (2006b) have also questioned their own gas discharge relaxation model as it fails to explain the difference between approach and separation force in an atomic fore microscopy (AFM) experiment conducted previously (Matsuyama and Hideo, 1995).

2.2.1.2 Insulator-Insulator Contact Charging

The mechanism of insulator-insulator tribocharging is the least physically understood of the three basic types of contact charging. Many theories consider that the transfer of charge from one insulator to another is caused by the same basic mechanisms applied to metal-insulator charging. Davies (1975) suggested that the charge transfer in the insulators can be correlated with their "Fermi levels", with electrons passing from the insulator with higher Fermi level to that with the lower.

The surface states theory has been supported by many authors for insulator-insulator charging. According to the theory electron states localised at the surfaces exist within the large band gaps characteristic of the insulators. The surface charge density arising due to the contact charging is controlled by the number density of these states (Bailey, 2001). The charge transfer between two materials in contact then occurs until the Fermi levels align as in metal-metal and metal-insulator contacts. With a lower number density of the states the charge transferred is limited to a lower value. There have been other theories (Fabish et al. 1976; Fabish and Duke,1977) stating that the transfer of charge between insulators is similar to that between metals in terms of electron exchange but the details of charge transfer are not clear. These studies do not consider the fact that upon physical contact insulators do not have free or nearly free electrons to exchange (Hogue et al., 2006).

In the triboelectric charging of insulators other charged entities such as ions or charged molecules with more freedom to move may play an important role (Bailey, 2001, Hogue et al. 2006). Ion exchange has been considered responsible by many researchers for metal-insulator charging. Ions can exist on the surface of the insulators in vibrational energy states forming weak bonds with the surface due to intermolecular forces or in a thin surface water layer as solvated ions. Most surfaces in the air will be covered by a thin water layer ranging in thickness between a monolayer to a macroscopic thin film (Cross, 1987). The solid -aqueous interface then acts as a charged double layer with ions of one polarity preferentially attracted to the surface. Hence the net charge on the surface of a solid material would be largely balanced by an opposite charge of ions.

Recently Hogue et al. (2006) studied the atmospheric air pressure dependence of surface charge density on triboelectrically charged insulators and found that it was unrelated to Paschen discharge or air breakdown. It was observed that the insulators discharged rapidly upon lowering the atmospheric pressure. Polymer samples were charged by a rubbing contact with wool or PTFE (polytetraflouroethylene) felt and *lowering* of atmospheric pressure resulted in the more rapid discharge. An ionic charge exchange mechanism was given as a possible explanation. Most of the surface charges were on volatiles and hence on lowering pressure they evaporating off the surface rapidly once their vapour pressure were reached. A residual surface charge (~20% of initial) was observed and explained to be a result of ions with lower vapour pressure than applied, or some minor electron exchange between the two surfaces.

2.2.1.3 Frictional Electrification

There have been different theories related to frictional electrification but none has been accepted universally (Harper, 1967). Kornfeld (1976) modelled the phenomenon of frictional electrification in insulators suggesting that solid insulators are not electrically neutral due to structural imperfections. Under atmospheric conditions, ions and other species from air adsorb on the surface of an insulator and compensate for its intrinsic electric field. Friction of one body against another mixes their surface layers and the compensation for the intrinsic field becomes disturbed leading to electrification of the bodies. Haenen (1979) in his experimental work related the

charge transferred, q, to the force of contact, F, for rubbing of metals with polymers by the equation

$$q = F^{\alpha} \tag{2.3}$$

α was between 0.3 and 1 and was mainly a function of the metal and to a lesser degree, the polymer. An increase in charge with rubbing velocity has generally been observed (Montgomery, 1959). The moisture content of the polymer and temperature are also important as they experimentally affect the charge density and polarity (Coste and Pechery, 1981).

Nakayama (1996) conducted scratching experiments with a diamond stylus on Al_2O_3 and S_3N_4, glass, and on PTFE specimens with an aim to clarify the relationship between the tribocharging phenomenon and the frictional resistance in a system of an insulating solid sliding on an insulating solid. Surface potentials and friction coefficients were measured simultaneously during scratching and it was found that the surface potential caused by tribocharging correlates positively with the friction coefficient except for PTFE. In the case of PTFE it was difficult to find a correlation but it was observed that when the surface potential of PTFE was at a minimum, the friction coefficient was also locally minimized. PTFE is known to be chemically stable and relatively inactive with respect to adsorption of molecules. So the experimental results of PTFE suggested that the correlation between the surface potential and the friction coefficient is influenced by the interaction between the solid surface and ambient gas molecules. Holscher et al. (2008) reviewed the principles of atomic-scale frictional behaviour of nanoscale contacts in relative motion. They concluded that the influence of real-life omnipresent surface adsorbates needs to be considered in friction models. This was based on the theory by He et al. (1999) which suggested that realistic contacts almost always lead to adsorbed, but mobile molecules (e.g. small hydrocarbons or water molecules) that are trapped between the sliding surfaces. These molecules prevent direct interaction of the surface potentials of the sliding interfaces by acting as spacers. Due to their mobility they simultaneously lock at surface potential minima for both sliders thus making the friction coefficient independent of the details of the surface geometry, e.g., of the apparent contact area.

A friction apparatus was constructed by Ohara et al. (2001) to understand the frictional electrification due to reciprocating friction between flat materials such as polymer films or LB layers deposited on flat substrates. The Langmuir-Blodgett (LB) method was used to obtain a surface model in this case. The LB layers have molecules with both hydrophobic and hydrophilic groups. Several molecules each with a different specific polar group bonded to a common hydrocarbon chain can be chosen. The measurement of electrification of such layers deposited under various conditions helps in understanding the influence of the attached atomic groups and molecular assembly on frictional electrification. This helps to construct a frictional electrification series of atomic groups based on both the polarity and magnitude of measured electrification charge and can be used to design new antistatic polymeric materials.

Frictional electrification is a complicated process and the work is still on to understand the charge transferred in various circumstances.

2.3 Non-Uniform Charge Distribution on Insulators

This section elaborates the review presented by Abrahamson and Marshall (2002) on non-uniformity of surface charge distribution and extends it further including some later studies. There have been various studies supporting surface non-uniformity of charge distribution in past years. Earlier work of Hull (1949) observed the distribution of static electricity on a larger surface like paper, separated from a metal surface. A special powder was used to demonstrate the distribution of positive and negative charges. It was evident that patches of positive and negative charges existed on the same sheet of paper with only a small (400 μm) neutral space between them.
Kunkel (1950) in his classical study reported that the dispersion of dust into a cloud led to almost equal numbers of positive and negative particles. He found that the average charge distribution for fine quartz particles was independent of the conditions of dispersion. It was concluded that electrification occurs during the initial phase of dispersion at the instant of separation of the two surfaces.

If different charges exist on different parts of the surface of the same particle, a dipole is indicated on that particle. The study carried out by Beisher and Winkel (1936)

found an indication of permanent dipoles on micron sized dye particles. The close-in approach of two dipoles was modelled. The dipole to dipole forces were predicted to affect both the rate of aggregation, and the self-aligning orientation. However, this work appears to have been regarded as a curiosity, and has not been more widely applied, probably because of the unusual properties of the materials it was applied to. These dye materials electrically polarised on cooling, an effect clearly shown on 5-mm long crystals. The ~10 μm aerosol making up the chains was the product of condensation of vapour, clearly going through cooling.

Electrostatic charging of particles involves applications in any office environment in form of the photocopiers and printers. The small size of particles (~ 2 μm -10 μm) used and the small distances involved, allow very intense electric fields to build up without the need of very high voltages. There has been lot of research work gone into adhesion of charged toner particles due to its critical importance in electro-photographic processes. The toner adhesion to the carrier, photoreceptor and paper strongly influence the image quality. In related toner studies (Hays, 1978; Lee and Ayala, 1985; Lee, 1986) electrostatic forces were found to account for the high magnitude of adhesion forces in comparison with van der Waals forces. It was suggested (Hays, 1978) that the electrostatic image forces can account for the observed toner-carrier adhesion if the toner particle is non-uniformly charged. The measured adhesion of a spherical charged toner particle was about four times larger than the calculated electrostatic image force based on a uniform distribution of (net) charge on the surface.

In a similar work Hays and Wayman (1989) studied the adhesion of triboelectrically charged dielectric spheres using an electric field detachment method. They conducted an experiment on charged dielectric spheres of styrene divinylbenzene with a nominal diameter 99 μm. After repeatedly detaching the sphere with a potential applied between closely spaced electrodes (space about 1.4 times the particle diameter) magnitudes of dipole and even quadruple moments were estimated using a fitted set of multipoles, put into a model giving the induced voltage versus time. They observed non uniformity of the surface charge by monitoring the charge induced on the lower electrode. The oscillatory component in the induced charge signal was observed and successfully attributed to *permanent* dipole and quadruple moments of the toner

particle. It was concluded that the adhesion of the spheres was dominated by electrostatic forces due to a non- uniform surface charge distribution.

Fowlkes and Robinson (1998) calculated electrostatic force on a dielectric sphere in contact with a grounded plane in an externally applied electric field (normal to the plane). They modified the simple expression for image force on a point charge to calculate the image force on the sphere by including a dielectrophoretic force (DEP).To model this force they represented the dielectric sphere and its image by a simple dipole. They further corrected the expression for DEP by the use of higher order multipoles. The solution set of multipoles and their images was found by simultaneously solving a set of three electrostatic equations.

Takeuchi (2006) determined the adhesion force of acrylic spherical powder on an aluminium substrate. The particles had a known q/d (charge to diameter) value determined by means of classification based on particle motion in a constant electric field under gravity. It was observed that even for particles with the same net charge and size there was a spread of 3-4 orders of magnitude in the adhesion forces. Also for similar q/m (charge to mass), the adhesion force of irregularly shaped toner was larger than that of spherical toner. The possible reason for both of the observations was attributed to non-uniform charge distribution on the surface of the particles.

In a contrary study Gady et al. (1999) measured toner to photoconductor adhesion as a function of an increase in the amount of silica additive on the surface of the toner. The force needed to remove the particles from a photoconductor was measured using an ultracentrifuge capable of spinning at 70,000 rpm. They observed an improvement in transfer efficiency with increase in silica concentration while dot integrity and resolution both degraded. They explained the contribution of van der Waals interactions and electrostatic forces to total particle adhesion forces on the basis of total particle removal force (for the toner particle calculated to be 970 nN at the 50% removal point). They predicted the contribution of electrostatic forces assuming non uniform charge distribution on each particle. It was argued that in such a case the charge density needed for the observed adhesion will result in electrical fields high enough to generate electrical discharges as the toner particle approached the photoconductor during development. Then they predicted the electrostatic force

contribution within the confines of the Paschen limit to be of the order of 30 nN which was far less than the measured force needed for detachment. Hence it was concluded that the adhesion force due to presence of localized charged patches was much smaller than the contributions due to van der Waals interactions (predicted to be 943 nN by the Johnson-Kendall-Robert theory of adhesion, 1971). It was observed that electrostatic forces associated with the charge on the toner became more significant with increasing silica concentration and the two types of interactions became comparable when silica concentration reached 2%. In their calculation of electrostatic force there could be a doubt about electric charge draining from the surface of the insulators (apparently as in this charge may be below the surface).

2.3.1 Existence of Patch Charges

One possibility for patch charges to arise on a surface was suggested to derive from different values of the work function over different areas of a material surface (Harper, 1967). The in equivalent regions can be due to differing surface preparation, uneven distribution of adsorbates, crystallographic orientation, or variations in local geometry. This theory was supported by Pollock et al. (1995) who emphasized the significance of patch charge in interaction between small particles. An estimation of dipole attraction between two particles due to these patch charges was made for two unequal like-sign charge patches on opposite ends of each particle. Gady et al. (1997) used an atomic force microscope to study attractive and separation forces between a polystyrene particle and a graphite substrate. The data indicated that a localised charge, generated triboelectrically due to contact of the sphere and substrate, had a dominant contribution to the interaction force.

In support of the theories explained in the previous section on adhesion of charged toner particles (based on non-uniform charge distribution), Jones (1995) presented a very simple patch charge model with the total particle charge divided into two fractions, one located in a patch on the surface directly adjacent to the planar substrate and the second located at the particle centre. He calculated the net electrostatic adhesion force on an isolated particle and showed its strong dependence on the patch charge fraction.

The explanation of electrostatic force due to patch charges was strongly supported by a later work of Sounilhac et al. (1999) who measured the force gradient between a tungsten tip and a flat oxide substrate using atomic force microscopy. Their patch charge model reproduced the experimental force versus separation distance well for reasonable patch charge densities, in contrast to the work by Gady et al. (1997). There also has been recent support for patch charges in the latest work of Matsuyama and Yamamoto (2006a) in their study of electrostatic forces between a partially charged dielectric particle and a conducting plane.

Abrahamson and Marshall (2002) proposed a theory based on the concept of non-uniform charge distribution. It states that patches of opposite permanent charge can occur on the *same* particle. They explained the formation of extended chains of particles in the gas phase based on patch electrical charges on each of the particles in the chain. They emphasized the existence of permanent electric dipoles which are composed of separated persistent charges of opposite sign on the same particle. Considering the dispersion of a heap of particles into a gas the surface of each pair of touching particles is left with patches of equal and opposite charge per contact on separation. In a given sample a few particles are left with net positive surface charge, a few with net negative and there are some with both positive and negative patches which result in dipoles or higher order multipoles. The study above leads to a conclusion that there is a strong need to establish a rigorous theory for the generation of patch charge on particles, leading to attractive electrostatic forces between them.
Figure 2.6 demonstrates the generation of permanent dipoles on particles using the idea of fixed electrical patch charges on them, from separation of particles during dispersion.

2.4 Magnetic Dipoles and the Analogy with Electric Dipoles

The concepts of magnetic and electric dipoles are analogous to each other and much behaviour of magnetic dipoles can be applied to electric dipoles. This section presents a brief overview on magnetic dipoles and its relation to electric dipoles.

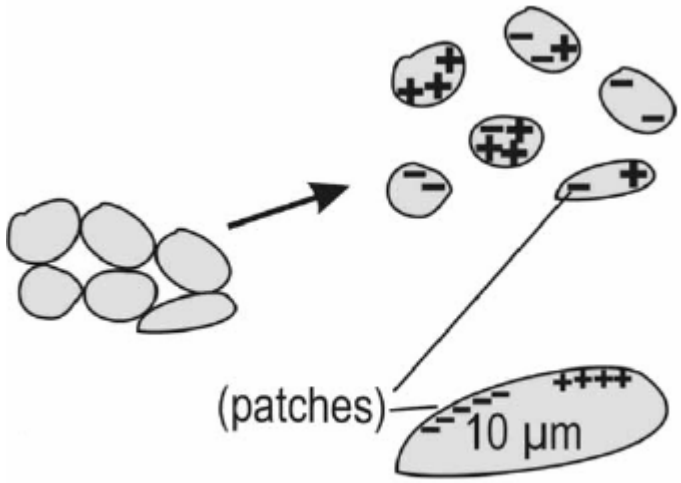

Figure 2.6: Formation of surface charges by dispersion of > 1 µm sized particles, with separation of initial contacts. Enlargement of one particle, showing patches of charge (Abrahamson and Marshall, 2002).

Helgesen et al. (1988) studied the aggregation of microspheres of sulfonated polystyrene containing 30% (weight) iron oxide in the form of evenly distributed grains in a thin shell near the surface. There was a tendency of the microspheres to form chains and open loops at high magnetisation whether a magnetic field was applied or not, showing the preference of alignment of the magnetic dipoles to each other. In an attempt to study the way particles respond to the application of a dipole inducing field Fermigier and Gast (1992) studied the aggregation of superparamagnetic latex particles with a mean diameter of 1.5 µm in a suspension. A dimensionless dipole strength λ was defined as the ratio of the energy of dipole-dipole interaction to the thermal energy (this was the energy of random diffusion via Brownian movement in a liquid). In most practical situations the dipolar interaction strength greatly exceeded the thermal energy (Fermigier and Gast, 1992). It was observed that the particles experienced attractive dipole interaction even at low solid volume fractions of ~ 0.004 (mean particle spacing of 7.6 µm) and aggregated tip to tip to form linear chains parallel to the applied field. Chains of dipoles bend in a way to attract each other if they are flexible (Gross and Kiskamp, 1997). Magnetorheological fluids (suspensions of magnetisable particles in a carrier fluid) were studied by Promislow et al. (1994). They observed that with an increase in magnetisation the rate of linear aggregation of magnetic particles in an aqueous

suspension exceeds the rate of aggregation by Brownian thermal diffusion (dipole strength, $\lambda \sim 1$).

Nuth and Berg (1994) observed similar coagulation of iron grains (~20nm) in the gas phase in the presence of a magnetic field. Magnetically induced dipole-dipole interactions between the grains led to the formation of streamers of fluffy iron aggregates and even small dust balls. They suggested that there was a significant role of magnetic dipole-dipole interaction in the initial stages of plantesimal accretion in protostellar nebulae. Later the spontaneous formation of iron aggregates was observed even in the absence of external magnetic fields by Withey and Nuth (1999). This strengthens the previous explanation of plantesimal formation as the agglomerates could form in a nebular environment that may be completely devoid of ambient magnetic fields. The single-domain iron grains could form via vapour phase nucleation such as in impact-generated vapour plumes or in thermal condensation zones. These grains should show greatly enhanced coagulation efficiency due both to the longer ranged attractive magnetic forces (Nuth and Wilkinson, 1995) and to enhanced sticking probabilities when magnetic grains collide with superparamagnetic, single domain, or multidomain grains (Withey and Nuth, 1999).

The rates and forms of aggregates formed by electric dipoles have been characterised alongside their magnetic counterparts by Abrahamson and Marshall (2002). Unlike the magnetic particles, in the case of electric charge there are both monopolar and dipolar particles so a wider variety of behaviour is expected. The electric dipole aggregation can be characterised on a similar basis of the particle concentration, the strength of the dipole and the time of aggregation. A capture distance x_c is defined at which the dipole energy is equal to the thermal energy ($\lambda = 1$). The approach of particles closer than the capture distance results in certain capture as the pair of particles cannot escape the attractive force by diffusion. The dimensionless dipole strength, λ thus defines the close-encounter geometry. If x is the mean particle separation in the suspension, the ratio x_c / x can define the geometry of the capture volume in relation to the diffusive volume. Both these dimensionless ratios, λ and x_c / x, are plotted to map out the course of aggregation giving the number of particles in an aggregate and its shape.

A characteristic time is defined as the average time t_B leading to collision in a dilute purely diffusive particle system.

$$t_B = \frac{d^2}{24D\phi} \tag{2.4}$$

where d is the particle diameter, D is the particle diffusivity (for a continuum fluid, $D = k_B T / 3\pi\mu d$, μ is the fluid viscosity), and ϕ is the volume fraction occupied by the particles. Promislow et al. (1994) has given a modification of this collision time to allow for dipole-dipole interaction in a three dimensional system of particles with magnetic dipoles induced by a field. They defined a capture volume for each particle defined by $U(x_c) = k_B T$ surface, and if another particle enters this capture volume, the two particles undergo ballistic aggregation. So with a scaling of ϕ by replacing it with the fraction ϕ_c of total volume within a radius of x_c of all particles, $\phi_c = \phi x_c^3 / (d/2)^3$ the modified characteristic time is given by

$$t_{BC} = \frac{1}{192}\frac{d^2}{D\phi}\left(\frac{d}{x_c}\right)^3 \tag{2.5}$$

Promislow et al. (1994) measured the average agglomerate size and plotted their data for a range of dipole strengths and volume fractions onto one curve with dimensionless time, t/t_{BC}.

2.5 Geophysical Context (Aggregation)

Dust particles in space accumulate charge by exposure to plasma and UV radiation or just by grain-grain contact and contact with various surfaces (Sternovsky et al., 2002). The electrostatic forces between these charged particles strongly influence their behaviour and can cause aggregation or dispersion of the particles. These forces are important in many astrophysical and planetary settings (Marshall and Sauke, 1999). Electrification due to dust-dust collisions has been observed in terrestrial dust storms (Karma, 1972). Studying the electrostatic interaction between these granular dust

particles can give rise to some evidence concerning the formation of fundamental cosmological systems.

In the dust nebula around a new born star the outward stellar winds are expected to disperse most of the unagglomerated dust in a few million years (Briceno et al., 2001). Any formation of planetesimals needs the progenitors to accrete in this given time frame. The agglomeration rate of micron-sized dust grains depends on a number of factors (Bridges et al 1996):

- their collision rate and any long range forces that would increase that rate,
- their collision inelasticity, and
- the adhesive forces that could stabilize the new assembly and prevent fragmentation as it grows larger.

Particulate aggregation is accepted to be responsible for the birth of stars from collapsing nebulae, the formation of planets through accretion processes, and the behaviour of planetary ring systems (Lewis et al., 1995). Van der Waals forces by themselves do not account for the rate of agglomeration of the micron-sized dust to ultimately form planetesimals (Ossenkopf, 1993) so the role of some long range forces is indicated. Electrostatic forces are the likely candidate to enhance agglomeration.

Particle dispersion experiments were conducted in the United States Microgravity Laboratory (USML) by Marshall et al. (1997). The apparatus consisted of eight miniature cloud chambers of 125 cm^3 internal volume. Each chamber was loaded with several grams of some selected granular materials. To disperse the grains 100 cm^3 compressed air at 184 kPa was pumped through the base of the chamber. The air escaped through chamber-wall screens and air motion damped out after ~30 seconds. The dispersed grains were then allowed to aggregate for up to 30 minutes while being video taped through the chamber windows. Instantaneous aggregation of grains of different materials like quartz and volcanic sand for grain sizes ranging from 100-800 μm was observed after cessation of air turbulence under microgravity conditions. Aggregation was observed for both insulating and conducting materials due to grain-grain attraction. Filamentary forms were found to be most prevalent with length of filaments varying with the concentration of particles. At high concentrations 3-

dimensional loosely bound assemblies were formed with diameters of several centimetres. These assemblies could attract particles from several centimetres distance at a velocity of 0.5-0.1 cm sec^{-1}. The process of aggregation was finished within the first few tens of seconds and no further significant development of aggregates was observed. The noticeable characteristic of these large aggregates was that no grains were ever repelled by them, ruling out a dominance of net charge (monopole) force. The traditional modelling of accretion based on random motion or gravitational forces appeared to underestimate the observed encounter potential by orders of magnitude (Marshall and Sauke, 1999) and hence the electrostatic aggregation seemed to be important.

Marshall and Cuzzi (2001) proposed that their aggregates must have a large dipole. The dipole-dipole interaction would cause faster aggregation and also higher resistance to aggregate shattering (Marshall and Cuzzi, 2001; Abrahamson and Marshall 2002). The possible formation of primary dipoles in space to fit in with the aggregation ideas of Abrahamson and Marshall was explained by Wang et al. (2005). In Wang's study cryogenic (5-100 K) amorphous water ice was considered responsible for agglomeration as it could acquire spontaneous dipoles. In normal high-temperature ice, water molecules have a random balance of "up" and "down" dipoles. However the water ice formed by vapour deposition on cold substrates (<165 K) becomes spontaneously polarised via partial alignment of the water molecules possibly due to the electrical asymmetry of the ice-vacuum interfaces (Iedema et al., 1998). The predicted dipole- dipole interactions between ice particles (Wang et al., 2005) was 3 orders of magnitude larger than the estimated van der Waals forces.

The aggregation in clouds of submillimeter quartz and volcanic ash particles in microgravity has been explained by Marshall et al. (2005) on the basis of the dipole model proposed by Abrahamson and Marshall (2002). Tribocharging due to collision of grains leads to monopoles from any imbalance of opposite charges, and to dipoles from irregular charge distribution. These dipoles were held responsible for observed filamentary structures. The grains rotated as they approached one another such that their dipole axes were mutually aligned and attractive. The end of the filament was more attractive than individual grains due to the configuration of electric field lines around the aggregate, hence leading to particle chains.

The main conclusions of the study (Abrahamson and Marshall, 2002; Marshall et al., 2005) are that monopole forces are dominant at large intergranular spacing but below a certain critical distance where dipole force equals monopole force, dipole forces become stronger. If r is the separation distance between the charges, monopole-monopole attraction varies as $1/r^2$ while dipole-dipole attraction varies as $1/r^4$. Inside the critical separation distance where force due to monopole is equal to force due to dipole the grains always attract one another due to rotation of dipoles into favourable directions despite of any monopole repulsion. Filament formation could be due to the monopole-monopole, monopole-dipole and dipole-dipole attractions but only dipole-dipole attractions can account for large aggregates attracting but not repelling grains in their vicinity (Marshall et al., 2005). This is a self organising property of dipoles. The dipole-driven aggregation, cohesion, and Coulombic friction could also be important contributors to the sedimentation dynamics of dry eruption plumes and clouds (Marshall et al., 2005).

2.6 Pharmaceuticals

An important manifestation of the problem of electrostatic particle charging in the pharmaceutical industry is a susceptibility to agglomeration in various processes such as tabletting and encapsulation. Pharmaceutical powders are usually semiconductors or insulators with small particle sizes and low bulk densities which provide ideal conditions for electrostatic effects.

There has been growing interest in delivering systemic drugs to the lungs in the latest studies (Schulz, 1998; Balachandran et al., 1997). Deposition of such drugs in lungs is highly dependent on the dry powder formulation in pressurised and dry powder inhalers. For such cases the electrostatic forces play a significant role as they affect adhesion in the inhaler as well as deposition in the lung airways. The particles get charged due to contact or friction in the inhaler and this charge later affects their deposition in the airways.

There have been single drug particle adhesion studies using AFM (atomic force microscopy) in order to understand the particle's interaction to wall material, to a carrier (material added to increase effective particle size, improve flow properties and

decrease agglomeration of the active ingredient) and interaction to itself. This helps to ensure that particles do not agglomerate or attach to container walls and can be dispersed in proper dosing amounts. Balachandran et al. (1991) in their mathematical model for particle deposition in lungs and airways showed that the deposition pattern in the lungs is extremely sensitive to the particle size as well as its charge and hence a precise knowledge of both is necessary. In a further development of their computer model (Balachandran et al., 1997) it was predicted that for particles of 2.2 μm electronic charges above 200 per particle the electrostatic forces become dominant for deposition over gravity sedimentation. Also with the smaller particle sizes sedimentation is negligible and electrostatic deposition becomes important. Two depositional processes were considered to occur from electrostatic charge: (a) that due to space charge (which was found to be negligible) and (b) that due to image charge within the wall which was always attractive. Smaller particles (< 5 microns) penetrated deeper towards narrower airways sections and alveolar regions where they are close to walls and hence image forces can be dominant. With more charge found desirable, the charge levels can be increased artificially (Bailey, 2001). Hence with a proper control of charge to mass ratio, control of particle deposition can be achieved (Balachandran et al, 1991, 1997).

In another study Eve et al. (2002) observed an increase in interaction force between the Salbutamol drug particle and PTFE on repeated contact due to tribocharging using an AFM point. Bunker et al. (2007) studied experimentally the electrostatic charging of single pharmaceutical particles by charging them by two different methods at relative humidity of 0.1%. Using AFM, single lactose particles attached to a cantilever were charged against glass (a) by repeated contacts and (b) by scanning across the surface. In the first method the particle was repeatedly contacted with the same surface in the normal direction and 16 force-curves were taken at different points over 3 x 3 μm areas on the glass surface. The force curves were recorded at an interval of 5 s and with a press-on force of 5 nN. In the second method, the particle was scanned over a 5 x 5 μm area on the glass for 256 lines with the same press-on force of 5 nN and a scan speed of 0.5 Hz. It was observed that tribocharging by scanning generated considerably more charge and more particle-surface adhesion force than repeated contacts. It has been acknowledged that further research into the electrostatic charging

of pharmaceutical powders is needed in particular for inhalation formulations (Chan, 2005).

The study presented in this thesis can lead to better understanding of behaviour of pharmaceutical powders with improved understanding of (a) the charge distribution over the different particles of a sample, (b) charge distribution over the surface of the particles and (c) and their electrostatic interactions.

2.7 Background Useful for the Dynamic Measurements Made in This Thesis

2.7.1 Fluid Dynamics

The following fluid dynamic descriptions have been applied to both particles and the gas flow around the *tip* of the central electrode of the sampler system used in this study. Flow about a sphere has been treated by Stokes (1850) and later by Lamb (1932). For very slow flow the velocity components in spherical coordinates have been expressed analytically (Bird et al., 1962) to be

$$u_{grsph} = u_{\infty}\left(1 - \frac{3}{2}\left(\frac{a}{r_{sph}}\right) + \frac{1}{2}\left(\frac{a}{r_{sph}}\right)^3\right) cos\,\theta \tag{2.6}$$

$$u_{g\theta} = -u_{\infty}\left(1 - \frac{3}{4}\left(\frac{a}{r_{sph}}\right) - \frac{1}{4}\left(\frac{a}{r_{sph}}\right)^3\right) sin\,\theta \tag{2.7}$$

Here u_{grsph} is the r-component of the gas velocity and $u_{g\theta}$ is the θ-component of gas velocity. These equations are valid for creeping flow which is characterized by the absence of eddying downstream from the sphere. Both the velocity components are zero at the surface of the sphere.

The equation for viscous drag experienced by a rotating sphere used for the *particle* has been given by Lamb while treating problems of steady rotation. For the steady motion of a fluid surrounding a solid sphere which is made to rotate uniformly about a diameter the couple experienced by the sphere is

$$G = -8\pi\eta R_p^{\,3} u_{\theta} \tag{2.8}$$

where R is the sphere radius (Lamb, 1932).

The drag coefficient of a sphere is related to Reynolds number by the expression $C_D = 24/Re$ by the well known Stokes drag law for small Re. Selecting one of many treatments of drag at higher particle Reynolds number we chose a convenient treatment by Abraham (1970). Abraham expressed the drag coefficient of a sphere for the range $0 \le \mathrm{Re} \le 5000$ by the expression

$$C_D = C_o[1 + \delta_o/(Re)^{1/2}]^2 \qquad (2.9)$$

where $C_o\delta_o^{\,2} = 24$ and dimensionless boundary layer thickness $\delta_0 = 9.06$.

2.7.1.1 Turbulence in a Jet

The particles sampled in this study were dispersed into an air jet and sampled along the jet centreline. There is a significant level of turbulence in a high velocity jet. A given body of fluid is said to be in a turbulent self-preserving state when all of its turbulent components are in equilibrium. An experimental investigation of the self-preserving turbulent axisymmetric jet was conducted by Wygnanski and Fiedler (1969). The jet emerged from a nozzle 26.4 mm in diameter (velocity 51 m/s in most cases) at a Reynolds number of 10^5. The nozzle was placed in the middle of a wall 2.29 m high and 2.44 m wide and the entire jet was enclosed in a cage (2.29 m high, 2.44 m wide, 5.2 m long and open on the far side) made out of two 0.016 mm mesh screens placed 0.064 m apart. Various quantities like mean velocity and turbulent intensities were measured with a linearised constant-temperature hot wire anemometer. It was concluded that the jet reached a self-preserving state about 70 jet diameters downstream of the nozzle.

The interpretations of Wygnaski and Fiedler (1969) have been applied in understanding the fluid flow in our equipment and used for design purposes. The variation of the mean velocity and turbulent intensities along the axis of the jet as predicted by them are given in Figure 2.7. Dimensionless distance *x/d* (ratio of diameter of nozzle to axial distance along centreline) has been plotted against both

dimensionless velocities $\frac{U_o}{\overline{U}_m}$ (ratio of the velocity at the nozzle exit to the mean velocity measured) and the rms turbulent velocities scaled by $\overline{U}_m$. It can be observed from the data that as the mean velocity reduces along the jet, the velocity fluctuations (u', v', w' in x, y and z direction respectively) reduce proportionally. We note that the turbulent velocities increase to a dimensionless value of around 0.25 by the time the jet becomes self-preserving.

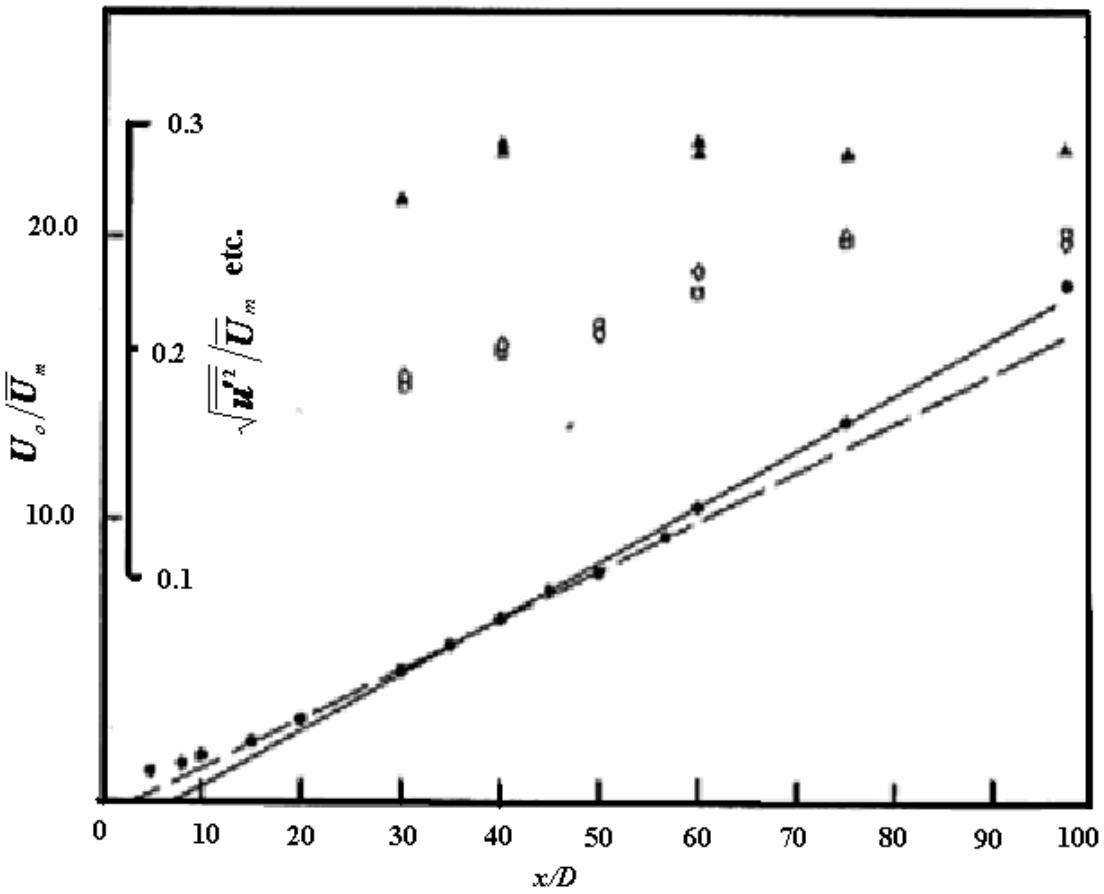

Figure 2.7: Variation of mean velocity and turbulent intensities along the jet centre-line. •, $\frac{U_o}{\overline{U}_m}$; ▲, $\frac{\sqrt{\overline{u'^2}}}{\overline{U}_m}$; □, $\frac{\sqrt{\overline{v'^2}}}{\overline{U}_m}$; ◊, $\frac{\sqrt{\overline{w'^2}}}{\overline{U}_m}$ (Wygnanski and Fiedler, 1969).

2.7.1.2 Flow Visualisation Techniques

The use of smoke and dye to observe fluid motion is one of the oldest visualisation techniques. This is an easy and inexpensive technique capable of providing significant insight into the phenomena of complex flows. Smoke can be generated by various

methods as reported in the literature like burning of tobacco, rotten wood, and wheat straw, and generated from reaction between titanium chloride and moisture, and from "smoke wires" (vaporizing hydrocarbon oils) (Mueller, 1983). It is essential for smoke particles to be small so that their motion reflects the motion of the flow, does not disturb the flow field significantly, has high reflective properties and be non toxic (Lim, 2000). Vaporising hydrocarbon oils gives good control of the quantity of smoke.

The "smoke wire" technique is an inexpensive method requiring only a metal wire, mineral oil and a power source. Smoke is produced by vaporizing oil from a fine wire heated by an electric current. Most commonly used wires are made of stainless steel, nichrome and tungsten owing to their strength and electrical resistivity. The wire size can be decided considering the speed and Reynolds number (Lim, 2000). A small diameter wire is good for low speeds as it produces sharp smoke and a larger diameter for high speeds as more surface area gives a higher smoking rate. Also a wire Reynolds number less than 20 will be ideal to minimize flow disturbance. For most applications the optimal size is about 0.1 mm in diameter. The wire needs to be coated evenly with oil for uniform smoke. The current and voltage applied to the wire are optimised as higher currents vaporize smoke quickly and lower currents produce smoke too faint to photograph.

2.7.2 Particle Imaging

Video cameras have been used for acquiring images for computer processing for many years. The earlier cameras were tube-type cameras and have now been replaced by solid-state sensor cameras, the simplest form of which is the CCD (charge-coupled device) (Russ, 2007).The CCD camera sensor contains an array of diodes each connected to a capacitor that function as "light buckets". Another design for sensors is the CMOS type (complimentary metal oxide semiconductor) which has a different fabrication approach. A CMOS sensor is organised like a computer memory chip and there is access to each pixel by 2D row-column addressing rather than reading the entire array as in a CCD. This is a potential advantage as it provides rapid updating for focussing, measurement of regions of interest, etc. Although the sensitivity and dynamic range of a CCD is greater than a CMOS (complimentary metal-oxide

semiconductor) sensor, CMOS devices are less expensive, more compact and rugged. Also they require lower voltages and lower power requirements which are important for portable devices. The camera used in the study presented here has a CMOS sensor in it.

2.7.3 Corona Discharge

A corona discharge is often produced when a high voltage is applied between electrodes in non-uniform field geometry. The discharge appears close to the sharp electrode where the electric field high enough to exceed the breakdown field of the gas. Any electron entering this region is accelerated and a certain fraction on collision with an atom has sufficient energy to detach an electron leaving a positive ion and an additional electron (Cross, 1987). This electron is also accelerated producing its own electron/ion pair. The process is continued and an avalanche of electrons forms close to the surface of the sharp electrode. The ionisation process of air leads to the emission of light and a bluish glow can be seen round the sharp electrode. The maximum electric field sustained by air (strictly at a flat surface) before it ionises is approximately $3\text{x}10^{6}$ Vm^{-1} and the surface charge density corresponding to the breakdown field by the Gauss law is $2.64\text{x}10^{-5}$ C/ m^2 (Cross, 1987).

Peek (1929) presented a semi-empirical formula for the field strength of onset of corona from a perfectly smooth wire on the axis of a cylinder.

$$E' = \delta'\left(A_g + \frac{B_g}{(r_0\delta')^{1/2}} \right) \tag{2.8}$$

where r_0 is the wire radius in metres and δ' is the relative air density given by

$$\delta' = \frac{T_0 P \delta_0}{T P_0} \tag{2.9}$$

Here δ_0, T_0 and P_0 are the density, absolute temperature and pressure of the air at 1 atmosphere and 25 $^{\circ}$C, T and P are the actual temperature and pressure, and A and B are the constants which are a function of the gas, g. For air A_g = $32.2\text{x}10^{5}$ Vm^{-1} and

B_g = 8.46x10^4 V/m$^{1/2}$. The right-hand side of equation can be multiplied by a roughness factor f (usually between 0.5 and 0.9) for wires in practical situations as they are not perfectly smooth. Some investigators have found a maximum difference of 6% between the (+) and (-) corona starting voltages and there is usually fair agreement between starting field values for direct current and for alternating current (taking the maximum field of an alternating current cycle) (Peek, 1929).

Schumann (1923) has summarised the experimental data on the corona discharge from thin wires. He derived a theoretical approximation that the corona inception field strength for an isolated sphere is nearly equal to that for an isolated wire with half the radius of the sphere (Hamamoto et al., 1992). This is in spite of the higher fields at the sphere surface for the same radius. The reason is that there is a higher probability that the electrons moving away from the high voltage sphere do not achieve enough energy to start an avalanche due to larger diffusion losses from the spherical geometry. Based on the assessment of Hamamoto et al. (1992), Harper (1967) approximated the maximum surface charge density for small spheres (from data on corona inception field strength for thin wires) as:

$$\sigma_H = 1.03\, x10^{-5}\, D_p^{-0.3} \text{ C/m}^2 \qquad (2.10)$$

where D_p is the diameter of the particle in metres. This equation gives the maximum surface charge density on the probe (500 μm diameter) used in this work for corona inception to be 1x10^{-4} C/m^2. From Gauss law the maximum charge density which can be sustained on any flat surface in air is 2.64x10^{-5} C/m^2 which is 25% of the value estimated from Equation 2.10.

In non-uniform field geometries the breakdown is stepwise, spreading out in voltage and sometimes in time as a sequence of events (Loeb, 1965). It has been recognised that as the potential was raised in such gaps a threshold is reached where some sort of breakdown (discharges) appeared at the highly stressed electrode with relatively low currents (in order of a microampere at relatively low potentials). These currents may be unsteady or fluctuating near the threshold. With increase in potential, the current increased linearly and the discharge became stable and steady. Thereafter the current increased somewhat faster than linearly, approaching a parabolic increase with

potential. The current and potential could be increased until a point was reached yielding a complete breakdown of the gap to a transient arc through the medium of a spark. The breakdown to a spark usually occurred at voltages from two to six times that for onset of the first glow and current. A great variety of phenomena with varied geometry, over an extended range of pressures and gases with varying degrees of purity and conditions of electrode surfaces has been observed. Loeb et al. (1950) experimentally studied corona breakdown and field in the gap between a hemispherically capped cylindrical point and a plane recording values along the axis of the cylinder. Their study indicates that for a point with radius 0.25 mm (as used in the study of this thesis), the threshold in air begins at about 5 kV and ranges to about 40 kV at breakdown. Under the same conditions H.W. Bandel (cited in Loeb et al. (1950)) observed the pre onset burst pulse threshold for hemispherically capped cylindrical points and was rather confusing in his reporting. For points of 0.125, 0.25, and 0.50 mm radius and gap lengths of 20, 40, 80 mm to the plane, the threshold voltage was 3540, 5280 and 7910 volts respectively (Loeb et al. , 1950). Based on our understanding of this reported data for 0.25 mm radius point at a gap length of 40 mm (geometry close to our experimental set up) the pre onset burst pulse threshold is 5280 volts.

3. Equipment Design

3.1 Operating Principle

The equipment has been designed to generate a non-uniform electric field. The idea behind using a non-uniform electric field is that monopoles can be attracted or repelled according to the applied field polarity, but the dipoles are always attracted towards higher field, once they have aligned themselves. As shown for the simple geometry of Figure 3.1, the negative end of the already aligned particle is in a higher field than the positive end. Therefore the dipole on the surface of the particle experiences a higher force in the direction defined by the negative charge. As a result of this there is net translation towards the higher field. If the probe is negative, and the particle has aligned itself, the same argument applies; i.e. the net force acting on the particle is again towards the probe tip.

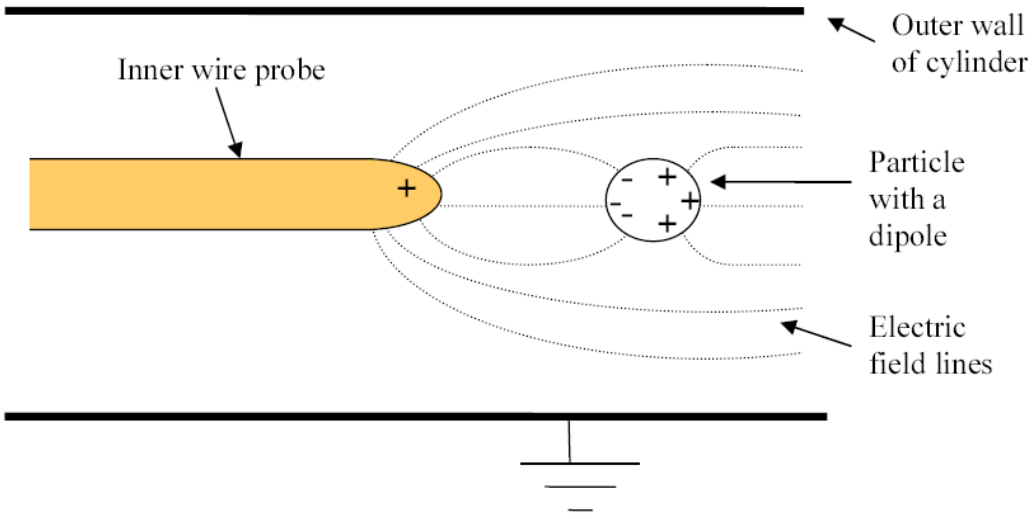

Figure 3.1: Spherical particle with a dipole in a non-uniform field

The simple geometry of a wire probe immersed in the suspension flow as shown in Figure 3.1 was chosen as the most convenient way to generate a non-uniform field. Application of high voltage to this probe was thought to provide a nearly spherical field around and in front of the tip of the probe. Figure 3.2 represents the expected surface variations, streamlines and contours of the electric field around the tip of the probe in 2D (axial symmetry) modelled in COMSOL Multiphysics software. The probe voltage was reversed in polarity frequently during a run, to allow a symmetrical

treatment of both positive and negative particles while flows and velocities remain constant (reducing possible distribution bias), and also to provide additional checks on the trajectory analysis when a polarity switch occurred during a trajectory. One expects that the charge parameters of a particle will remain constant before and after such switches.

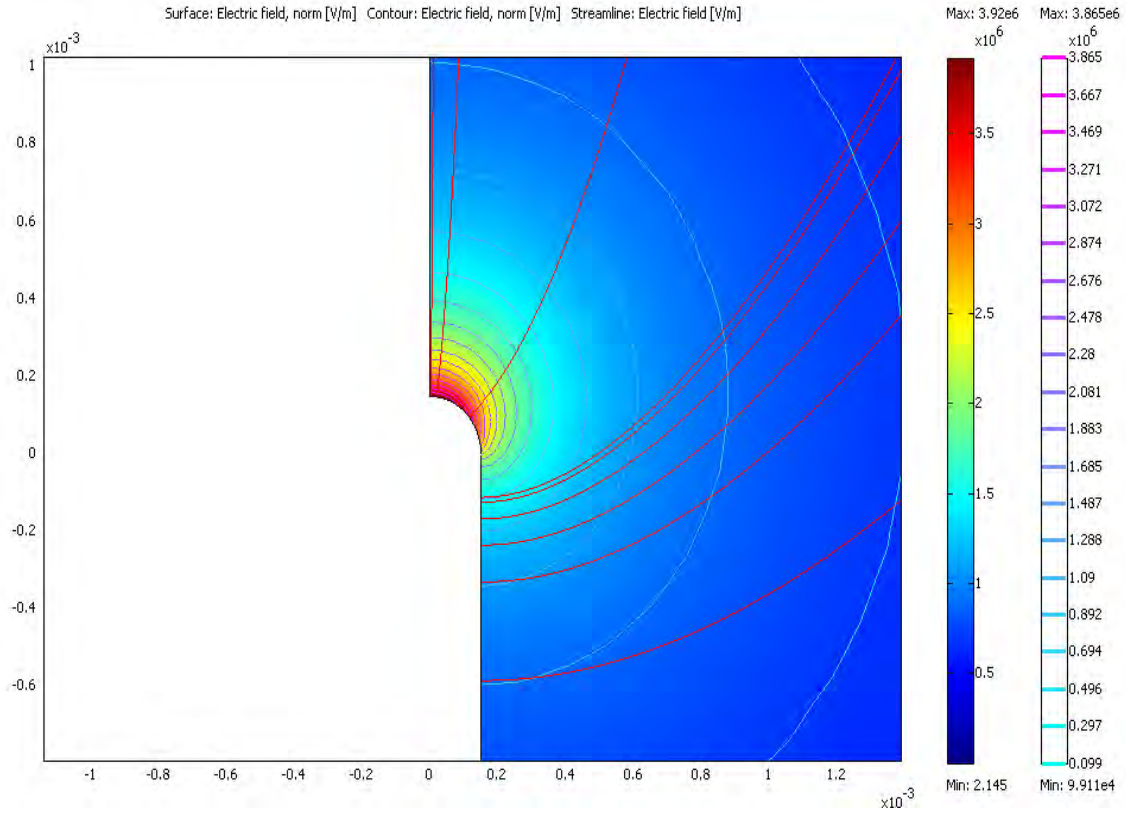

Figure 3.2: Expected electric field around the rounded tip of wire probe at 10 kV voltage supply (see Chapter 5 for a more detailed description and discussion).

3.2 Equipment Layout

The experimental apparatus consists of a sampler head, laser unit, high speed camera, high voltage AC power supply, brush feeder and a bag filter. Figure 3.3 depicts a flow schematic of the experimental system, showing the relationship between the sampler unit, laser, high-speed camera, and the high-voltage power supply. The following sections describe each of these units in detail.

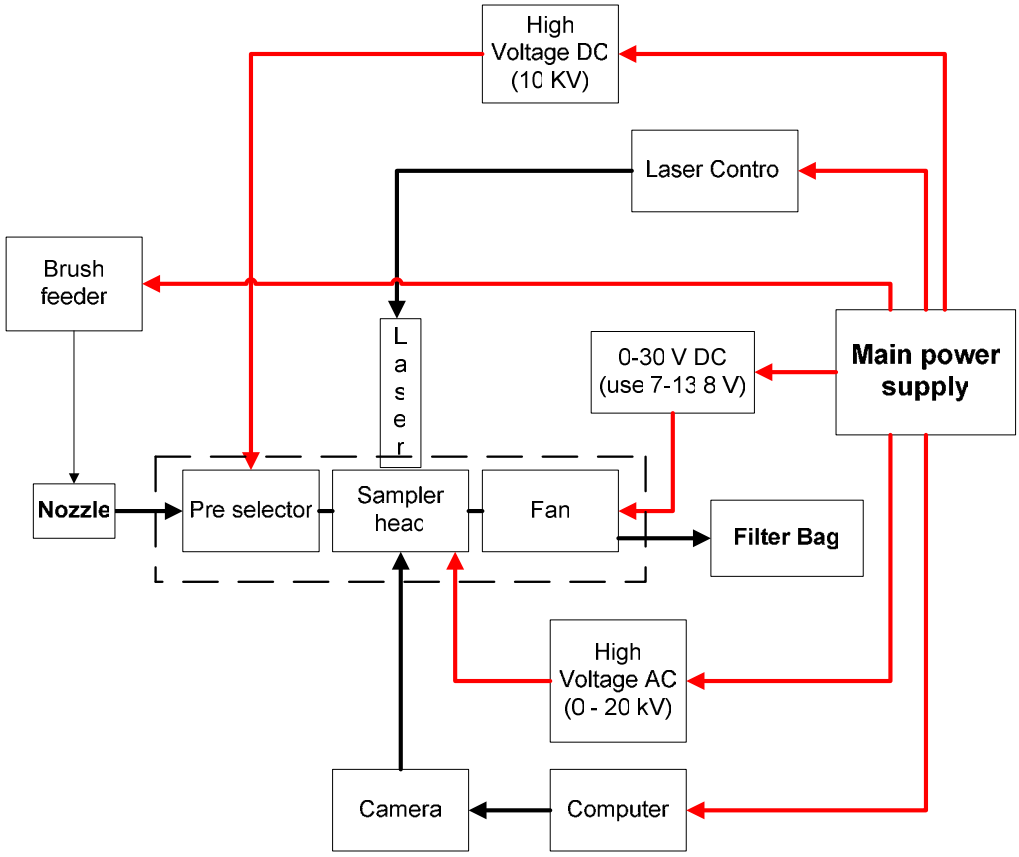

Figure 3.3: Block Diagram of the Experimental Apparatus

3.3 Sampler Head

The sampler head has been built around a cylindrical tube of stainless steel with inner diameter 100 mm and length 500 mm, aligned horizontally for this study. This tube acts both as the outer electrode and the channel for the particle/air suspension flows. It provides housing to the whole assembly and can be divided into three main sections. The first and the last sections are 150 mm long and the middle section is 200 mm long.

In the **first section** some preselection of particles with respect to net charge is performed by using a parallel plate electrostatic preselector upstream of the probe. The **middle section** has the probe which acts as an inner electrode and is supported by a spider arrangement. The probe has been made from the end of a fine tungsten wire purchased from New England Precision Grinding Inc. (2007) with its both ends rounded. This wire probe is nominally of 500 µm diameter with a hemispherical tip and is mounted midway along the tube on its centreline, 250 mm from the inlet. The

diameter of the probe was measured with an ultramicroscope (Olympus BX60, Japan) with a ProgRess CF scan camera (S/N 1308-21-0202, Jenoptik, Germany) attached. The standard operating procedure from the manual of the ultramicroscope was followed. Figure 3.4 (a) shows the wire probe as seen under the microscope with 5X zoom. The diameter of the probe was measured from its image by plotting a line across its shank. The length of the line was 190±1 pixels as shown in Figure 3.4(a). For the same view (image resolution) the size of one mm on a standard stage micrometer, was measured by plotting two lines at two different positions across its width on the image. The length of this line was 372±1 pixels (Figure 3.4 (b)). The sizes of probe and scale were compared and the diameter of the probe tip was approximated to be 510±5 μm. The probe is attached to a high voltage supply which is introduced from the back end of the sampler head (Figure 3.4 (c)). This section has two circular windows; one is at the top of the tube for the laser to pass through and the second is on the side of the tube in front of the camera for capturing images. The **third section** has a spider form of vortex breaker installed in it. At the exit end of the 100 mm diameter tube there is a propeller fan of the same diameter as the tube. This fan helps to pull air through the tube and therefore remove large velocity gradients around the probe if required. The small diameter wire has been chosen to give a high concentrated field.

The geometry of this sampler head along with a photograph is given in Figure 3.6.

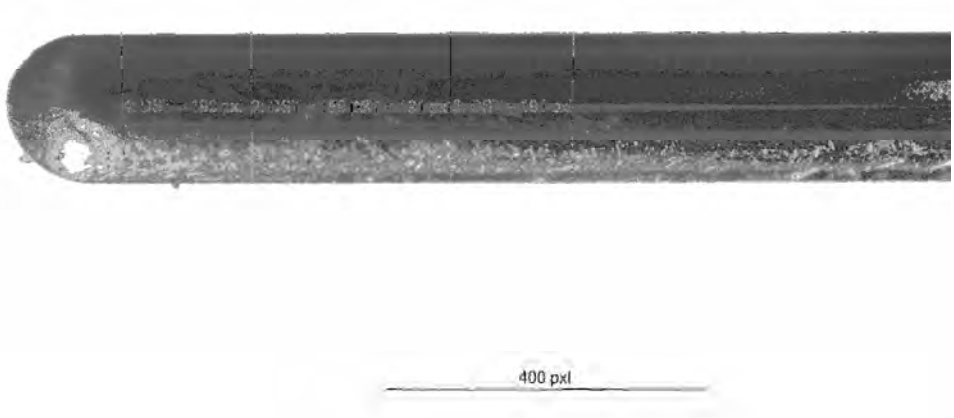

(a)

Figure 3.4 (a): A closer view of the rounded tip of the probe wire along with the lines plotted to measure its diameter in pixels.

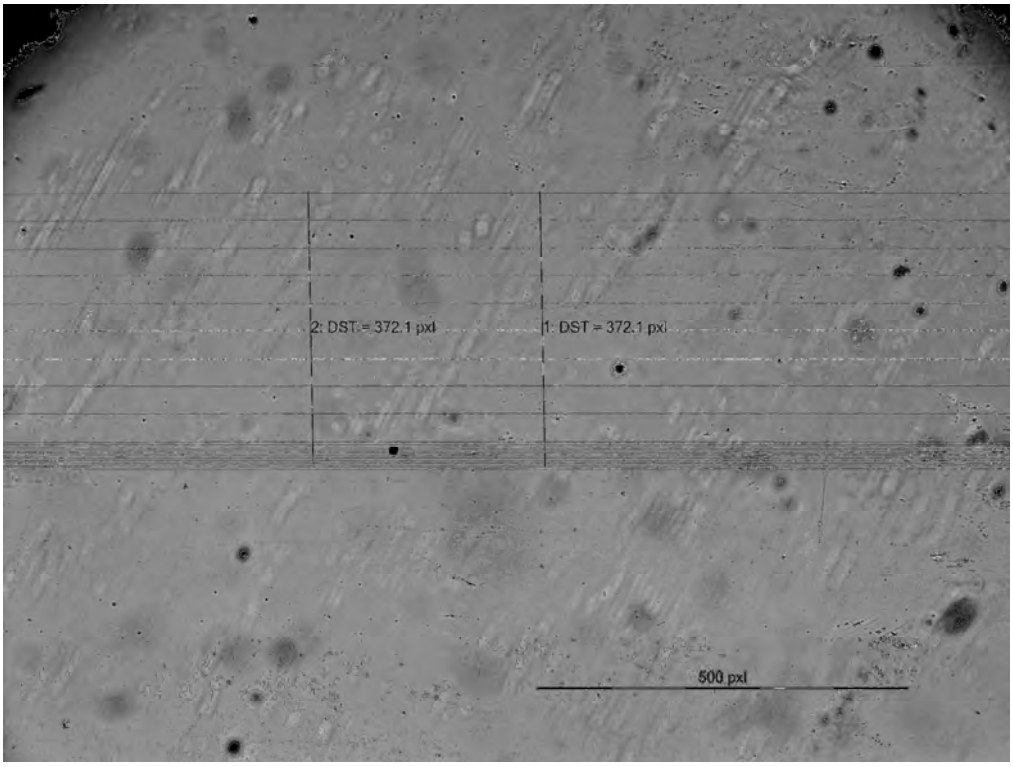

(b)

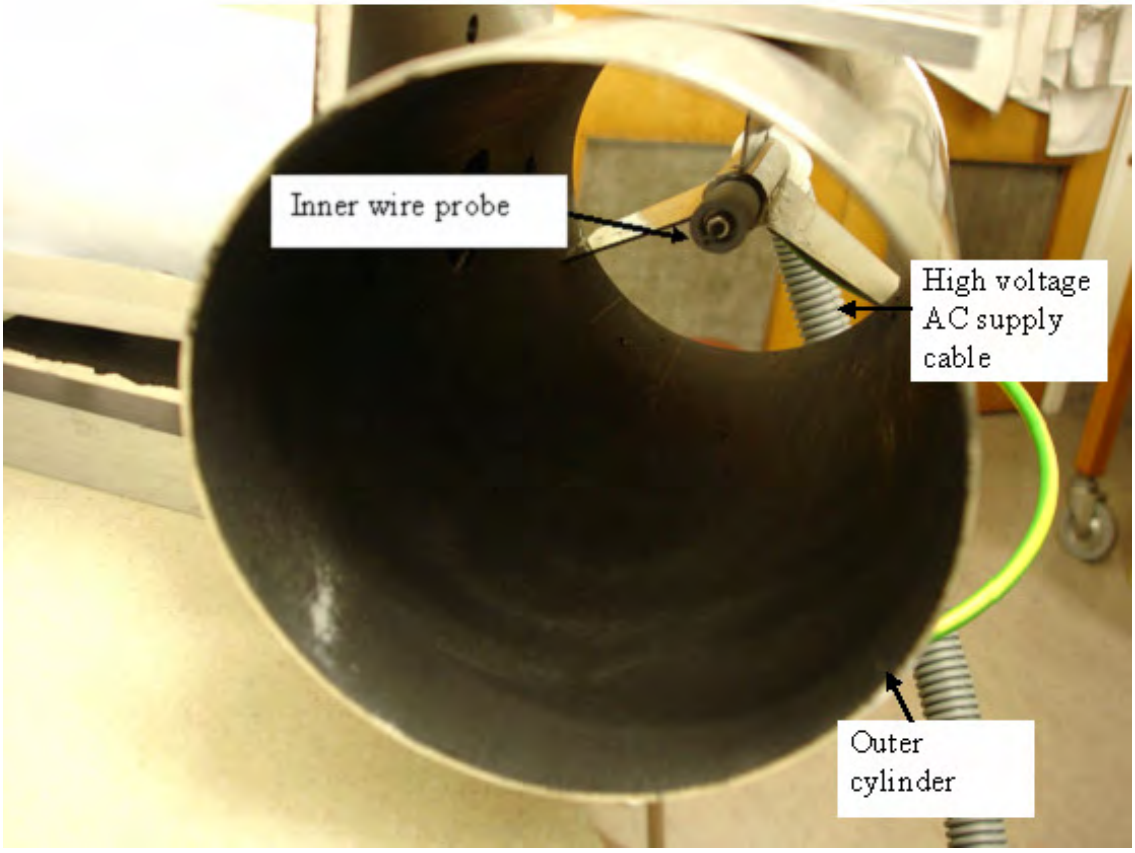

(c)

Figure 3.4 (b): size of a one mm scale measured in pixels by plotting lines at two different positions (c): Inner wire probe inside the sampler head (too small to see clearly).

3.3.1 Preselector Plates

The preselector has two 150mm long, 50mm wide and 0.5mm thick parallel plates, situated to the left and right of the centreline by 5 mm. They have been installed vertically in the cylinder and the edges are rolled to minimise local fields off the edges. Each of the two plates is supported by a plastic extension of 70 mm length glued on it so that the plate and the tip of inner electrode are 30 mm apart. The plates installed in their housing along with the plastic extension are shown in Figure 3.5. The whole unit is fitted inside the outer stainless steel tube. The extensions were used to guide the flow emerging out of the plates towards the probe tip through the 30 mm gap.

The plates have been designed to give 100% efficiency for collection of 90 μm sized particles. One of the plates of the preselector is normally set at -10 kV with respect to ground. The design steps involved in calculating the dimensions of plates are explained in the following section.

Design Steps for the Plates:

The following values were assumed to design the plates:

- Viscosity of air, $\eta_{air} = 1.8 \times 10^{-5}$ Pa s
- Diameter of particle, $D_p = 90 \times 10^{-6}$ m
- Axial velocity, $u_a = 20$ m/s
- At 10 kV voltage, the electric field between the plates assumed to be 10 mm apart is given by E_o = 10,000 V/ 10 x 10^{-3} m = 1 x 10^6 V/m.

The terminal velocity of the particle was calculated by balancing the aerodynamic drag from the Stokes law with the electrostatic force experienced by the particle in the applied electric field. The charge on the particle was assumed to be the saturation charge (maximum charge which can be acquired by a particle in a uniform electric field, in which there is only one polarity of ions) from the Pauthenier limit (Cross, 1987). From the terminal velocity of the particle, the collection time for the particle to be collected on the plates in a laminar flow was calculated and based on this time the dimensions of the plates were assumed. Then applying a full mixing model, the

Deutsch equation was used to estimate the efficiency of collection which was nearly 99%. As a safety factor the assumed length of the plates was increased by 50% which made total length 150 mm and width 50 mm. This was to ensure that most of the charged particles were collected in the plates (See Appendix A.1 for detailed calculations).

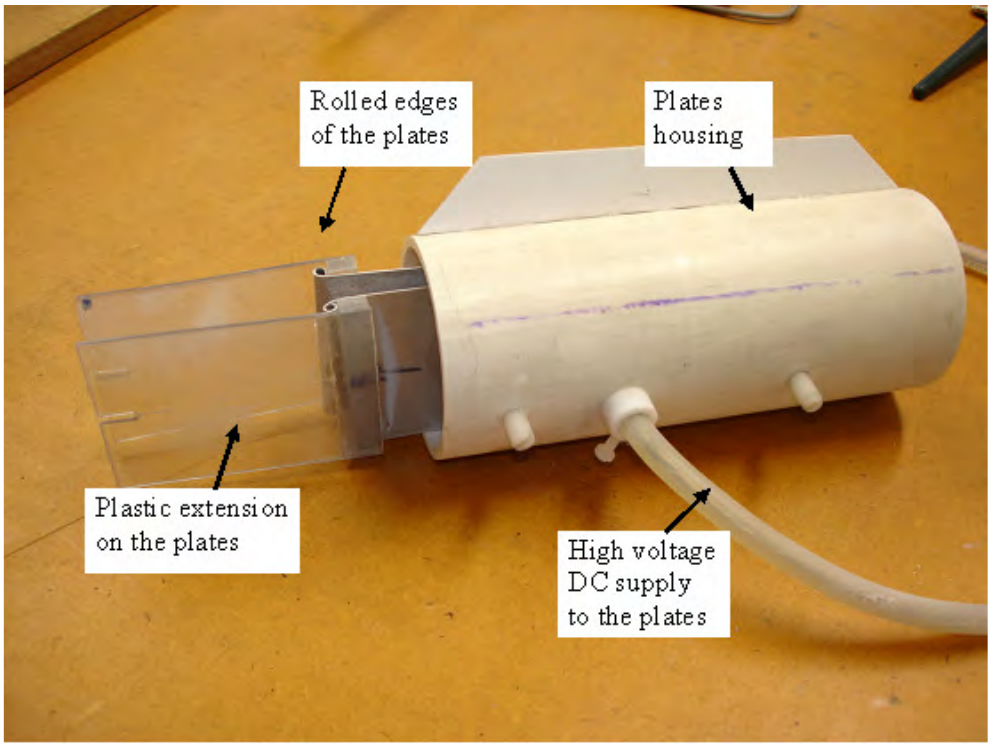

Figure 3.5: Plastic extensions glued on the pre selector plates.

3.4 Laser Unit

The diode based red laser (Roithner Lasertechnik, Austria, RLT67300T, 670nm) is rated at 300 mW of continuous optical output, but is capable of pulsing. The laser diode is temperature-stabilised to 25°C by a thermoelectric heat pump. The laser output is initiated by a TTL (transistor-transistor logic) signal on the control line. The rise and fall time is fast, allowing pulses of 500 ns to be created. After enlarging the cylindrical beam with a suitable diverging and converging lens, the beam is converged in one direction and expanded in the other, into a rectangular sheet of dimensions 10 x 0.8 mm. The laser diode controller controls various aspects of the laser operation such as power supply, temperature control and pulse timing which includes pulse duration, pulse period and number of flashes per frame. The number of flashes per frame can vary from 1 to 33 and the laser can also be run continuously if desired.

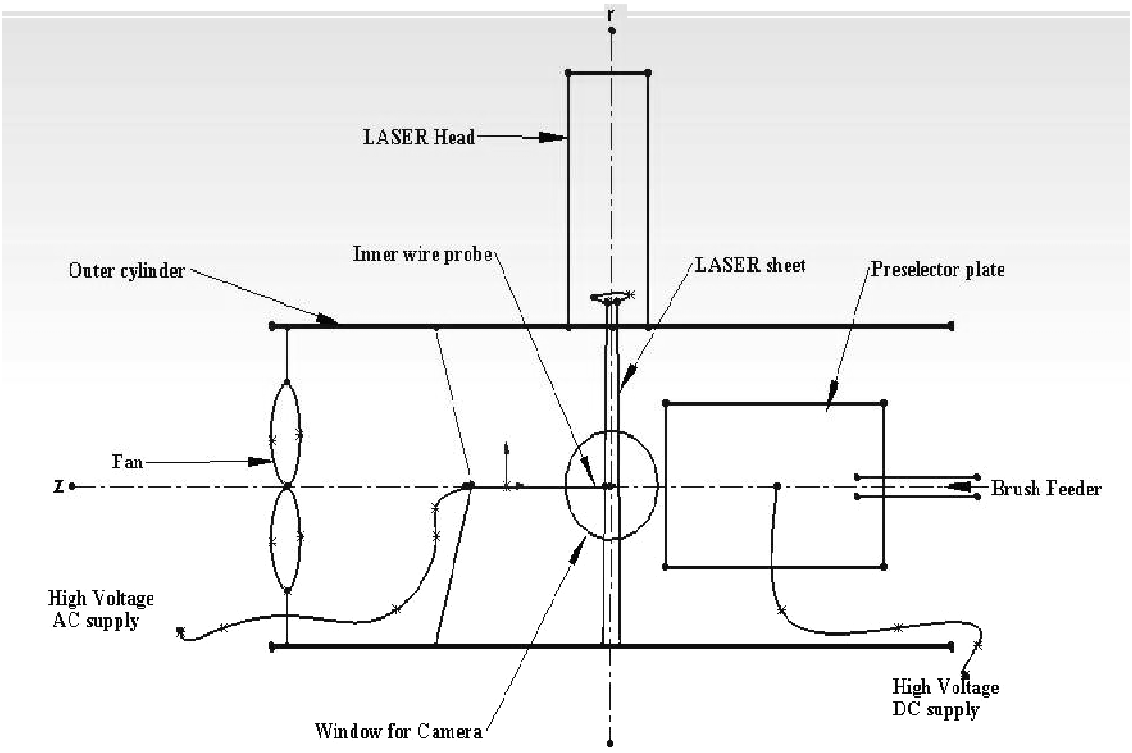

(a)

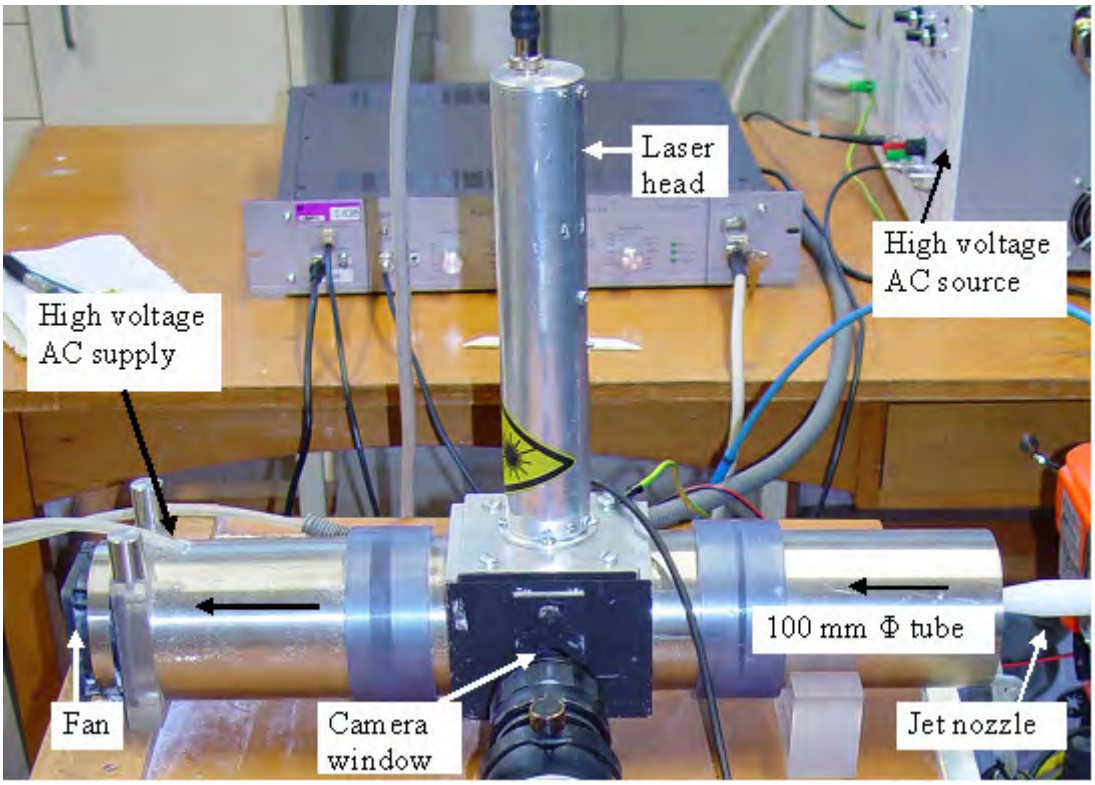

(b)

Figure 3.6: (a) Sectional view of the sampling unit arrangement in the plane of the laser sheet and perpendicular to the camera axis (b) Photograph of the sampling unit.

The pulse width can be between 500 ns and 5 ms and the pulse period (pulse width plus the time gap between the two pulses) can be varied from 1 μs to 160 ms.

There are two inputs provided at the front panel, a *trigger* input and an *enable* input. The trigger input initiates a pulse sequence, as programmed by the switches on the front panel, on either a positive (rising edge) or a negative (falling edge) TTL transition, as set by the toggle switch. The *enable* input has been pulled high internally by a resistor, and driving this low externally prevented trigger pulses from initiating a pulse sequence. For turning on the laser, the power is switched on and as soon as the diode reaches 25ºC, the temperature-good light (the green light on the front panel of laser controller) turned on indicating that the laser key switch can then be switched on. Depending on the front panel settings of the controller, and any trigger signals present, laser emission will then be present.

The laser head has been mounted perpendicularly on the sampler tube in line with the tip of the probe to illuminate particles close to the probe in a plane perpendicular to the axis of the video camera. For the experimental purposes the laser was pulsed at 200 mW power level. For most of the runs the pulse width was 20 μs with a pulse period of 160 μs. This combination was optimum to have sufficient gap, without any overlapping, between consecutive images of the particle on a frame. An increase in pulse width or decrease in pulse period led to an image of the particle as a continuous streak which was not desirable for analysis, as the position of particle with each time step could not be predicted. The camera triggered the laser at the start of each capture. Figure 3.7 shows the detailed representation of the laser assembly with positions of diode and lenses.

The laser was categorised under class 3B products under NZ standards (AS/ NZS 2211.1:2004). It was potentially hazardous to view the direct beam or specular reflection by the unprotected eye. So it was necessary to wear laser goggles for eye protection for the whole time during experimentation. Also the entrance to the laboratory was posted with a standard laser warning sign (See Appendix A.2 for more details).

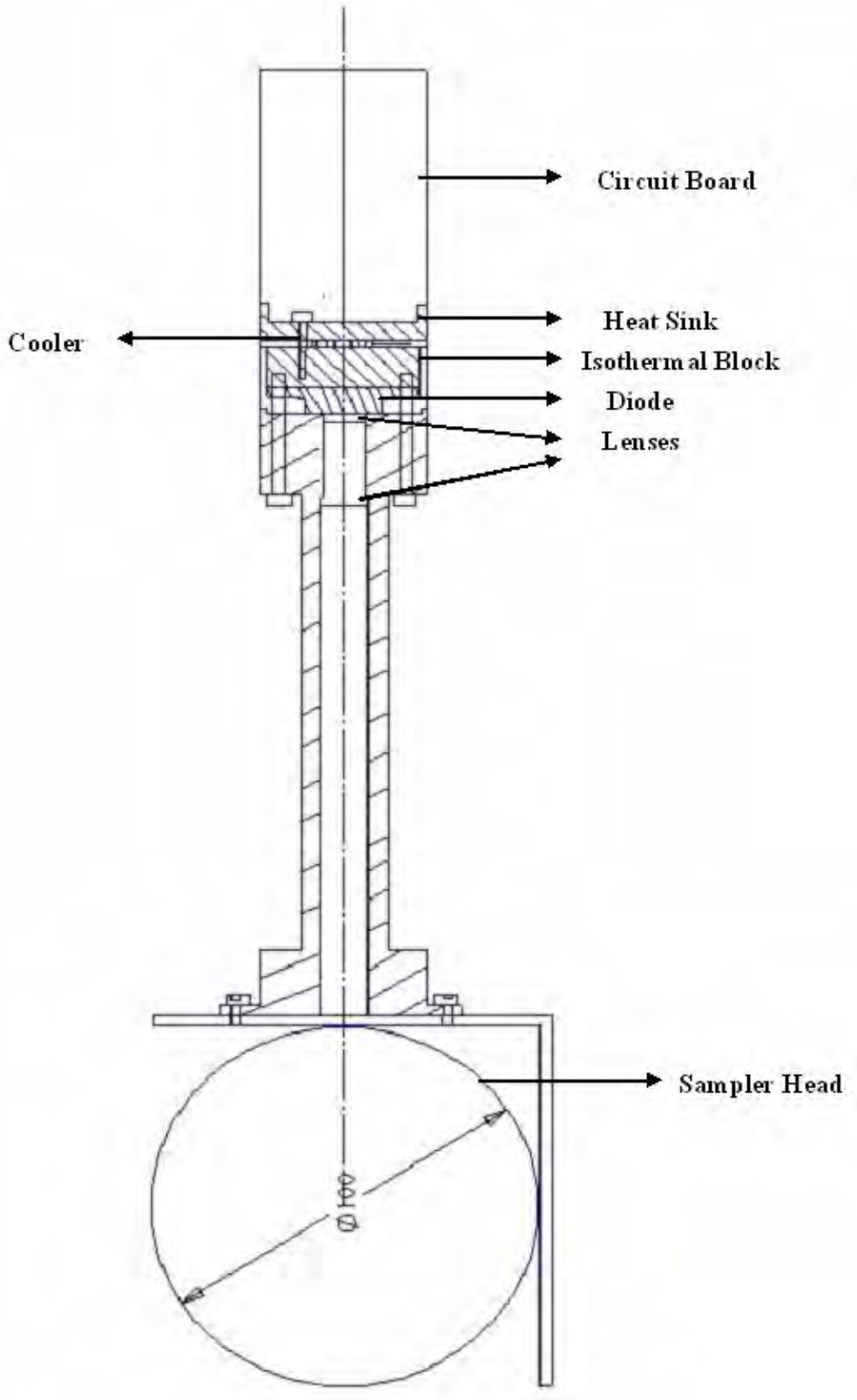

Figure 3.7: Schematic representation of flash laser unit

3.5 High Speed Camera

The high speed camera is from Canadian Photonics Lab (Model CPL MS50K, bought in Feb'03) and it has a CMOS sensing array. It is operated by a camera program (CPL Mega Speed MS50K) via computer and thus images can be visualised on a computer screen. The camera can be operated up to 50,000 frames/s but for all experiments in this thesis it was operated at a speed 489 frames/s with an image resolution of 1200x1020 pixels (the maximum available). A complete field of view of 6.5x5.5 mm around the probe has been provided by mounting an 85 mm focal length compound lens (F 1.9, Super-Takumar, Asahi Opt.Co.) on the end of a 230 mm extension tube attached to the camera. The field depth was measured with the help of a travelling microscope by attaching a thin rod on it. The rod was moved in and out of focus across the width of the laser sheet and the range of distance was noted for which the rod stayed in focus. The depth of field value from this procedure was approximated to be 0.85 mm. The camera views through a circular plain glass window (made from a microscope slide) on the side of the tube. The images of glass spheres were dim and lacked sharpness. So the glass window was later removed in an attempt to enhance the image quality for glass spheres. Figure 3.8 shows the photograph of the camera as installed in experimental set up.

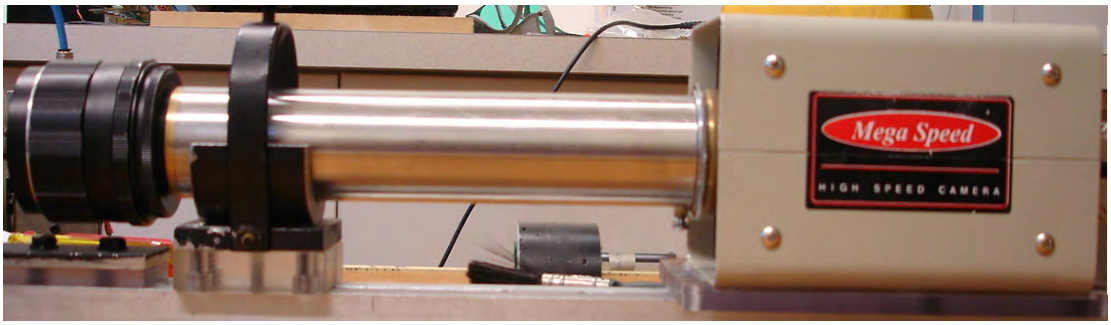

Figure 3.8: High speed camera with attached extension tube and an 85 mm camera lens.

3.6 High Voltage AC Supply

The AC supply has been designed to generate a maximum output square wave voltage of about 40 kV peak to peak at the rate of 1mA current. The output frequency ranges between 20-200 Hz. The alternating supply has been used in order to change the

polarity of the probe voltage after several frames in the same run. It has been in particular designed to provide constant voltage in between the changes in polarity. In order to indicate which polarity existed during the exposure of a video frame, the supply waveform is sent to the laser driver, which halves the frequency of pulsing when the output voltage is positive. The period of the square wave can be varied to control the number of frames captured under one polarity.

For this work the controls were set so that approximately six frames could be captured for each peak of the waveform at an output frequency of 40 Hz. This setting was chosen so that mostly particle trajectories under one polarity could be captured without any effects of transition. Figure 3.9 presents a sample of the square waveform for 8 KV voltage supply as read from an oscilloscope. The rise and decay time can be approximated (Figure 3.9) to be close to half a millisecond. This is about ¼ th of a frame period at 489 frames/s.

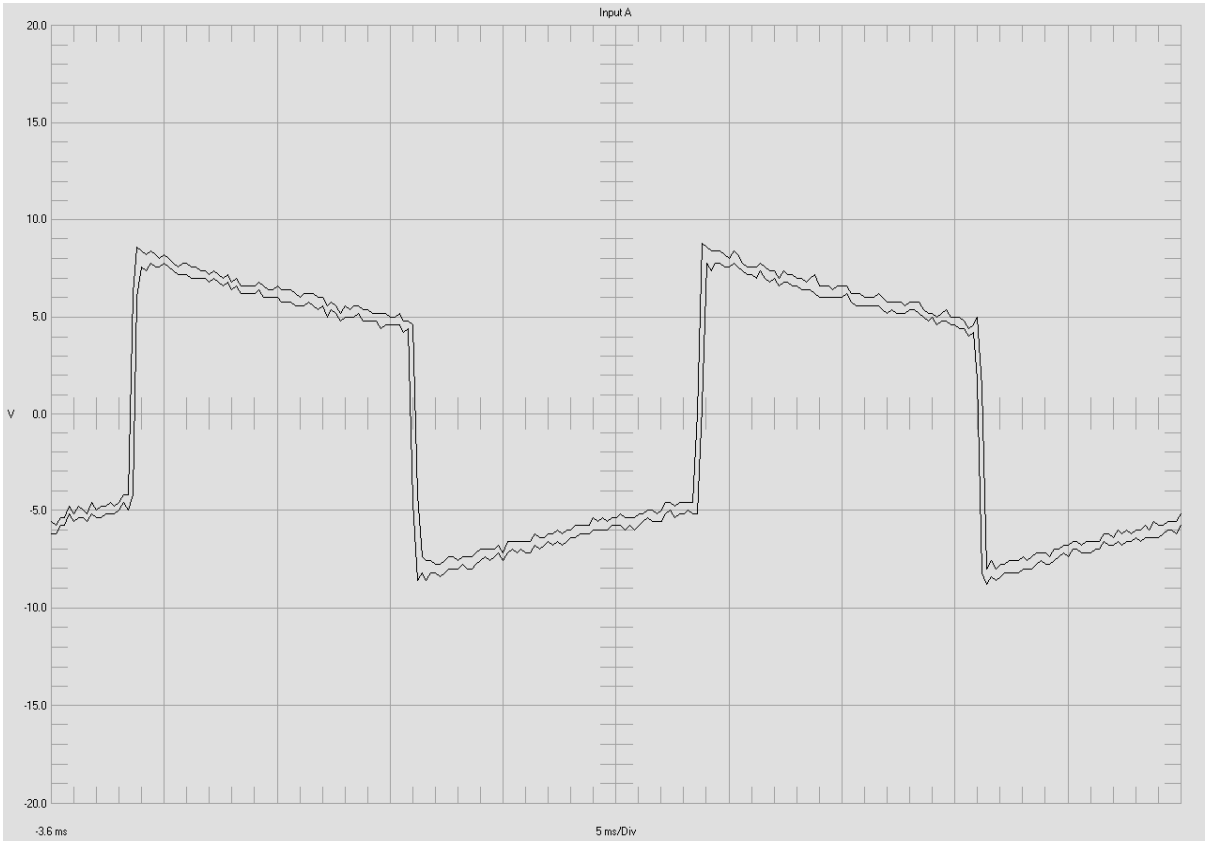

Figure 3.9: Square waveform at 8 KV voltage supply.

3.7 Brush Feeder

The brush feeder is capable of metering in small flows the particles introduced in the feeder air. Figure 3.10 shows the brush feeder driven by two drills. Particles are filled into the brass syringe (chosen to be13.2 mm internal diameter, ID). The bottom drill pushes the piston upwards which forces the powder towards the rotating nylon brush driven by the top drill. The particles are blown off the brush by an air flow through a brass tube 11 mm ID and 25 mm length. The feed rate of particles depends on the size of syringe chosen. For this work the volume fraction of solids in the feed was $5x10^{-4}$ (decided by the size of piston). The rotating brush picks up the particles which are blown off the brush by compressed air introduced at the top of the brush. The particle laden air is then directed through the nozzle and towards the preselector plates in the sampler head.

3.7.1 Nozzle Design

Particles exiting from the brass tube pass through a nozzle. In initial experiments the nozzle was a polyacetal tube of 3 mm ID and 90 mm length. The polyacetal tip was 220 mm upstream of the probe. A small diameter nozzle was chosen to get a dilute flow but later the nozzle diameter was increased to 10 mm ID to reduce the jet velocity and therefore the velocity fluctuations due to turbulence (Wygnaski and Fiedler, 1969).

3.8 Bag Filter

The bag filter is a polyester fibre bag (Canterbury Filter Services Limited) attached at the exit end to recover the particles blown out by the propeller fan. The bag size was calculated on the basis that the maximum velocity through the 100 mm ID tube achieved by the fan at the bag surface was 7 m/s, and the desired velocity through the bag for adequate filtration should be 40 mm/s.

By initially assuming a 0.2 m bag diameter and 1 m length, the calculations for the filtration velocity through the bag were made. The filtration velocity is given by the

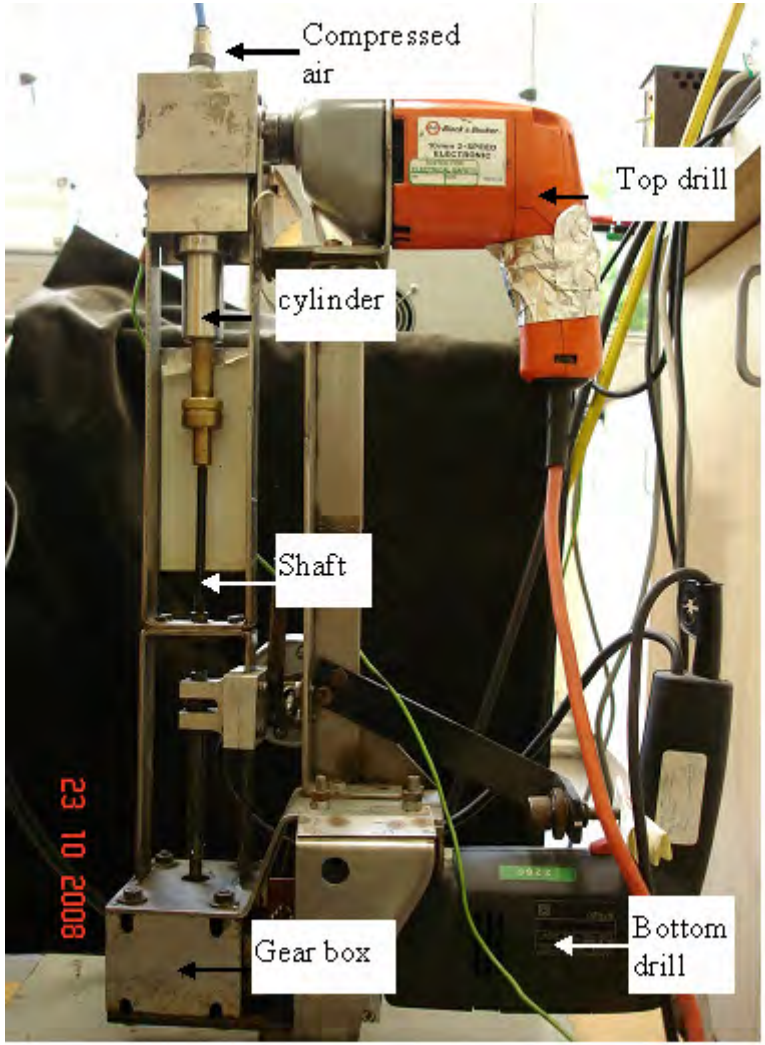

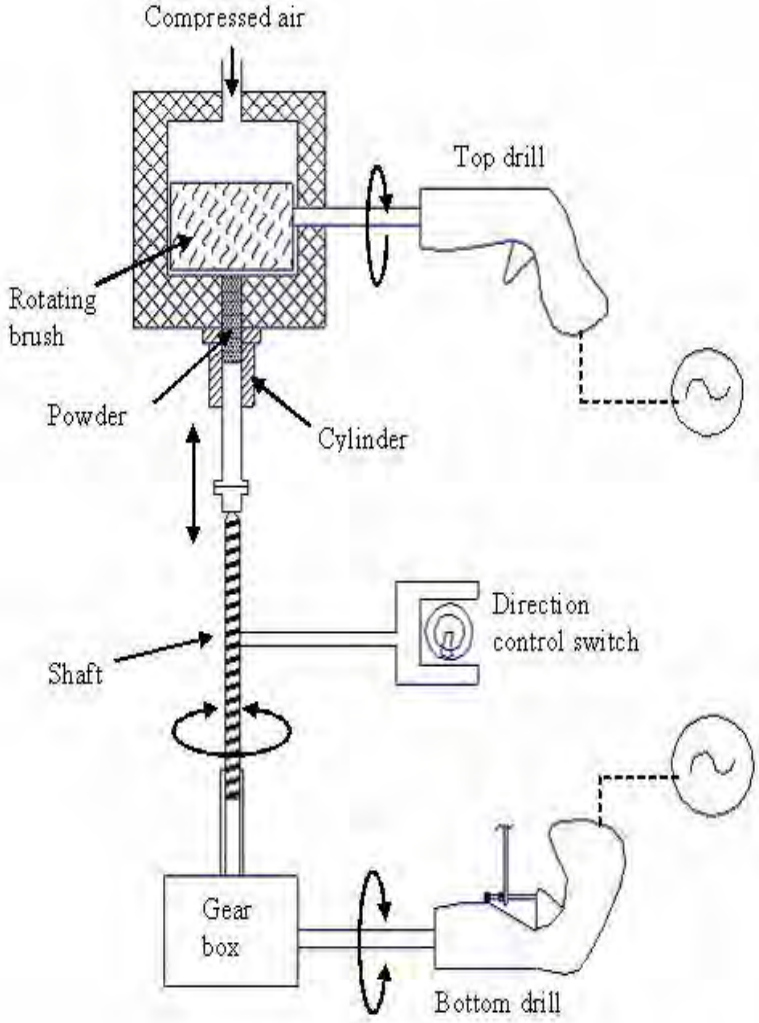

Figure 3.10: Sectional view of two drill brush feeder

flow rate divided by the area of the bag. The flow rate through the sampler with 7 m/s velocity is 0.055 m^3/s. The area of the bag is the sum of the area of the cylinder plus the area of the cross section at the end. Using these values the velocity through the bag will be 83.3 mm/s .This is double the value of the best velocity assumed. So if diameter of bag is doubled velocity in bag will be halved (40 mm/s). Considering all the requirements a bag with 40 mm diameter and 1 m length was finalised. Figure 3.11 shows the complete experimental arrangement used in the final experimentation (without the bag attached).

3.9 Test Particles

For experimental purposes different samples of spherical particles have been used among which polymer particles and glass bubbles were perfect spheres and others (fertiliser) were irregular in shape or even agglomerated (milk powder). Surface microscopy of these particles was performed with a high resolution FESEM (field emission scanning electron microscope), JEOL JSM 7000F (JEOL Ltd., Japan). Sticky carbon tape was fixed on a clean SEM stage and particles were pasted onto the top surface of the carbon tape. To prevent sample contamination, care was taken not to touch the sample or FESEM stage with bare hands. The samples were then placed in a gold coater and coated with gold by a K975X, Turbo coater (Emitech, UK). Gold coated samples were then placed inside the FESEM stage cell and a step by step procedure according to operating instructions for the FESEM, JEOL JSM 7000F system was followed to take the pictures of the particles.

3.9.1 Acrylic Particles

The particles first used for experiments were cross-linked acrylic spheres from Esprix technologies. These were odourless white Methacrylic copolymer particles $(C_{10}H_{14}O_4.C_5H_8O_2)_x$. Properties given by the manufacturer were (a) true specific gravity of the particles 1.19, (b) refraction index of 1.49, (c) multi-dispersed with mean diameter 20µm (grade MR-20G) 20µm, (d) multi-dispersed with mean diameter 90 µm (grade MR-90G), (e) mono-dispersed with size 20.0 ± 1.50 µm (grade MX-2000). Figure 3.12 (a - c) show the scanning electron microscope images of the three acrylic samples.

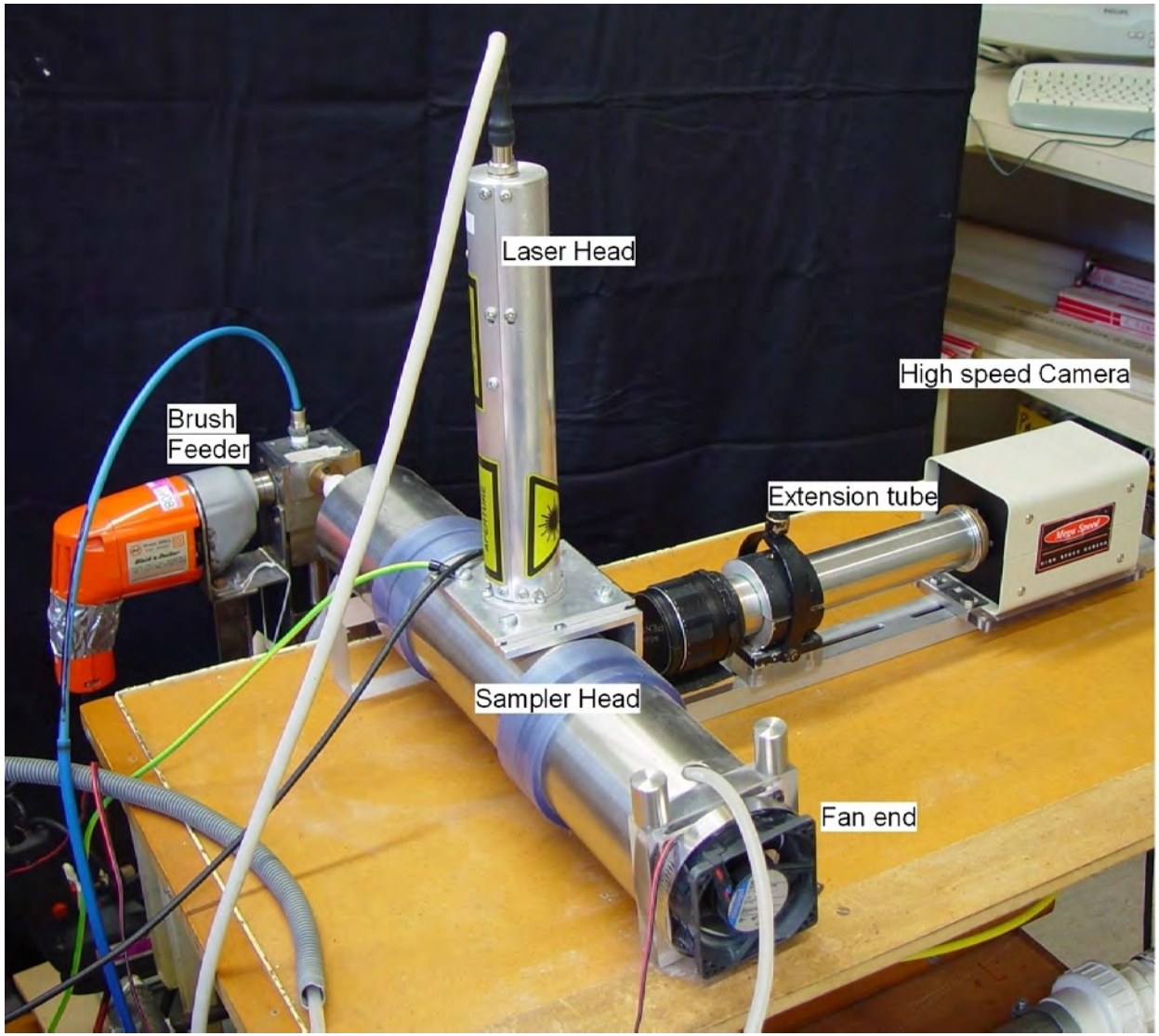

Figure 3.11: Photograph of the sampling head, including the mounted camera, laser and electrical connections

3.9.2 Glass Bubbles

These were multi-disperse borosilicate glass bubbles supplied by 3M Ltd. (K15 Scotchlite) sized 4 to 100 μm with a mean size of 37 μm and a refraction index of 1.51. Figure 3.12 (d) shows the scanning electron microscope images of glass bubbles. 3M listed the particle density as 150 kg/m^3, indicating that the glass wall thickness was less than 1% of the diameter. Glass bubbles were chosen for more rapid orientation of permanent dipoles (having less rotational inertia) and also to minimize any induced dipoles (having less bulk polarisable material close to the probe).

3.9.3 Whole Milk Powder

Whole milk powder was supplied by New Zealand Milk Products (Fonterra Co-operative Group Limited) with a bulk density of 1250 kg/m^3 and a refractive index of 1.095 (Keogh et al, 2003) has been used. The particle size distribution ranges from 18 to 700 μm. The individual or primary particles are spherical but in the sample received they are in agglomerated form with an unstructured arrangement. Figure 3.12 (e) shows the FESEM images of the milk powder.

3.9.4 Fertiliser

A nitrogen based fertiliser has been used supplied by a local farmer. Its bulk density has been measured to be 1517 kg/m^3 and a refractive index value of 1.5 has been assumed based on its composition. The particles are irregularly shaped with sharp ends. Figure 3.12 (f) shows the scanning electron microscope images of the fertiliser particles.

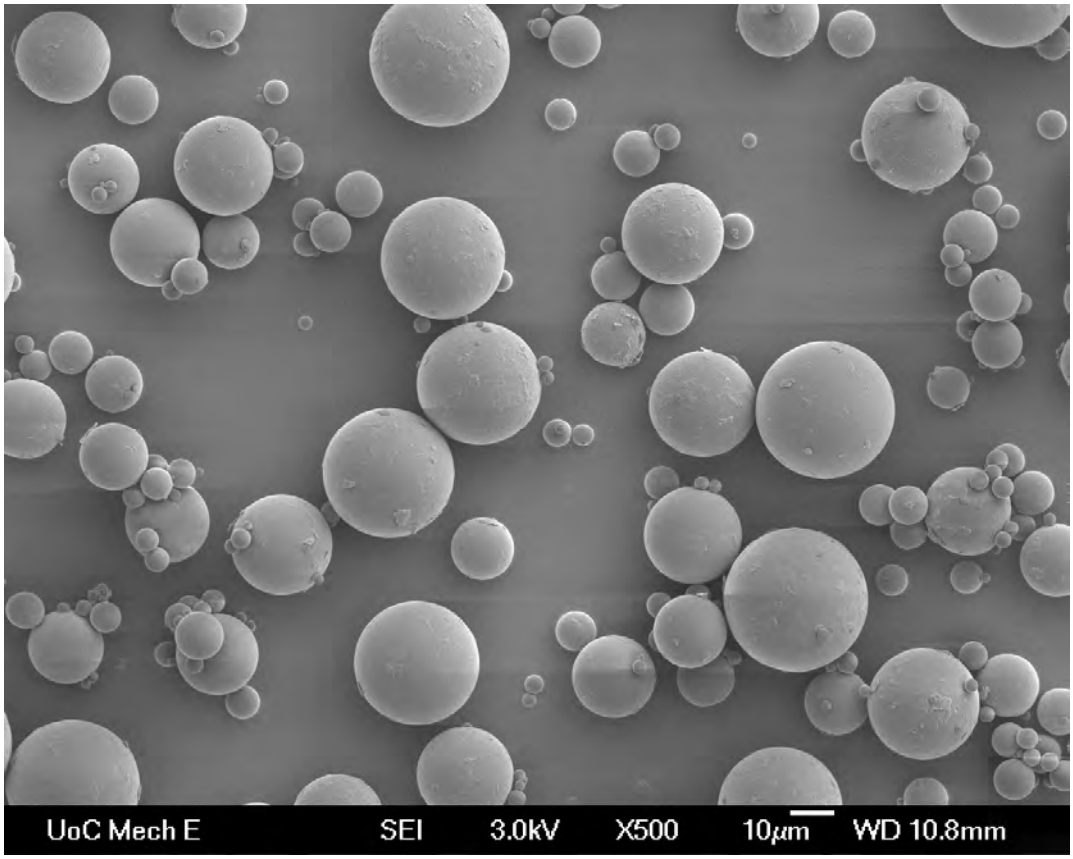

Figure 3.12: (a) MR-20G acrylic sample at X500 magnification.

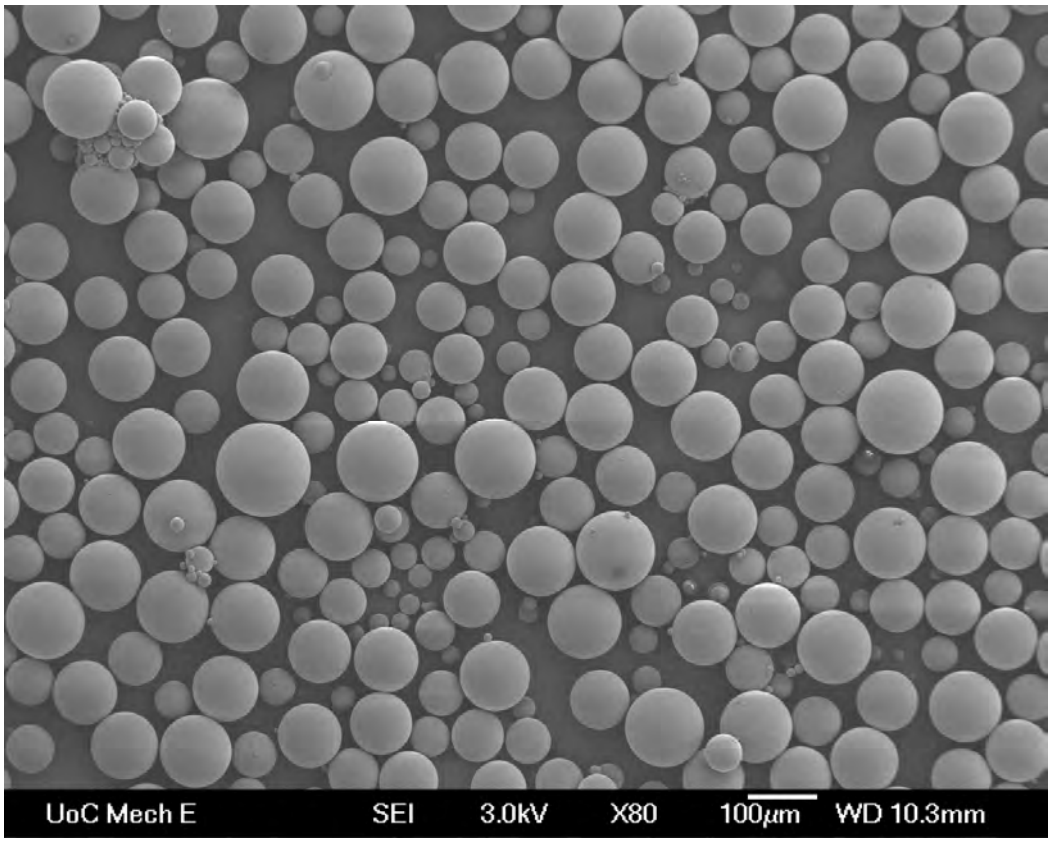

Figure 3.12: (b) MR-90 G acrylic sample at X80 magnification.

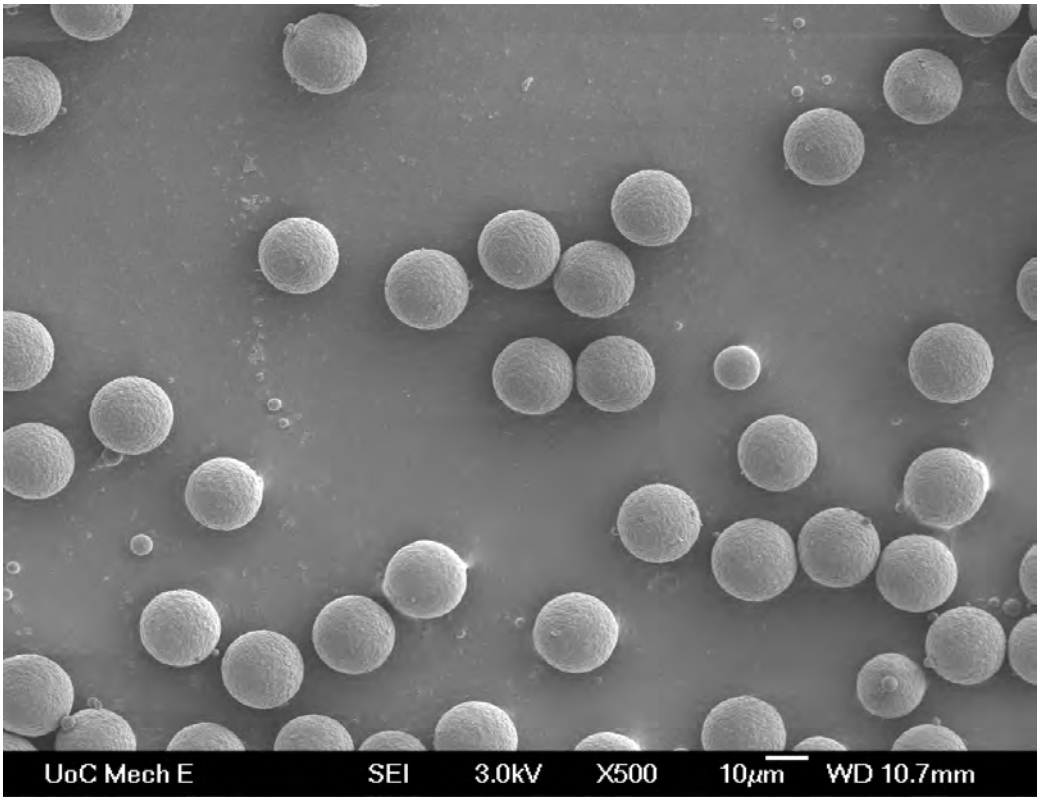

Figure 3.12: (c) MX-2000 mono disperse acrylic sample at X500 magnification.

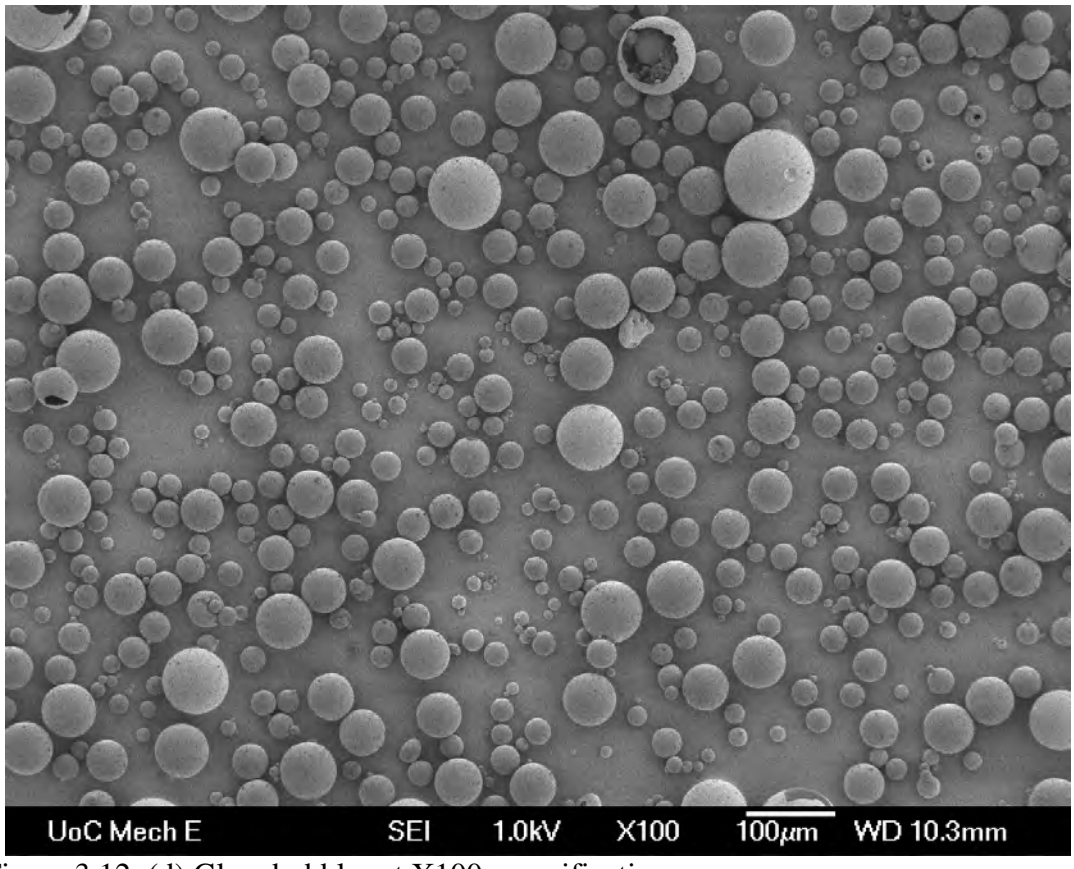

Figure 3.12: (d) Glass bubbles at X100 magnification.

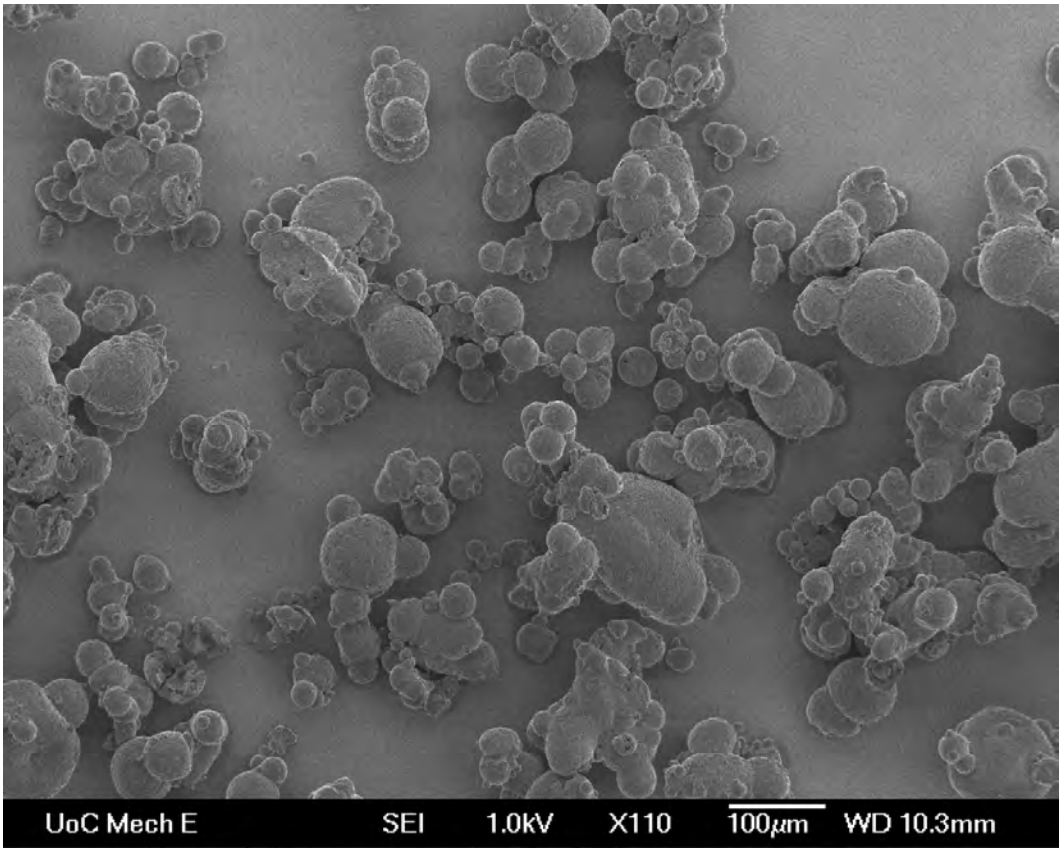

Figure 3.12: (e) Whole milk powder at X110 magnification.

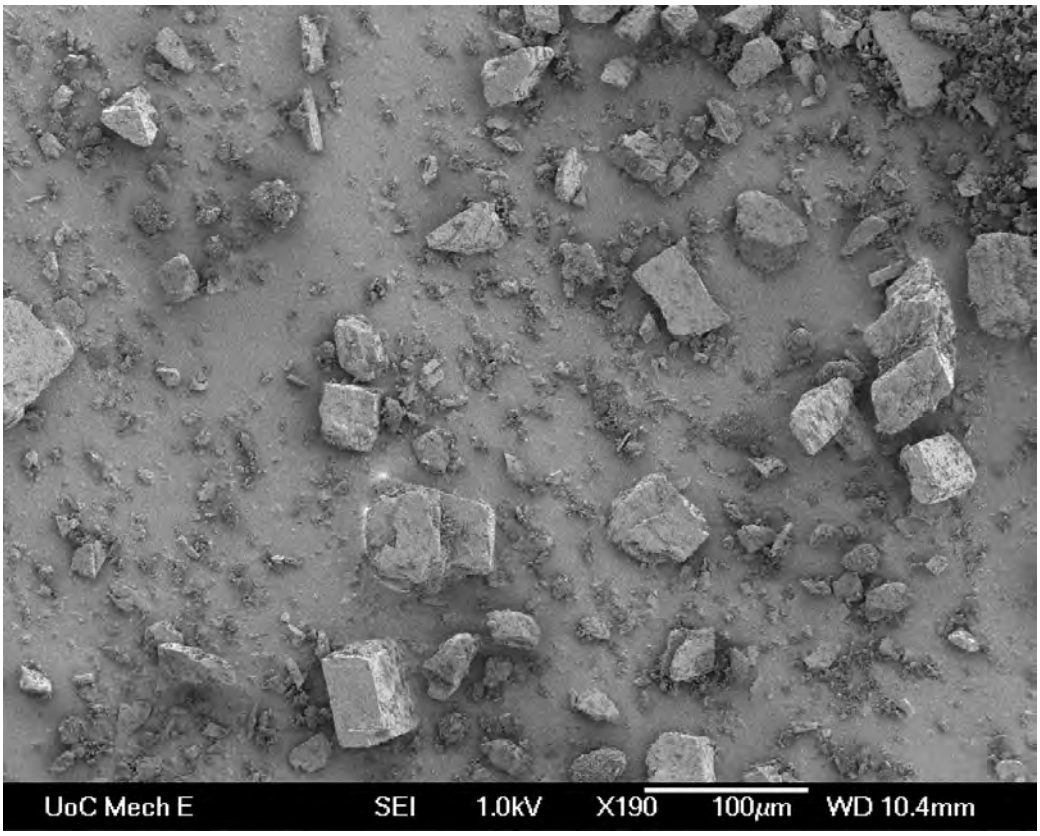

Figure 3.12: (f) Fertiliser powder at X190 magnification.

3.10 Obolensky Filter and Nano Ammeter

The in-house designed and fabricated (Inst. # 2035, Chemical and Process Engineering, University of Canterbury, built in 1995) Obolensky filter was used to measure average charge on the sample particles. The results from charge measurements using this filter served as a comparison for the experimental net charge values derived from the probe measurements. Figure 3.13 (a) depicts the cross sectional view of the filter and Figure 3.13 (b) its installed position. The filter contains a bed of stainless steel wool which is has insulation around it to avoid electrical contact with the outer surface. Any charges built up on the steel wool by capture of charged particles flow through a connecting wire to a grounded nano-ammeter (model 285, Monroe electronics). A nano-ammeter was necessary for this purpose in order to read down to sufficiently small current values. The nano-ammeter was used in the range ± 20.00 nA with a resolution of 0.01 nA.

3.11 Flow Visualisation

After the measurements of charge and dipoles the equipment was modified for flow visualization. The idea was to visualize the flow just upstream of the probe by introducing a “smoke wire” in the sampler head. In the flow visualisation setup a fine nichrome wire (diameter 0.274 mm, transverse Reynolds number 18) was mounted across the sampler head along its centreline about 4 mm in front of the probe tip. A 24V DC power supply with current about 0.8 to 1 amp was used to produce smoke of sufficient quantity. Fig 3.14 (a), (b) and (c) show the smoke wire arrangement around the probe.

Before starting the experiment the wire was coated with an even layer of paraffin oil using a brush. To initialise the run a pulse of current was passed through the wire. It was heated on the passage of current and smoke was produced due to the oil vaporizing from the wire surface. The camera was also triggered by the pulse. The images were captured with the high speed camera and with continuous laser illumination. The frame rate was set at 45 frames/s with an exposure time of 5040 μs to get good quality images of the smoke.

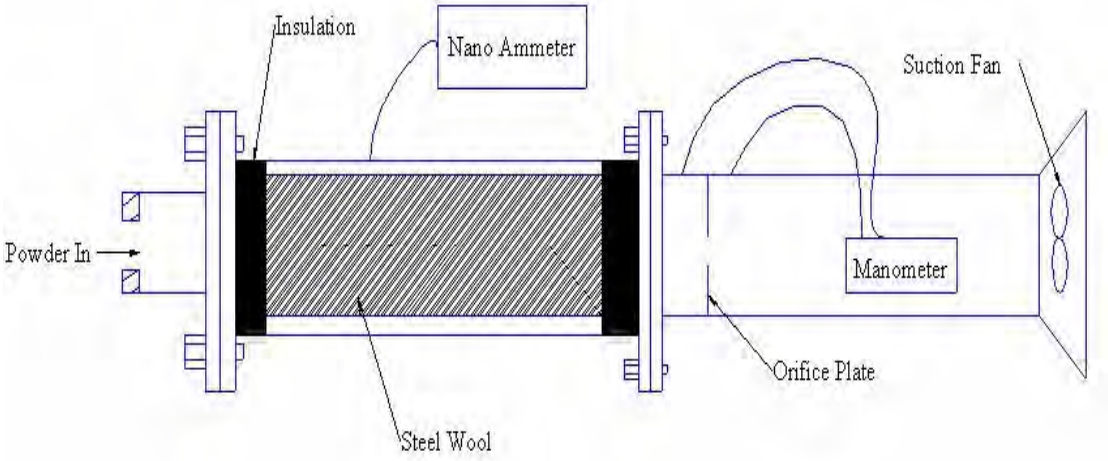

(a)

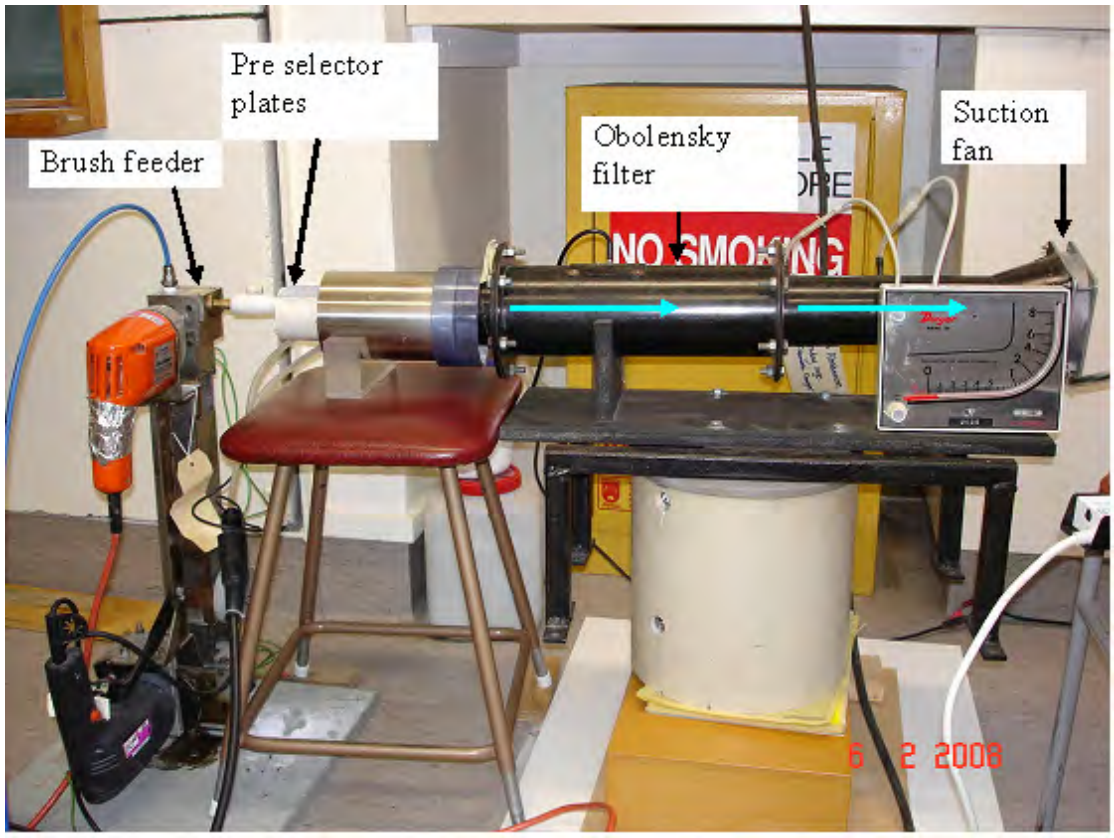

(b)

Figure 3.13: (a) Sectional view of the Obolensiky filter (b) Obolensiky filter installed with the brush feeder and sampling head preselector plates

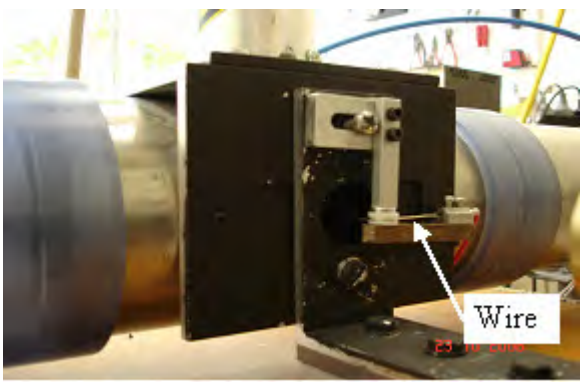

(a)

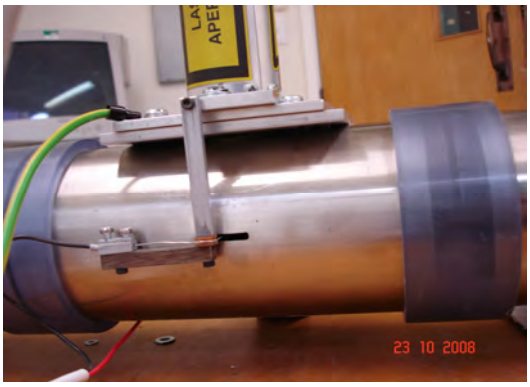

(b)

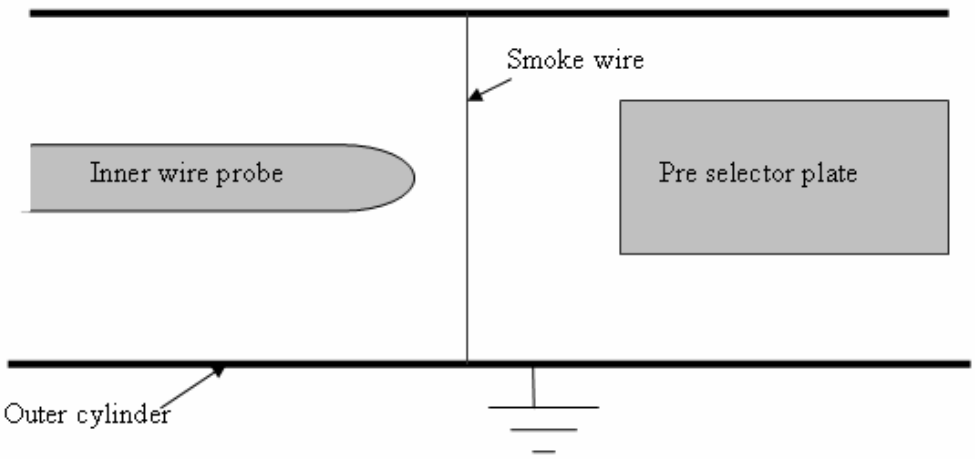

Figure 3.14: Smoke wire arrangement across the sampler head (a) front end (b) back end (c) top view of the smoke wire relative to plates and the probe.

4. Theoretical Model

4.1 Introduction

Particle trajectories have been theoretically modelled using conservation of particle momentum in two dimensions. Both the translational and rotational motion of the particles has been described using the respective drag forces and the electrostatic forces. The following sections explain the equations used to model the particle motion through the air, its behaviour under the effect of electrostatic forces and the assumptions involved. A backward difference time integration of the momentum equations was carried out in an Excel spreadsheet.

4.2 Momentum Conservation Equation

The rate of change of particle velocity has been calculated through particle momentum conservation as in equation 4.1, using drag force, $F_{d,}$ and electrical force, $F_{el,}$ as the dominant forces acting,

$$m\frac{d\vec{U}_p}{dt} = \vec{F}_d + \vec{F}_{el} \tag{4.1}$$

where m is the mass of the particle, U_p is the velocity of the particle. This vector equation was applied in both z and r directions. The gravitational force has been almost always neglected for the test particles owing to their low density and small size.

A time step of 1 μs was chosen for integration. The relative velocity of particle, U_{rel}, was evaluated in both axial and radial directions from the initial velocities calculated from experimental trajectory which provided the basis for calculating the force applied over next time step. The sum of forces was used to calculate acceleration and hence the next position of the particle.

4.3 Translational Drag Force Calculation

The total drag force F_d on the particle has been calculated by the general drag equation for a sphere involving a variable drag coefficient, and the correlation proposed by Abraham (1970) was used, satisfactory for particle Reynolds numbers Re_p from 0 to 6000. This drag force F_d was resolved in the z and r directions with the direction of F_d opposing the direction of U_{rel} (relative velocity) found from the velocities of the previous time.

The relative velocity of the particle with respect to the air has been calculated as

$$U_{rel} = \sqrt{\left(u_{pr} - u_{gr}\right)^2 + \left(u_{pz} - u_{gz}\right)^2} \tag{4.2}$$

The Abraham expression for C_D is

$$C_D = \frac{24}{\delta_o^2}\left[1 + \frac{\delta_o}{Re_p^{1/2}}\right]^2 \tag{4.3}$$

Here the dimensionless boundary layer thickness $\delta_o = 9.06$ and the Reynolds number of particle is given by

$$Re_P = \frac{D_P \rho_{air} U_{rel}}{\eta_{air}} \tag{4.4}$$

The drag force was then calculated from the expression defining C_D;

$$F_d = \frac{C_D A_P U_{rel}^2 \rho_{air}}{2} \tag{4.5}$$

where A_p is the projected area of the particle. Figure 4.1 shows schematically a typical particle trajectory bending away from the probe, with axes, velocities, and various angles used in the analysis. The probe tip centre was considered as the origin for both radial and axial positions in cylindrical co-ordinates.

To evaluate the components of velocity the flow field has been calculated in the spreadsheet assuming that the flow around the hemispherical tip is close to that

around a sphere. Thus Stokes' equations for creeping flow over a sphere (Bird et al. 1962) were used. The relevant angles and points used in modelling the flow, particularly θ_{stk} the angle of the particle relative to the downstream direction of the gas flow used by Stokes in his model, are shown in Figure 4.1.

The equations used to find components of gas velocity were derived from creeping flow over a sphere. Equation 4.6 gives the radial component (in spherical coordinates) of gas velocity and equation 4.7 gives the θ (rotating) component of the gas velocity, again in spherical coordinates, with the origin at the tip centre.

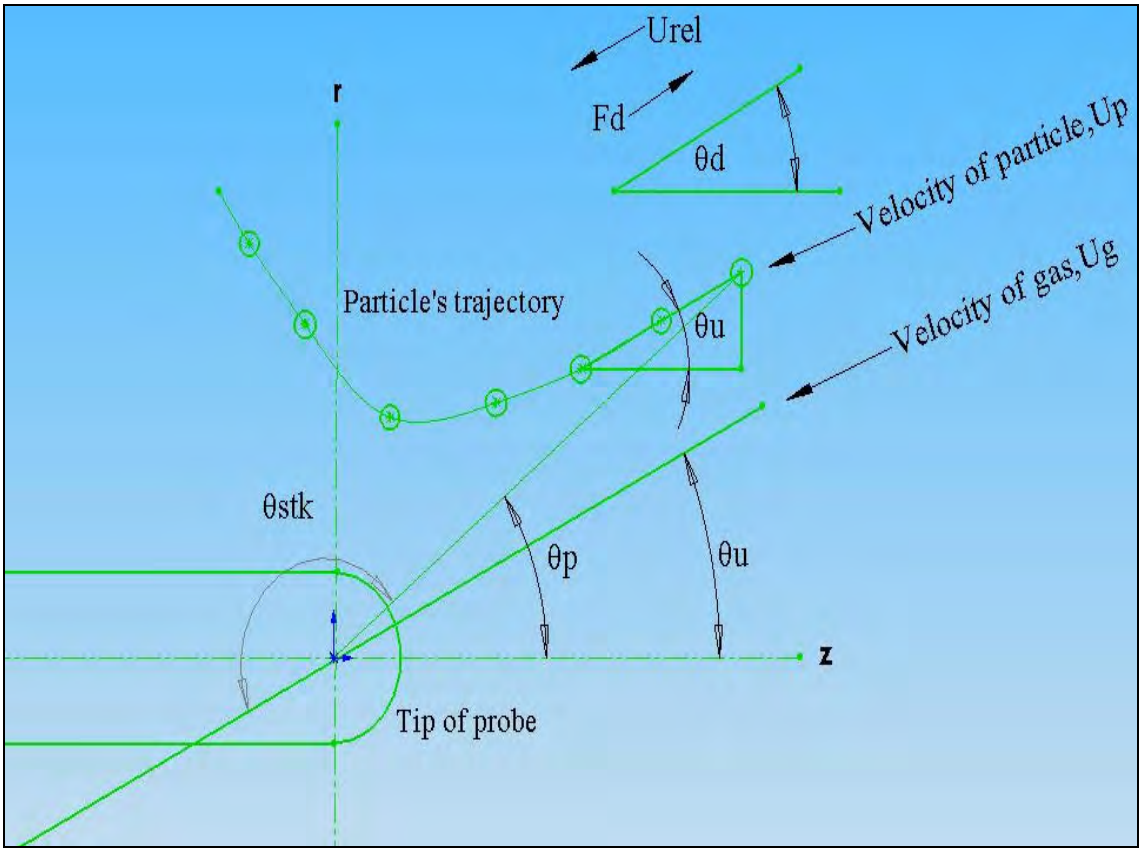

Figure 4.1: Relevant angles and points used for modelling particle trajectories around a high voltage probe pointing upstream (θ_u and θ_p are the angles of gas and particle velocities, θ_d is the angle of drag force, all relative to the z axis and θ_{stk} is the Stokes angle, particle position angle relative to the gas approach axis). Relative velocity $\vec{U}_{rel} = \vec{U}_p - \vec{U}_g$

$$u_{gr_{sph}} = u_\infty \left(1 - \frac{3}{2}\left(\frac{a}{r_{sph}}\right) + \frac{1}{2}\left(\frac{a}{r_{sph}}\right)^3\right) cos\ \theta_{stk} \qquad (4.6)$$

$$u_{g\theta} = -u_{\infty}\left(1-\frac{3}{4}\left(\frac{a}{r_{sph}}\right)-\frac{1}{4}\left(\frac{a}{r_{sph}}\right)^{3}\right) sin\ \theta_{stk} \tag{4.7}$$

Converting the spherical components into cylindrical components gives equations for gas velocities in z and r directions. For the z direction,

$$u_{gz} = u_{gr_{sph}}\ cos\left|\theta_p\right| + u_{g\theta}\ sin\left|\theta_p\right| \tag{4.8}$$

where the modulus of θ_p has been used.

For the r direction, to follow the correct sign convention the condition on θ_p was applied such that if $\theta p \geq 0$ (gas flow downwards)

$$u_{gr} = u_{gr_{sph}}\ sin\left|\theta_p\right| - u_{g\theta}\ cos\left|\theta_p\right| \tag{4.9}$$

Otherwise if the gas flow is upwards, a negative sign is applied

$$u_{gr} = u_{g\theta}\ cos\left|\theta_p\right| - u_{grsph}\ sin\left|\theta_p\right| \tag{4.10}$$

From the components of gas and particle velocities, calculations were made of the drag angle, θ_d, the angle made by relative motion of particle with the horizontal axis.

$$tan\ \theta_d = \frac{u_{pr} - u_{gr}}{u_{pz} - u_{gz}} \tag{4.11}$$

The drag force components in the z and r directions were then calculated using the drag angle. For both cases the motion towards the probe was in a negative direction, hence a negative sign

$$F_{d_{axial}} = -F_d\ cos\left|\theta_d\right| * sign(u_{pz} - u_{gz}) \tag{4.12}$$

$$F_{d_{radial}} = -F_d\ sin\left|\theta_d\right| * sign(u_{pz} - u_{gz}) \tag{4.13}$$

The above drag force components were used in the final calculations. In next section the procedure to calculate electrostatic forces will be summarised.

4.4 Electrostatic Force Calculations

The electrostatic force has been taken as the sum of the monopole force $\vec{F}_{mono}$, dipole force $\vec{F}_{dip}$, induced dipole force $\vec{F}_{ind}$ and the image force $\vec{F}_{image}$ due to both the monopole and dipole charges.

$$\overrightarrow{F_{el}} = \overrightarrow{F_{mono}} + \overrightarrow{F_{dip}} + \overrightarrow{F_{ind}} + \overrightarrow{F_{image}} \tag{4.14}$$

All of these forces act along the probe-centre to particle-centre direction, and so can be simply evaluated as a function of the separation of these centres r_{sph} (the radial position of the particle in spherical coordinates).

4.4.1 Monopole Force $\vec{F}_{mono}$

The monopole force on a particle with net charge q_{net} moving in an electric field E is given by

$$\overrightarrow{F_{mono}} = q_{net}\ \vec{E} \tag{4.15}$$

The equation for the radial electric field between concentric spheres is given by (Cross, 1987)

$$\vec{E} = \frac{V}{\left(\frac{1}{a} - \frac{1}{b}\right) r_{sph}^2} \tag{4.16}$$

where in this thesis a is the probe tip radius, b is the tube radius and V is the probe voltage. Substituting for the spherical electric field in equation 4.15 the force on the particle due to net charge (monopole) is given by

$$\overrightarrow{F_{mono}} = \frac{q_{net} V}{\left(\frac{1}{a} - \frac{1}{b}\right) r_{sph}^2} \tag{4.17}$$

4.4.2 Dipole Force $\vec{F}_{dip}$

The dipole force is the product of the dipole moment P and the gradient of electric field

$$\overrightarrow{F_{dip}} = P\left(\frac{d\vec{E}}{dr_{sph}}\right) \tag{4.18}$$

Substituting for the gradient of electric field from differentiating equation 4.16 we get an equation for dipole force as

$$\overrightarrow{F_{dip}} = \frac{-2PV}{\left(\frac{1}{a}-\frac{1}{b}\right)r_{sph}^3} \tag{4.19}$$

We choose arbitrarily to represent the dipole moment as

$$P = q_{dip} \times 2R_p \tag{4.20}$$

where q_{dip} is defined as the equivalent charge at each end of the particle diameter.

4.4.3 Induced Dipole Effect $\vec{F}_{ind}$

From Cross 1987, the induced dipole on a spherical grain is given by

$$P = \left[\frac{(\varepsilon-1)}{(\varepsilon+2)}\right]\frac{\vec{E}R_p^{\,3}}{\kappa} \tag{4.21}$$

where E is the imposed external electric field at the position of the grain, R_p is the grain radius, κ is Coulomb's constant ($1/(4\,\pi\,\varepsilon_o)$)and ε_r is the permittivity of the grain *relative* to that of a vacuum. We will call the factor in the square brackets U (multiplication factor) such that

$$P = U\frac{ER_p^{\,3}}{\kappa} \tag{4.22}$$

and

$$U = \frac{\varepsilon_r - 1}{\varepsilon_r + 2} \tag{4.23}$$

For non conducting grains, U is less than one, becoming zero, as expected in the limit $\varepsilon_r = 1$ (no excess permittivity). Typical permittivities are expected to be greater than 4. For purpose of estimation, U can be taken to be unity representing the worst case ($\varepsilon_r = \infty$, fully conducting, so that charges can move freely in response to the field), so that for a conducting sphere

$$P = \frac{ER_p^{\,3}}{\kappa} \tag{4.24}$$

As induced dipole is aligned to the field gradient and substituting for P in equation 4-19 from equation 4-22, and for k, the induced dipole force for a solid spherical particle is

$$\vec{F}_{ind} = U \frac{-8\pi\varepsilon_o V^2 R_p^{\,3}}{\left(\frac{1}{a} - \frac{1}{b}\right)^2 r_{sph}^{\,5}} \tag{4.25}$$

In our calculations a strong induced dipole in the grains caused by the applied electric field is an undesirable effect as it can mask the existence of a permanent dipole (with force $\vec{F}_{dip}$).

4.4.3.1 Calculation of Multiplication Factor U for Different Geometries

Multiplying equation 4.23 top and bottom by ε_e, the permittivity of the medium outside the sphere, gives a more general expression for U

$$U = \frac{\varepsilon_i - \varepsilon_e}{\varepsilon_i + 2\varepsilon_e} \tag{4.26}$$

where in this study air is the external medium, i.e. $\varepsilon_e = \varepsilon_o$. Equation 4.26 has been used for calculation of U for all solid particles except for the glass bubbles in which case a different method has been used owing to its geometry.

Following Roth and Dignam (1973), Ko et al. (2004) calculated the *U* factor for a single-shell spherical cell with an isotropic, dielectric membrane as

$$U = \frac{(2\varepsilon_m + \varepsilon_i)(\varepsilon_m - \varepsilon_e)R_e^3 + (\varepsilon_i - \varepsilon_m)(2\varepsilon_m + \varepsilon_e)R_i^3}{(2\varepsilon_m + \varepsilon_i)(2\varepsilon_e + \varepsilon_m)R_e^3 + 2(\varepsilon_i - \varepsilon_m)(\varepsilon_m - \varepsilon_e)R_i^3} \tag{4.27}$$

where ε is the permittivity and *R* the radius; the subscripts *e*, *m* and *i* correspond to the external medium, the membrane and the internal space respectively.

For the case of glass bubbles the internal and external medium is air and the membrane is a shell of glass. So $\varepsilon_i = \varepsilon_o = \varepsilon_r$

$$U = \frac{(2\varepsilon_m + \varepsilon_o)(\varepsilon_m - \varepsilon_o)R_e^3 + (\varepsilon_o - \varepsilon_m)(2\varepsilon_m + \varepsilon_o)R_i^3}{(2\varepsilon_m + \varepsilon_o)(2\varepsilon_o + \varepsilon_m)R_e^3 + 2(\varepsilon_o - \varepsilon_m)(\varepsilon_m - \varepsilon_0)R_i^3} \tag{4.28}$$

Substituting $\varepsilon_r = \frac{\varepsilon_m}{\varepsilon_o}$ and rearranging

$$U = \frac{(2\varepsilon_r + 1)(\varepsilon_r - 1)\left(1 - \left(\frac{R_i}{R_e}\right)^3\right)}{(2\varepsilon_r + 1)(2 + \varepsilon_r) + 2(1 - \varepsilon_r)(\varepsilon_r - 1)\left(\frac{R_i}{R_e}\right)^3} \tag{4.29}$$

Refractive index of Glass, μ = 1.51

So dielectric constant, $\varepsilon_r = \mu^2 = (1.51)^2 = 2.28$

The apparent density of a particle is given by

$$\rho_a = \frac{mass\ of\ shell}{volume\ of\ particle} \tag{4.30}$$

In this case the apparent density of the glass bubbles, ρ_a = 150 kg/m^3 (3M Ltd., 2007)

Substituting the formulae for the volume of particle and rearranging in equation 4.30

$$\rho_a = \rho_s\left(1 - \left(\frac{R_i}{R_e}\right)^3\right) \tag{4.31}$$

where R_i is the internal radius and R_e is the external radius. Further simplification gives

$$\frac{R_i}{R_e} = \left(1 - \frac{\rho_a}{\rho_s}\right)^{\frac{1}{3}} = \left(1 - \frac{150}{2640}\right)^{\frac{1}{3}} = 0.9807 \tag{4.32}$$

Using equation 4.29 the value of U_{iso} comes out to be 0.0195 for glass bubbles.
The thickness of the shell can be found as,

$$\frac{Thickness}{R_e} = \frac{(R_e - R_i)}{R_e} = 0.0193 \tag{4.33}$$

i.e. the thickness is almost 2% of the radius. For example for a 60 µm diameter sphere the shell is expected to be 30 x 0.0193 = 0.58 µm thick.

4.4.4 Image Force $\vec{F}_{image}$

An electrical image is defined as an electrified point or system of points on the far side of a surface which would produce on the near side of the surface the same electrical action which the actual electrification of that surface really does produce (Cross, 1987). The electrical action on a particle positioned above the surface (on the near side) is considered.

The image energy interaction with a point charge q, a distance z above a conducting flat surface is given by

$$u_p = \frac{-q^2}{4z} \tag{4.34}$$

Here q can also be the net charge on a particle and z the distance of the centre of charge from the surface. So to calculate the force on the particle this equation can be differentiated w.r.t. z

$$F_p = \frac{q^2}{4z^2} \tag{4.35}$$

For this study the equation used for the image force in the case of a monopole charge sitting a distance (r_{sph}-a) from the surface of the conducting (spherical) probe of radius a (in SI units) has been given by

$$F_{image\ net} = \frac{-q_{net}^2}{16\pi\varepsilon_o\left(r_{sph}-a\right)^2} \tag{4.36}$$

where Q_{net} is located at the centre of the particle.

To a first approximation, the image force for the dipole charge is given by

$$F_{image\ dip} = \frac{-q_{dip}^2}{16\pi\varepsilon_o\left(r_{sph}-R_p-a\right)^2} \tag{4.37}$$

where one of the two hypothetical Q_{dip} charges which make up the dipole (assumed aligned with E and r_{sph}) is very close to the surface, i.e. at a gap of ((r_{sph}-a)-R_p) from the probe surface. The contribution of other charge on the other side of the particle can be ignored in comparison, e.g., for a 60 µm particle with a 10 µm closest approach due to roughness to a 250 µm radius probe, the far charge contributes $\frac{10^2}{70^2} \approx \frac{1}{50}$th of that of the near charge.

4.4.5 Final Equation for Electrostatic Force

Substituting expressions for each of the above forces in equation 4.14 the final expression for electrostatic force is

$$F_{el} = \frac{q_{net}V}{(1/a-1/b)r_{sph}^{\ 2}} - \frac{2PV}{(1/a-1/b)r_{sph}^{\ 3}} - U\frac{8\pi\varepsilon_o V^2 R_p^{\ 3}}{(1/a-1/b)^2 r_{sph}^{\ 5}} - \frac{q_{net}^2}{16\pi\varepsilon_o\left(r_{sph}-a\right)^2} - \frac{q_{dip}^2}{16\pi\varepsilon_o\left(r_{sph}-R_p-a\right)^2} \tag{4.38}$$

The electrostatic force with negative sign implies attractive force towards the probe and a positive value implies repulsive force directing away from the probe. In equation 4.38 a, b, r_{sph}, P, U, R_p and ε_o always remain positive whereas Q_{net} can be both negative and positive and Q_{dip} depends on sign of V. So it can be observed that

the monopole force can be attractive or repulsive but the induced dipole force and the image forces due to monopole and dipole always remain attractive to the probe. The dipole force will depend on the alignment of the dipole and becomes attractive once the dipole has aligned in the direction of the electric field.

After this the net electrostatic force F_{el} was resolved into its radial and axial components. To decide what sign each component should have, the region in the front of the probe was divided into two parts as shown in Figure 4.2. These two regions were considered as analysis was done mainly for particles approaching the probe tip from its front end.

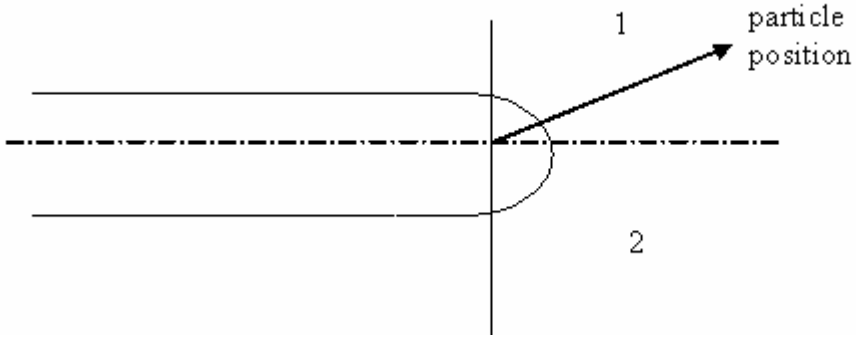

Figure 4.2: Regions of particle position in front of the probe used to predict sign for components of electrostatic force.

The axial component of net electrostatic force $F_{el\ axial}$ is given as

$$F_{el\ axial} = F_{el}\ cos\left|\theta_p\right| * Sign(z) \tag{4.39}$$

and the radial component of net electrostatic force $F_{el\ radial}$ is given as

$$F_{el\ axial} = F_{el}\ sin\left|\theta_p\right| * Sign(r) \tag{4.40}$$

The sign convention followed is explained in Tables 4.1 and 4.2.

Table 4.1: Sign convention for region 1

F_{el}	$Cos\ \theta_p$	$Sin\ \theta_p$	F_{el} axial	F_{el} radial
+ve	+ve	+ve	+ve	+ve
-ve	+ve	+ve	-ve	-ve

Table 4.2: Sign convention for region 2

F_{el}	$Cos\ \theta_p$	$Sin\ \theta_p$	F_{el} axial	F_{el} radial
+ve	+ve	-ve	+ve	-ve
-ve	+ve	-ve	-ve	+ve

θ_p mentioned in Table 4.1 and 4.2 is the angle the particle's r_{sph} makes with the centre line of probe as defined in Figure 4.1.

4.5 Rotational Drag Force Calculation

In an electric field the dipole will exert a torque on the particle to orient itself in the direction of the field. We assumed that the dipole charges do not move along the particle surface. The angular acceleration of the particle has been calculated from the angular momentum conservation equation, using the component of local field which is perpendicular to the dipole, acting on the dipole strength to provide turning torque, and using viscous drag forces to resist.

The angular momentum conservation of the particle is given by

$$J\frac{du_\theta}{dt} = \left(\vec{P}\times\vec{E}\right) - \vec{G} \tag{4.41}$$

where u_θ = angular velocity of the particle.

The drag torque G for a sphere of radius R_p is calculated as (Jeffrey, 1915)

$$G = 8\pi\eta\, u_\theta R_p^3 \tag{4.42}$$

For a solid spherical particle, the moment of inertia

$$J = \frac{2}{5}mR_p^2 \tag{4.43}$$

where m = mass of the particle.

Vectors P and E can be expressed in component form as

$$\vec{P} = P_y i + P_z j + P_r k \tag{4.44}$$

$$\vec{E} = E_y i + E_z j + E_r k \tag{4.45}$$

The magnitude of dipole strength *P* is then given as

$$P = \sqrt{P_r^2 + P_z^2 + P_y^2} \tag{4.46}$$

The cross product $\vec{P} \times \vec{E}$ in terms of its components can be calculated as

$$\vec{P} \times \vec{E} = (P_z E_r - P_r E_z)i + (P_r E_y - P_y E_r)j + (P_y E_z - P_z E_y)k \tag{4.47}$$

It was assumed that the particle dipole alignment was perpendicular to the *r* direction when it came out of the plates, so calculations were made for the dipole alignment during the trajectory flight using these three dimensional equations.

The angular acceleration in the *r* direction from equation 4.39 is

$$J \frac{du_{\theta r}}{dt} = \left(\vec{P} \times \vec{E}\right)_r - \vec{G}_r \tag{4.48}$$

Substituting the r-component of $\vec{P} X \vec{E}$ from equation 4.46 and torque from equation 4.42

$$\frac{du_{\theta r}}{dt} = \frac{5}{2mr_p^2}\left(\left(P_y E_Z - P_z E_y\right) - 8\pi\eta R_p^3 u_{\theta r}\right) \tag{4.49}$$

Similar equations can be written for angular acceleration in the *z* and *y* directions. For z and y direction the angular acceleration is given by

$$\frac{du_{\theta z}}{dt} = \frac{5}{2mr_p^2}\left(\left(P_r E_y - P_y E_r\right) - 8\pi\eta \ R_p^3 u_{\theta z}\right) \tag{4.50}$$

$$\frac{du_{\theta y}}{dt} = \frac{5}{2mr_p^2}\left(\left(P_z E_r - P_r E_z\right) - 8\pi\eta \ R_p^3 u_{\theta y}\right) \tag{4.51}$$

Figure 4.3 represents the angles between the direction of components of vector *P* and the co-ordinate axes. The angles $\theta_y, \theta_z, \theta_r$ calculated by integrating the gradients were then used to calculate components of vector *P* using equation 4.49, 50 and 51.

$$P_r = \frac{P_y}{tan\ \theta_z} \tag{4.52}$$

$$P_z = P_y \ tan\ \theta_r \tag{4.53}$$

$$P_y = \sqrt{\frac{P^2}{\left(\frac{1}{tan\ \theta_z}\right)^2 + (tan\ \theta_r)^2 + 1}} \tag{4.54}$$

The components of electric field in the *r* and *z* directions were calculated as

$$E_z = E\ cos\ \theta_p \tag{4.55}$$

$$E_r = E\ sin\ \theta_p \tag{4.56}$$

$$E_y = 0 \tag{4.57}$$

for particles travelling in the r-z plane with y = 0, i.e. the plane of the laser sheet.

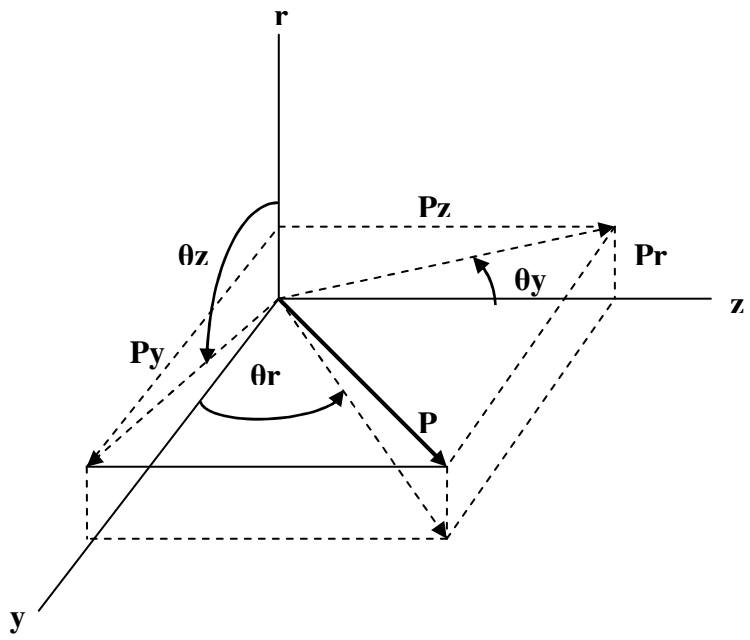

Figure 4.3: The angles between direction of vector *P* and the co-ordinate axes.

Using the dot product between vector *P* and *E* the angle between them was calculated. This angle, θ_T (Figure 4.4) gives direction of the torque experienced by the dipole in the electric field.

$$cos\ \theta_T = \frac{P.\ E}{|P|\,|E|} \tag{4.58}$$

$$cos\ \theta_T = \frac{P_r\ E_r + P_z E_z + P_y E_y}{|P|\,|E|} \tag{4.59}$$

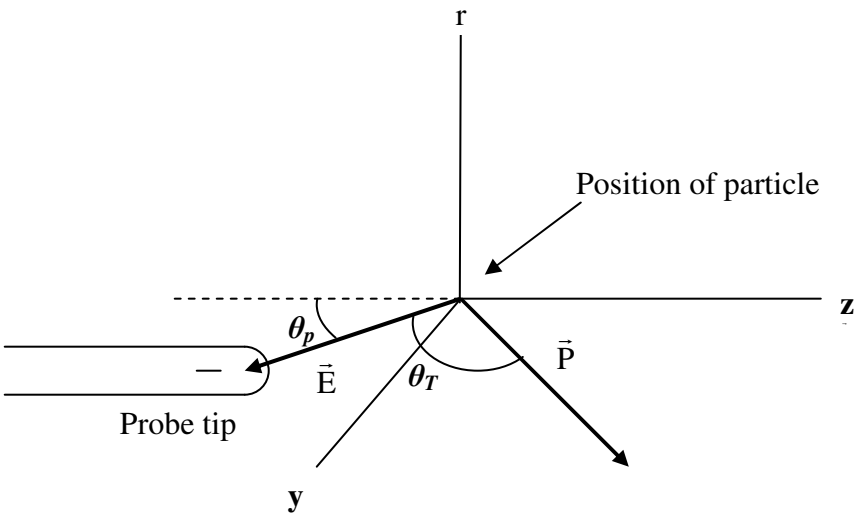

Figure 4.4: Dipole-to-field angle θ_T.

The initial conditions assumed were

$\theta_y = 90°$, $\theta_z = 270°$, $\theta_r = 180°$, P_y = -P, $P_z = 0$, and $P_r = 0$

Calculations were made to predict the time required for θ_T to change from 90° (initial position) to 0° or 180° depending on whether the electric field direction is pointing away or towards the probe (probe positive or negative respectively). Also for spherical shells (e.g. hollow glass bubbles) the moment of inertia,

$$J = \frac{2}{3} m R_p^2 \tag{4.60}$$

and hence a correction was made for this in the calculations.

Note that the position of the origin (position of the particle) in Figure 4.4 is in the r-z plane passing through the centreline of the probe.

5. COMSOL Simulation

5.1 Background of COMSOL

COMSOL Multiphysics is a powerful tool for modelling and solving all kinds of scientific and engineering problems based on partial differential equations. It offers modelling and analysis power for many application areas such as fluid dynamics, heat transfer, electromagnetics, structural mechanics, optics, transport phenomena, chemical reactions etc. The package can import or export geometries to combine PDE-based modelling, simulation, and analysis with other modelling techniques. It provides an integrated graphical user interface where the models can be built and solved by using predefined physics mode, PDE modes, or a combination of them - multiphysics modelling. The model can be built by defining the relevant physical quantities such as material properties, loads, constraints, sources, and fluxes. The first step is to create the geometry and then various constants and variables can be set. When the parameters have been defined the package automatically meshes the geometry or it can be done manually as well. After this the problem is solved from a set of iterative and non-iterative solvers. The solver can be chosen manually or the package sets up a default solver for the chosen application mode and automatically detects linearity and symmetry in the model. There are a wide range of tools provided for plotting and post processing any model quantity. For the purposes of this study the COMSOL Multiphysics version 3.4 was used. In particular the COMSOL multiphysics and the chemical engineering application modes were used for modelling the electric field and turbulence inside the model geometry.

5.2 Electrostatics

The electrostatics part of the electromagnetics mode (in COMSOL multiphysics) is used to model applications involving high-voltage apparatus, electronic devices, and capacitors. The static electric fields are modelled using the electric potential V given as

$$E = -\nabla V \tag{5.1}$$

This equation combined with the constitutive relationship between electric flux density, D, and electric field intensity, $E, D = \varepsilon_0 E + P$, represents Gauss' law as Poisson's equation

$$-\nabla \cdot (\varepsilon_0 \nabla V - P) = \rho \tag{5.2}$$

where P is the electric polarization vector and ρ is the electric charge density. The default scalar variable is the permittivity of vacuum with value 8.854×10^{-12} F/m.

5.2.1 Model Geometry

A 3D model geometry domain was created as in Figure 5.1 to predict the electric field and potential inside the sampler head. A cylinder of diameter 100 mm and length 300 mm was drawn to replicate the experimental geometry to predict the electric field. The preselector plates drawn were 150 mm long, 50 mm wide and 0.5 mm thick. The plates were 10 mm apart from each other and 30 mm away from the tip of the probe. The wire was of 500 µm diameter and 100 mm long mounted on the centreline towards the exit end. Voltage was applied to the wire probe and one of the preselector plates.

5.2.1.1 Boundary Conditions

Electric Potential: The electric-potential boundary condition $V = V_0$ specified the voltage at a boundary. The voltage was set to 10 kV for all boundaries of the probe and 10 kV for all boundaries of one of the two preselector plates.

Ground: The general boundary condition V = 0 specifies zero potential. This condition was applied to all the remaining boundaries (excepting the probe and one plate).

A normal mesh with 183960 tetrahedral mesh elements and 8930 triangular boundary elements was used. The stationery linear solver with adaptive mesh refinement was used to solve the problem. It is important to select a mesh that minimizes the error in

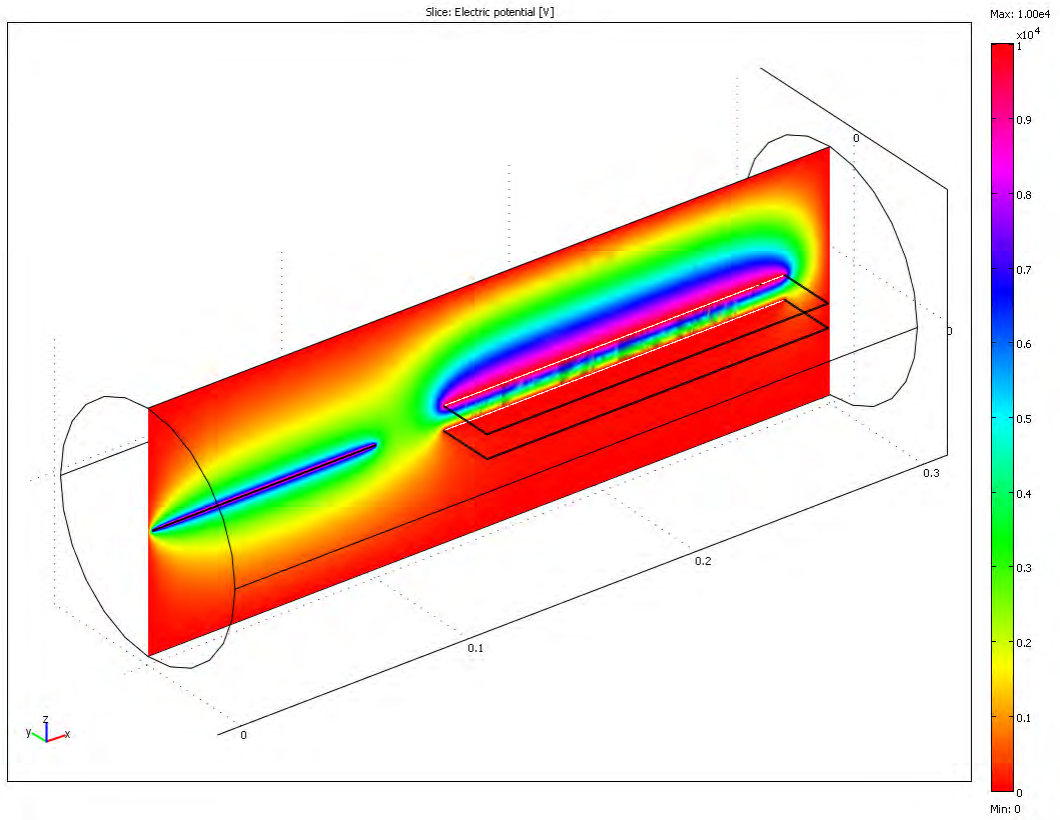

(a)

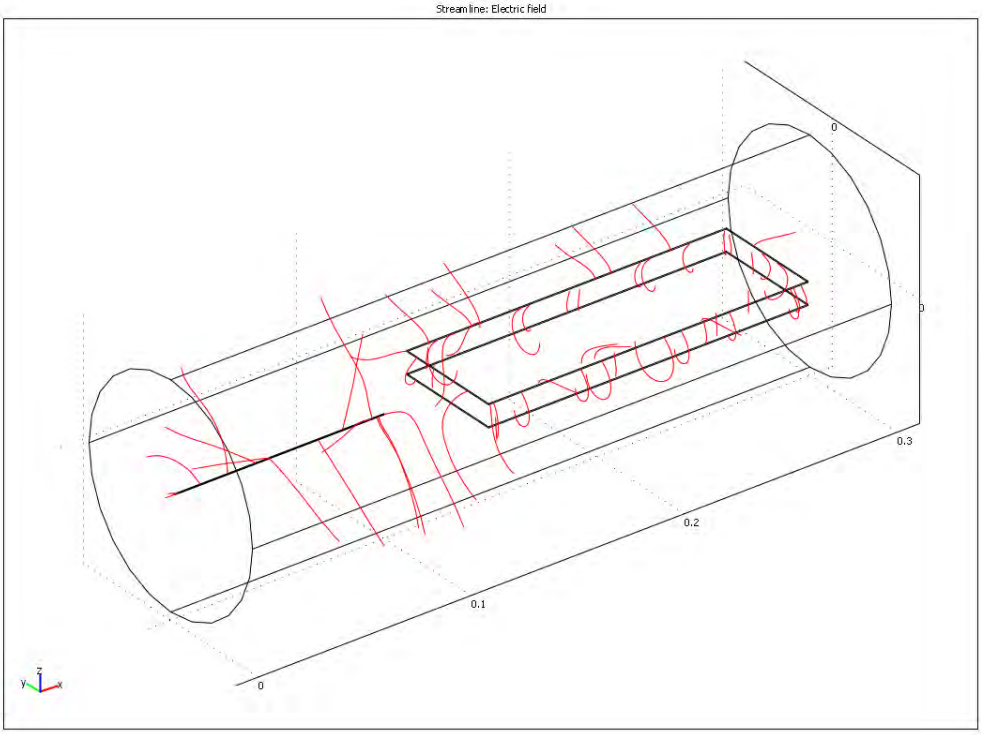

(b)

Figure 5.1: (a) Electric potential variation across a slice cut in the middle of the geometry at an applied voltage of 10 kV (b) Electric field streamlines emerging from the surfaces.

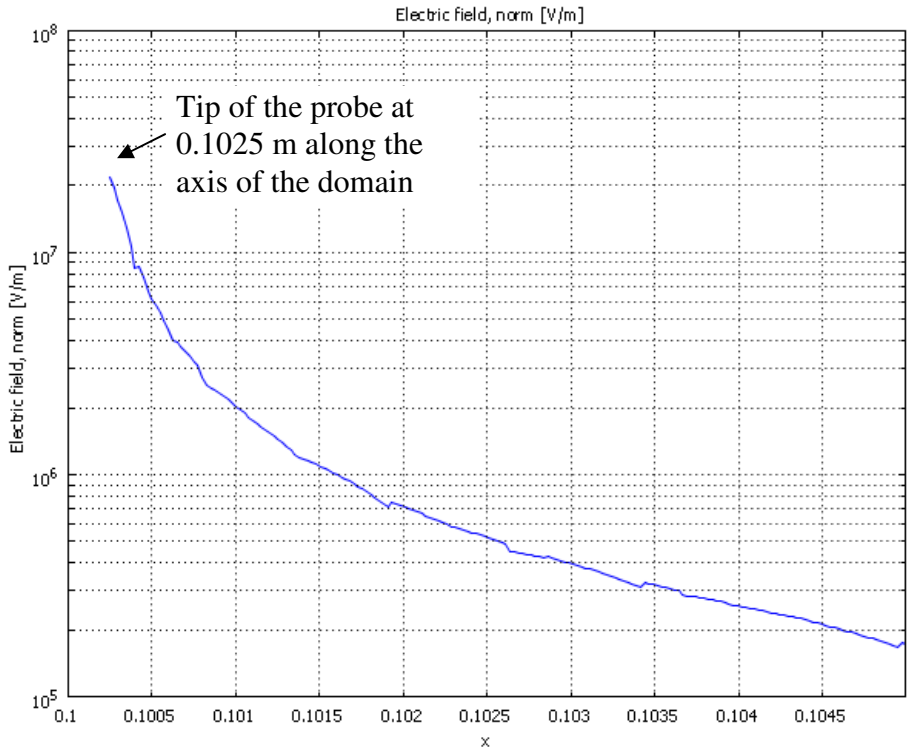

(a)

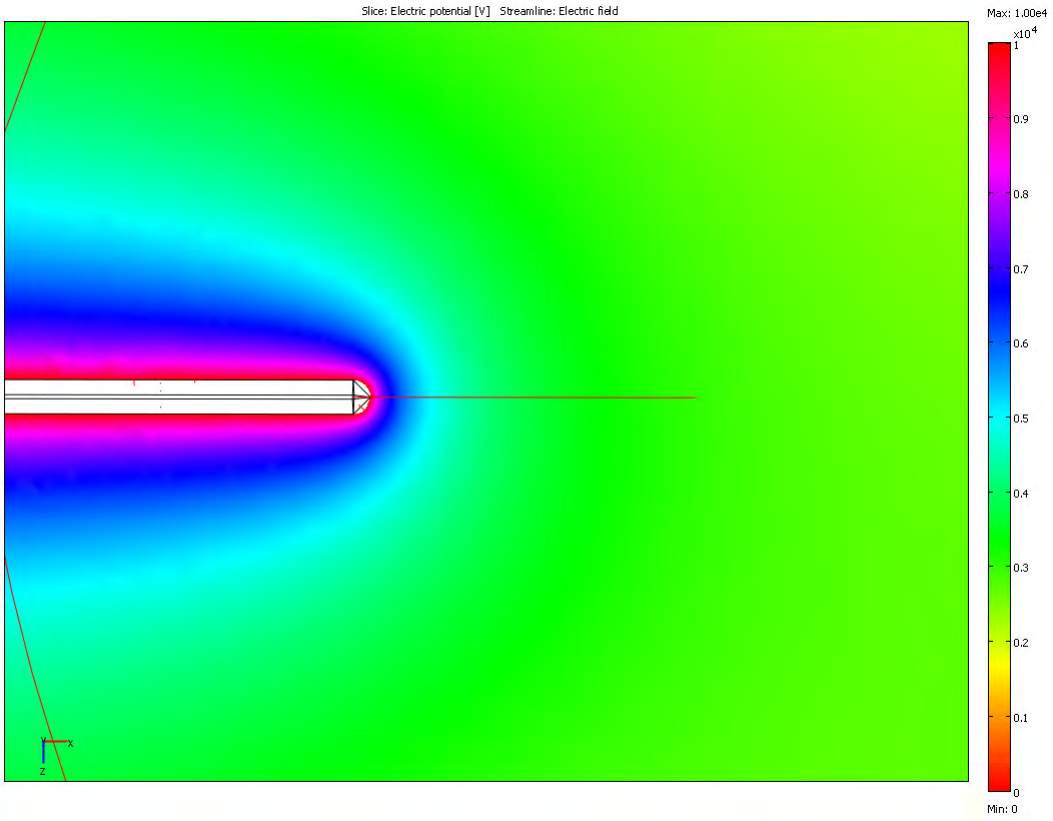

(b)

Figure 5.2: (a) Electric field variation from the tip of the probe to 5 mm along the probe axis (centreline of the geometry) (b) Electric potential regions close to the tip of the probe at an applied voltage of 10 kV.

the quantities of interest. Adaptive mesh generation identifies the regions where high resolution is needed and produces an appropriate mesh.

Figure 5.1(a) shows the voltage variations across a slice cut through the middle of the model geometry in the z-x plane and Figure 5.1(b) shows the electric field streamlines emerging from the boundaries on which voltage was applied. Figure 5.2 (a) and (b) give a closer view of the variation in electric field and potential close to the tip of the probe. The electric field at the tip itself with 10 kV applied is 2.16×10^7 V/m. The electric field generated by COMSOL for the experimental geometry will be later compared to the electric field, assumed for particle trajectory modelling (equation 4.16) later in discussion.

5.2.2 Comments

The model was difficult to solve because of the 3D geometry, high aspect ratio and intricate geometry parts. This resulted in difficulty of creating a fine mesh and a high memory was required due to the large number of iterations required for the solver. The default element type was set to Lagrange-linear to find the solution. Despite choosing adaptive mesh refinement, the irregularities in the field curve in the final solution (Figure 5.2) can be observed.

5.3 Principles used in the Fluid Dynamics Mode

The flow field around the probe in the sampler head of the experimental set up was modelled using the chemical engineering module. The chemical engineering module can model equipment and processes in chemical engineering related to fluid flow, mass and heat transport, and chemical reactions. For this work the momentum balance application mode from fluid dynamics was chosen to solve for laminar flow and turbulent flow. Among various options for turbulent flow models, the k-ω turbulence model was successful in solving and predicting the flow field.

The Navier-Stokes equations describe the phenomena of mass and momentum transport. Their most general form for a compressible Newtonian fluid are given by equation 5.1 to equation 5.3 (chemical engineering module, user's guide).

Conservation of mass

$$\frac{\partial \rho}{\partial t} + \nabla.(\rho u) = 0 \tag{5.3}$$

Conservation of momentum

$$\rho \frac{\partial u}{\partial t} + (\rho u.\nabla)u = -\nabla p + \nabla.\tau + F \tag{5.4}$$

Conservation of energy

$$\rho C_p \left(\frac{\partial T}{\partial t} + (u.\nabla)T \right) = -(\nabla.q) + \tau : S - \frac{T}{\rho} \frac{\partial \rho}{\partial T}\bigg|_p \left(\frac{\partial p}{\partial t} + (u.\nabla)p \right) + Q \tag{5.5}$$

where ρ is the density, u is the velocity vector, p is pressure, τ is the viscous stress tensor, F is the body force, C_p is the specific heat capacity at constant pressure, T is absolute temperature, q is the heat flux vector and Q contains the heat sources. S is the strain rate tensor:

$$S = \frac{1}{2}\left(\nabla u + (\nabla u)^T\right) \tag{5.6}$$

The operation ":" denotes a contraction between tensors defined by

$$a : b = \sum_n \sum_m a_{nm} b_{nm} \tag{5.7}$$

Assuming that the fluid is Newtonian the viscous tensor becomes:

$$\tau = 2\eta S - \frac{2}{3}\eta(\nabla.u)I \tag{5.8}$$

where η is the dynamic viscosity and I is the identity operator.

Most of the applications assume flow to be incompressible; that is ρ is constant or nearly constant. Equation 5.3 then reduces to

$$\nabla.u = 0 \tag{5.9}$$

and the stress tensor in equation 5.6 becomes

$$\tau = \eta\left(\nabla u + (\nabla u)^T\right) \tag{5.10}$$

These assumptions put together give the following momentum equation

$$\rho \frac{\partial u}{\partial t} + \rho(u.\nabla)u = -\nabla p + \nabla.\eta\left(\nabla u + (\nabla u)^T\right) + F \tag{5.11}$$

5.3.1 Turbulent Flow

Analysis of fluid flow fundamentally depends on the (dimensionless) Reynolds number (*Re*)

$$Re = \frac{\rho U L}{\eta} \tag{5.12}$$

where *U* denotes a velocity scale and *L* denotes a representative length.
If we multiply equation 5.11 by *L* and divide by η we get

$$\frac{\rho L}{\eta}\frac{\partial u}{\partial t} + \frac{\rho L u(u.\nabla)}{\eta} = -\frac{L\nabla p}{\eta} + L\nabla.\left(\nabla u + (\nabla u)^T\right) + \frac{FL}{\eta} \tag{5.13}$$

All the terms in equation 5.12 are dimensionless. From the second term on the left hand side of equation 5.13 it can be observed that the solution of the equation will be a function of *Re*.

This number represents the ratio between inertial and viscous forces. At low Reynolds number (the second term vanishes) viscous forces damp out all disturbances which is called laminar flow. At high Reynolds number, the damping in the system is low and if Reynolds number is high enough the flow field ends up in a chaotic state called turbulence. All the industrial applications regarding fluid flow generally involve turbulence.

The Navier - Stokes equations can also be used for turbulent flow simulations.
In the statistical representation of turbulent flow, the mean quantities are of main interest. The detailed modelling of turbulent fluctuations can be avoided by statistically averaging the Navier - Stokes equations. This leads to the Reynolds-averaged Navier-Stokes (RANS) equations. According to Reynolds-averaged representation, flow quantities can be divided into an average value and a fluctuating part,

$$\phi = \bar{\phi} + \phi' \tag{5.14}$$

where ϕ can represent any scalar quantity of the flow. Substitution of quantities in this form in the Navier –Stokes equation gives the RANS equations:

$$\rho \frac{\partial U}{\partial t} + \rho U.\nabla U + \nabla.\left(\overline{\rho u' \otimes u'}\right) = -\nabla P + \nabla.\eta(\nabla U + (\nabla U)^T) + F \tag{5.15}$$

$$\nabla.U = 0 \tag{5.16}$$

where U is the averaged velocity field , $\otimes$ is the outer vector product. The left hand side of equation 5.15 gives the correlation between fluctuations in different directions and is called the Reynolds stress tensor (composed of nine terms but only six are independent). Because this method results in a hierarchy of equations and statistical unknowns this requires imposing assumptions about the flow. In this case the unknown statistical terms have been modelled by an eddy viscosity approach which is the most common closure method. In the eddy viscosity closure, turbulence is assumed to be of a purely diffusive nature. With this assumption the Reynolds stress tensor is expressed as

$$\rho\left(\overline{u' \otimes u'}\right) - \frac{\rho}{3} trace\left(\overline{u' \otimes u'}\right) I = -\eta_T \left(\nabla U + (\nabla U)^T\right) \tag{5.17}$$

where η_T is the eddy (turbulent) viscosity and *trace* is the sum of the elements on main diagonal of the matrix. The second term can be written as

$$\frac{\rho}{3} trace\left(\overline{u' \otimes u'}\right) I = \frac{2}{3}\rho k \tag{5.18}$$

where k is the turbulent kinetic energy.

It has been observed that the k-ω model behaves better close to walls and generally predicts free shear flows more accurately compared to *k-ε* and other turbulence models. The k-ω model however shows strong dependence on the free-stream values of k and ω for external flows. Initially the *k-ε* model was used to try to find a solution

for turbulence in the model geometry but it did not converge and no solution could be found. So *k-*ω model was finally used to find the solution.

5.3.1.1 k-ω *Turbulence Model*

This is a two-equation model which solves a transport equation for the turbulent kinetic energy k together with a transport equation of ω, the dissipation per unit turbulent kinetic energy. The turbulent viscosity is given by

$$\eta_T = \rho \frac{k}{\omega} \tag{5.19}$$

The transport equations for turbulent kinetic energy and ω are respectively

$$\rho \frac{\partial k}{\partial t} + \rho U.\nabla k = \nabla.[(\eta + \sigma_k \eta_T)\nabla k] + \frac{1}{2}\eta_T \left(\nabla U + \nabla U^T\right)^2 - \rho \beta_k k\omega \tag{5.20}$$

$$\rho \frac{\partial \omega}{\partial t} + \rho U.\nabla \omega = \nabla.[(\eta + \sigma_\omega \eta_T)\nabla \omega] + \frac{\alpha}{2}\eta_T \frac{\omega}{k}\left(\nabla U + \nabla U^T\right)^2 - \beta \rho \omega^2 \tag{5.21}$$

The following closure constants and functions were used:

$$\alpha = \frac{13}{25}\ , \qquad \beta = \beta_0 f_\beta\ , \qquad \beta_k = \beta_{k,0} f_{\beta,k}\ , \qquad \sigma_\omega = \sigma_k = \frac{1}{2}$$

$$\beta_0 = \frac{9}{125}, \qquad f_\beta = \frac{1+70\chi_\omega}{1+80\chi_\omega}, \qquad \chi_\omega \equiv \left|\frac{\Omega_{ij}\Omega_{jk}S_{ki}}{(\beta_{k,0}\omega)^3}\right| \qquad \beta_{0,k} = \frac{9}{100}$$

$$f_{\beta,k} = \begin{cases} 1 & \chi_k \le 0 \\ \dfrac{1+680\chi_k^2}{1+400\chi_k^2} & \chi_k \rangle 0 \end{cases}, \qquad \chi_k = \frac{1}{\omega^3}\nabla k.\nabla \omega$$

(from *k-*ω model by Wilcox, 1998)

The tensors, Ω_{ij} and S_{ij} are the mean rotation-rate tensor and the mean strain –rate tensor, defined by

$$\Omega_{ij} = \frac{1}{2}\left(\frac{\partial U_i}{\partial x_j} - \frac{\partial U_j}{\partial x_i}\right), \qquad S_{ij} = \frac{1}{2}\left(\frac{\partial U_i}{\partial x_j} + \frac{\partial U_j}{\partial x_i}\right) \tag{5.22}$$

5.3.2 Model Geometry

The incompressible Navier –Stokes equations were used to predict the flow field for a laminar flow through the sampler head at a Reynolds number equal to 1 and the k-ω turbulence model was used to predict the flow field at a Reynolds number equal to 1000. To simplify the modelling, a small domain was used to predict the flow field around the probe tip only, which was of immediate interest to this study. The domain geometry consisted of a cylinder of both diameter and length of 100 mm, with a fine wire of diameter 500 μm and a rounded end extending halfway through it along its centreline. Laminar flow was solved for 2-D axial symmetry space dimension and the turbulence flow was solved in 3-D space dimension. The boundary conditions used were as follows.

5.3.2.1 Boundary Conditions for Laminar Flow Analysis

Inlet: The normal inflow velocity was specified as 0.05 m/s across the entire inlet, with a uniform pressure of 0 Pa.

Outlet: The *Pressure, no viscous stress* boundary condition was used for the outlet.

Wall: The default boundary condition for a stationary solid wall was used. The condition prescribes u = 0 which means that the fluid at the wall is not moving. Similar wall conditions were also given to the boundaries of the wire and the outer wall of the cylinder.

2D and axial symmetry: The centreline was set at a symmetry boundary with axial symmetry.

The mesh was refined resulting in 3892 triangular elements. The stationery linear solver was used to solve the problem. Figure 5.3(a) shows the predicted velocity field contours across the model geometry.

5.3.2.2 Boundary Conditions for Turbulent Flow Analysis

Inlet: The values for mean initial velocity U_0, turbulent kinetic energy, k_0 and specific turbulence dissipation rate, ω_0 were specified at the inlet boundary. For a uniform initial velocity of 3 m/s, k_0 and ω_0 were calculated as

$$k_0 = 1.5(iU_0)^2 \tag{5.23}$$

where *i* is the turbulent intensity.

$$\omega_0 = k^{0.5} / (0.3D) \tag{5.24}$$

D is the hydraulic radius of the channel. For a cylinder of diameter 100 mm the hydraulic radius is 25 mm. The inlet velocity of the gas was set at 3 m/s. The turbulent intensity was assumed to be 0.15 for the jet flow (Wygnanski and Fiedler, 1969) and hence the calculated value of k_0 used for solving the model was 0.034 m^2/s^2 and ω_0 was 24 s^{-1}. The initial pressure was set to 0 Pa.

Outlet: The "*Pressure, no viscous stress"* boundary condition was used for the outlet.

Wall: For the wall treatment, the logarithmic wall function was used by the turbulence model. This function also assumes that the computational domain begins a distance δ_w from the real wall with flow parallel to the wall.

The mesh was coarse with 30398 tetrahedral mesh elements and 2440 triangular boundary elements. The stationery linear solver with adaptive mesh refinement was used to solve the problem. Figure 5.4(a) shows the predicted velocity field streamlines across the model geometry along with the variations over a slice cut through the middle of the geometry and Figure 5.4(b) gives a closer view of the velocity field close to the tip of probe. A domain including the complete geometry (equipment) used in the experiments was difficult to solve due to the memory requirements and intricate parts so a smaller domain was chosen.

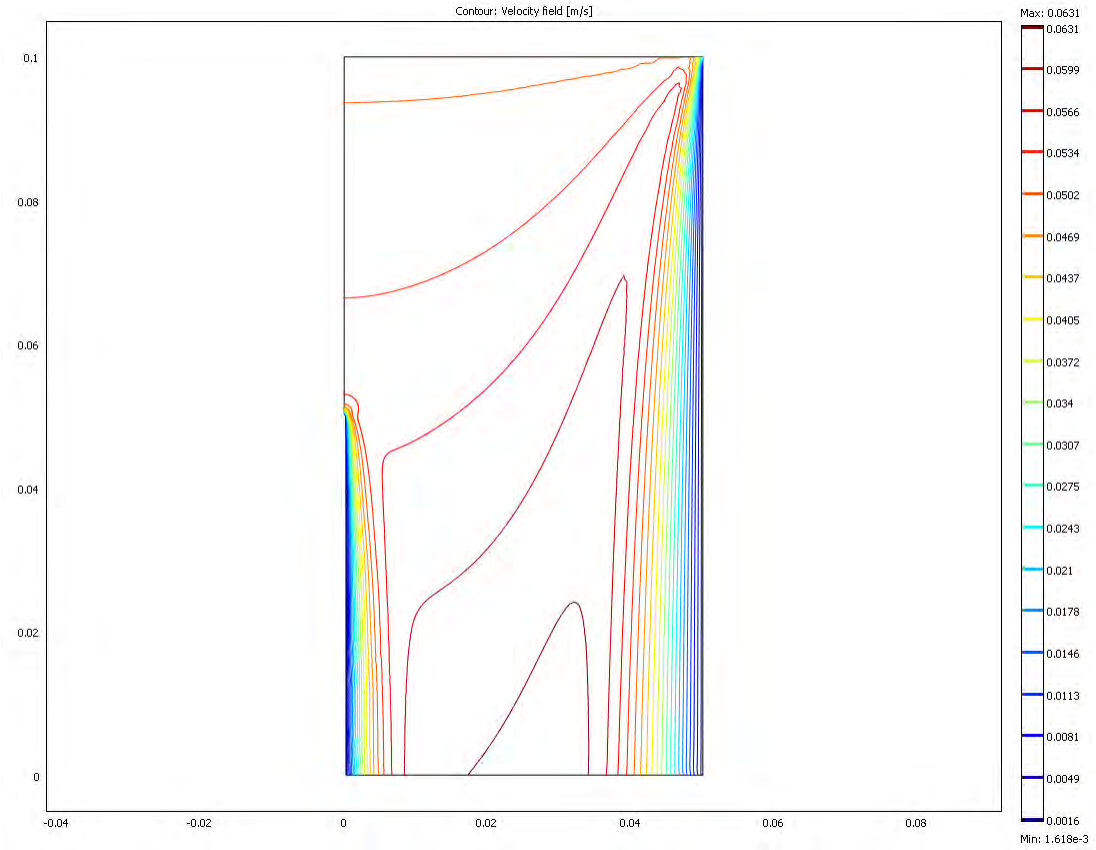

(a)

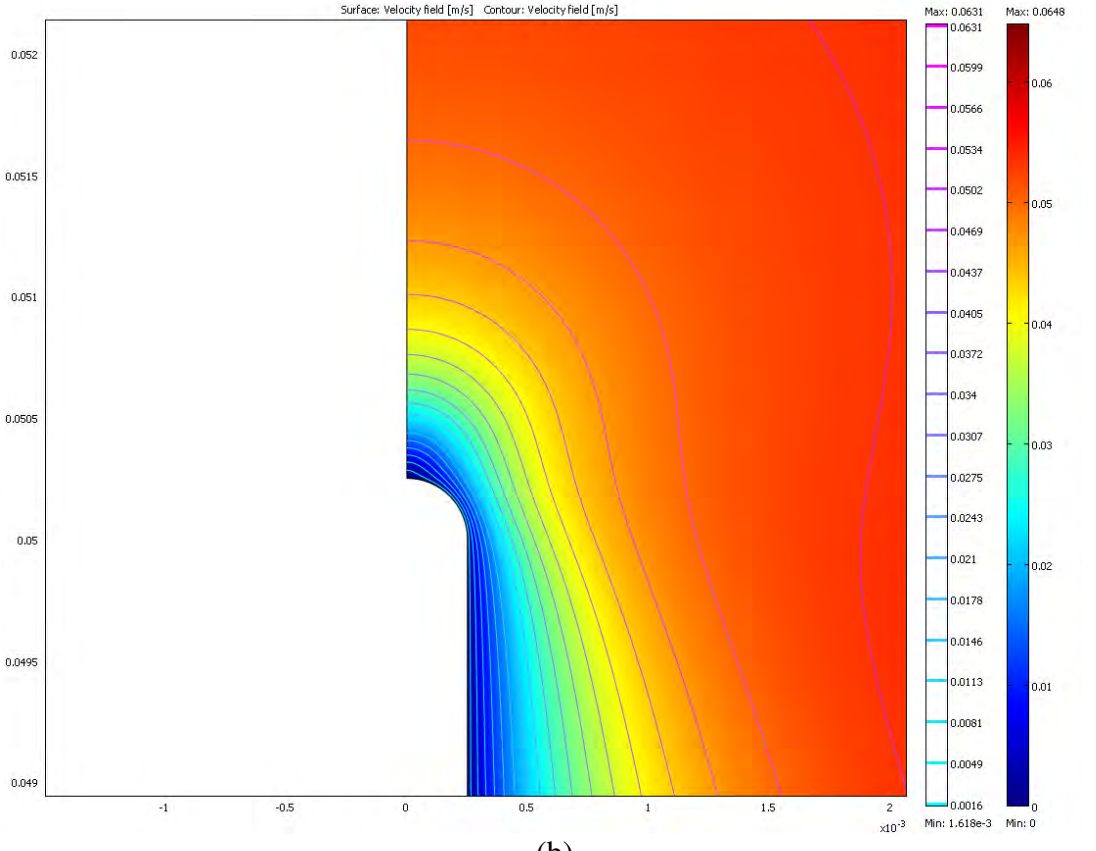

(b)

Figure 5.3: (a) Velocity field contours across the 2D geometry for laminar flow (b) closer view of the velocity field surfaces and contours close to the tip of probe.

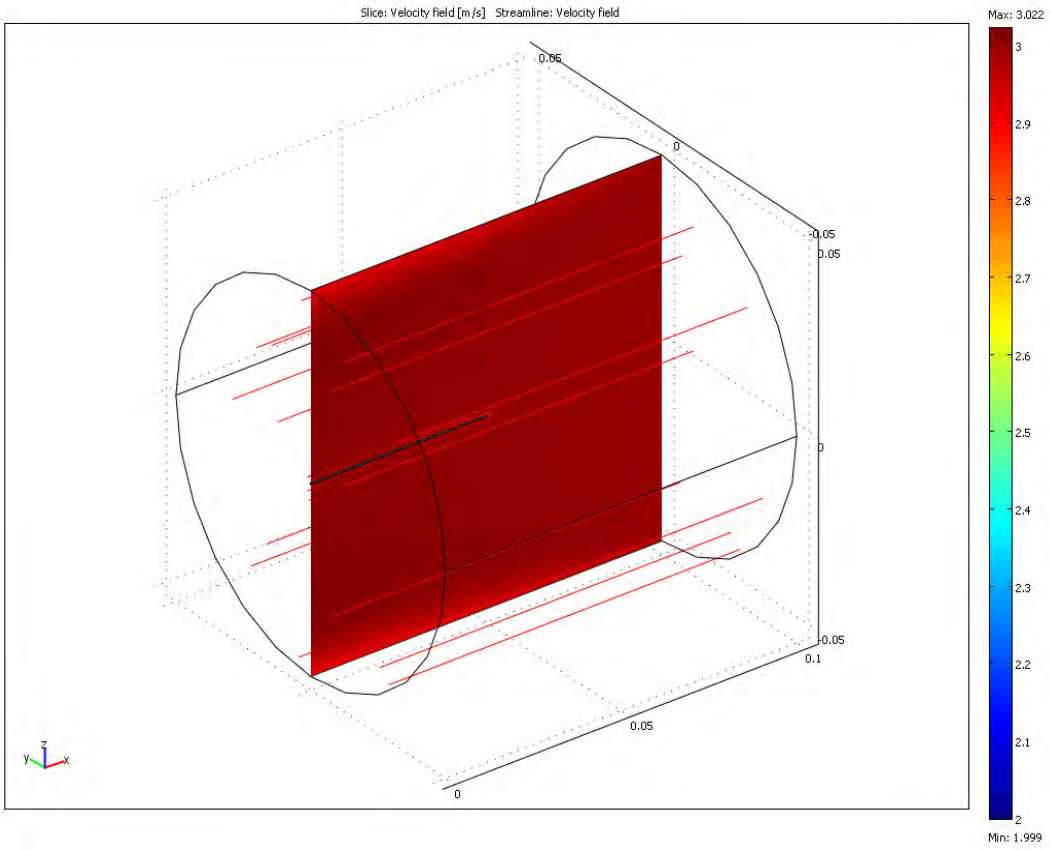

(a)

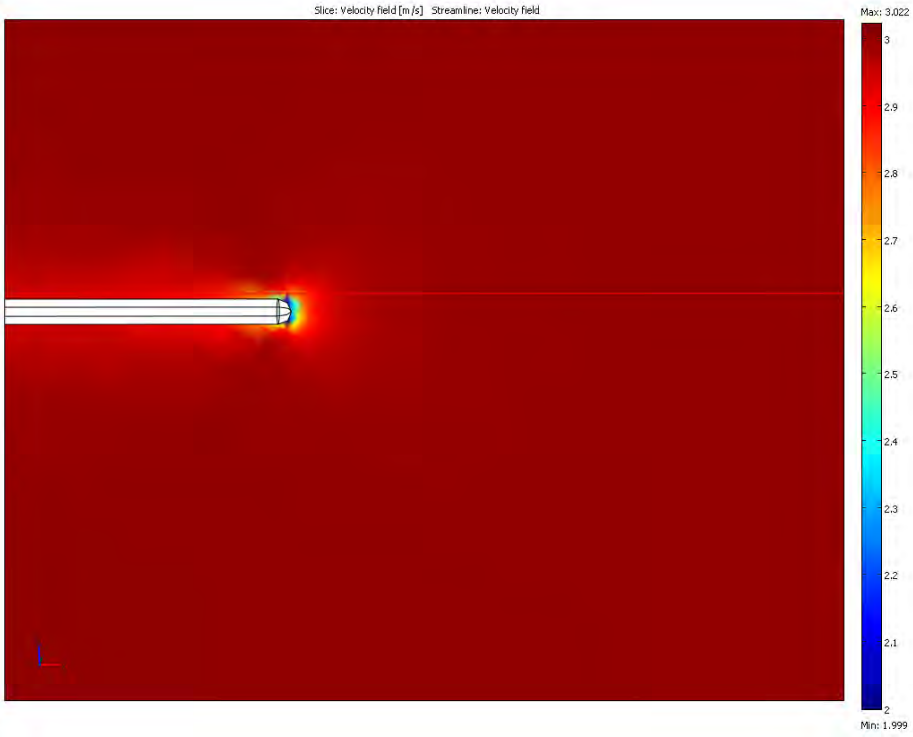

(b)

Figure 5.4: (a) Velocity field streamlines across the model geometry along with the surface variations over a slice cut in the middle of the geometry for turbulent flow (b) a closer view of the velocity field close to the tip of the probe.

6. Measurement of Net Charge and Dipoles

6.1 Development Stages of Measurement Technique

The measurement technique was based on imaging the trajectory of particles under the influence of an inhomogeneous electric field. At the beginning of the experiments, trial runs were carried out on a simple arrangement consisting of a sampler head, high speed camera, laser unit and high voltage AC supply as shown in Figure 6.1. Later modifications were made in the set up to counter different problems arising during the trial runs.

6.1.1 Initial Experimental Set up

The sampler head in the initial experimental set up (Figure 6.1(b)) was built around a 200 mm long cylindrical tube and a wire probe was mounted along its centreline with a spider support. The sample was fed inside the sampler head being metered by a vibrating hopper feeder. Compressed air was passed through a jet ejector which carried the feed falling from the feeder end into the sampler head (Figure 6.1(a)). During experimentation with this set up various problems were encountered. The images acquired were blurred (as shown in Figure 6.2) and hence it was difficult to identify individual particles with their boundaries. It was mandatory to acquire a clear and sharp image of the particles. Also it was realised that on a single frame the particle density was high and it appeared that differently charged particles influenced the trajectories of their nearest neighbours. Apart from this, the flow was relatively uncontrolled and there was a need to meter it more precisely in order to estimate volume fractions of the solid feed. These problems and the measures undertaken to solve them have been discussed in the following sections.

6.1.2 Particle Imaging and Related Problems

The first trial images were obtained of stationery particles, by pasting a black tape on a glass slide and gluing alumina particles to it. The slide was placed inside the

sampler head in the field of view. Different problems were identified by looking at the trial images, such as “speckle”, “flare” and lack of sharpness as shown in Figure 6.2.

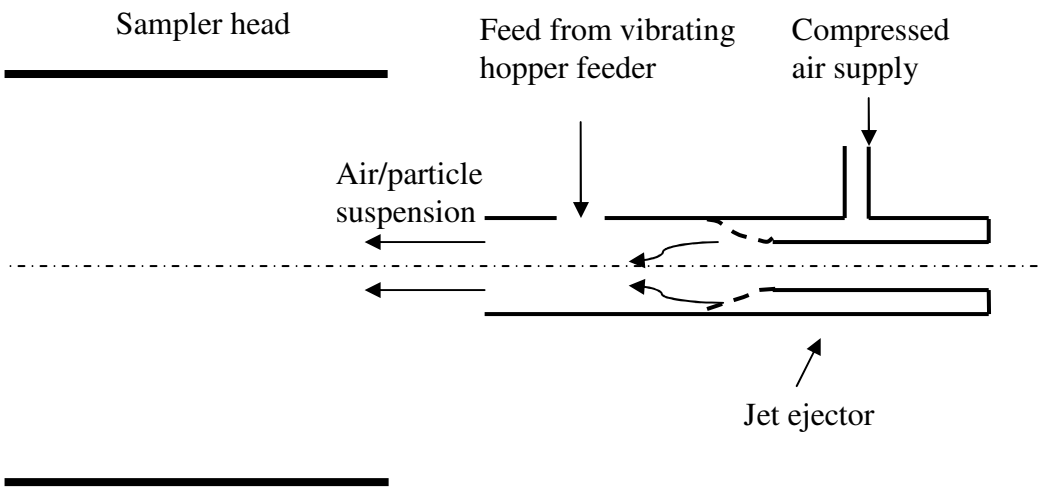

(a)

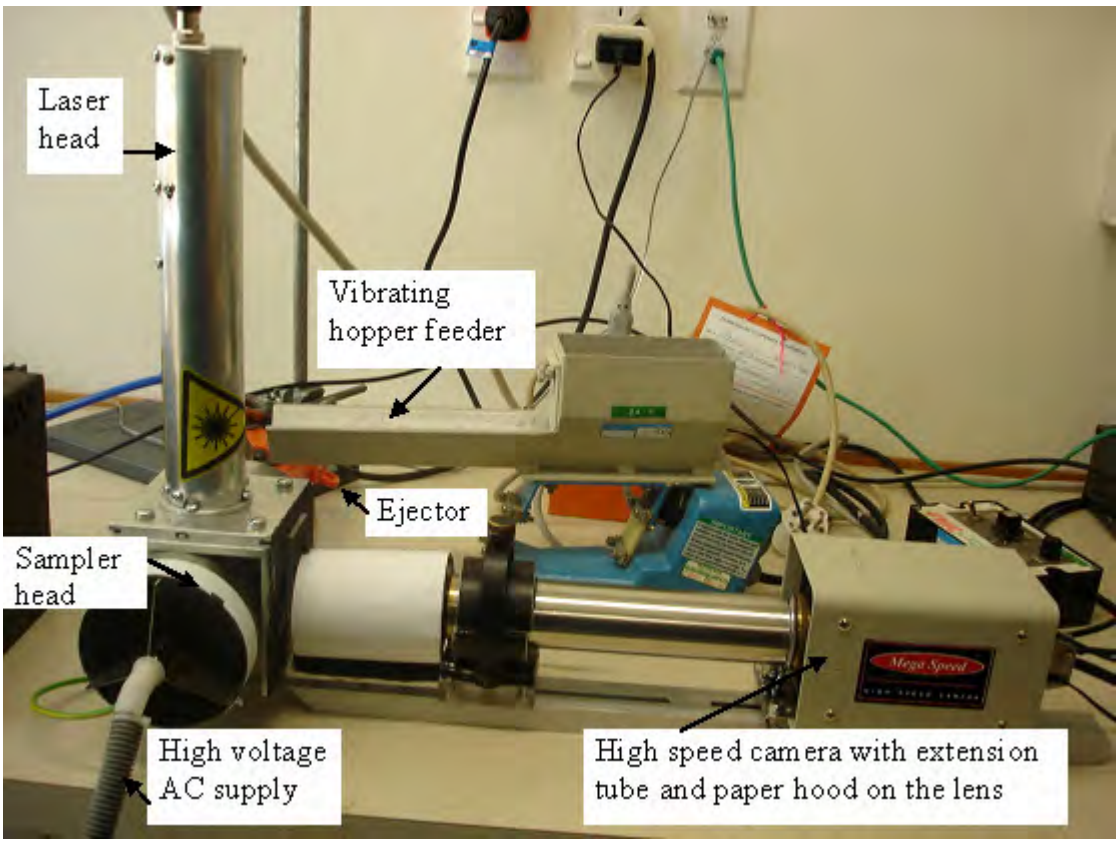

(b)

Figure 6.1: (a) Feeding arrangement in the initial setup using a jet ejector (b) First experimental set up.

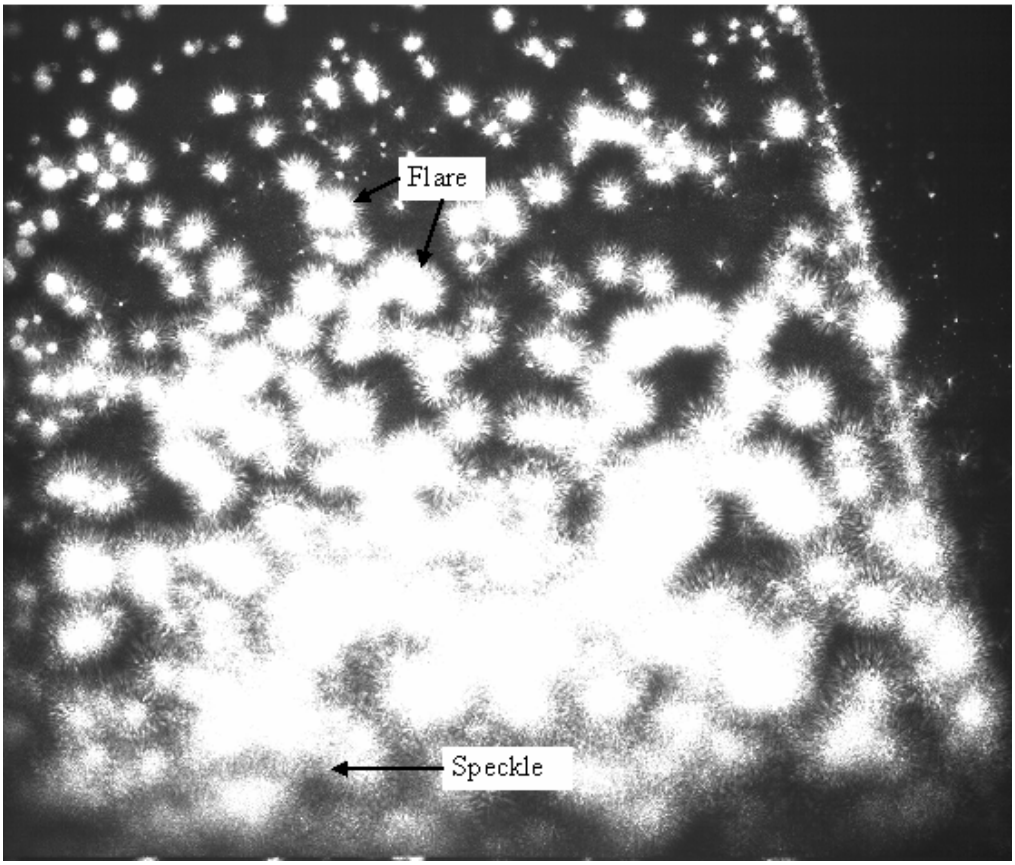

Figure 6.2: Distorted image.

6.1.2.1 Speckle

The image of the particles appeared to have a granular surface with a fine distribution of dark and light patches. This was identified as “speckle”, generally related to the use of a coherent light beam in the experimental setup for illuminating the particles for imaging. It was found from literature that generally due to the coherent laser light, all the images of any point on an object are coherent. This means that the waves which have been scattered from each point on the illuminated surface have similar direction, amplitude, and phase, and are capable of exhibiting interference. Due to the interference of diffracted images the intensity of resultant light varies randomly. This leads to speckle due to which the object illuminated by laser appears to be covered with a fine granular structure.

With a wider camera aperture, the speckle becomes smaller because the size of the diffraction pattern of a lens decreases as the aperture of the lens is increased. If the diameter of the lens is 2a and distance between the lens and the plane of observation

is "*d*" and $\alpha = a/d$, then the diameter ε_d of the smallest grains of the speckle in the plane is given by (Francon, 1979)

$$\varepsilon_d = \lambda / \alpha \qquad (6.1)$$

This comes from the fact that the smallest speckles have diameters of the order of magnitude of the diffraction pattern of the image-forming lens. The aperture size also affects other aspects in imaging discussed in next sections and hence an optimum aperture size was needed to reduce speckle and also to cover the other aspects. Also it was later observed that the speckle was not dominant in images of moving particles.

6.1.2.2 Depth of Field

Another important factor to be considered was the "depth of field" which is the distance between the nearest and farthest objects that appear in acceptably sharp focus in a photograph. It was necessary for this sharp focus field to be deep enough such that a particle could easily stay within it to capture its complete trajectory. On the other hand, a narrow field would reduce the number of particles on an image helping in an easier analysis (while still following a single particle trajectory). The depth of field is mainly influenced by two factors- aperture size and focal length. Larger apertures and smaller focal distances produce a narrower depth of field. Lenses with large focal length of about 100 mm are often used for magnifications when one is unable to get closer to the subject. They appear to create a much shallower depth of field mainly because they are used for higher magnification. This may be due to their longer focal length; they flatten perspective and appear to have a shallow depth of field.

On the other hand the aperture size also affects the image quality. Among the light rays passing the lens tube and the aperture, some may be diffracted as shown in Figure 6.3. If the aperture is large (*i.e.*, a large diaphragm), because the ratio of the diffracted light and the non-diffracted light is so small and is negligible, diffraction does not contribute to the loss-of-quality very much as in Figure 6.3(a). However, when the aperture is small (*i.e.*, a small diaphragm), the amount of light that can pass through the aperture is reduced and hence the proportion of diffracted light becomes significant. As a result, the quality of the image is also reduced (as in Figure 6.3(b)).

Therefore, closing down the apertures (*i.e.*, using a small diaphragm) all the way down to the smallest available aperture may reduce the quality of an image.

At the same time, because of curvature inaccuracy away from the centreline, the optical quality of a lens increases as diaphragm closes down. This improvement will reach only to a certain point. After this, the quality goes down because of the impact of diffraction as explained just above. So an optimisation was done by conducting trial runs to get an appropriate depth of field and good quality images.

The lens used was with 85 mm focal length which magnified the view and also allowed sufficient light to enter the lens. The range for aperture size varied from 1.9 (maximum open) to 16 (minimum open) for the camera lens. The experiments were started at maximum aperture size 1.9 and after trying different combinations to combat the problems discussed above, the aperture of the lens was optimised at a reduced value of 8. For this aperture size the depth of field was measured to be 0.85 mm (procedure in Section 3.5).

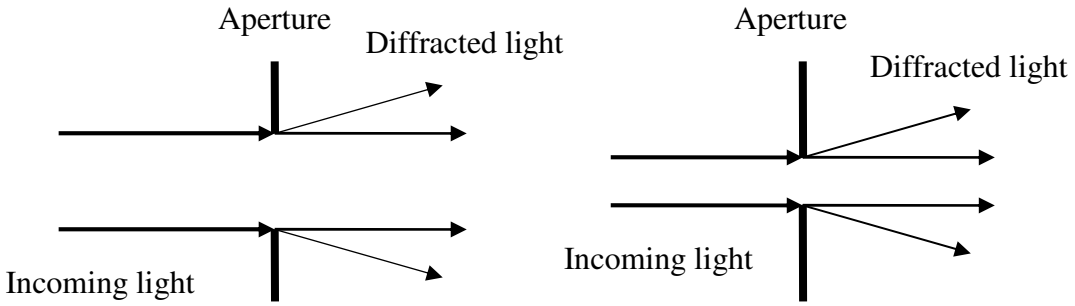

(a) (b)

Figure 6.3: Diffracted light through (a) Wide aperture (b) narrow aperture

6.1.2.3 Lens Flare

The boundaries of individual particles were still not well defined and shiny spikes could be observed emerging from the outer edges in the image of the particles. This problem was identified as “lens flare”, caused by internal reflections in the lens as well as non-image light. It reduces the image quality leading to distorted object boundaries. The flare problem was dealt with by painting matt black colour on the

inner surface of the sampler tube and surfaces facing the camera. Black velvet felt was inserted inside the extension tube. A paper hood was placed to cover the lens to reduce non image light (white cylinder in Figure 6.1(b)). Again a compromise was made among the different possible aperture openings to reduce non-image light by trial runs while keeping in mind the other factors discussed previously (Section 6.1.1 and 6.1.2).

After all the improvement steps were adopted the image quality was enhanced and sharper particle boundaries were observed as shown in Figure 6.4. The aperture size was fixed to 8 for most of the runs with acrylic and glass particles (shiny surfaces). It was opened one size further to 5.6 for whole milk and fertiliser particles which were small in size and better images could be captured by increasing the aperture size. These particles had less reflective surfaces in comparison with the other two samples, hence opening the aperture one size further did not lead to flare problem as discussed above.

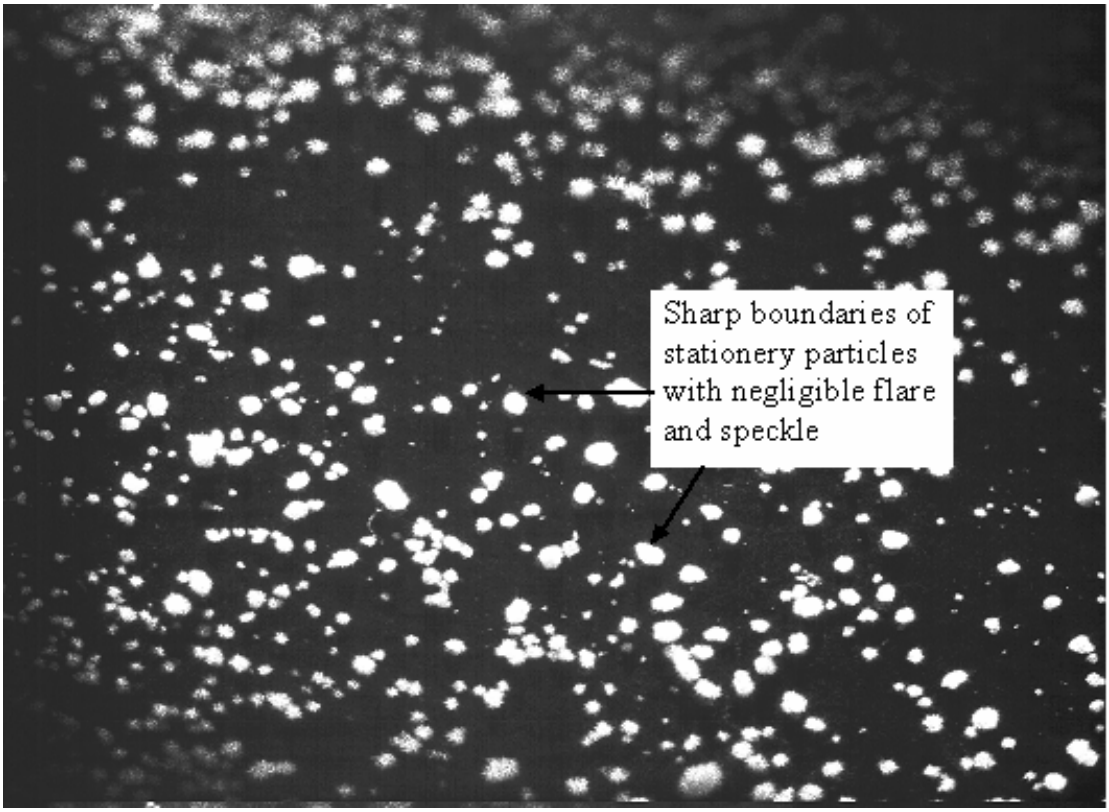

Figure 6.4: Improved image after modifications.

6.1.3 Modified Feeding Arrangement

The vibrating hopper feeder was replaced by a brush feeder to feed the powder into the sampler head. The brush feeder delivered an accurately metered flow and the dilution of the exit flow (volume fraction of particles to air) could be controlled by using cylinders of varying sizes. The working of the brush feeder has been explained in detail in section 3.7. A polyacetal nozzle was attached at its exit end with an opening of 3 mm (this size used only in early trial runs) to get a concentrated jet which could flow through the laser sheet and also along the focal plane of the image-acquiring lens.

6.1.4 Pre Selector Plates and DC Supply

A set of parallel plates enclosed in a cylindrical tube was attached as an extension of the feed end of the sampler head, with a DC voltage applied to one of the plates as shown in Figure 6.5. The aim was to preselect the highly charged particles by capturing them on the plates and thus dilute the flow towards the probe tip. There was an additional advantage that detection of dipoles can be easier on almost neutral particles as in that case the contribution of force due to net charge will be small. Also it was assumed that during motion between the plates the dipole will orient in the direction of the field applied between the plates. Hence the preset direction will enable the prediction of rotation of dipoles while modelling the particle orientation.

6.1.5 Pulse Identification

The video file captured resulted in 489 frames each run. Due to the AC supply either polarity of probe voltage could operate on any individual frame. Prior knowledge of this polarity was necessary for predicting the polarity of charge on the particle. So modifications were made to the laser driver. The AC voltage supply and laser driver were connected with signal wires. The AC waveform was sent through these to the laser driver which in turn halved the number of flashes during positive polarity, but made no change during negative polarity.

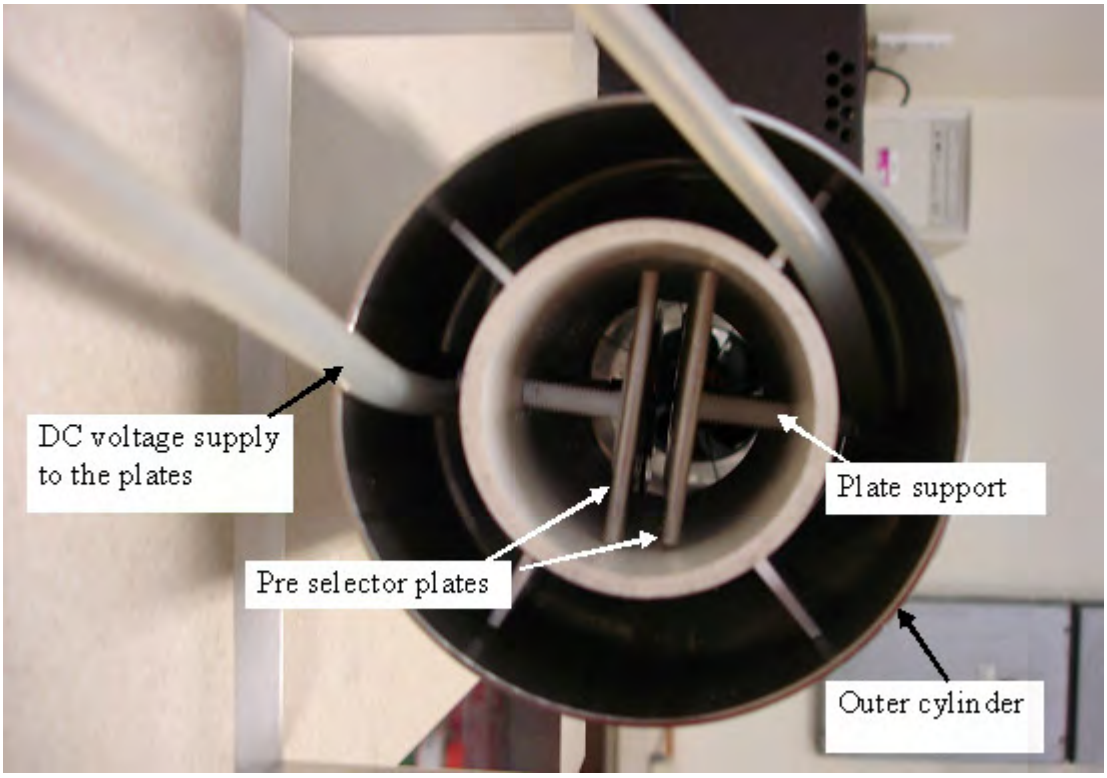

Figure 6.5: Pre selector plates.

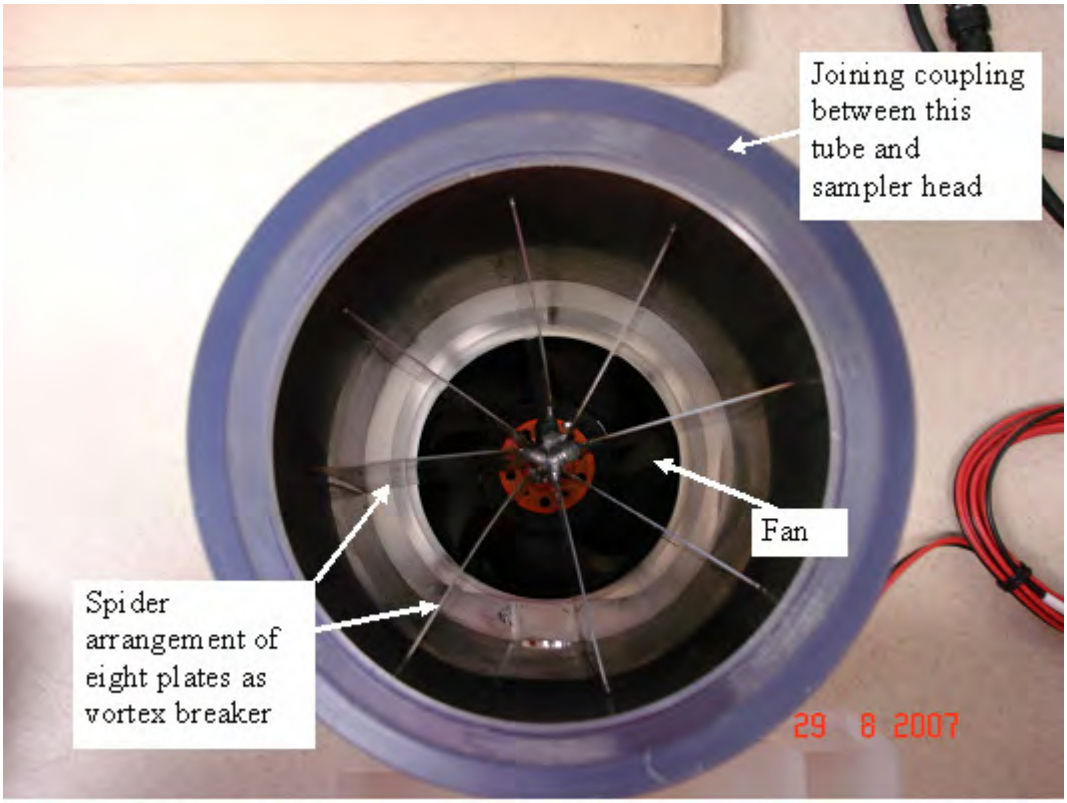

Figure 6.6: Vortex breaker with fan at the end.

6.1.6 Fan and Vortex Breaker

The high air velocity at the nozzle exit is expected to lead to increased turbulence in the jet (Wygnaski, 1969). This largely results from shear between the jet and surrounding gas. Hence a fan was attached at the exit end of the sampler head to bring air around the jet at a similar velocity, to make the velocity more uniform, and to reduce shear. Also with preselection plates at the inlet of the sampler head the distance particles need to travel to enter the field of view increased and it was assumed that the larger sized particle may begin to drop out at low air flow rates. The fan will also assist the flow of particle/air suspension through the sampler head. A vortex breaker was fitted in front of the fan to avoid induced rotation in the flow (propagating upstream) due to the fan blade rotation. It had eight 100 mm long plates in a spider arrangement and was enclosed in a cylindrical tube of the same diameter as the sampler tube as shown in Figure 6.6. This tube was attached as a downstream extension to the sampler tube and the fan was fitted at its far end. The fan was also useful to drive air through the bag filter which was attached at the exit end.

6.1.7 Filter Bag

The powder samples used had very fine micron sized particles. During each run some amount of the sample powder spread in the surrounding air. This sample powder (particularly glass bubbles) caused irritation in eyes, nose and throat. In order to combat this, a bag filter was attached at the exit end over the fan to collect the fine powder.

6.1.8 Nozzle Design

The nozzle design (Figure 6.7) was altered at a later stage when it was realised that an increase in nozzle diameter at the same flow will reduce the turbulence (Wygnaski, 1969). This is expected to reduce any mismatch of initial particle and gas velocities, assumed zero for the analysis of particle trajectories. The inside diameter was increased from 3 mm to 10 mm.

6.2 Experimental Method

A dilute flow ($5x10^{-4}$ volume fraction) of spherical dielectric particles was continuously supplied by an air jet from the brush feeder. The particles were carried by air flows of 0.25 L/s through the polyacetal nozzle from the brush feeder for 15 s. This suspension emerged from the nozzle into the sampler head tube along its axis, and flowed around the metal high voltage probe which pointed upstream. Close to the probe, video images were taken of particle trajectories. The camera was triggered from the computer to begin a 1s frame capture at the selected frame rate of 489 /s. Multiple images were possible through the use of multiple laser flashes for each video frame, leading to a sequence of particle positions along the trajectory within each frame. The probe voltage was reversed every 6 frames for all experiments of this thesis (with AC supply dial settings at 5.2 which means 40 Hz).

6.3 Data Analysis

6.3.1 Selection of Frames

Each run produced approximately 489 frames depending on the memory assigned to computer. Due to the large amount of data, a selection procedure was followed to select frames for analysis. The major criterion for selection was the clarity in the images of a particle. Only those frames were chosen in which the successive positions of the particle were easy to identify. This was possible only on frames in which the particle was close to the focal plane (within the depth of field) throughout its trajectory so that each image was sharp and clear. Also preferably selected were those frames which had about seven or more images of a particle in a particular trajectory. This was done to interpret the complete path followed by a particle without and with the influence of the applied electric field. Most of the particles showed bending in their path once they were under the influence of electrostatic forces. In a few cases the same particle could be tracked on consecutive frames so in such situations all the consecutive frames were used in sequence to generate one continuous trajectory.

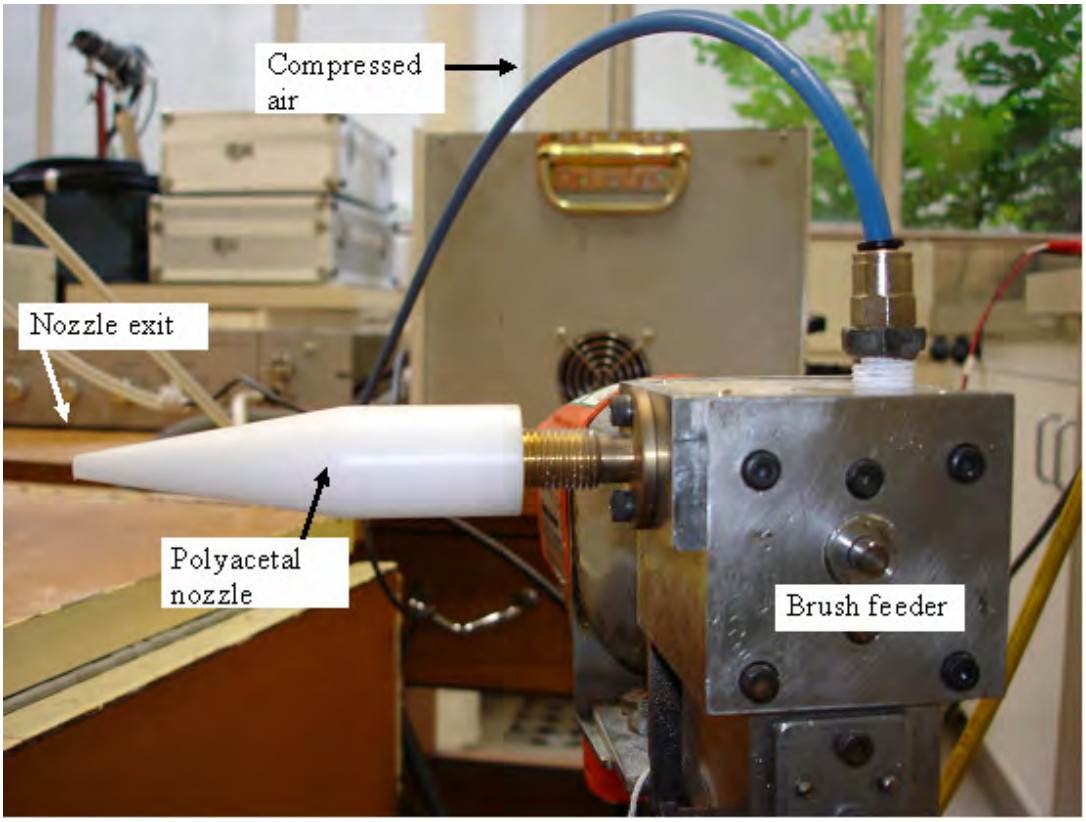

(a)

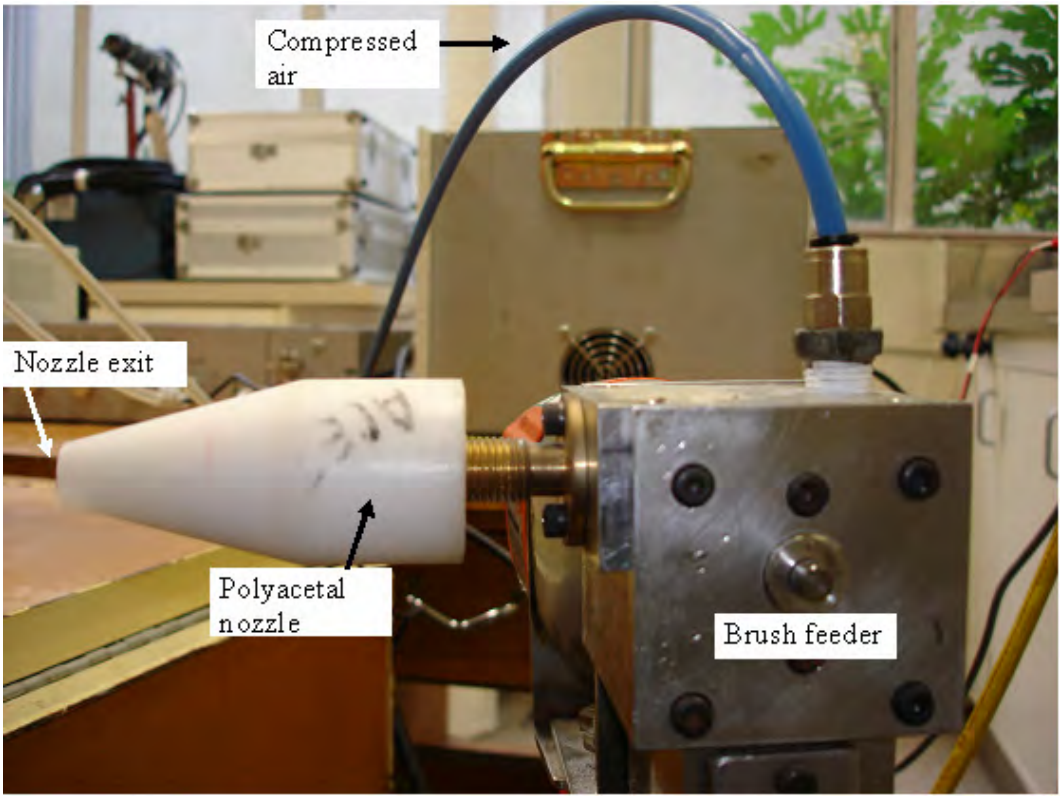

(b)

Figure 6.7: Polyacetal nozzle (a) before modification (b) after modification.

6.3.2 Image Analysis

At the beginning of the experimental runs the scale of the image was measured by photographing a high-precision scale positioned in the plane of the light sheet. A field of view of 6.5 mm x 5.5 mm could be imaged through the 85 mm focal length lens carried on a 230 mm extension tube. Individual frames were examined later on the computer with Sigma Scan Pro 5 image analysis software. If necessary, particle positions from several consecutive frames were linked together in one analysis. For images from a single run, the origin was identified as the centre of the hemispherical tip of the probe. The origin had a radial and axial co-ordinate and all the distances were measured with respect to the origin. The size of each pixel was calculated using the calibrated scale of the image in a particular direction and dividing it with the number of pixels in that direction. The size of one pixel as calculated for this study with the optics as described above was 5.44 ± 0.1 μm in both radial and axial directions.

There were two different methods followed for mathematical analysis of particles. In the first method, software calculated the centre of mass to define the particle position for each exposure by a flash pulse and then a least square minimisation technique was used for the fitting of the particle trajectory. In the second method, a manual procedure was followed to trace the particle centre and also for fitting its trajectory. The following paragraphs describe both of these methods. Also described are the limitations of the first method, leading to the use of the second method in producing the final results.

First Method

In the trial runs using this method, the particle position was measured by calculating its centre of mass in both co-ordinates using Sigma scan Pro. This was done using a fill measurement in which a threshold brightness value was chosen in between 0 to 256 (range of brightness). This threshold was the minimum brightness value among all the pixels which define the particle boundaries. From the threshold value a look up table was created and applied to the image such that all the pixels with brightness above the threshold were white and all below were black. The software calculated the

centre of mass in each co-ordinate by averaging the co-ordinate value of all white pixels (defining the particle image). The two coordinates of the centre of masse were used to calculate the distance in pixels of the particle position relative to the origin and converted into metres by multiplying it by the size of one pixel. The diameter of the particle was calculated from its 2D area by counting the number of pixels in the image and multiplying it with the area of one pixel. The diameter was the diameter of a circle with the same area as that found for the particle. This data of the particle relative position and diameter was than inserted manually into an Excel sheet for fitting the model. On the Excel sheet the experimental positions were compared with estimated theoretical positions at particular time intervals. The target sum of error squares was first calculated from the difference between the experimental and theoretical values of cylindrical radius, $r_{cyl.}$

$$\sum SS = \left(r_{exp} - r_{mod\,el}\right)^2 \qquad (6.2)$$

Solver was used to minimise the target sum of squares by fitting five parameters i.e. initial particle axial and radial position, and gas velocity, net charge and dipole charge for each particle trajectory. The sum of errors squared was minimised and from the values of the parameters the net charge and dipole strength (dipole charge* diameter of the particle) were obtained. It was soon realised that the experimental points had error in both directions (radial, r_{cyl} and axial, z) and using the least squares method with only one variable (r_{cyl}) did not give an accurate solution. So there was a need to apply the least squares method with error in both directions which was a complex procedure.

In an attempt to automate the procedure the image processing toolbox of MATLAB was also used to process the images. The data extracted from the images could then be transferred for optimisation but due to the problems realised later regarding optimisation (those discussed in the previous paragraph) this procedure was also rejected. The final procedure followed has been explained in the following paragraph.

Second Method

Owing to the transparency of the glass bubbles, their images depended on localised side-refracted /reflected light from the laser sheet. Thus, only the tops and bottoms of particles were visible in the form of small light patches. Hence the fill measurement to identify the projected area of the particle could not be performed for these particles. Even in the case of acrylic spheres only the top and bottom patches were visible with the top patch larger than the bottom one. Due to this constraint the centre of a particle was taken to be the midpoint between the farthest pixels of each pair of light patches and the diameter was the average of the total distance between these two patches for all images of particles on a frame.

The analysis of final experimental images used in the results reported in this thesis began with a "histogram equalisation" operation. The intensity histogram of a gray scale image is a plot in which the number of pixels in the image within a particular gray scale level is plotted as a function of the image's gray scale level. The gray scale interval is between 0 and 255. The histogram equalisation operation stretched the brightness range of all pixels in the image to the maximum range of 0 to 255 and hence increased the clarity of image. The starting image and its intensity histogram are shown in Figure 6.8 and the modified image along with its intensity histogram is shown in Figure 6.9. Then from the tops and bottoms of each particle, the image centre of the particle was calculated by averaging the values of extreme pixels each side. Then the relative distances of the particle from the origin was calculated by subtracting the axial and radial coordinates in pixels from the origin coordinates. This distance in both directions in pixels was converted to microns by multiplying with the size of one pixel. Then the final experimental data was moved to the Excel sheet for fitting the model. The fitting of experimental positions by integrating momentum conservation equations derived net charge and dipole moment values for each particle. This procedure is explained in the next section.

6.4 Modelling and Fitting Particle Trajectories

Particle momentum conservation was used in two directions in the plane of the light sheet; both axially (z direction) and radially (r direction). Components of the various

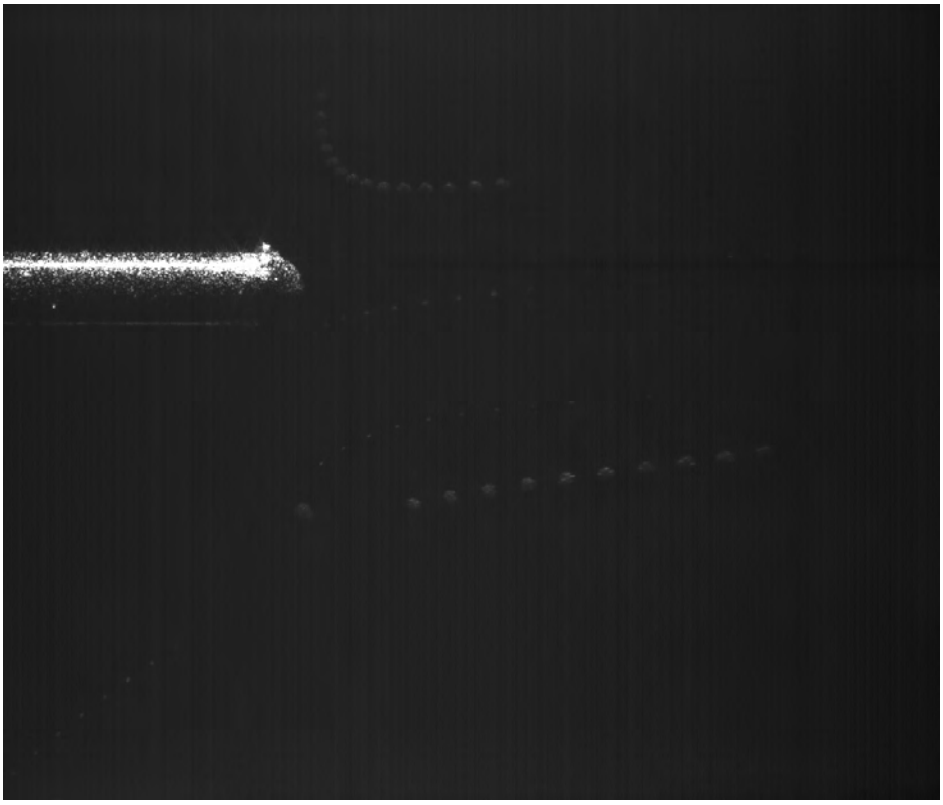

(a)

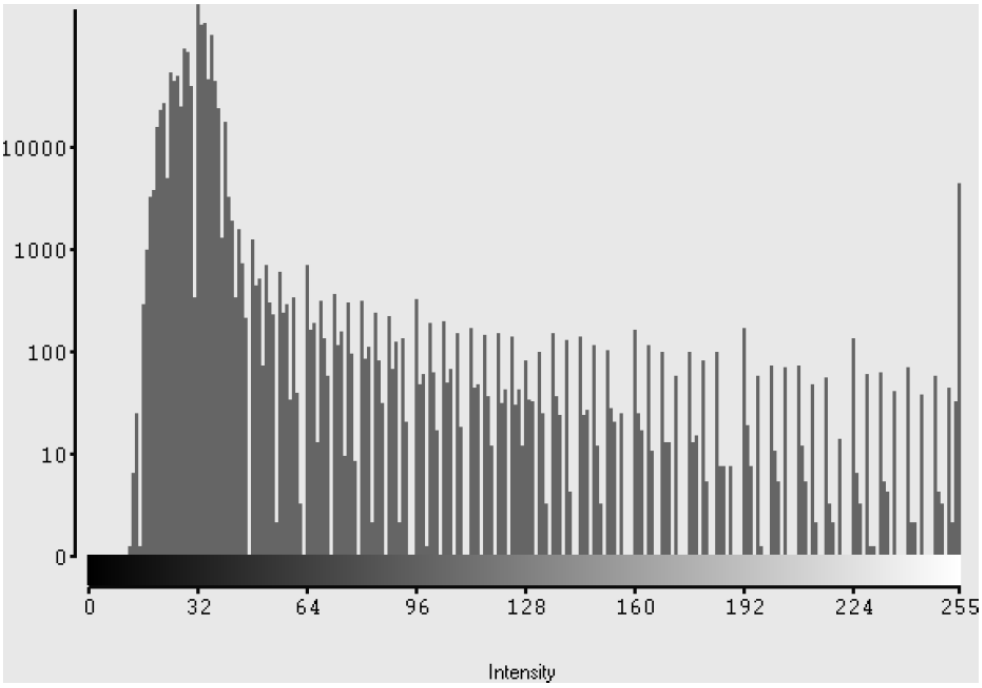

(b)

Figure 6.8: (a) Actual image of acrylic particle trajectories (b) Histogram stretch of the image (from Sigma scan Pro).

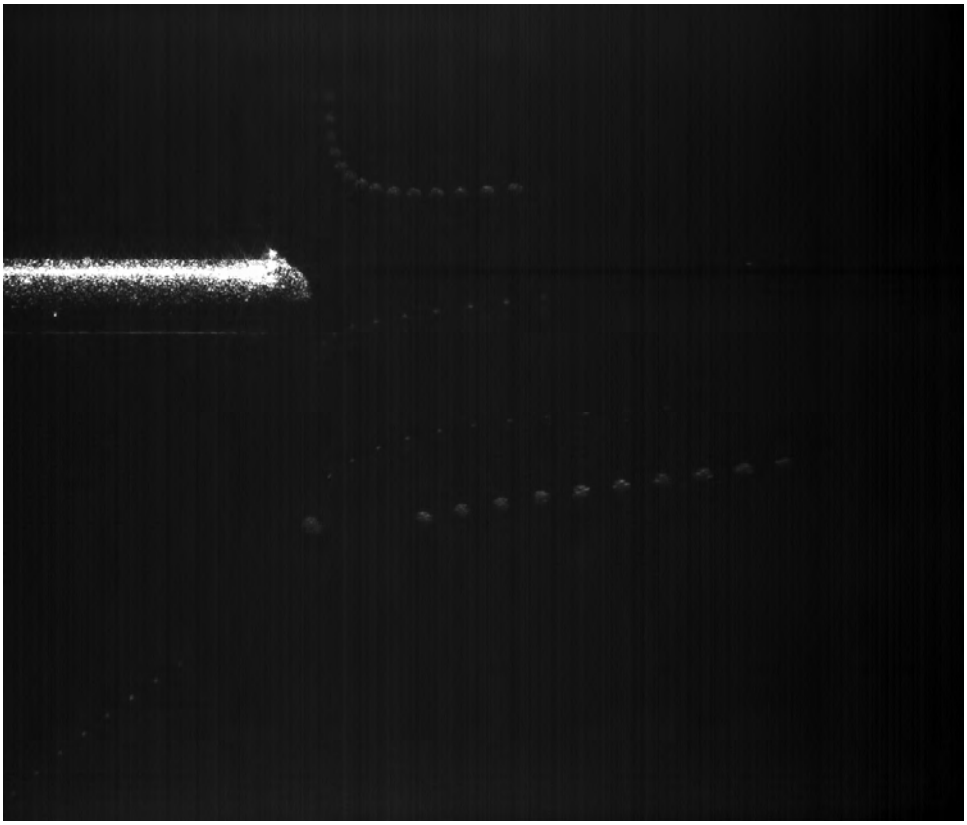

(a)

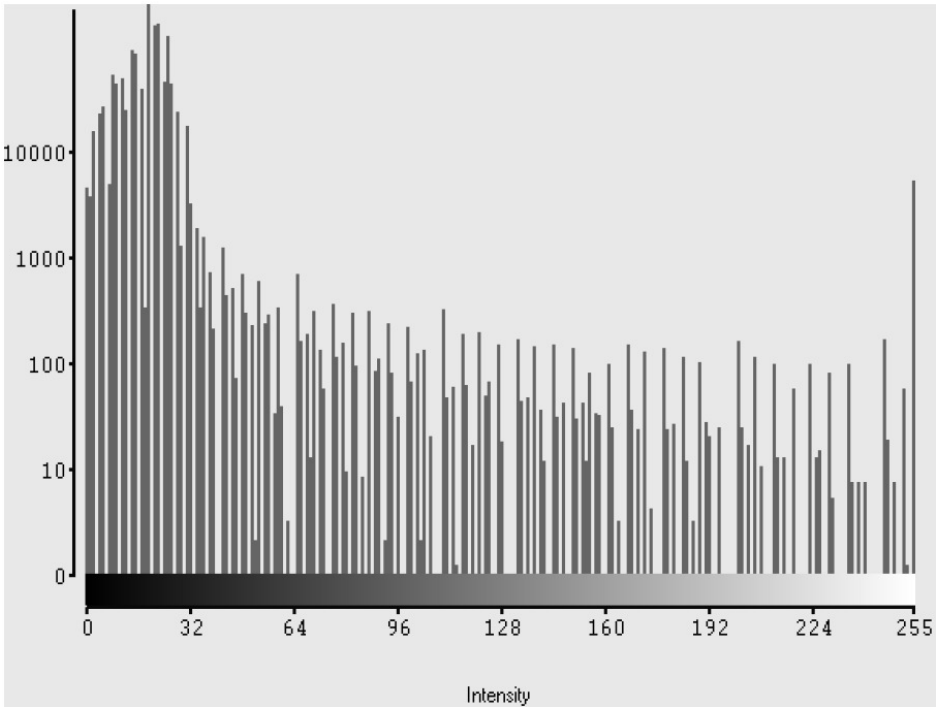

(b)

Figure 6.9: (a) The image of acrylic particle trajectories (Figure 6.8 (a)) after modification (b) Histogram stretch of the modified image after histogram equalisation (from Sigma scan Pro).

forces thought to be acting (drag, electrical) were included in these momentum equations (Chapter 4), and the discretized forms were integrated with Excel spreadsheets to predict particle z and r at each time interval. These were fitted to the photographic z and r by adjustment of force parameters. Estimation of drag force presumed knowledge of the gas velocity and direction during the trajectory. It was assumed that these values fluctuated somewhat between trajectories because the flow had the turbulence of the nozzle jet. For each trajectory, the initial velocity (magnitude and direction) of the *particle* while entering the field of view was assumed to be that of the *gas* during the whole trajectory. All electrical forces were taken to be along the radius r_{sph} from the particle centre to the probe tip centre. The different electrical forces had different dependencies on this "spherical radius" so that the net charge force dominated at large radii, with dipole forces becoming important closer to the probe, and image charge forces important even closer. This suggested a sequential method of fitting parameter values for the trajectory.

The procedure used for fitting the integrated distances to experimental distances was then as follows:

1. The first few particle positions on the frame were used to calculate the radial and axial velocities of the particle, and were assumed to be those of the gas, giving the velocity and angle of gas approach to the probe. The calculated values were substituted into the model equations on the Excel sheet. This step fixed the first two positions of the modelled trajectory with the given experimental trajectory.
2. The monopole charge on the particle was varied to fit the model to points closer to the tip of the probe. Usually in a trajectory of 9-10 experimental points the monopole charge alone was adjusted to fit positions 3-7 of the trajectory.
3. Dipole moment ("dipole charge" times diameter of a particle) was varied together with some minor adjustment of monopole charge to fit points even closer to the probe. Points closer to the probe imply the last 3-4 positions of a trajectory approaching the probe. This approximation will be different for a particle being repelled at a considerable distance (~2 mm) from the probe, where particle net charge is high.

4. Image forces were calculated by using the fitted monopole charge with minimum separation distance equal to the radius of the particle and the fitted dipole charge with minimum separation distance of 10 microns (roughness on probe surface). This latter assumes full alignment of the dipole with the probe field as the particle approaches the surface and ignores the contribution of the charge at the other end of the dipole.

The rotation of dipole (and particle) was then calculated to predict the time taken by the dipole to orient in the direction of the electric field and hence the dipolar force to be fully effective as explained in Section 4.5. The complete fitting of modelled and experimental trajectory resulted in prediction of monopole charge and dipole strength of individual particle.

7. Results

The trajectories presented here are typical of about 200 analyzed. Distributions of net charge and dipole strength have been obtained. For all measurements reported here the pulse interval for laser flash was kept at 160 μs with pulse duration of 40 μs and camera capture rate 489 s^{-1}. A good fit meant that predicted points agreed with image points both in trajectory path and distance along the path. Error bars are for 1 pixel image error in both directions. The preselector plate voltage was at 10 kV for almost all runs. The images were processed to increase the clarity such that minimum data is lost. For all images initially the contrast was maximised where the redistribution of intensities sharpens the image and then the particle trajectory was traced. In the case of the transparent acrylic and glass particles only the top and bottom of each particle could be marked out. Whole milk particles and fertiliser particles were easier to view and the whole of the particle periphery could be outlined. Due to this difference, different procedures were followed after the initial image sharpening, in each case to calculate the position of particle.

The polarity of the voltage on the probe was identified by the number of flashes on a given frame which counts to approximately 13 in the case of negative polarity and 7 for a positive polarity. In all the images presented in this section the light patches representing the particle are filled with red colour and the probe has been outlined with blue for a clear view. The parameters used in calculations are listed in Table 7.1.

Table 7.1 List of parameters and values measured or assumed

Probe tip radius, a	2.5×10^{-4} m
Tube inner radius, b	0.05 m
Permittivity of free space, ε_o	8.85×10^{-12} F/m
Viscosity of air, η_{air}	1.8×10^{-5} Pa s
Density of air, ρ_{air}	1.2 kg/m^3

For simplicity, the first examples have been chosen to show typical error analysis and sensitivity to assumptions, where fits were obtained with only net charge considered, without the existence of dipoles. These “net-charge only” cases did not need the addition of a dipole to provide an acceptable fit, but as explained later on, dipoles could have been present.

7.1 Variation of Net Charge

Figure 7.1 shows an actual image of the trajectory of a 120 µm acrylic particle. The particle continued its path onto the second of two consecutive frames so data from both the frames was added to get a complete picture. At the last few positions both the top and bottom light patch can be clearly seen. The flight path is straight until the particle is repelled close to the probe tip. Experimental and predicted particle trajectories (Figure 7.2 to Figure 7.9) were compared to obtain the fitting error for net charge. Fitting errors determined by adjustment of net charge over the range so that fitted points remained within the experimental error limits resulted in maximum error of around 10%.

The particle's trajectory of a120 µm acrylic particle shown in Figure 7.1 has been analysed in Figure 7.2. Figure 7.3 presents a 65 µm glass particle being repelled from the probe tip. Figure 7.4(a) shows another enhanced image of a 120 µm acrylic particle produced by adding two consecutive images. The particle approaches from above the centreline and is sharply repelled backwards below the centreline. This particle has been analysed in Figure 7.4(b). It can be observed in Figure 7.5 and 7.6 that the net charge value fitted for the similar sized milk particles strongly repelled are also close to each other. The first attractive trajectory of a 70 µm milk particle has been presented in Figure 7.7 in which the particle finally sticks to the probe after passing the origin (centre of the tip). Figure 7.8 and 7.9 show similar fittings for 50 and 45 µm fertiliser particles being repelled.

7.2 Variation of Approach Angle of Gas

It was normally assumed that the gas approaches at the same angle as that of the particle. The first two particle positions were used to calculate the gas approach angle. In order to predict the sensitivity of fitting to this assumption, experimental and predicted particle trajectories (Figure 7.10 to Figure 7.13) have been demonstrated for the variation of approach angle of gas within the experimental error limits. It can be observed that an error of ± 5º does not make any remarkable difference in the predicted trajectories. For a variation of ± 20º (Figure 7.11) the trajectory goes beyond the limits of error.

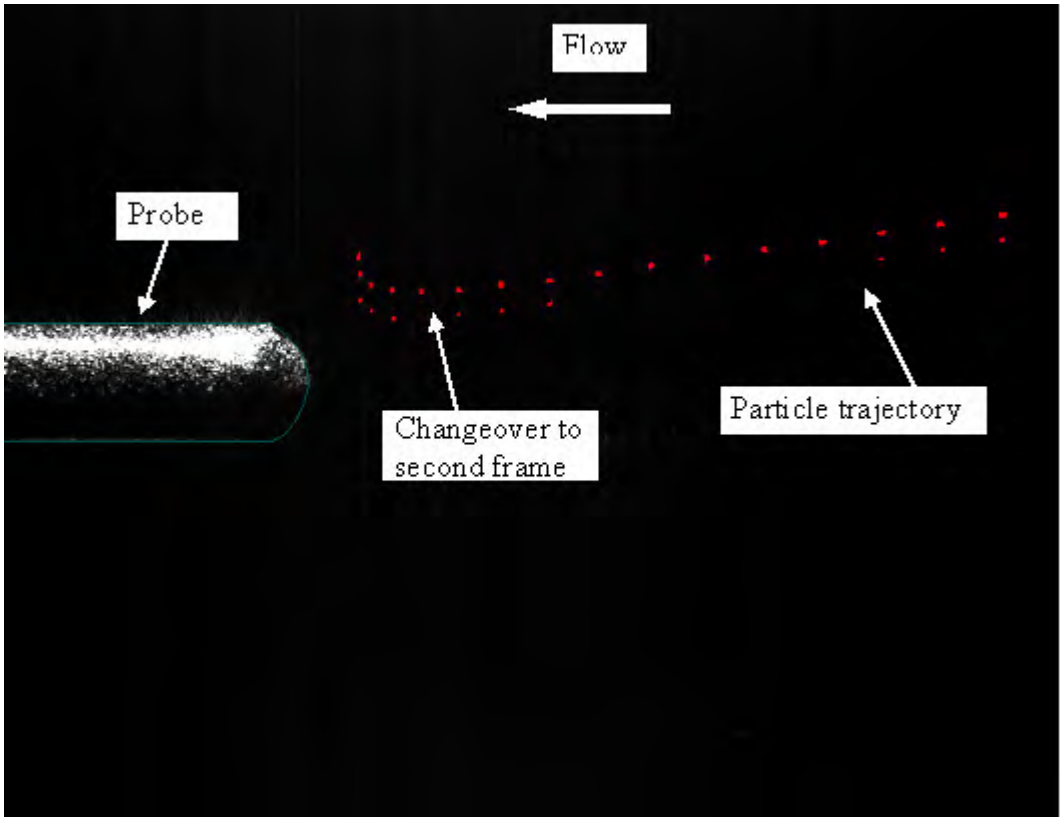

(a)

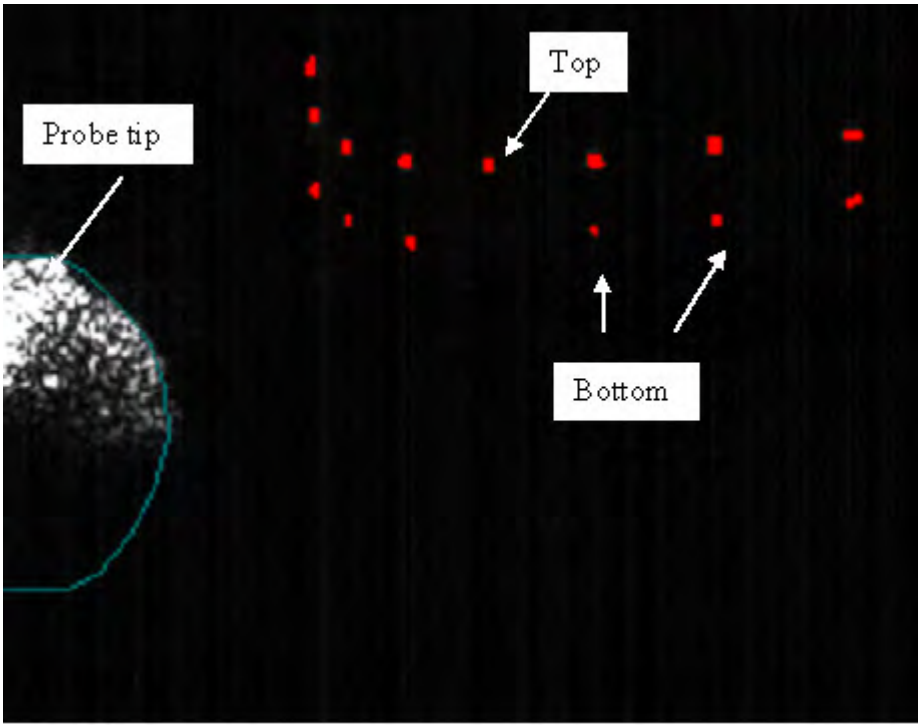

(b)

Figure 7.1: (a) Actual image of a 120 µm acrylic particle being repelled close to the probe tip at probe voltage -10 kV (b) A closer view of the particle and probe tip.

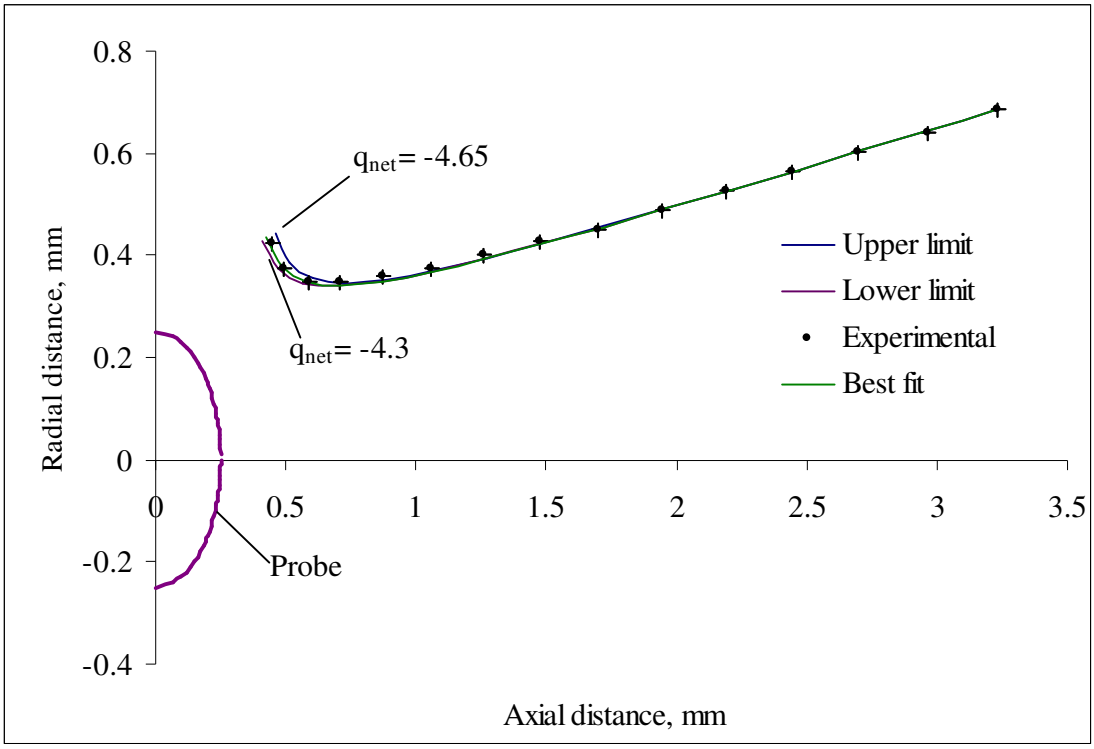

Figure 7.2: Experimental and predicted particle trajectories for a 120 µm acrylic particle at probe voltage -10 kV with best fitted net charge q_{net} = -4.42x10^{-13} C. Within experimental error maximum fitted net charge q_{net} = -4.65x10^{-13} C and minimum fitted net charge q_{net} = -4.3x10^{-13} C i.e. ±5%.

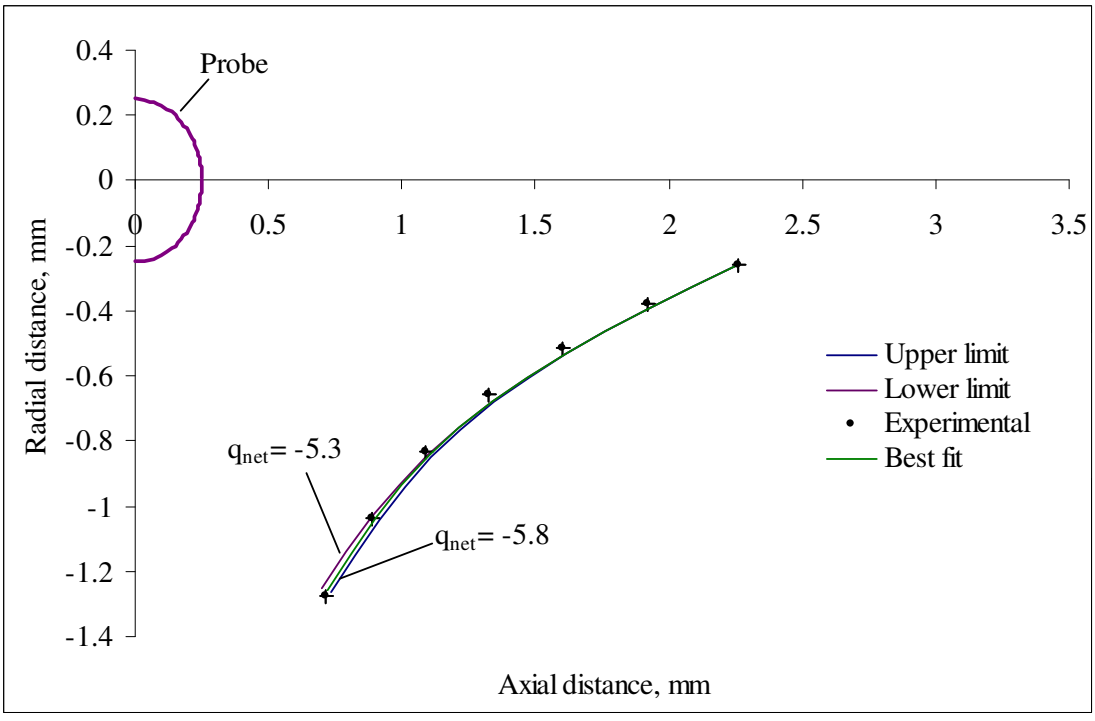

Figure 7.3: Experimental and predicted particle trajectories for a 65 µm glass bubble at probe voltage -6 kV with best fitted net charge q_{net} = -5.6x10^{-14} C. Within experimental error maximum fitted net charge q_{net} = -5.8x10^{-14} C and minimum fitted net charge q_{net} = -5.3x10^{-14} C i.e. ±6%.

(a)

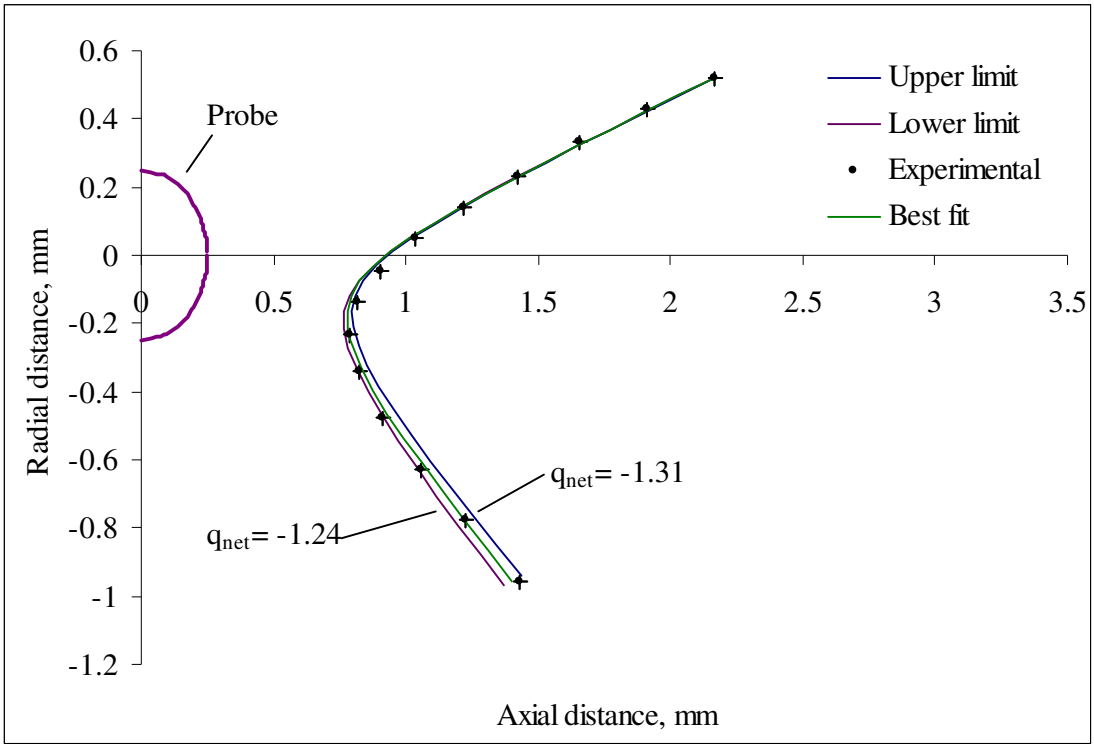

(b)

Figure 7.4: (a) Actual image of a 120 µm acrylic particle being repelled at probe voltage -6 kV (b) Experimental and predicted particle trajectories for the 120 µm acrylic particle with best fitted net charge q_{net} = -1.27x10^{-12} C. Within experimental error maximum fitted net charge q_{net} = -1.31x10^{-12} C and minimum fitted net charge q_{net} = -1.24x10^{-12} C i.e. ±3%.

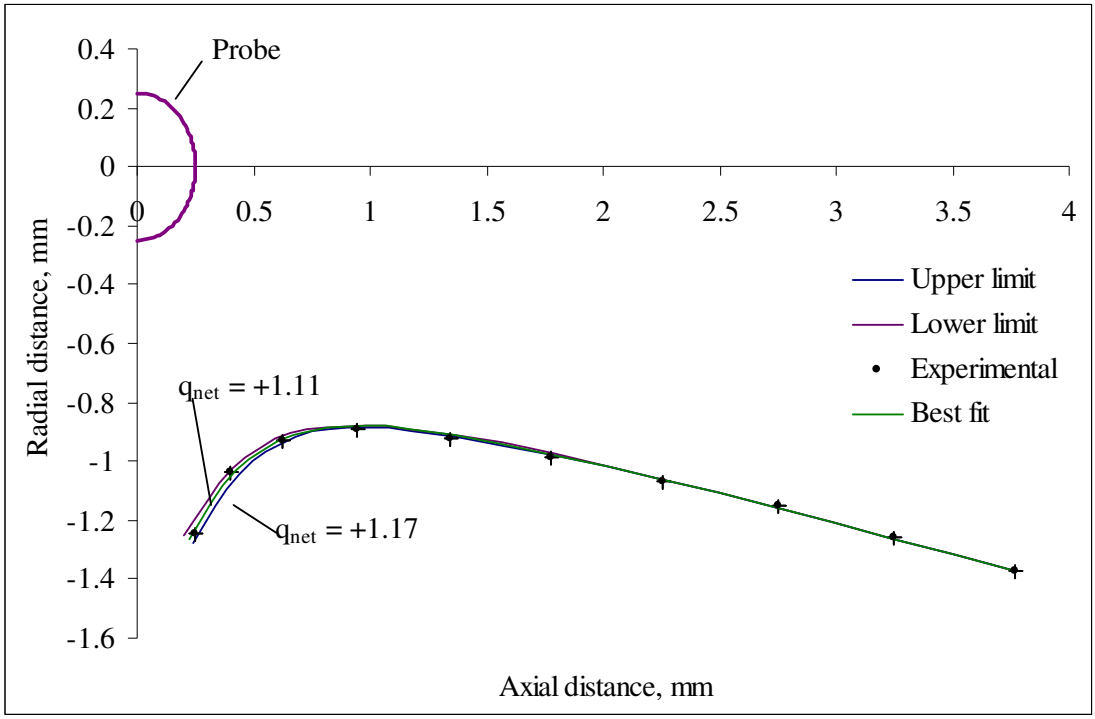

Figure 7.5: Experimental and predicted particle trajectories for a 55 µm milk particle at probe voltage +6 kV with best fitted net charge q_{net} = +1.14x10^{-13} C. Within experimental error maximum fitted net charge q_{net} = +1.17x10^{-13} C and minimum fitted net charge q_{net} = +1.11x10^{-13} C i.e. ±3%.

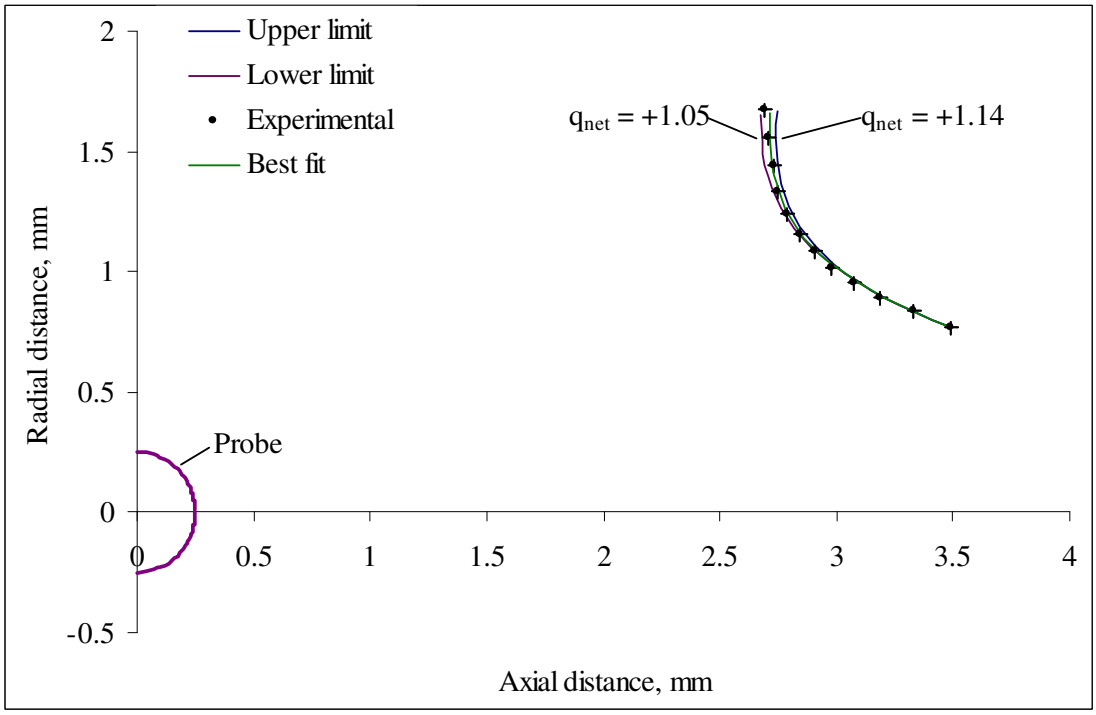

Figure 7.6: Experimental and predicted particle trajectories for a 50 µm milk particle at probe voltage +6 kV with best fitted net charge q_{net} = +1.1x10^{-13} C. Within experimental error maximum fitted net charge q_{net} = +1.14x10^{-13} C and minimum fitted net charge q_{net} = +1.05x10^{-13} C i.e. ±5%.

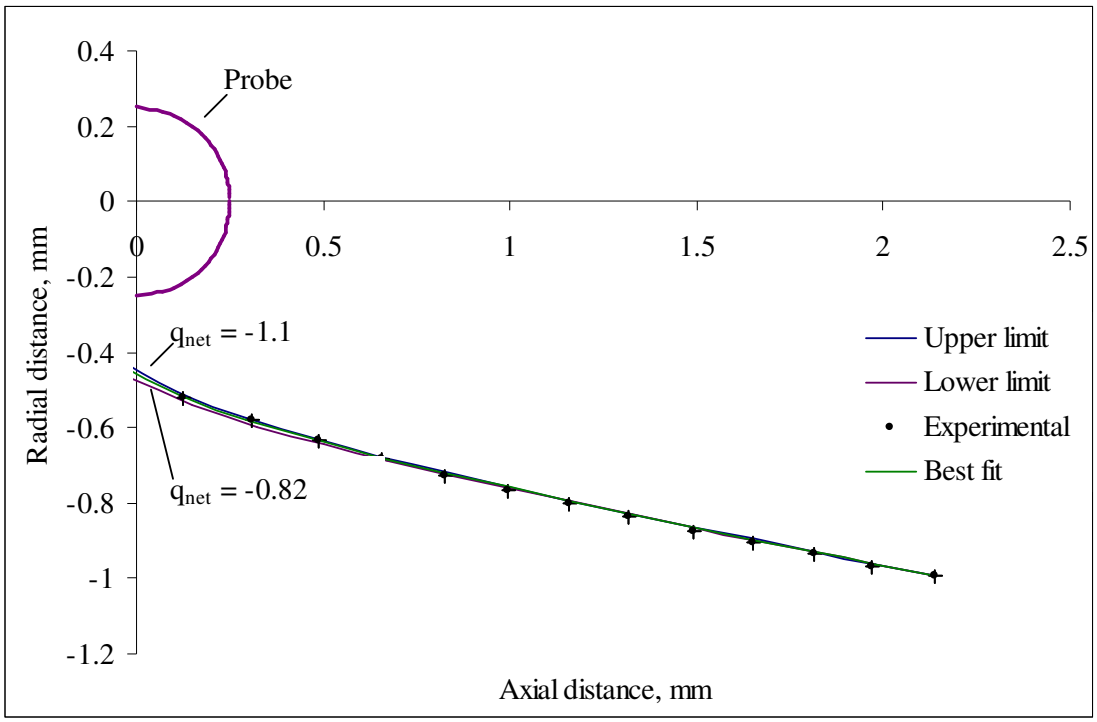

Figure 7.7: Experimental and predicted particle trajectories for a 70 µm milk particle at probe voltage +5 kV with best fitted net charge q_{net} = -1x10^{-14} C. Within experimental error maximum fitted net charge q_{net} = -1.1x10^{-14} C and minimum fitted net charge q_{net} = -8.2x10^{-15} C i.e. ±2%.

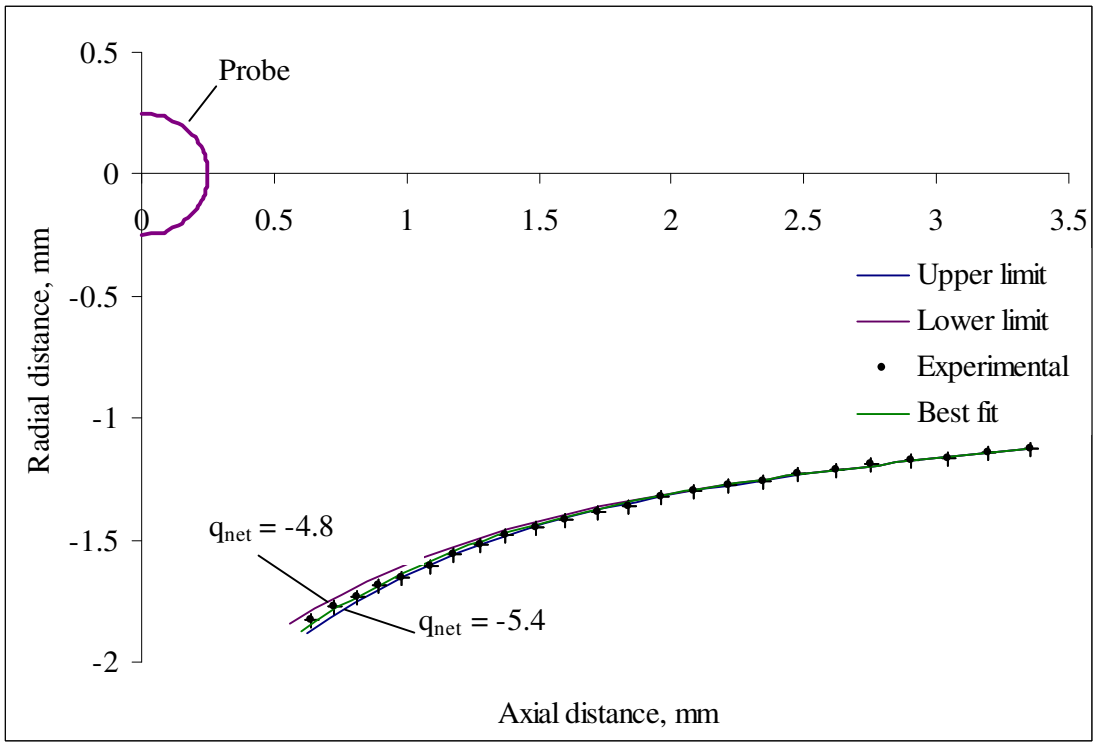

Figure 7.8: Experimental and predicted particle trajectories for a 50 µm fertiliser particle at probe voltage -6 kV with best fitted net charge q_{net} = -5.2x10^{-14} C. Within experimental error maximum fitted net charge q_{net} = -5.4x10^{-14} C and minimum fitted net charge q_{net} = -4.8x10^{-14} C i.e. ±8%.

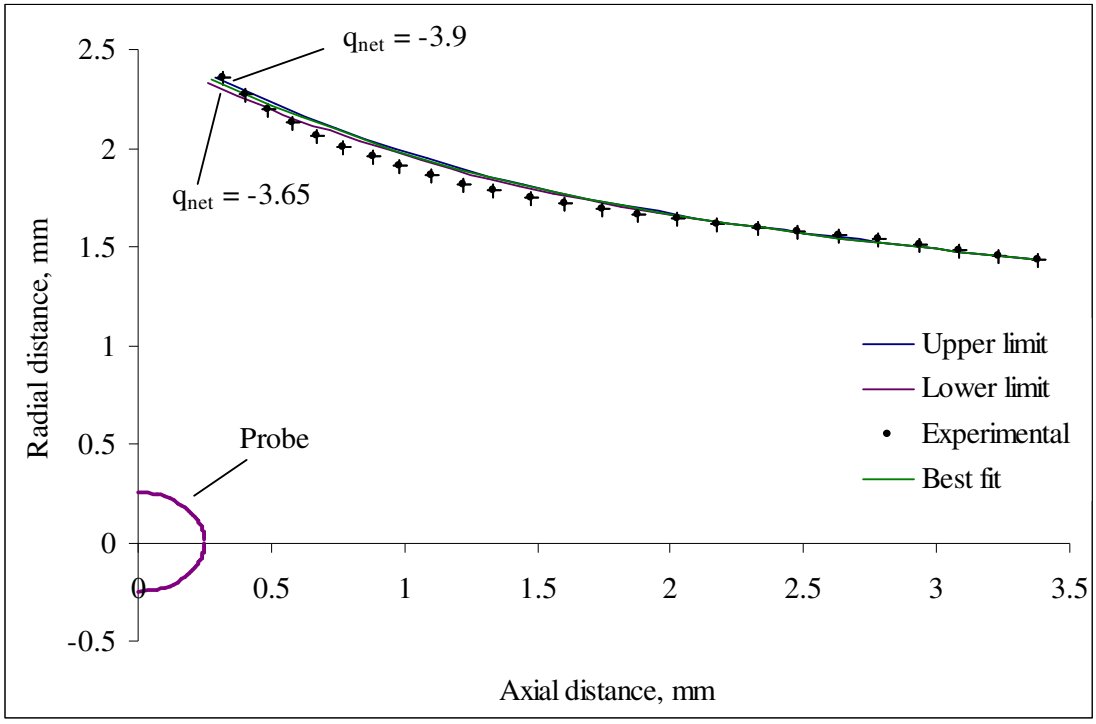

Figure 7.9: Experimental and predicted particle trajectories for a 45 µm fertiliser particle at probe voltage -6 kV with best fitted net charge q_{net} = -3.8x10^{-14} C. Within experimental error maximum fitted net charge q_{net} = -3.9x10^{-14} C and minimum fitted net charge q_{net} = -3.65x10^{-14} C i.e. ±4%.

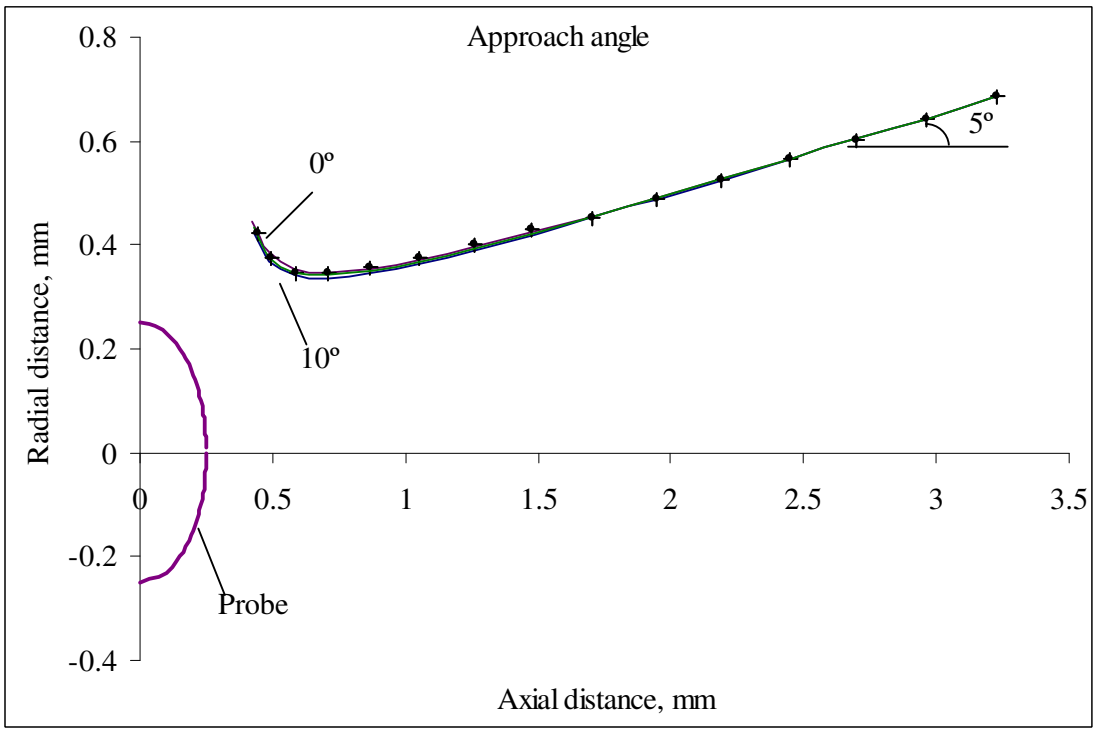

Figure 7.10: Experimental (•) and predicted particle trajectories for the 120 µm acrylic particle fitted in Figure 7.2 with varying approach angle of gas. The variation of approach angle is within experimental error.

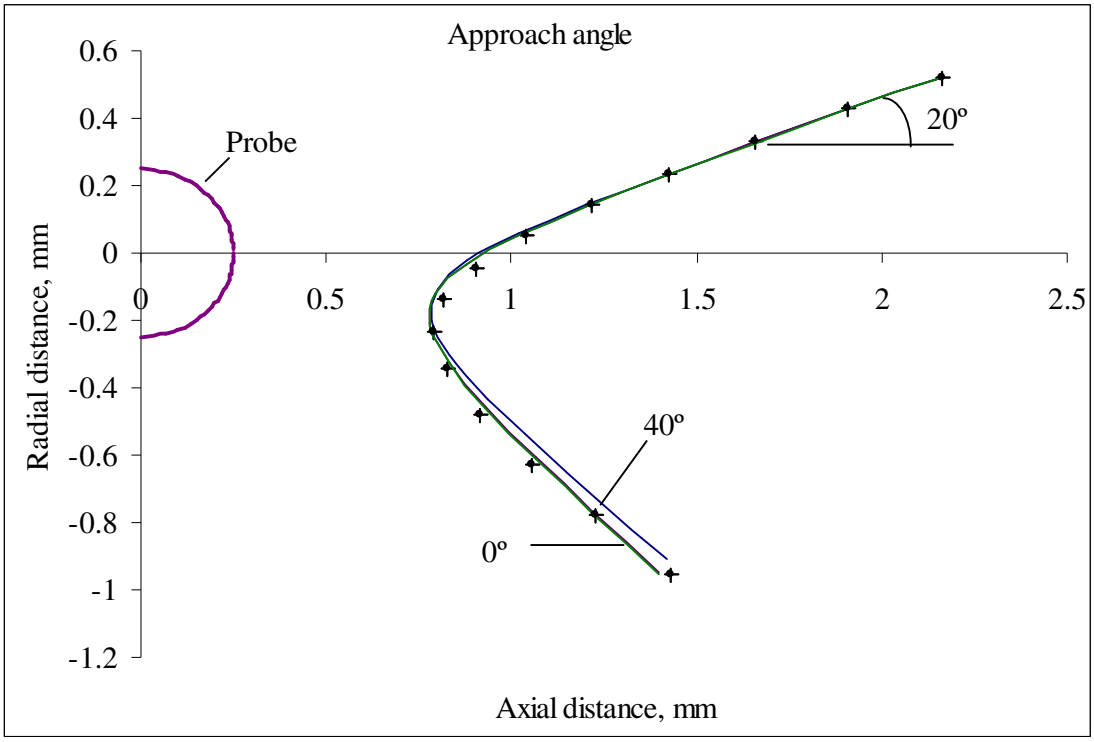

Figure 7.11: Experimental (•) and predicted particle trajectories for the 120 µm acrylic particle fitted in Figure 7.4 with varying approach angle of gas. The variation of approach angle is exceeding experimental error.

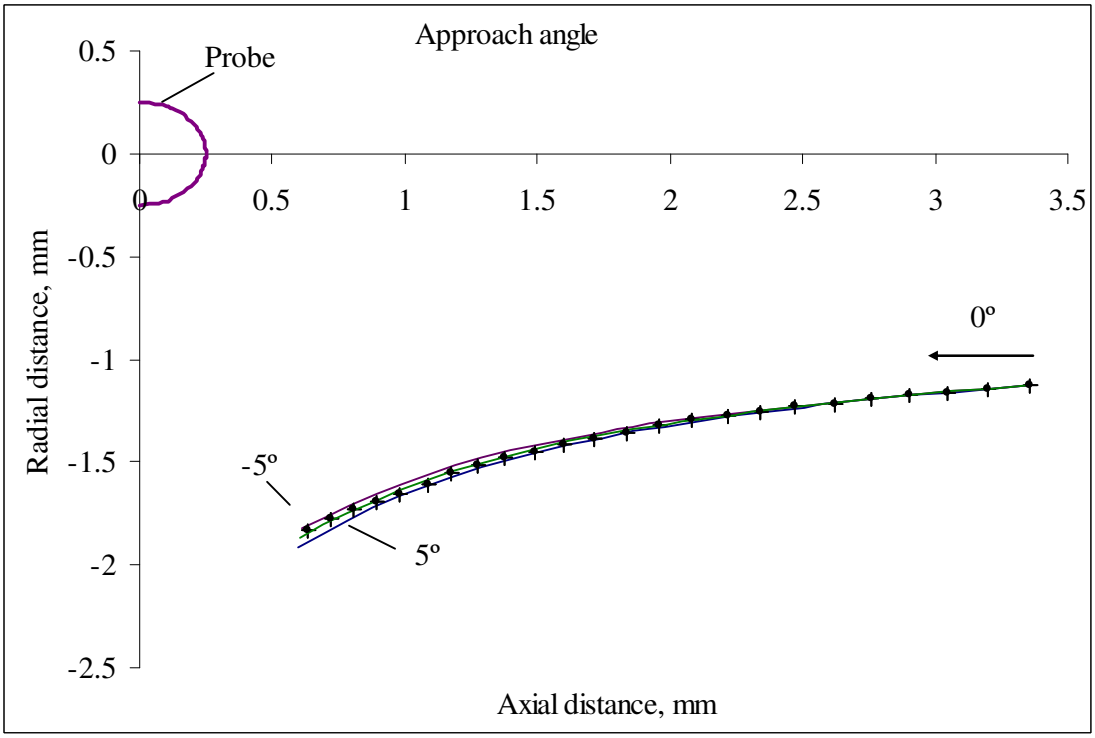

Figure 7.12: Experimental (•) and predicted particle trajectories for a 50 µm fertiliser particle fitted in Figure 7.8 with varying approach angle of gas. The variation of approach angle is within experimental error.

7.3 Net Charge Measurements

This section presents the measurement of net charge on individual particles without consideration of any dipole effects. Figure 7.14 to Figure 7.22 show net charge measurements for different particles with more in appendix A. Some figures have combined analysis of two or more particles from different frames. Figure 7.14 to Figure 7.16 show net charge measurements for acrylic particles. It can be observed (Figure 7.15) that the particle may adjust its position after sticking to the probe. Due to this there is some discrepancy in fitting the last point for the 92 µm particle in Figure 7.16. Generally the charge values for smaller particles (~30 µm) were less than those of larger particles (~90 µm). The particles with size close to 30 µm had charges in the range of 10^{-15} C. Measurements of net charge for glass particles have been presented in Figure 7.17 to Figure 7.19. Most of the particle trajectories analysed were in regions 1 and 2 of Figure 4.2 i.e. the right hand side of the origin. But for study purposes some trajectories which reached to the left side of the origin were also analysed, e.g., for the 108 µm particle in Figure 7.18. There was no stop for the presence of probe (on the shank side of the probe) so the last modelled point has gone beyond that, i.e. into the surface of the probe when actually it should be sitting on the surface. For the 55 µm particle in Figure 7.18 and the 60 µm particle in Figure 7.19 there is some discrepancy when fitting the last point, presumably due to particle movement after reaching the surface.

Figure 7.20 and Figure 7.21 present net charge measurements for milk particles. The milk particles were easy to visualise as a whole particle (Figure 7.20(a)). The sample had non-uniform agglomerates which had formed during manufacture. The particles were sticky and as the flow approached the probe some of them attached to the surface of the probe (Figure 7.20(a) and 7.21(a)) and a flare due to dispersion of the laser sheet falling on them could be observed. The surface of probe was difficult to outline in such cases and its far end (away from the tip) was used to identify the top surface position, with the probe geometry and size being filled in from previous experience. Figure 7.22 show net charge measurements for fertiliser particles. There were a large number of fines in the fertiliser sample which stuck to the probe and formed a uniform layer on its surface. A uniform glow on the probe's surface (Figure 7.22(a)) could be observed in this case. This layer may have provided electrical

shielding, affected the trajectory of particles close to the probe. For more net charge measurements please refer to Appendix A.4.

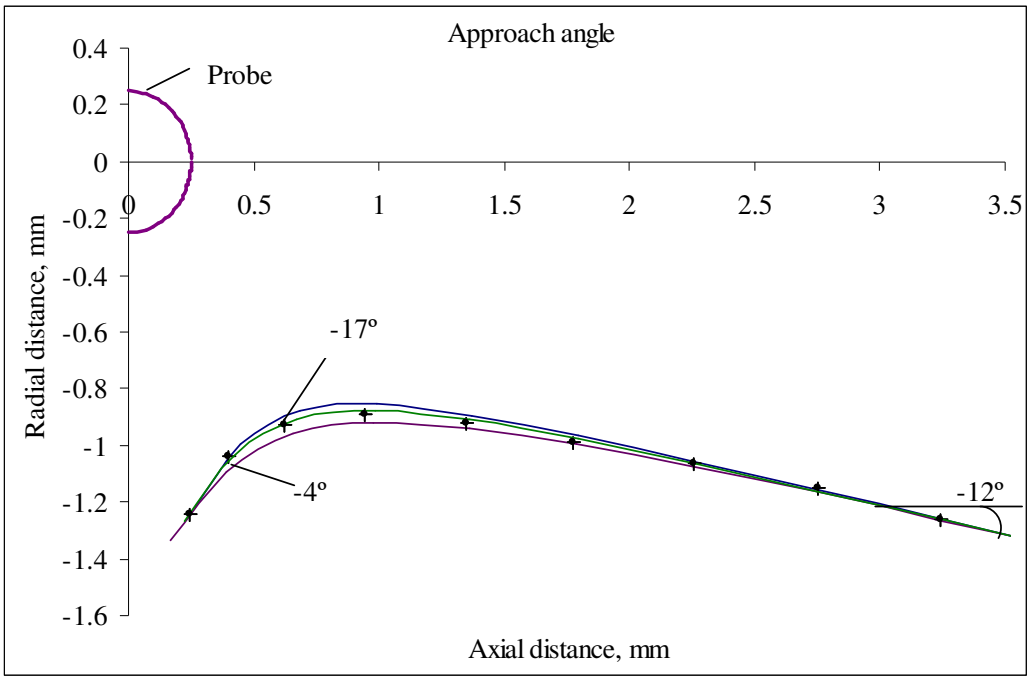

Figure 7.13: Experimental (•) and predicted particle trajectories for a 55 µm milk particle with varying approach angle of gas. The variation of approach angle is within experimental error.

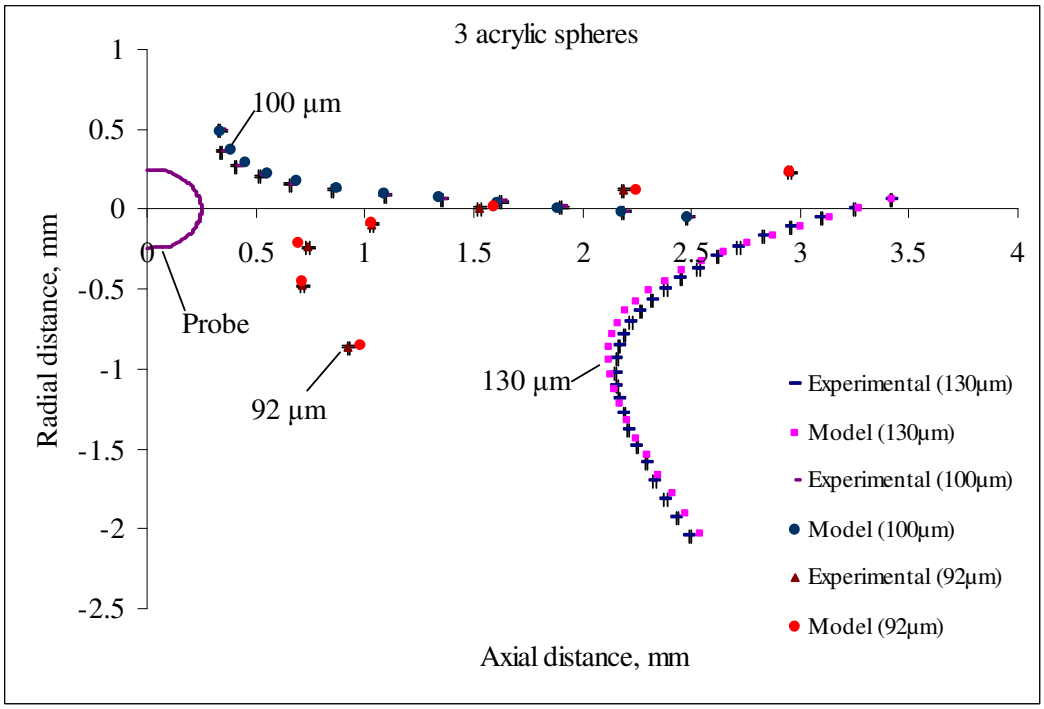

Figure 7.14: Experimental and predicted particle trajectories for a 130 µm acrylic particle with probe voltage -18 kV with fitted net charge q_{net} = -7.6x10^{-13} C, a 100 µm acrylic particle with probe voltage -14 kV with fitted net charge q_{net} = -2.44x10^{-13} C and a 92 µm acrylic particle with probe voltage -18kV with fitted net charge q_{net} = -9.7x10^{-13} C.

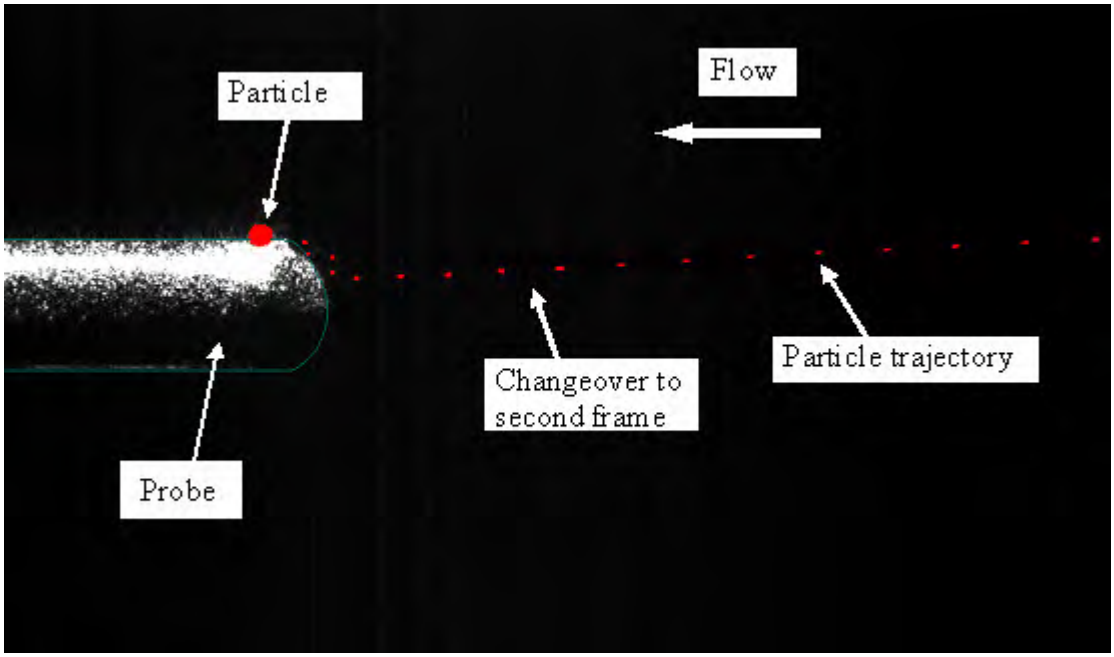

(a)

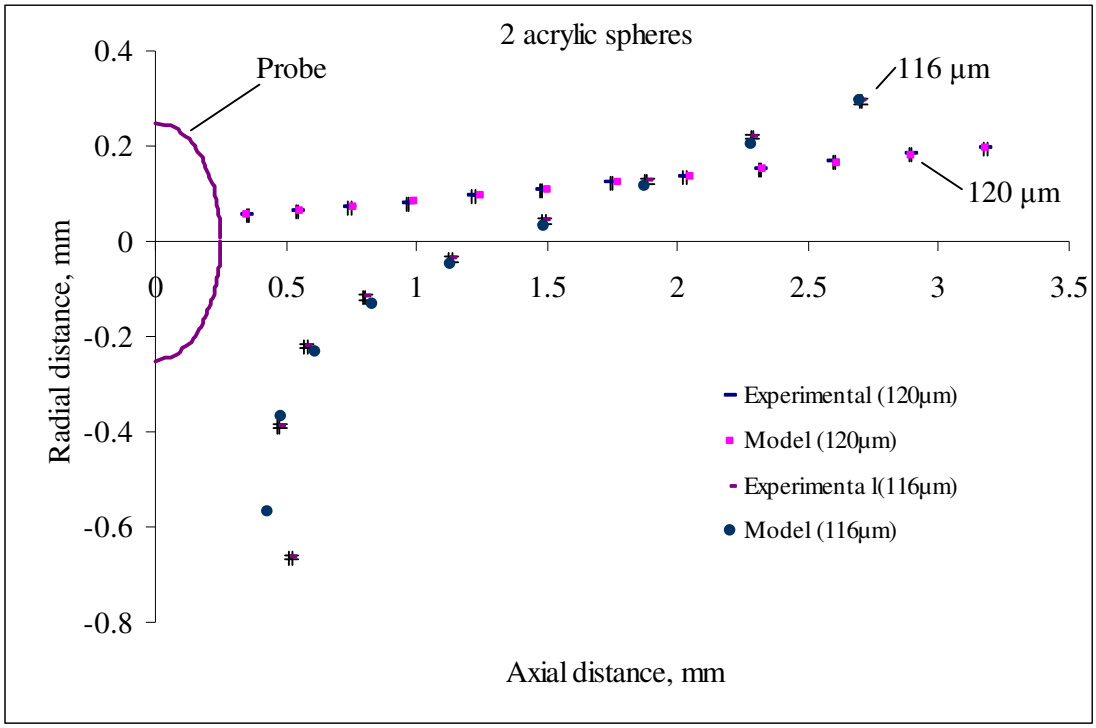

(b)

Figure 7.15: (a) Actual image of a 120 µm acrylic particle at probe voltage -10 kV (b) Experimental and predicted particle trajectories for the 120 µm acrylic particle with fitted net charge q_{net} = -3x10^{-13} C and a 116 µm acrylic particle with probe voltage +10 kV with fitted net charge q_{net} = +2.8x10^{-13} C.

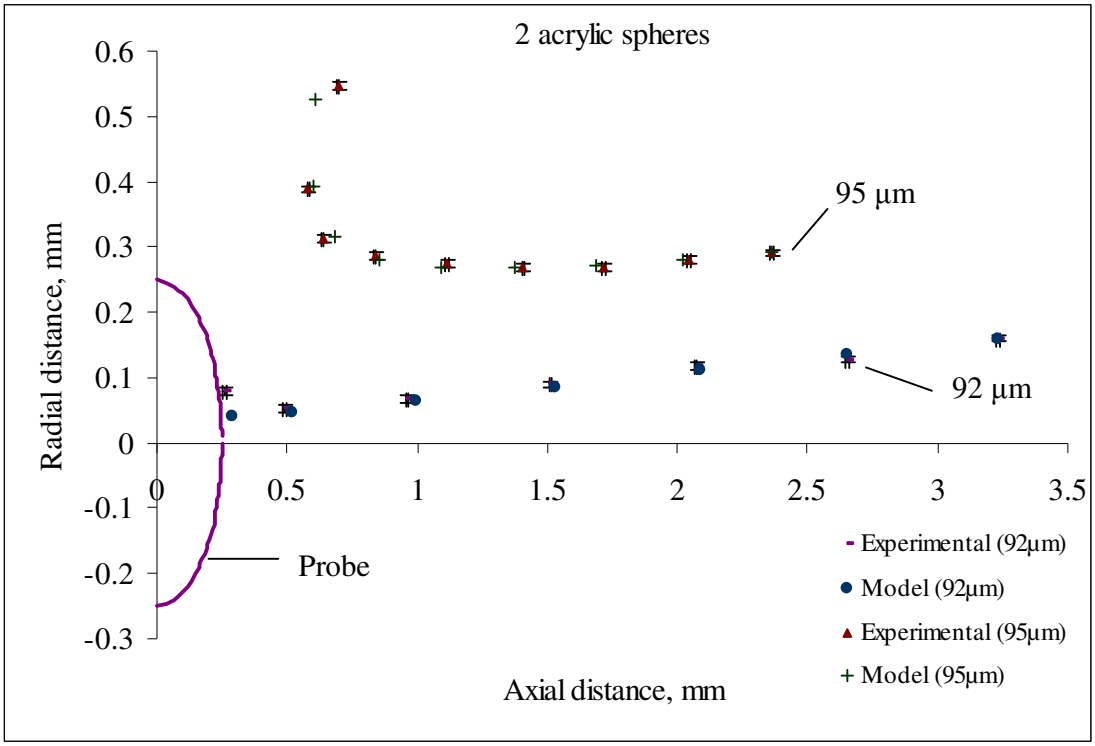

Figure 7.16: Experimental and predicted particle trajectories at probe voltage -6 kV for a 92 µm acrylic particle with fitted net charge q_{net} = -6.5x10^{-13} C and a 95 µm acrylic particle with fitted net charge q_{net} = -8x10^{-13} C.

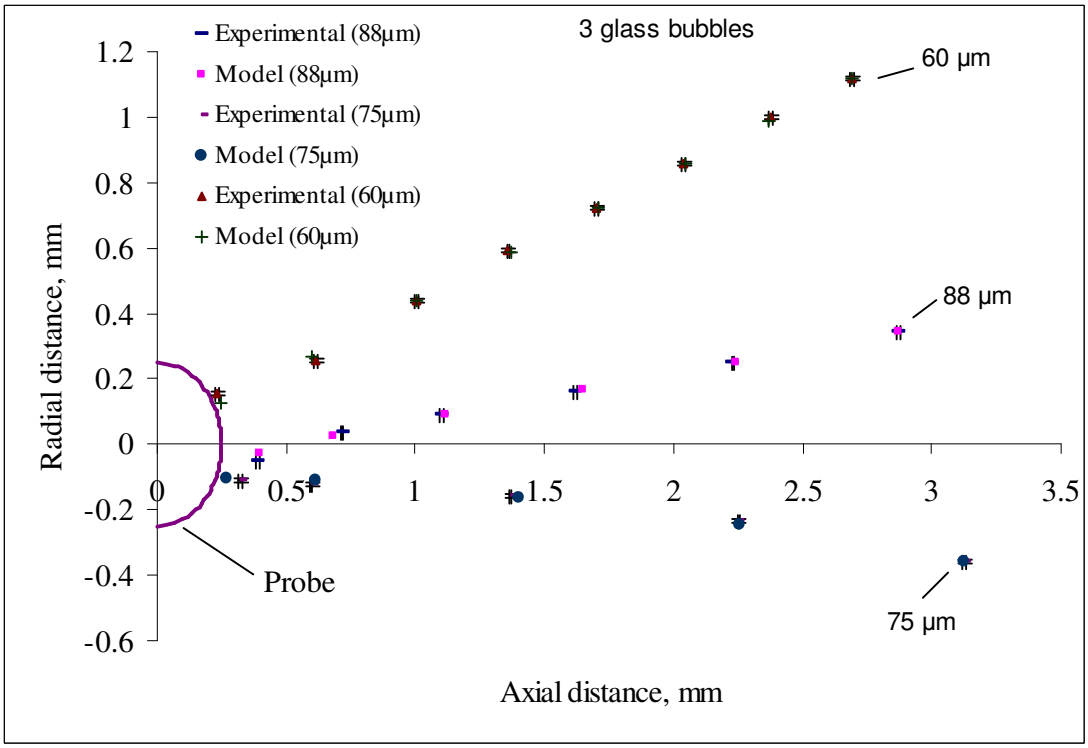

Figure 7.17: Experimental and predicted particle trajectories for an 88 µm glass particle with probe voltage -6 kV with fitted net charge q_{net} = -2.7x10^{-13} C, a 75 µm glass particle with probe voltage -10 kV with fitted net charge q_{net} = -4x10^{-14} C and a 60 µm glass particle with probe voltage -6 kV with fitted net charge q_{net} = +3.9x10^{-14} C.

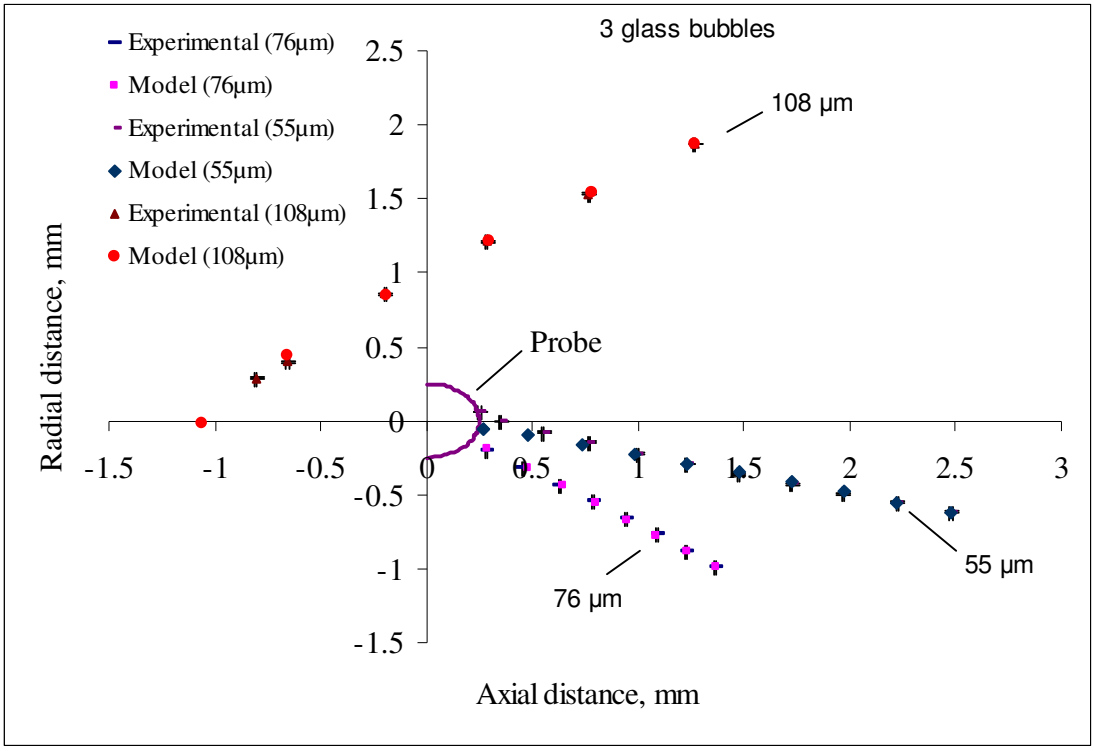

Figure 7.18: Experimental and predicted particle trajectories at probe voltage -6 kV for a 76 µm glass particle with fitted net charge q_{net} = -1.05x10^{-14} C, a 55 µm glass particle with fitted net charge q_{net} = +5x10^{-15} C and a 108 µm glass particle with fitted net charge q_{net} = +1.25x10^{-13} C (last modelled point into the probe as there was no stop for presence of probe along the shank).

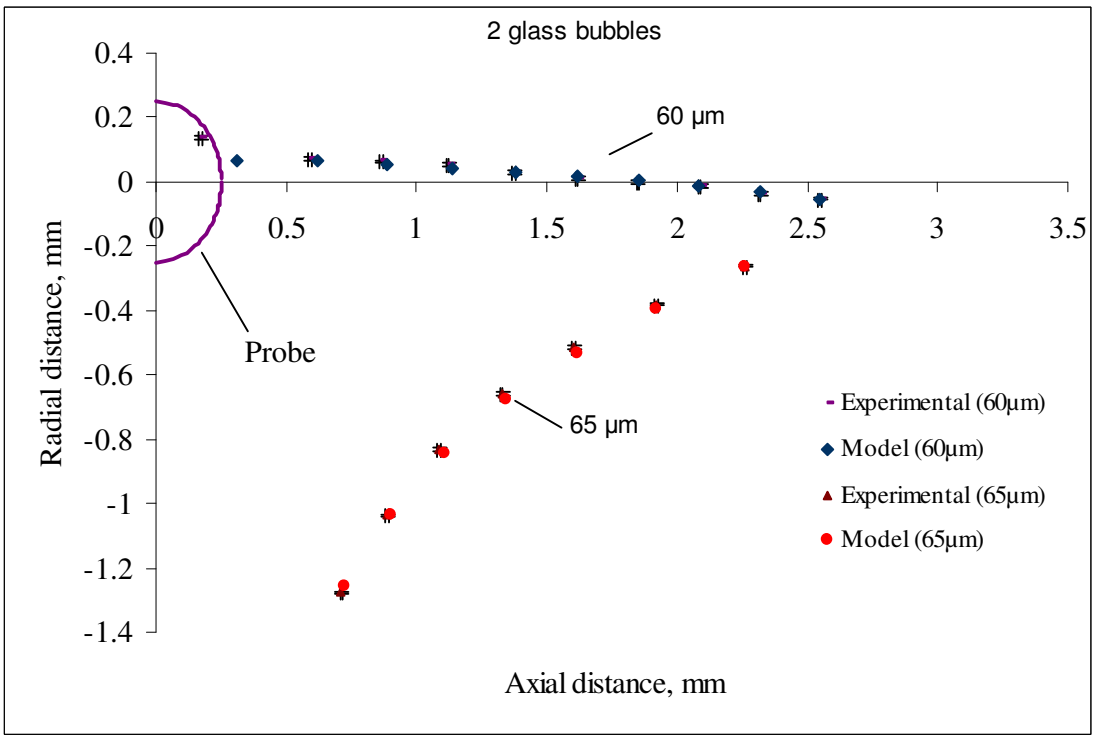

Figure 7.19: Experimental and predicted particle trajectories at probe voltage -6 kV for a 60 µm glass particle with fitted net charge q_{net} = +1x10^{-14} C and a 65 µm glass particle with fitted net charge q_{net} = -5.6x10^{-14} C.

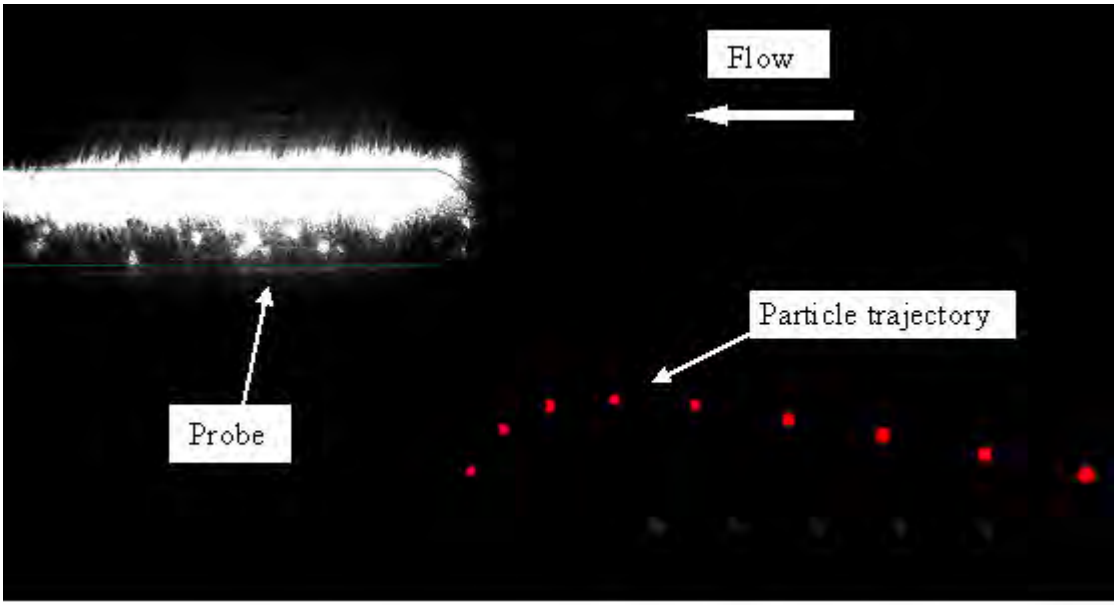

(a)

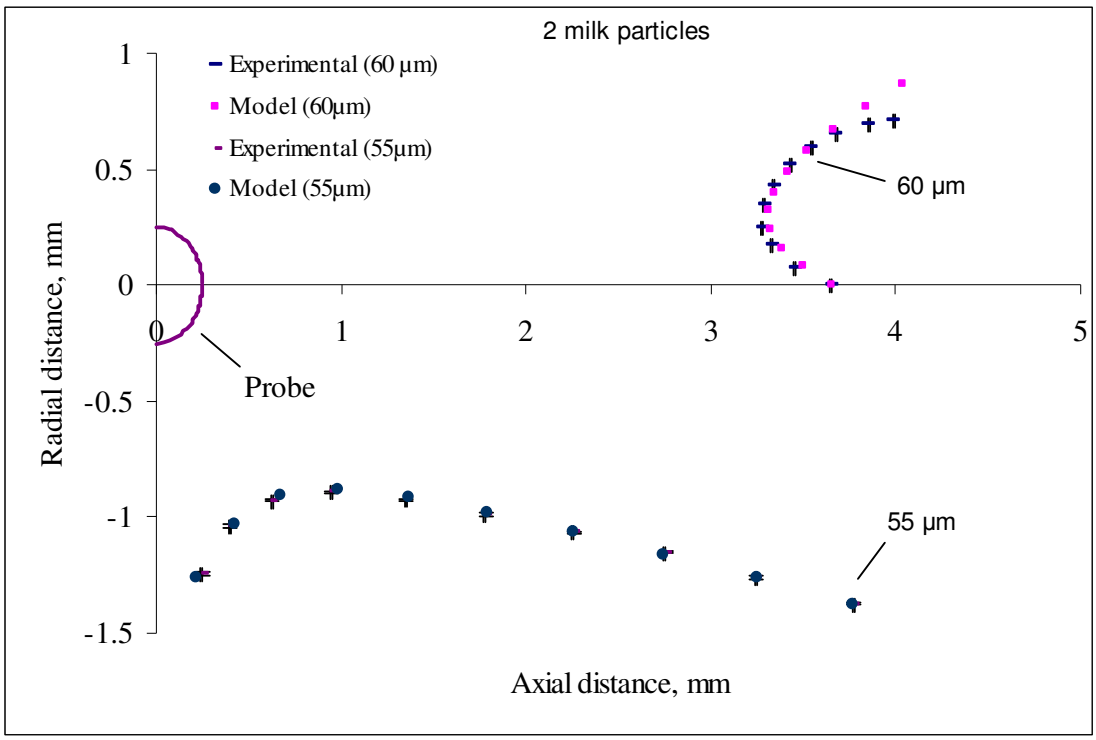

(b)

Figure 7.20: (a) Actual image of a 55 µm milk particle at probe voltage +6 kV
(b) Experimental and predicted particle trajectories for the 60 µm milk particle with fitted net charge q_{net} = +5.2x10^{-13} C and a 55 µm milk particle with probe voltage +6kV with fitted net charge q_{net} = +1.14x10^{-13} C.

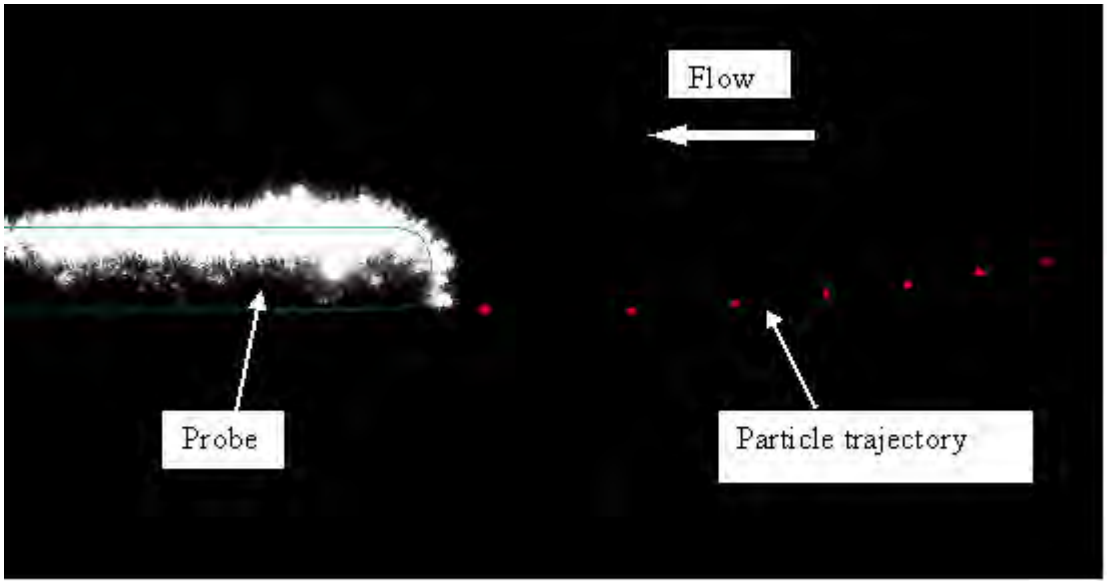

(a)

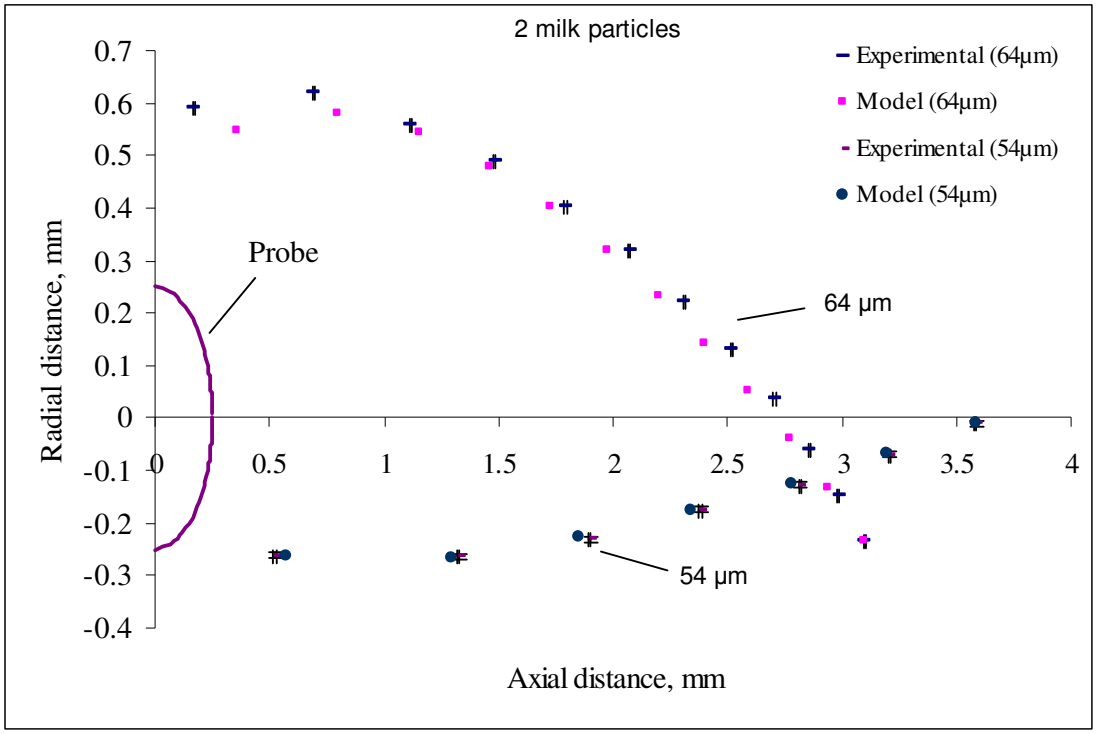

(b)

Figure 7.21: (a) Actual image of a 64 µm milk particle at probe voltage +4 kV
(b) Experimental and predicted particle trajectories for the 64 µm milk particle with fitted net charge q_{net} = -1.7x10^{-13} C and a 54 µm milk particle with probe voltage +5 kV with fitted net charge q_{net} = -2.18x10^{-13} C.

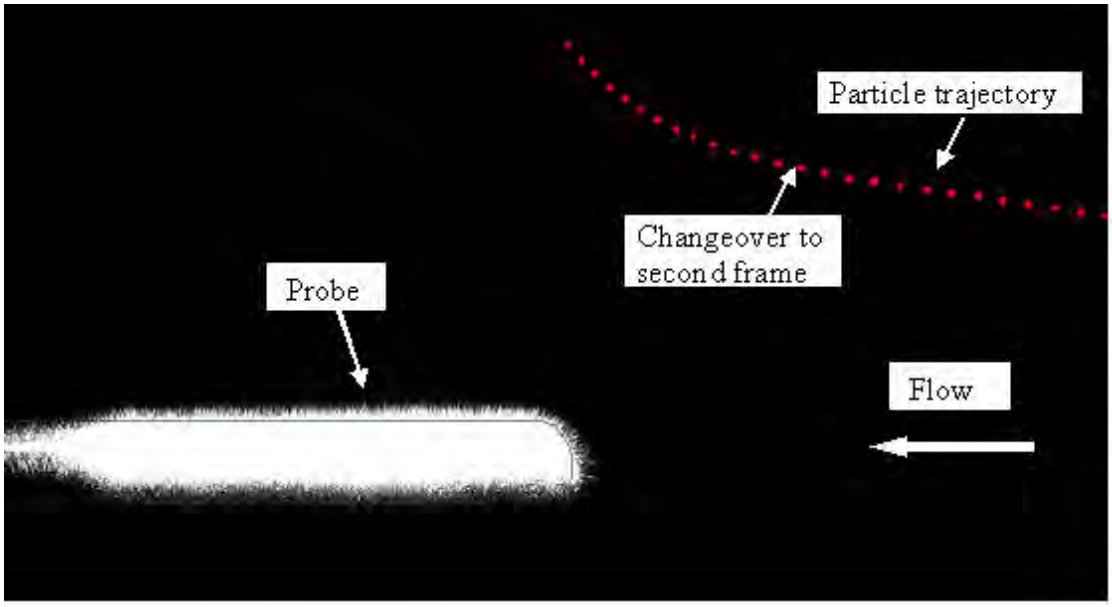

(a)

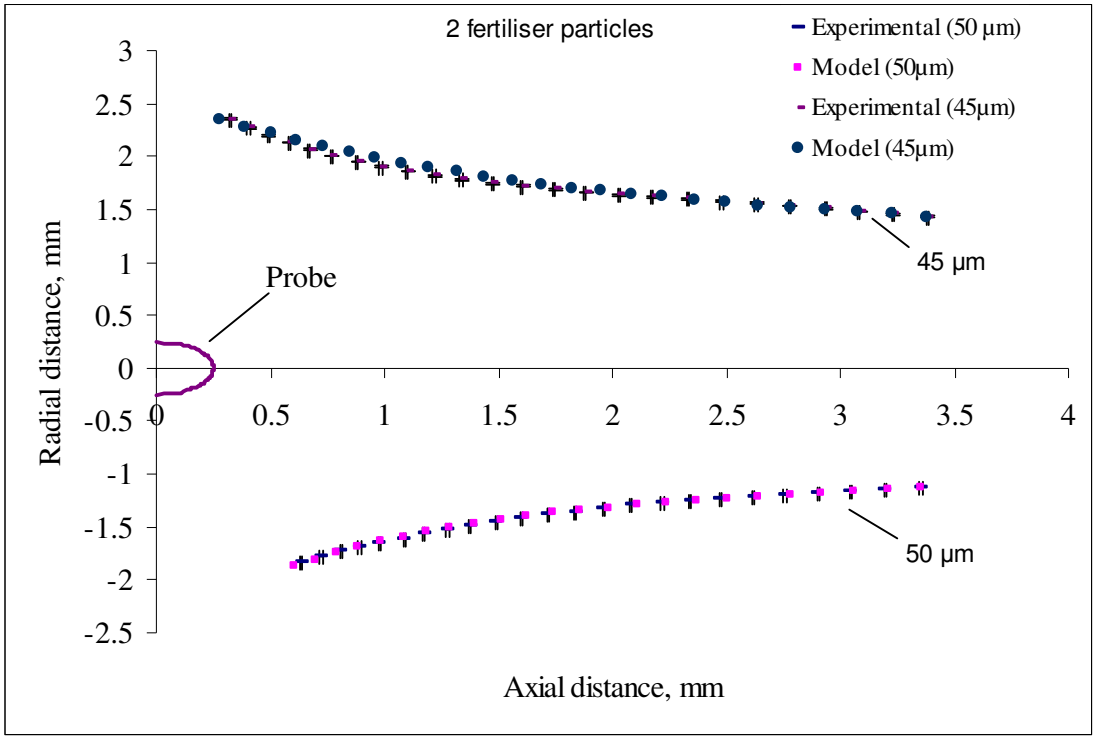

(b)

Figure 7.22: (a) Actual image of a 50µm fertiliser particle at probe voltage -6 kV (b) Experimental and predicted particle trajectories for the 50 µm fertiliser particle with fitted net charge q_{net} = -5.2x10^{-14} C and a 45 µm fertiliser particle with probe voltage -6kV with fitted net charge q_{net} = -3.8x10^{-14} C.

7.4 Net Charge and Dipole Measurements

There were cases while fitting the model where assuming solely net charge gave wide deviation close to the tip of the probe. The addition of a dipole force in the equations then gave a good fit up to the probe. Figure 7.23 to Figure 7.30 present such trajectories of glass particles for which the fitted "dipole" (defined by the fitted dipole moment divided by the particle diameter) charges may exceed the fitted net charge. The 80 μm glass particle (Figure 7.23) was initially being repelled (slowing down) as it approached the probe, so if it held only a simple net charge its trajectory should have moved away from the probe. Actually it bent towards the probe and stuck to it. This unexpected behaviour could not be explained on the basis of net charge and the addition of an attractive dipole force could fit the whole trajectory well. The fitted dipole charge was approximately 3.5 times higher than the net charge. The trajectory of an 88 μm glass particle in Figure 7.24 could almost be explained with net charge alone but with both a net charge and a dipole charge a closer fit was obtained. There were particles, e.g., Figure 7.25 for which either net charge or dipole charge could successfully give a good fitting with experimental points.

In Figure 7.26(b) there is a discrepancy in fitting the last point of the trajectory. By looking at the image in Figure 7.26(a) it seems as if the particle had adjusted its position after touching the probe which has been observed in several cases. For an 82 μm glass particle in Figure 7.27 fitting of both net charge and dipole charge still gave error but fitting with only net charge the trajectory lies far away from the experimental points (slowing down but on the same path). Trajectories with dipole give better fit for the particle going beyond the origin (left of tip centre) (Figure 7.28). There were also trajectories, e.g., Figure 7.30 in which a similar kind of fit was obtained for both dipole and no dipole charge.

Some of the trajectories of other particles apart from glass which had been analysed on the basis of net charge alone were reanalysed to check for any existence of dipole behaviour. Several such examples are shown in Figure 7.31 to Figure 7.38. It was found that most of the trajectories which were explained by net charge alone (Figure 7.20(b), 7.32, 7.34, 7.36 and 7.21(b)) could be equally explained with the existence of some dipole charge together with the net charge (Figure 7.31, 7.33, 7.34, 7.37 and

7.38 respectively). For more net charge and dipole charge measurements please refer to Appendix A.5.

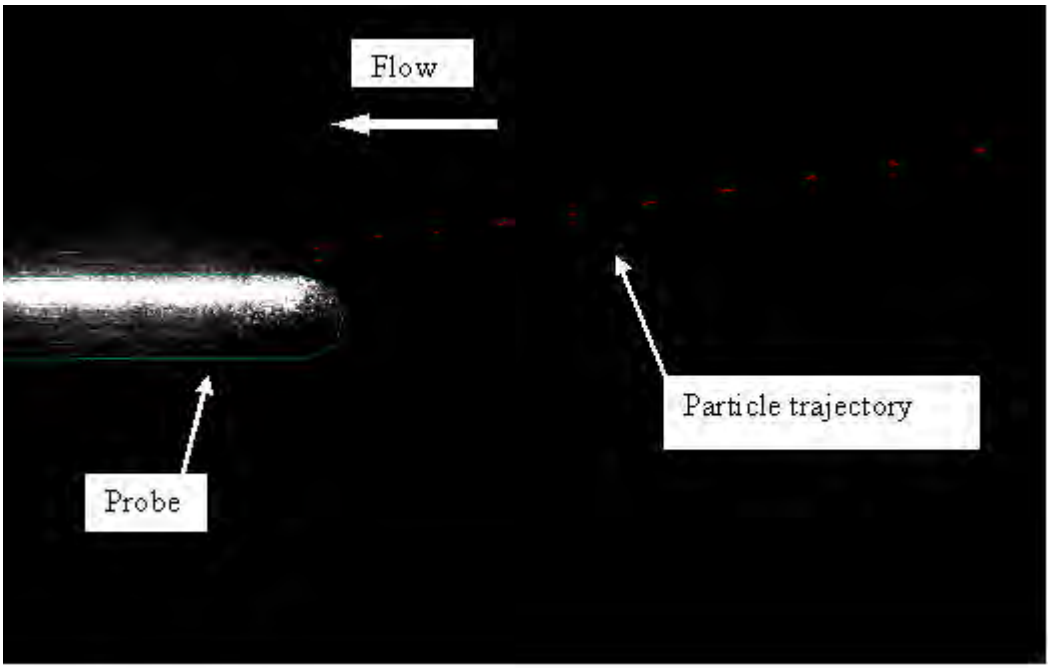

(a)

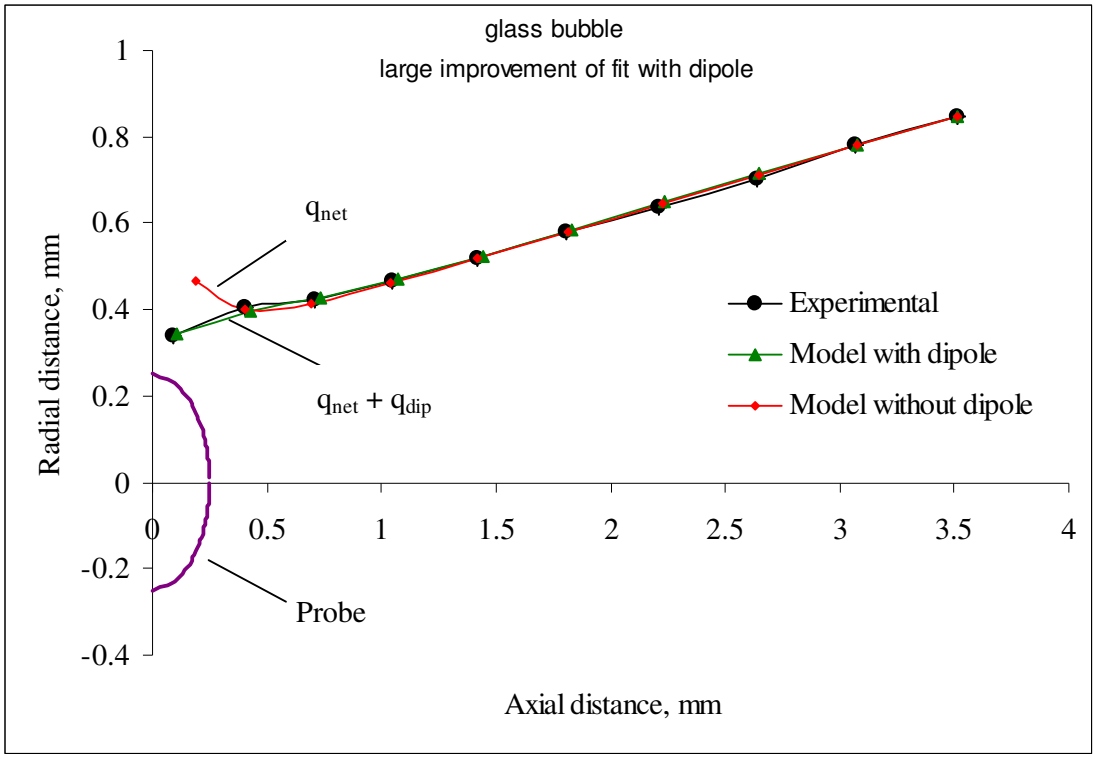

(b)

Figure 7.23: (a) Actual image of an 80µm glass particle at probe voltage -6 kV
(b) Experimental and model trajectories for the 80µm glass particle. For only net charge fitted the charge is q_{net}= -4x10^{-14} C and for both net charge and dipolar charge fitted the values are q_{net}= -7.5x10^{-14} C and q_{dip}= 2.7x10^{-13} C.

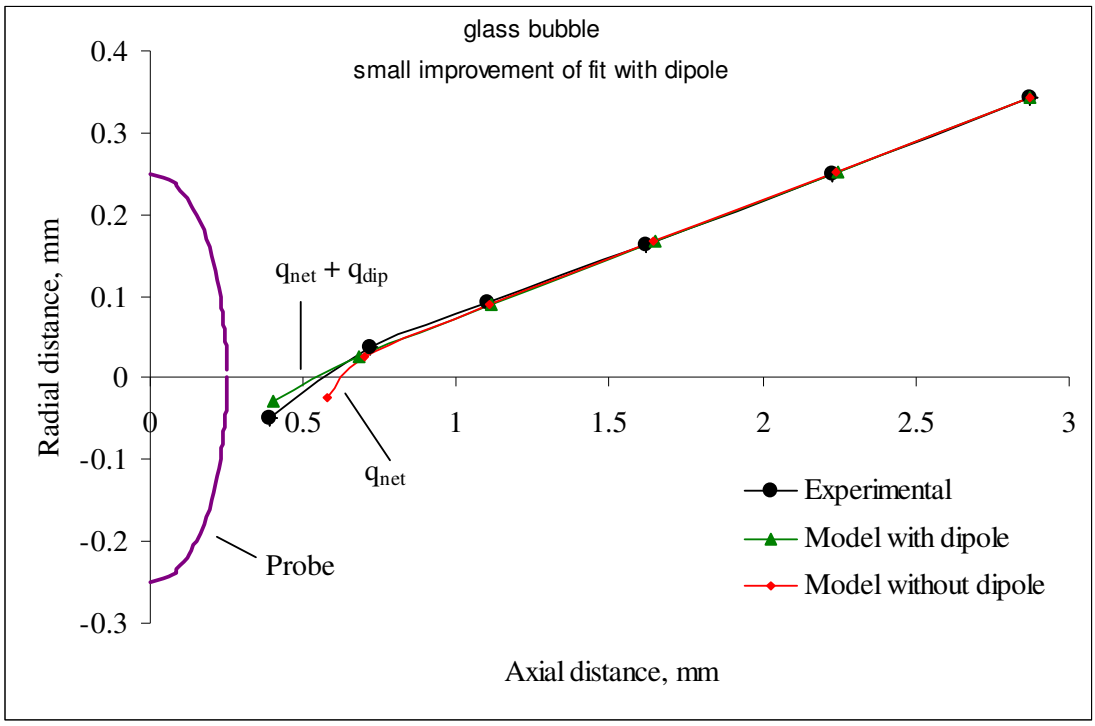

Figure 7.24: Experimental and model trajectories for an 88 µm glass particle at probe voltage -6 kV. For only net charge fitted the charge is q_{net}= -2x10^{-13} C and for both net charge and dipolar charge fitted the values are q_{net}= -2.65x10^{-13} C and q_{dip}= 6x10^{-13} C.

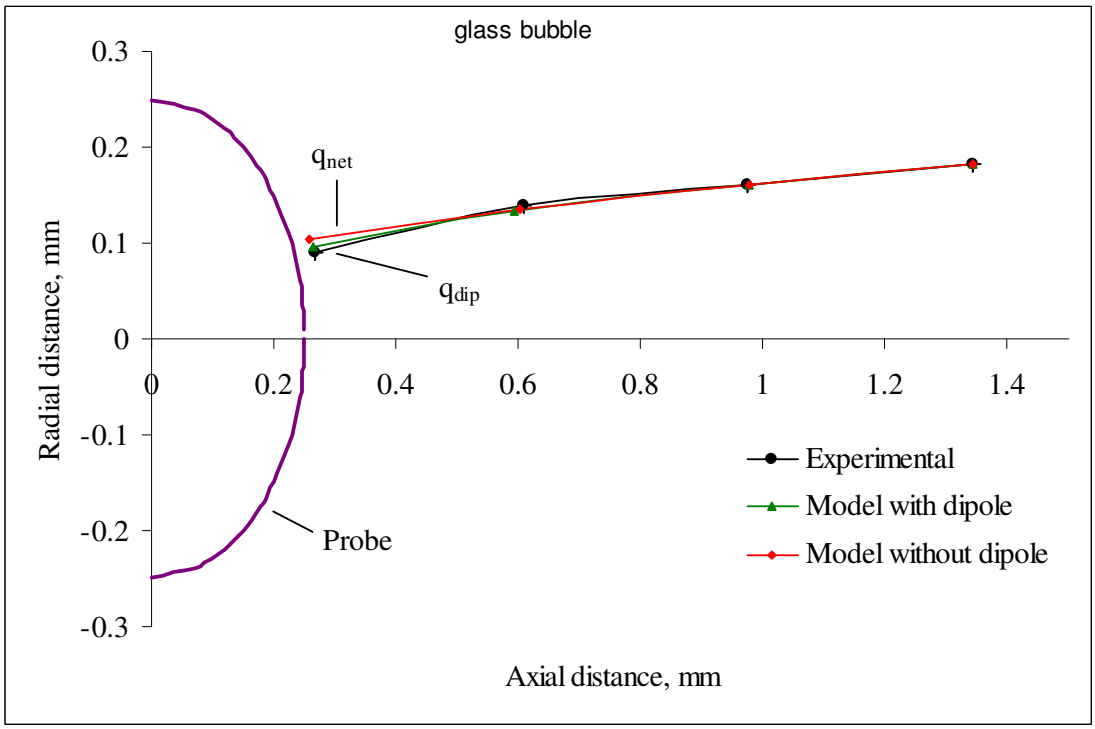

Figure 7.25: Experimental and model trajectories for a 60 µm glass particle at probe voltage -6 kV. For only net charge fitted the charge is q_{net}= +1.1x10^{-14} C and for both net charge and dipolar charge fitted the values are q_{net}= 0 C and q_{dip}= 1.1x10^{-13} C.

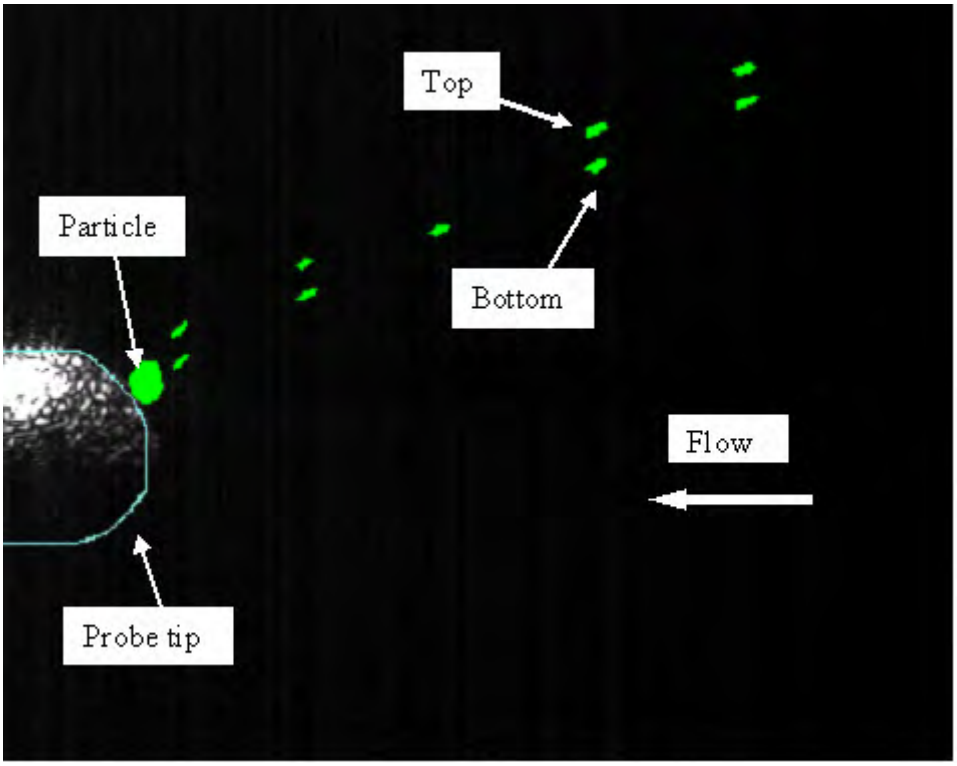

(a)

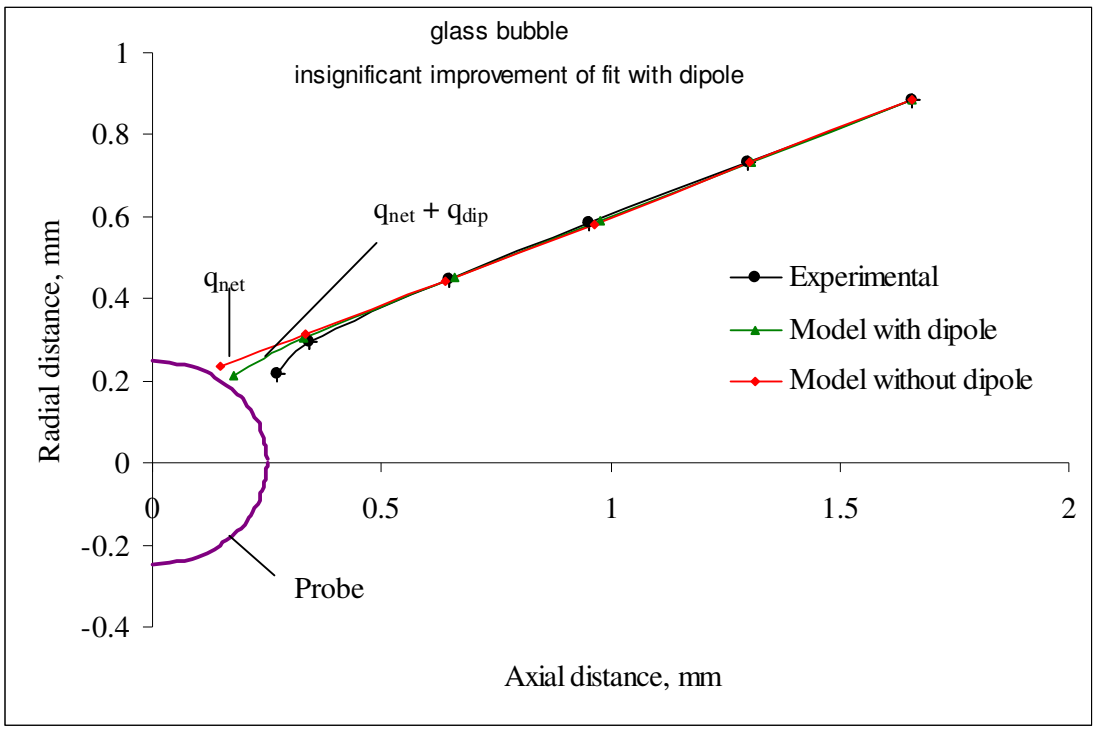

(b)

Figure 7.26: (a) Actual image of a 60 µm glass particle close to the probe tip at probe voltage -7 kV (b) Experimental and model trajectories for the 60 µm glass particle. For only net charge fitted the charge is q_{net}= -2x10^{-15} C and for both net charge and dipolar charge fitted the values are q_{net}= -2.5x10^{-14} C and q_{dip}= 2x10^{-13} C.

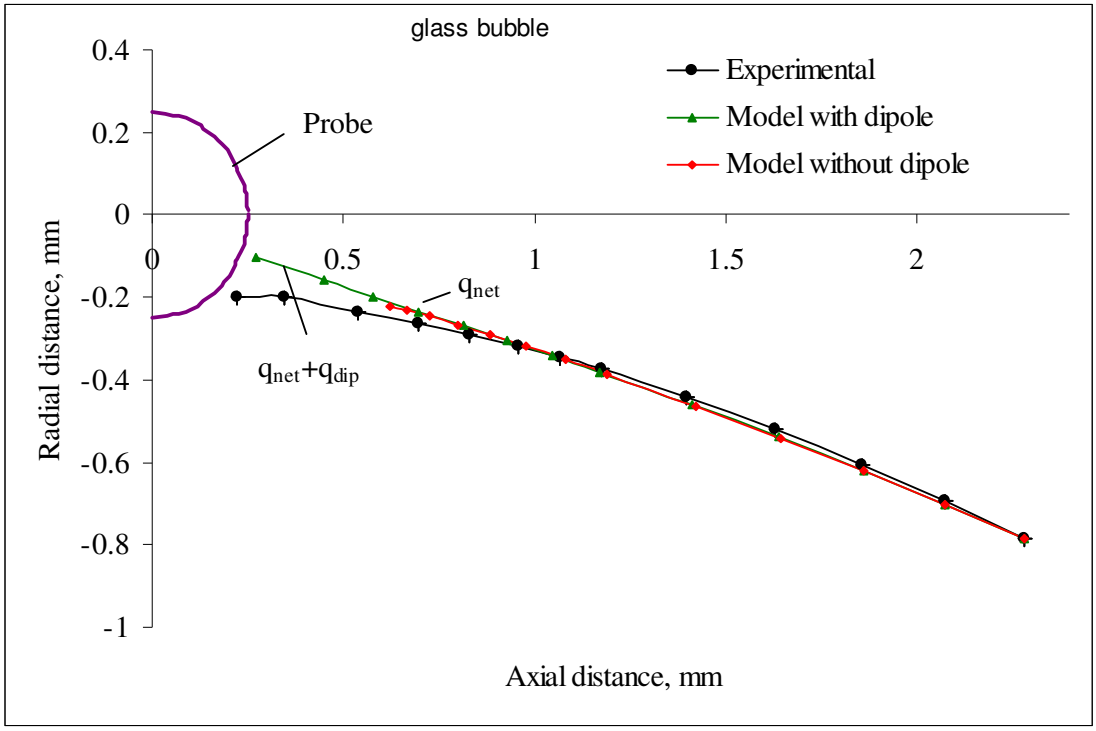

Figure 7.27: Experimental and model trajectories for an 82 µm glass particle at probe voltage -6 kV. For only net charge fitted the charge is q_{net}= -1x10^{-14} C and for both net charge and dipolar charge fitted the values are q_{net}= -8x10^{-15} C and q_{dip}= 5x10^{-14} C.

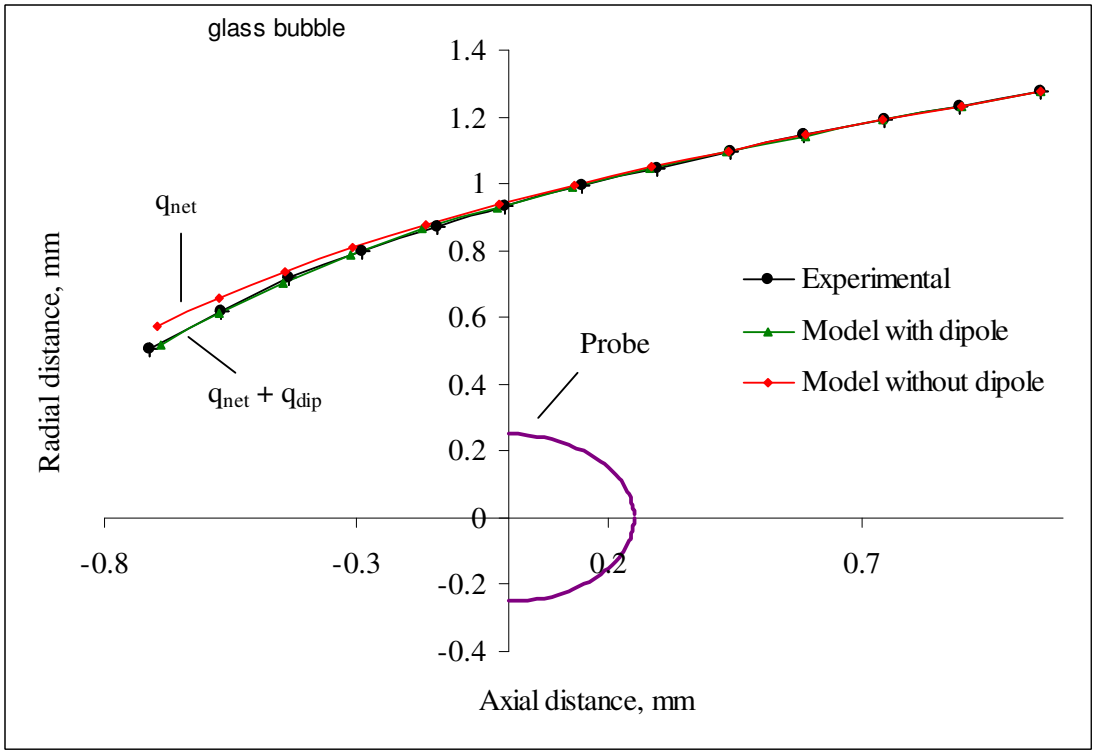

Figure 7.28: Experimental and model trajectories for a 65 µm glass particle at probe voltage -6 kV. For only net charge fitted the charge is q_{net}= +4x10^{-15} C and for both net charge and dipolar charge fitted the values are q_{net}= +3.3x10^{-15} C and q_{dip}= 1.2x10^{-14} C.

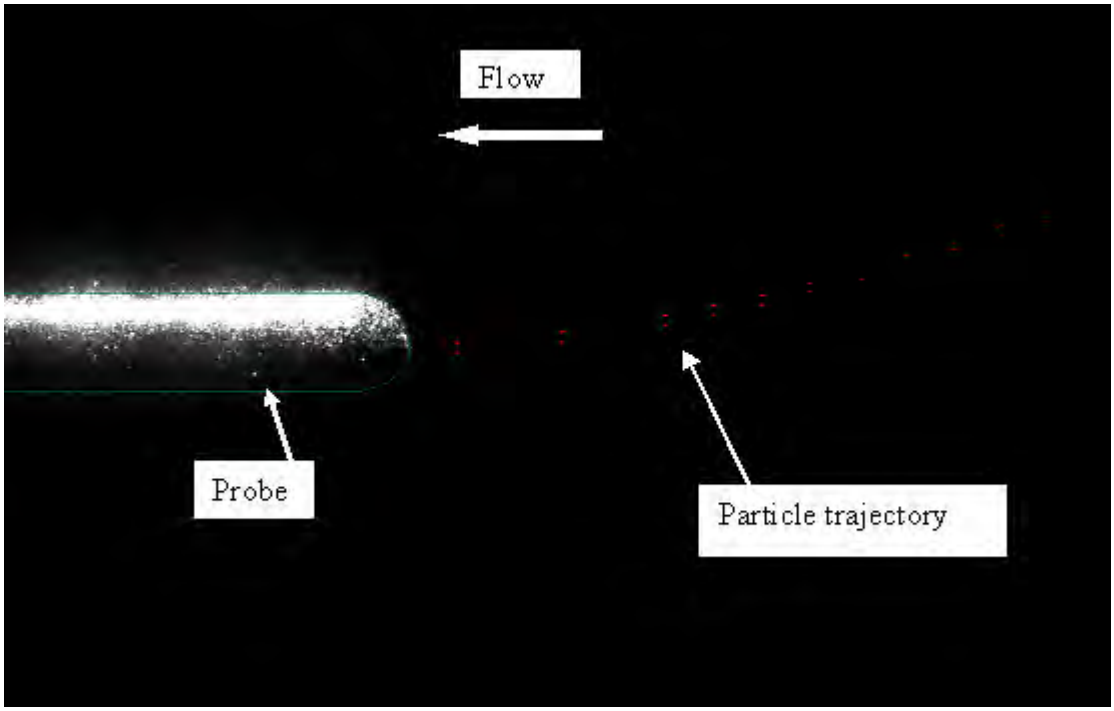

(a)

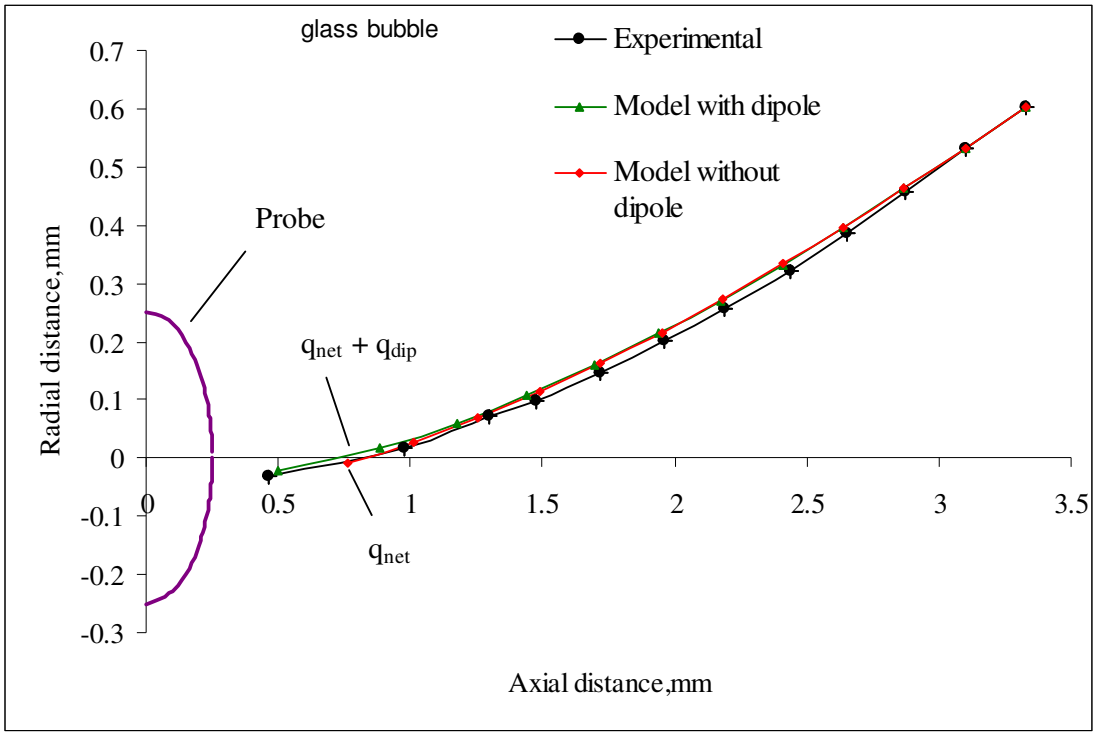

(b)

Figure 7.29: (a) Actual image a 70 µm glass particle at probe voltage -6 kV
(b) Experimental and model trajectories for the 70 µm glass particle. For only net charge fitted the charge is q_{net}= +1.2x10^{-14} C and for both net charge and dipolar charge fitted the values are q_{net}= +3x10^{-15} C and q_{dip}= 3x10^{-13} C.

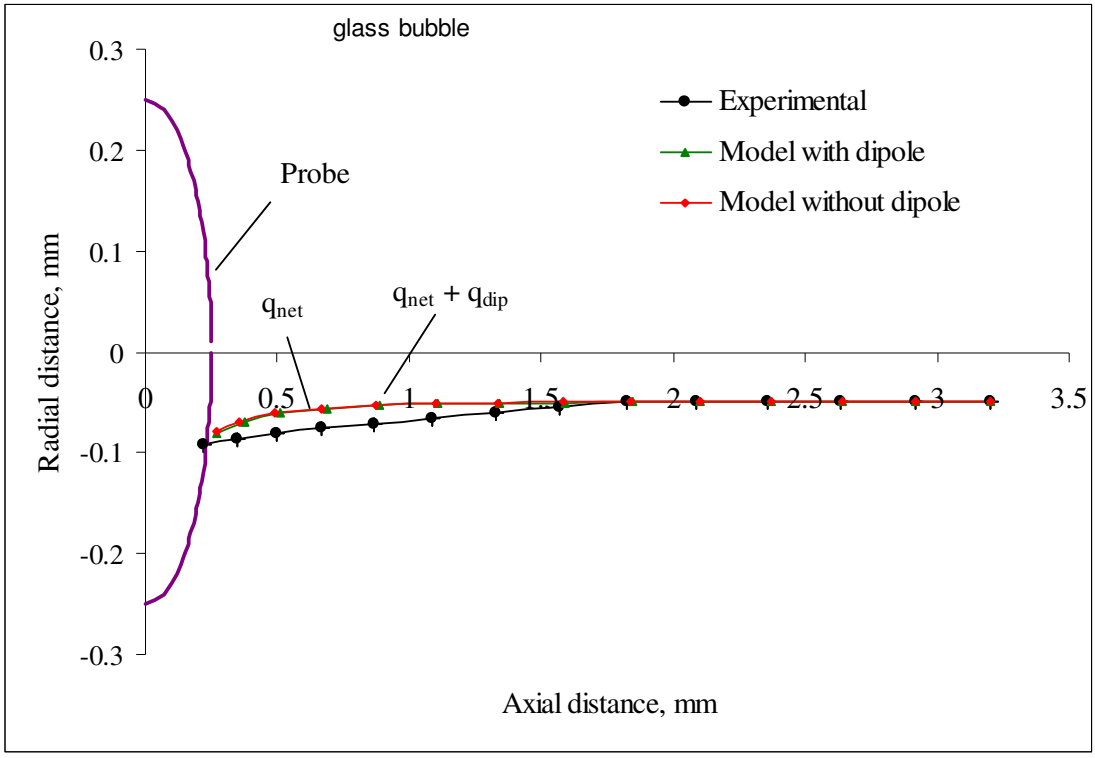

Figure 7.30: Experimental and model trajectories for a 65 µm glass particle at probe voltage -6 kV. For only net charge fitted the charge is q_{net}= -6.5x10^{-15} C and for both net charge and dipolar charge fitted the values are q_{net}= -8.2x10^{-15} C and q_{dip}= 7x10^{-15} C.

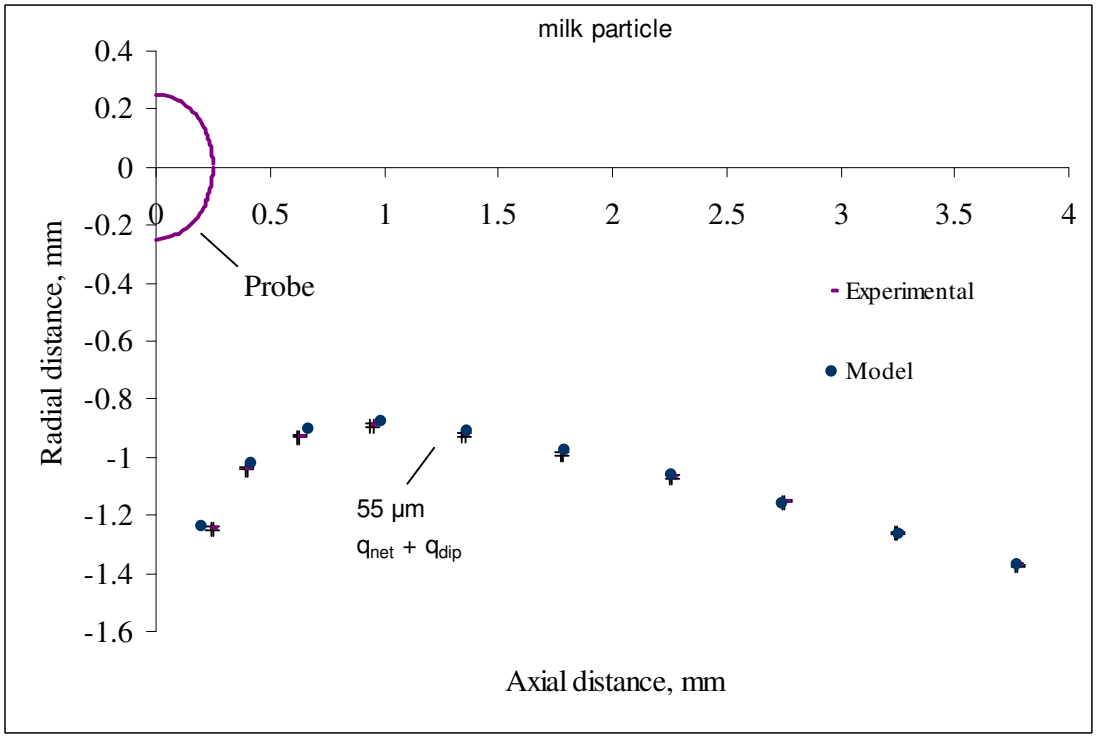

Figure 7.31: Experimental and predicted particle trajectories for a 55 µm milk particle at probe voltage +6 kV with fitted net charge q_{net} = +1.21x10^{-13} C and dipolar charge q_{dip} = 1.4x10^{-13} C.

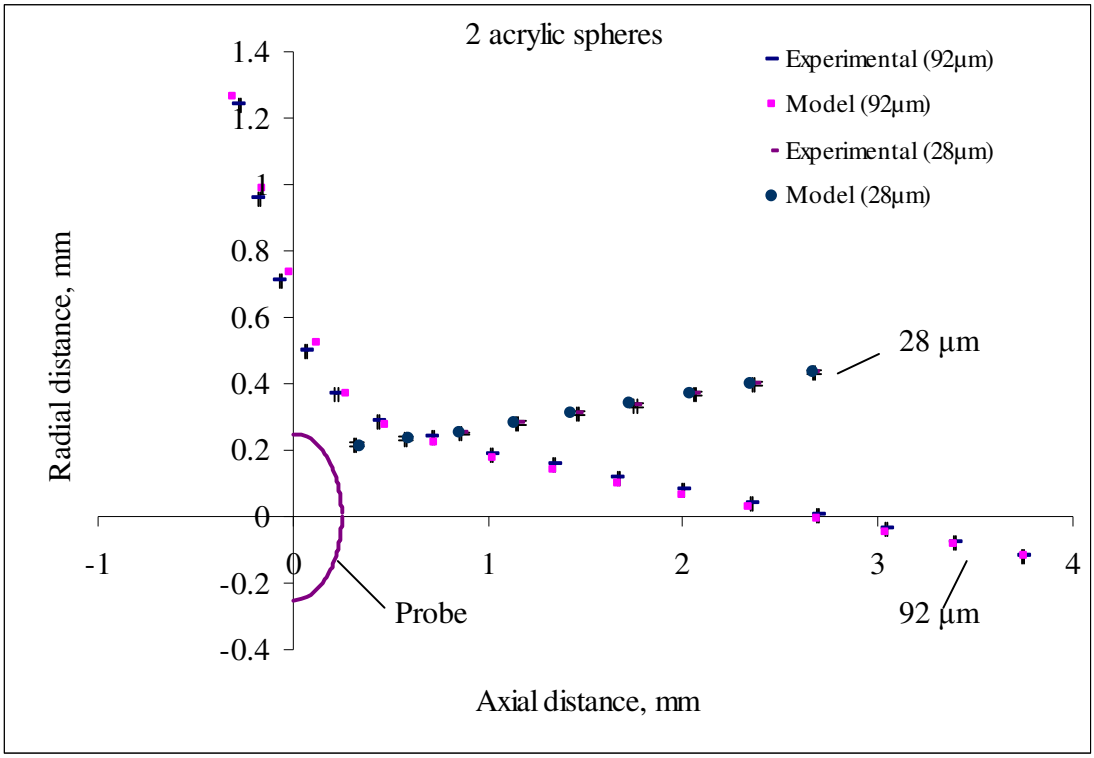

Figure 7.32: Experimental and predicted particle trajectories for a 92 µm acrylic particle at probe voltage -5 kV with fitted net charge q_{net} = -3.6x10^{-13} C and a 28 µm acrylic particle with probe voltage -10 kV with fitted net charge q_{net} = -2.8x10^{-15} C.

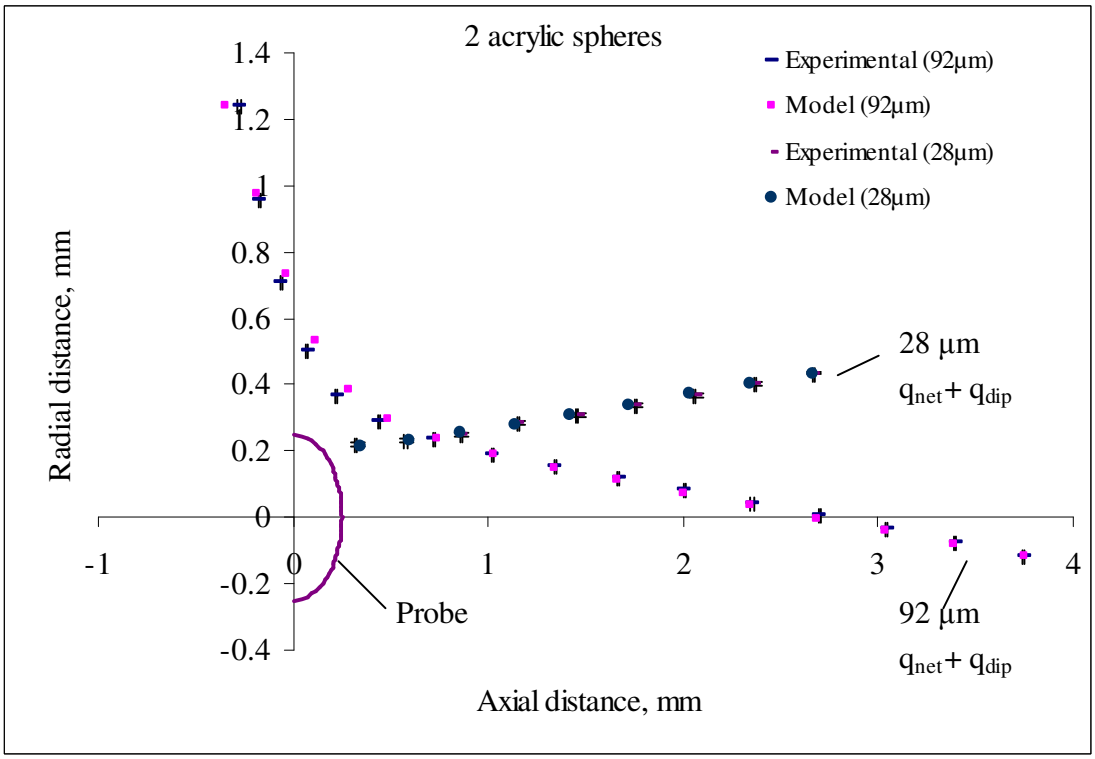

Figure 7.33: Experimental and predicted particle trajectories for a 92 µm acrylic particle at probe voltage -5 kV with fitted net charge q_{net} = -4x10^{-13} C, dipolar charge q_{dip}= 1.5x10^{-13} C and a 28 µm acrylic particle with probe voltage -10 kV with fitted net charge q_{net} = -3.1x10^{-15} C, dipolar charge q_{dip} = 5x10^{-15} C.

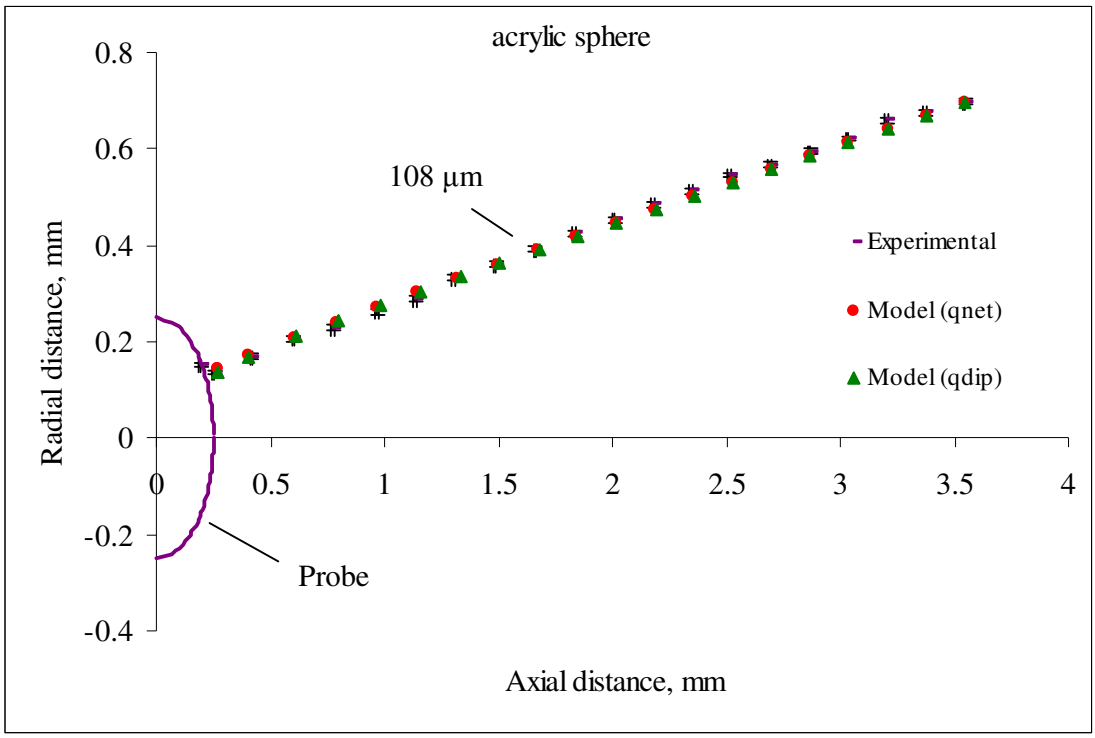

Figure 7.34: Experimental and predicted particle trajectories for a 108 µm acrylic particle with probe voltage -4 kV. For only net charge fitted net charge $q_{net} = +9\text{x}10^{-14}$ C and for only dipolar charge fitted the dipolar charge $q_{dip} = 6.5\text{x}10^{-13}$ C.

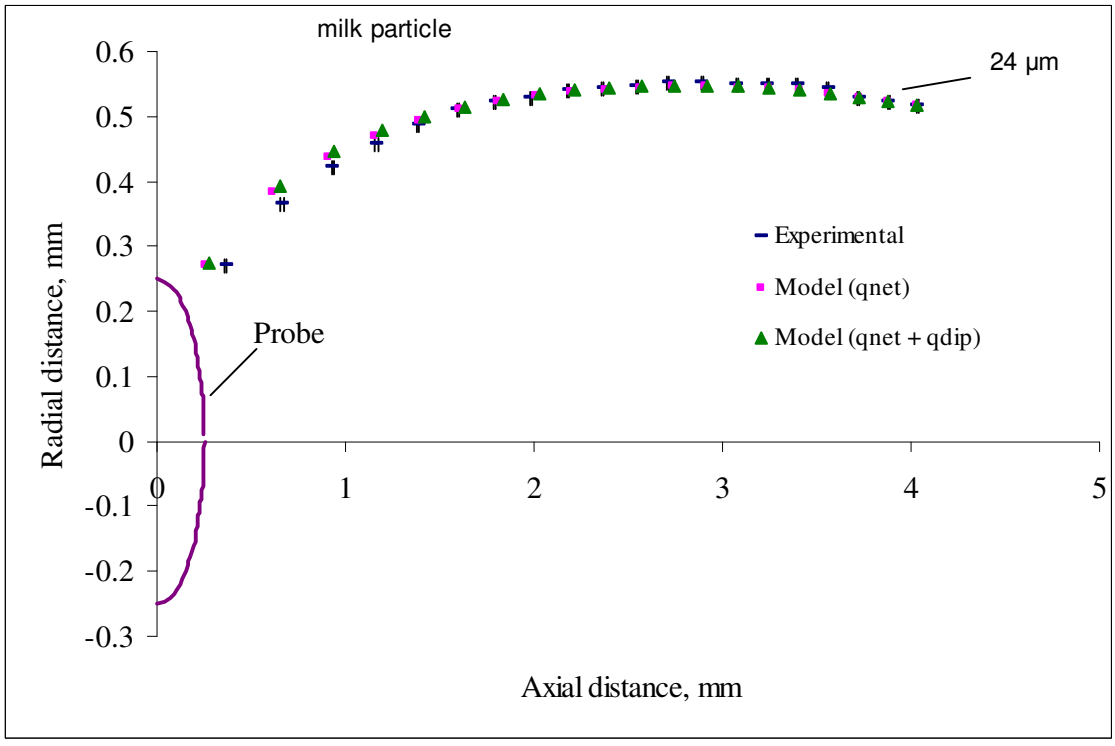

Figure 7.35: Experimental and predicted particle trajectories for a 24 µm milk particle with probe voltage -5 kV. For only net charge fitted the charge is $q_{net} = +1.55\text{x}10^{-14}$ C and for both net charge and dipolar charge fitted the values are $q_{net} = +1.3\text{x}10^{-14}$ C and dipolar charge $q_{dip} = 9\text{x}10^{-14}$ C.

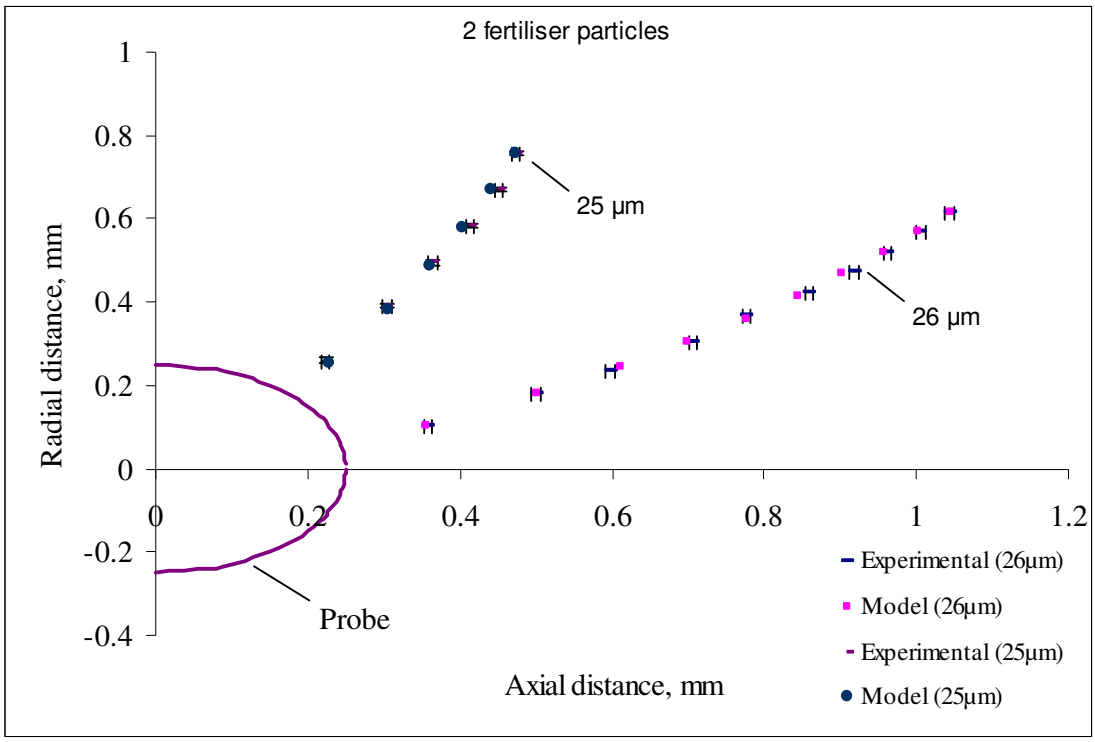

Figure 7.36: Experimental and predicted particle trajectories for a 26 µm fertiliser particle with probe voltage -6 kV with fitted net charge q_{net} = +3x10^{-15} C and a 25 µm fertiliser particle with probe voltage -6 kV with only fitted net charge q_{net} = +1.2x10^{-15} C.

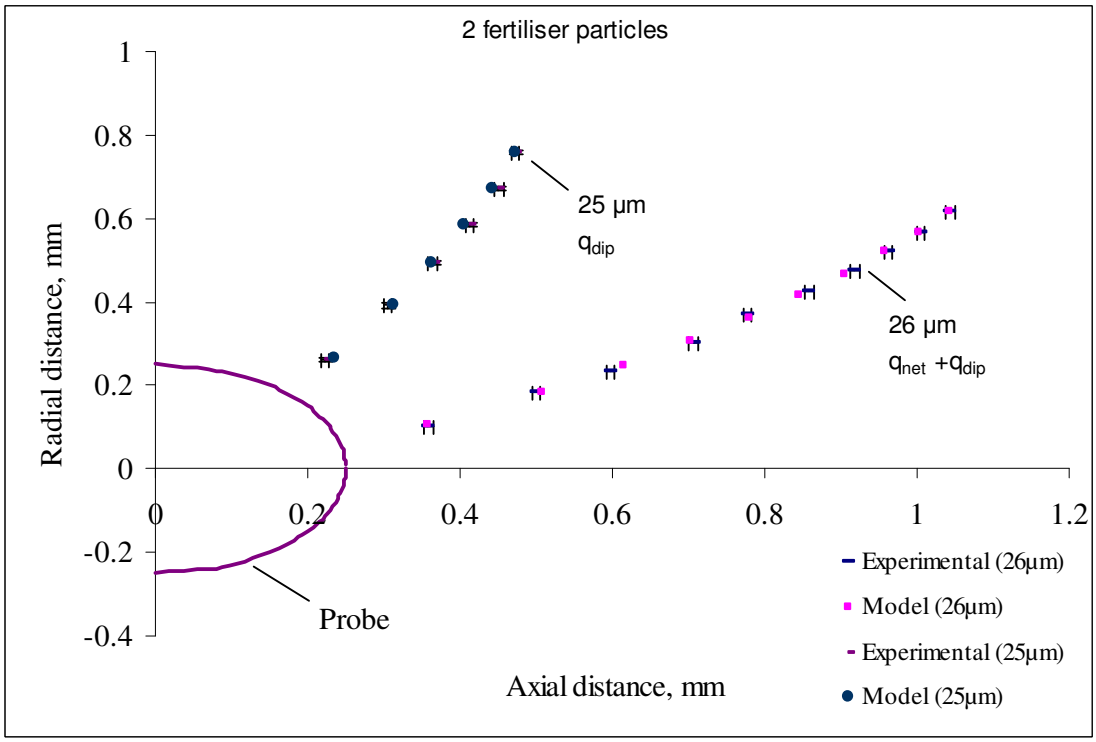

Figure 7.37: Experimental and predicted particle trajectories for a 26 µm fertiliser particle with probe voltage -6 kV with fitted net charge q_{net} = +2.4x10^{-15} C, dipolar charge q_{dip} = 1x10^{-14} C and a 25 µm fertiliser particle with probe voltage -6 kV with only fitted dipole charge q_{dip} = 1.45x10^{-14} C.

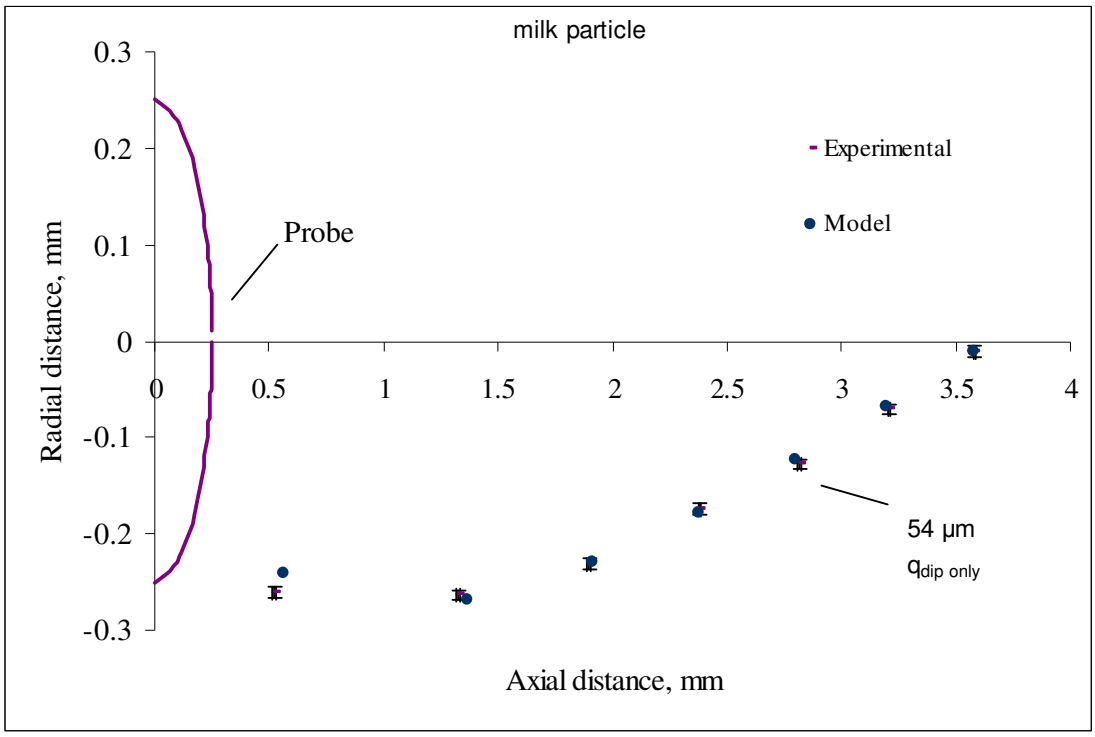

Figure 7.38: Experimental and predicted particle trajectories for a 54 µm milk particle with probe voltage +5 kV with only fitted dipolar charge $q_{dip} = 4.35 \times 10^{-12}$ C.

7.5 Distributions of Net Charge and Dipole

In this section the graphs present the number distribution of charge over the particles in the samples analysed. Different markers have been used to distinguish the polarity of probe voltage under which the particle was studied. Figure 7.39 presents the distribution of net charge with particle size for the acrylic sample. A part of the graph has been magnified in Figure 7.40 to show the distribution of charge among the low charged (within the range of $\pm 10^{-13}$ C) particles. The net charge distribution for the milk powder sample is given in Figure 7.41 and 7.42. Similarly Figures 7.43 and 7.44 shows the net charge distribution for the fertilizer sample. In the case of glass particles the graphs in Figure 7.45 shows the distribution of net charge. The central part of this distribution has again been magnified in Figure 7.46

.

Figure 7.47 presents the two directional distributions of monopole (net) charge and dipole charge for glass bubbles, with an enlargement shown in Figure 7.48. Figure 7.49 gives the distribution of dipole charge with particle size for the glass bubbles.

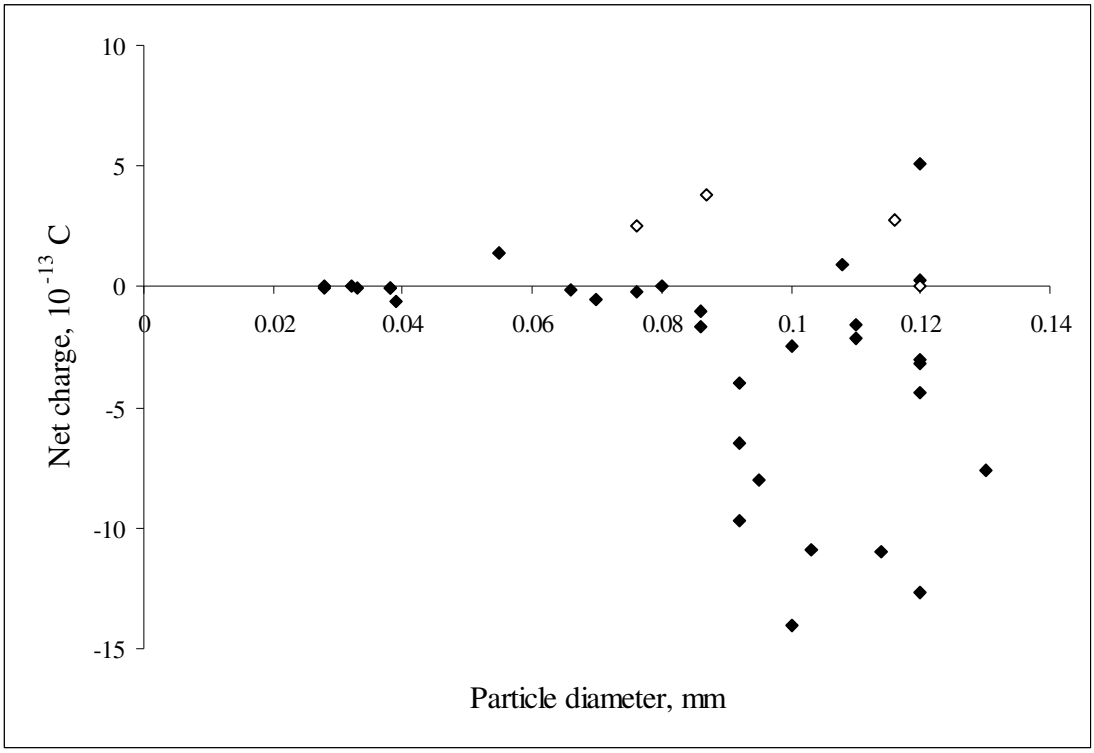

Figure 7.39: Distribution of net charge for acrylic particles – total sample of 42 particles. ♦, negative probe polarity; ◊, positive probe polarity.

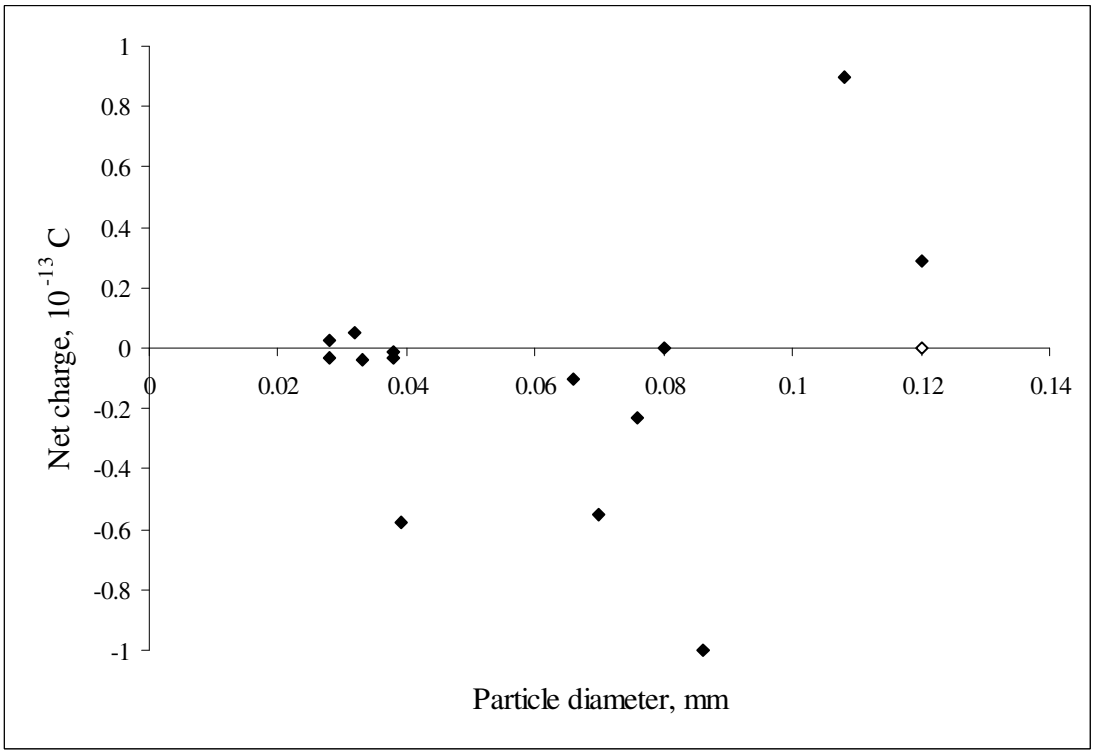

Figure 7.40: Distribution of net charge for acrylic particles – low charge part of sample in Figure 7.37. ♦, negative probe polarity; ◊, positive probe polarity.

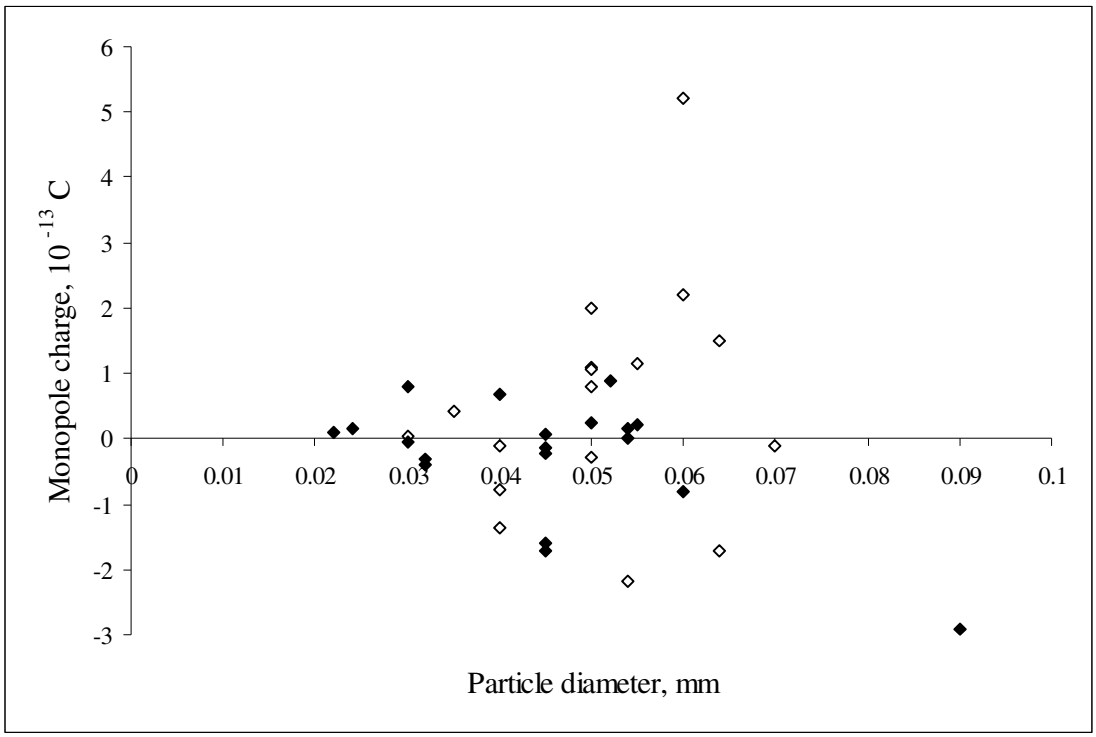

Figure 7.41: Distribution of net charge for milk particles – total sample of 37 particles. ♦, negative probe polarity; ◊, positive probe polarity.

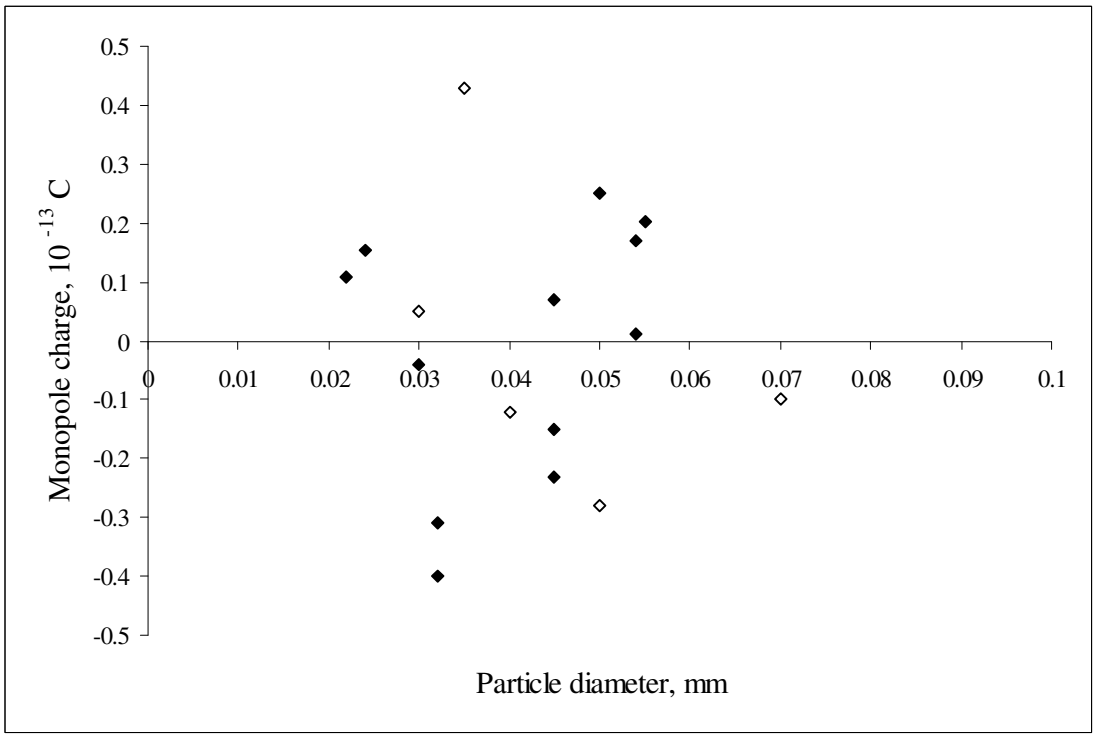

Figure 7.42: Distribution of net charge for milk particles – low charge part of sample in Figure 7.41. ♦, negative probe polarity; ◊, positive probe polarity.

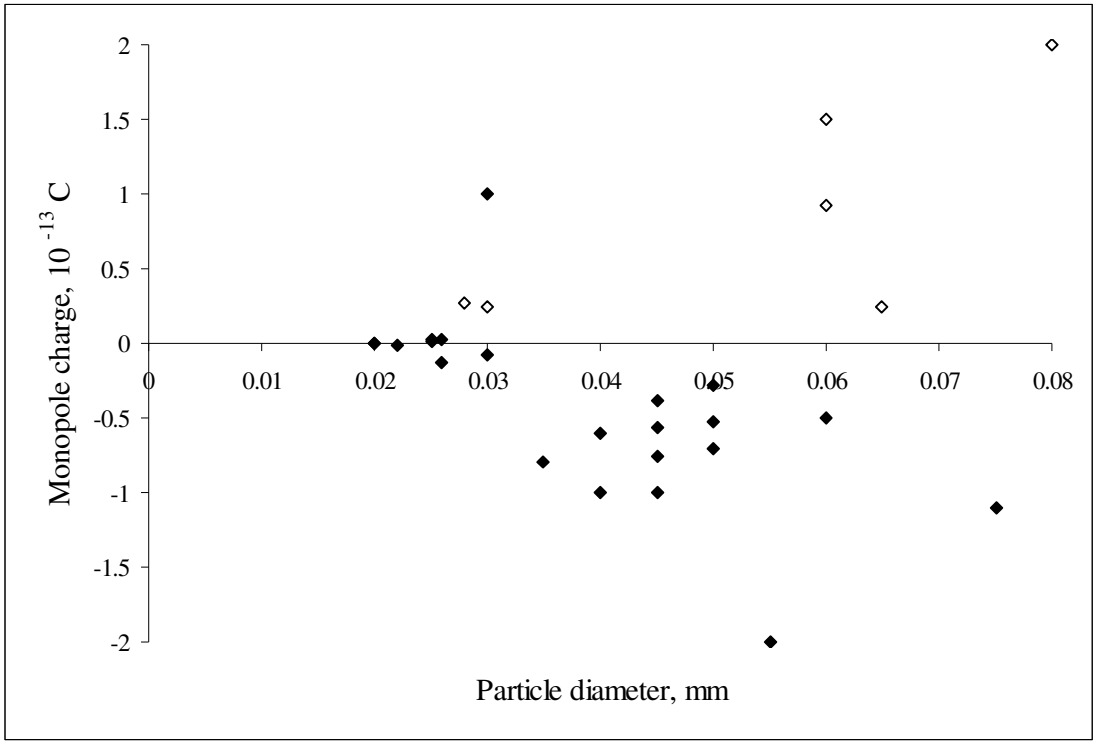

Figure 7.43: Distribution of net charge for fertiliser particles – total sample of 30 particles. ♦, negative probe polarity; ◊, positive probe polarity.

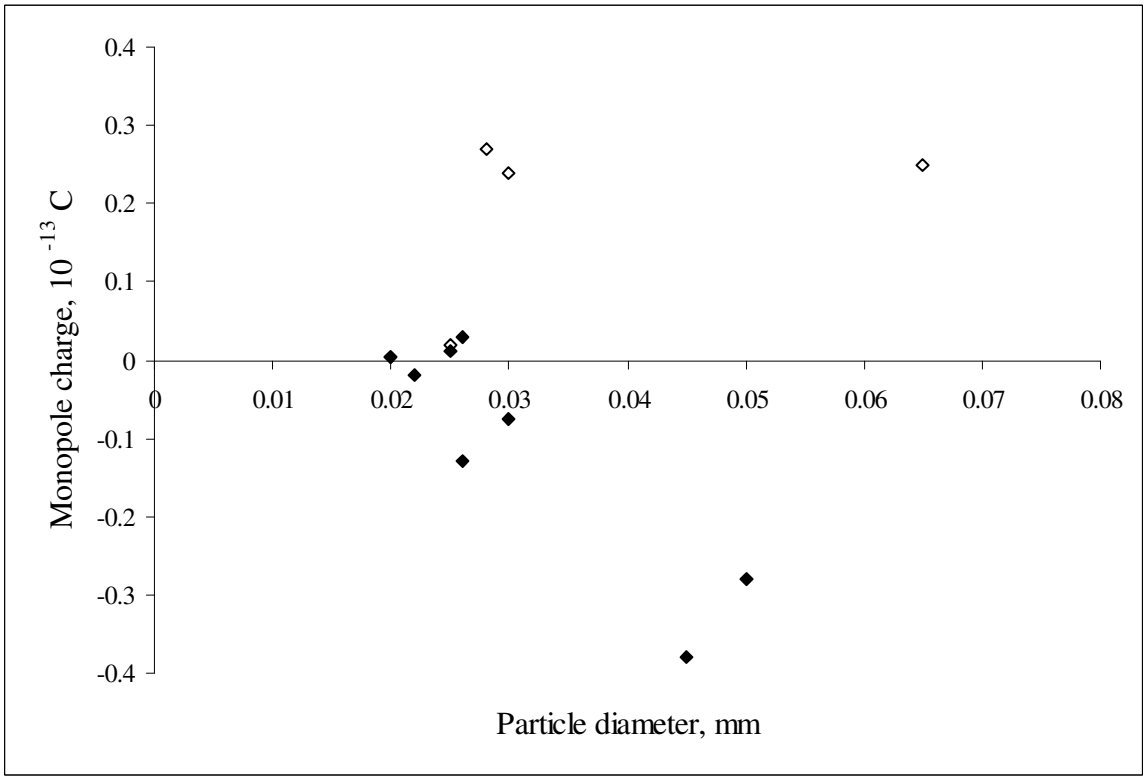

Figure 7.44: Distribution of net charge for fertiliser particles – low charge part of sample in Figure 7.43. ♦, negative probe polarity; ◊, positive probe polarity.

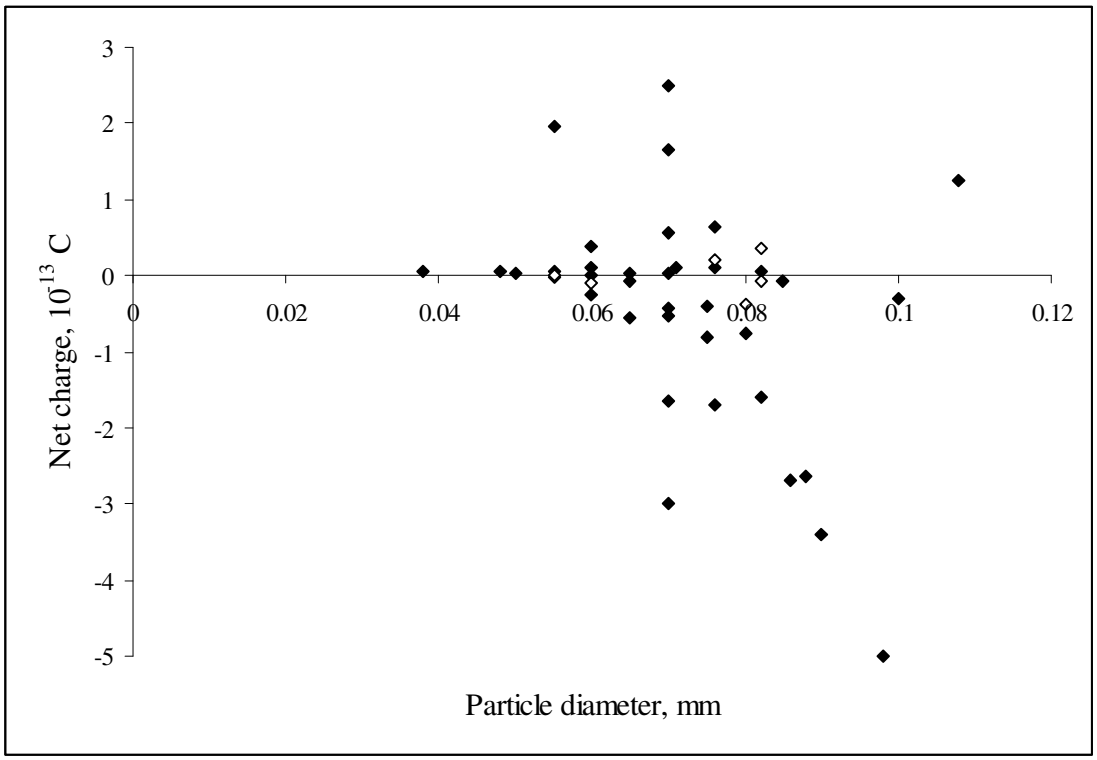

Figure 7.45: Distribution of net charge for glass bubble particles – total sample of 44 particles. ♦, negative probe polarity; ◊, positive probe polarity.

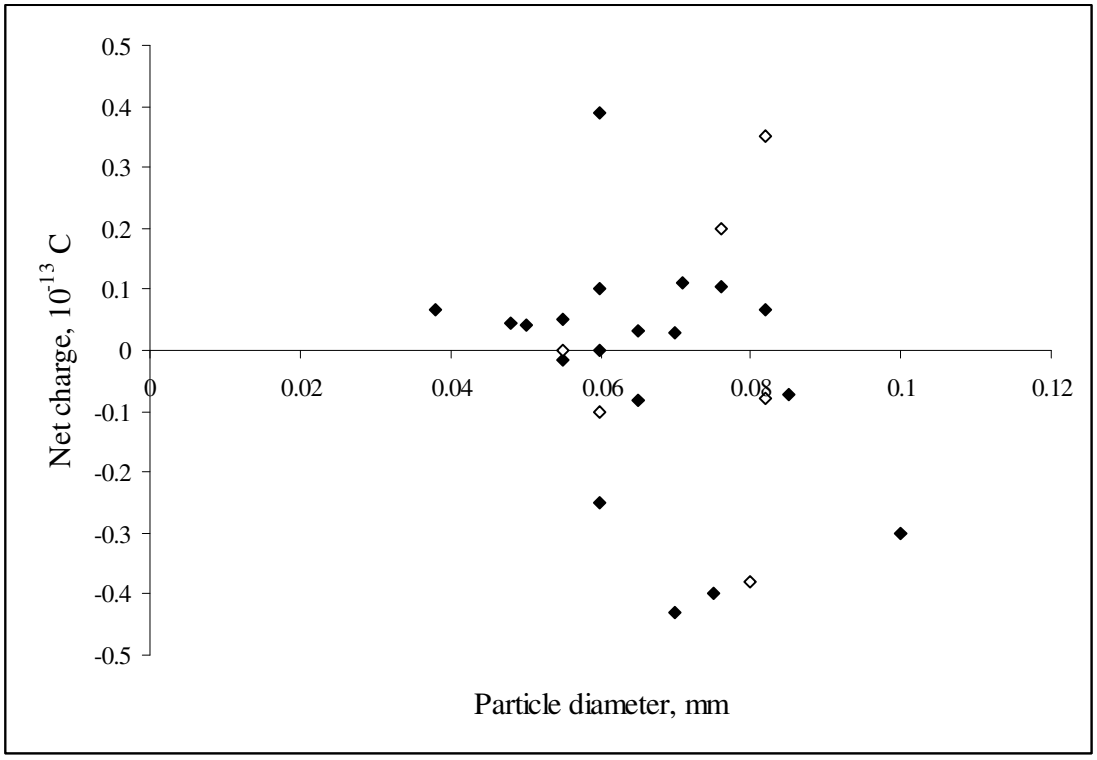

Figure 7.46: Distribution of net charge for glass bubble particles – low charge part of sample in Figure 7.39. ♦, negative probe polarity; ◊, positive probe polarity.

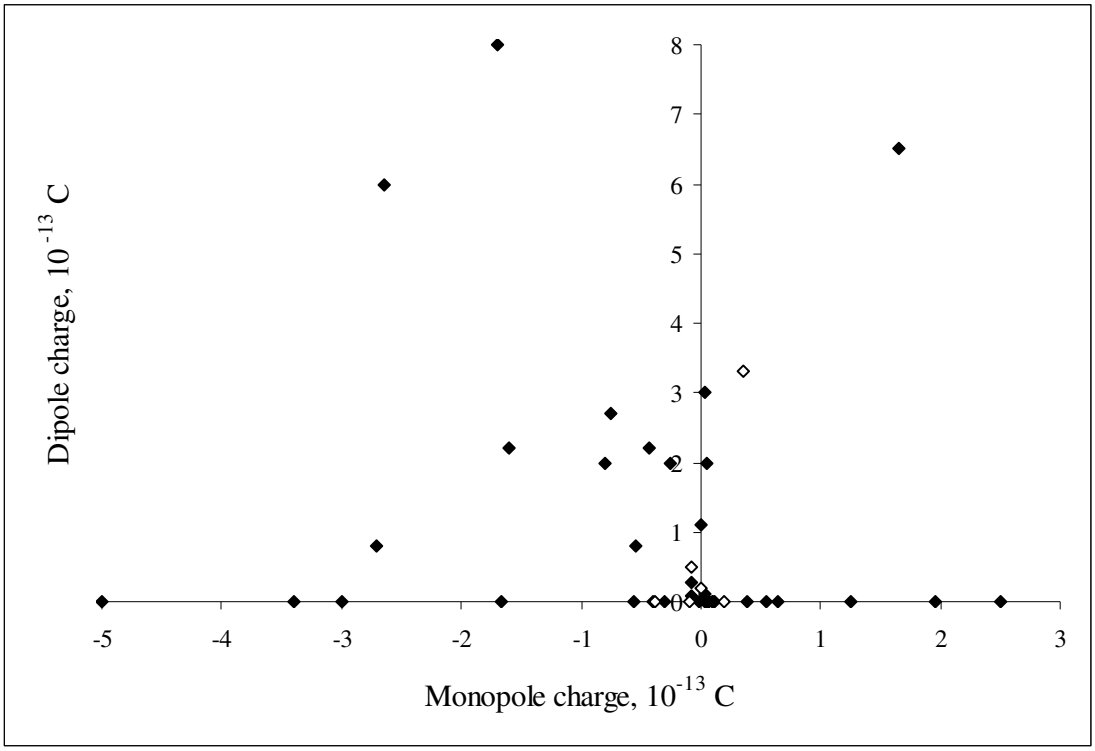

Figure 7.47: Distribution of monopole and dipole charge for glass bubbles – total sample of 44 particles. ♦, negative probe polarity; ◊, positive probe polarity.

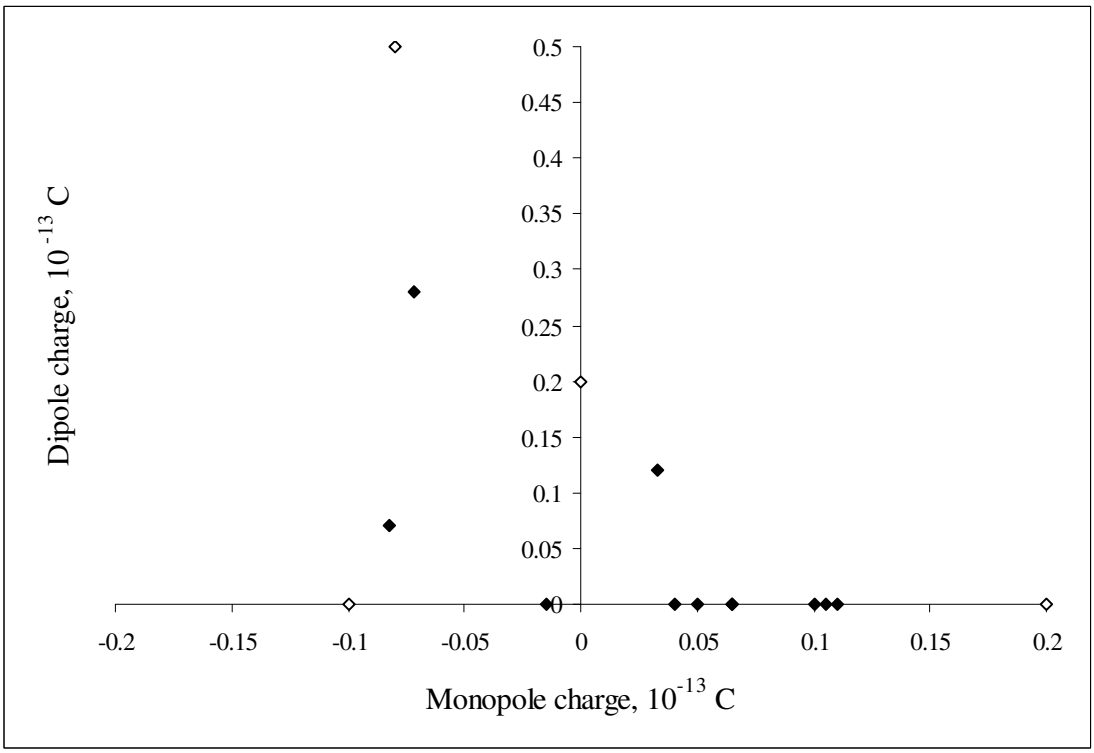

Figure 7.48: Distribution of monopole and dipole charge for glass bubble particles – low charge part of sample in Figure 7.39. ♦, negative probe polarity; ◊, positive probe polarity.

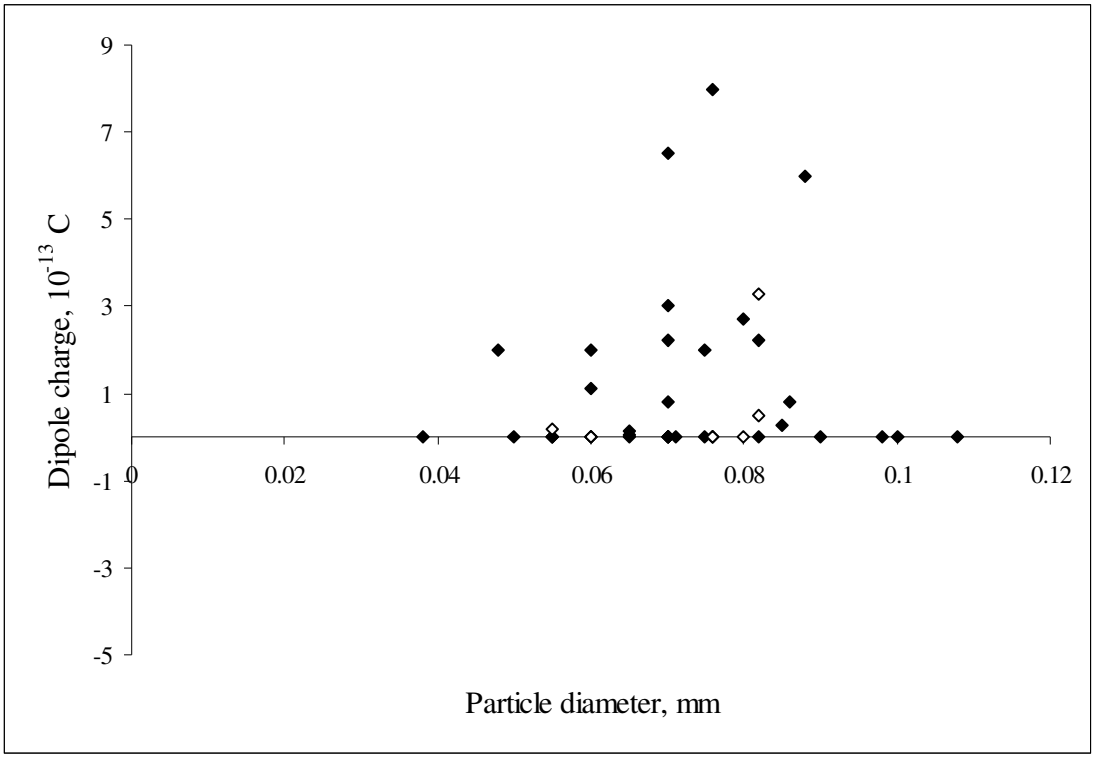

Figure 7.49: Distribution of dipole charge for glass bubble particles – total sample of 44 particles. ♦, negative probe polarity; ◊, positive probe polarity.

7.6 Obolensky Filter Results

This section presents the representative results from various experimental runs using the Obolensky filter to estimate an average charge on the particle samples. The brush feeder with the cylinder of 13.5 mm internal diameter was used to introduce the particle/air suspension inside the filter. Figure 7.49 and 50 present data for acrylic spheres giving the current recorded at regular time intervals during flow of sample through the filter. These experiments were conducted on acrylic spheres for both conditions, with (Figure 7.49) and without pre selector plates (Figure 7.50). Assuming an average current of 9 nA from Figure 7.49 the average charge on the particles is estimated to be $+2.53 \times 10^{-14}$ C. Similarly with an average current of 8.2 nA from Figure 7.50, after passing through the preselector plates, average charge on particles is estimated to be $+2.3 \times 10^{-14}$ C. This also proved useful to predict the effect of preselector plates on the mean charge. For calculation details please refer to Appendix A.6.

The mean charge on glass spheres was also estimated as they gave the most meaningful results indicating presence of dipoles. Figure 7.51 presents data for the glass spheres. Assuming an average current of -6 nA average charge on particles is estimated to be -1.2×10^{-14} C. For calculation details please refer to Appendix A.6.

7.7 Smoke Results

These runs were done with the normal flow of 0.24 L/s, through the normal nozzle (10 mm ID) in the normal position (220 mm upstream of the probe) without particles. The smoke wire was used with 10 ms of 0.8 A current. Figure 7.52 shows the smoke as it flowed past the tip of the probe. The probe tip has been outlined for clarity as smoke has made the image hazy. The change in direction of flow of gas is depicted by smoke flow in Figure 7.53 and 7.54. There was one other frame in between these two frames. The change in the smoke flow direction (from upward to downward direction) can be observed in the figures. The direction has been marked by drawing a line parallel to the flow whose length also indicates the distance travelled during that particular frame time.

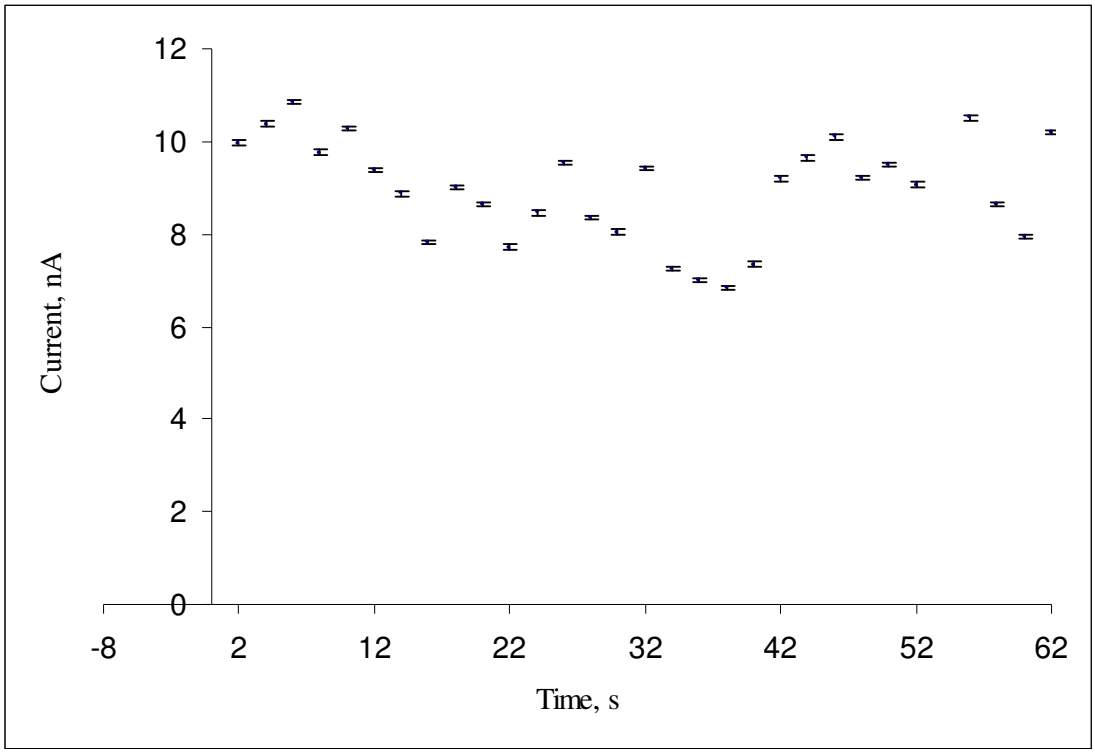

Figure 7.49: Current vs. time data for acrylic spheres without pre selector plates.

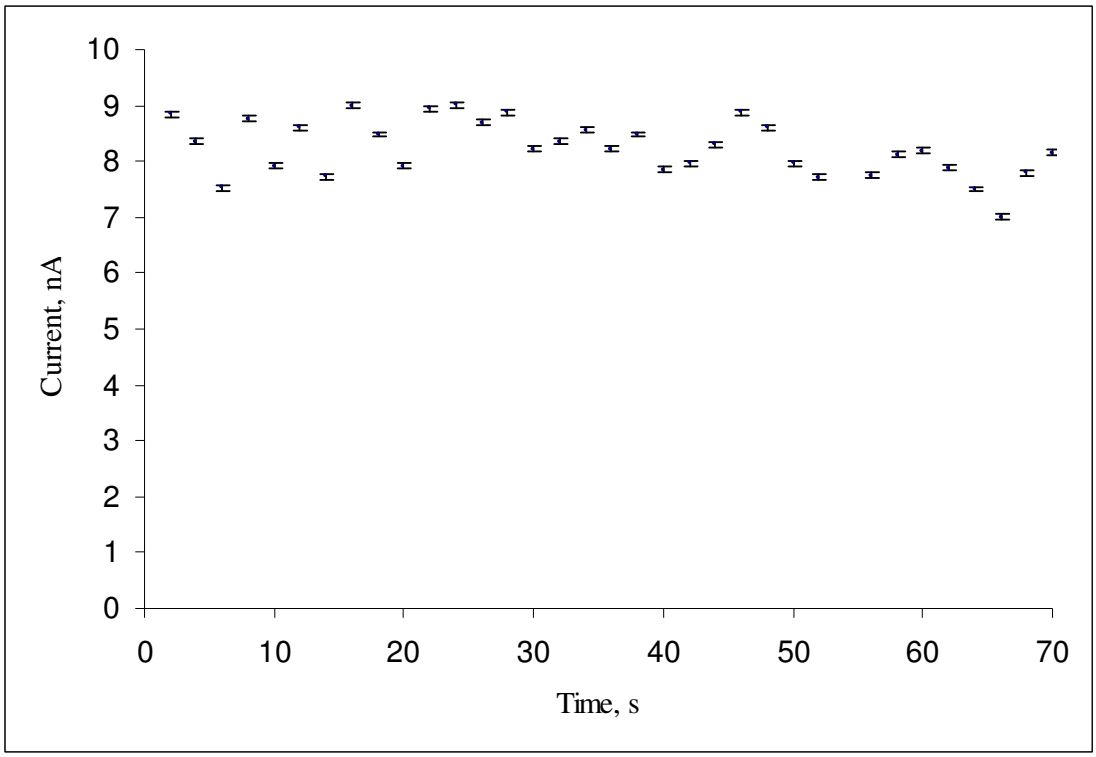

Figure 7.50: Current vs. time data for acrylic spheres with pre selector plates at 8 kV.

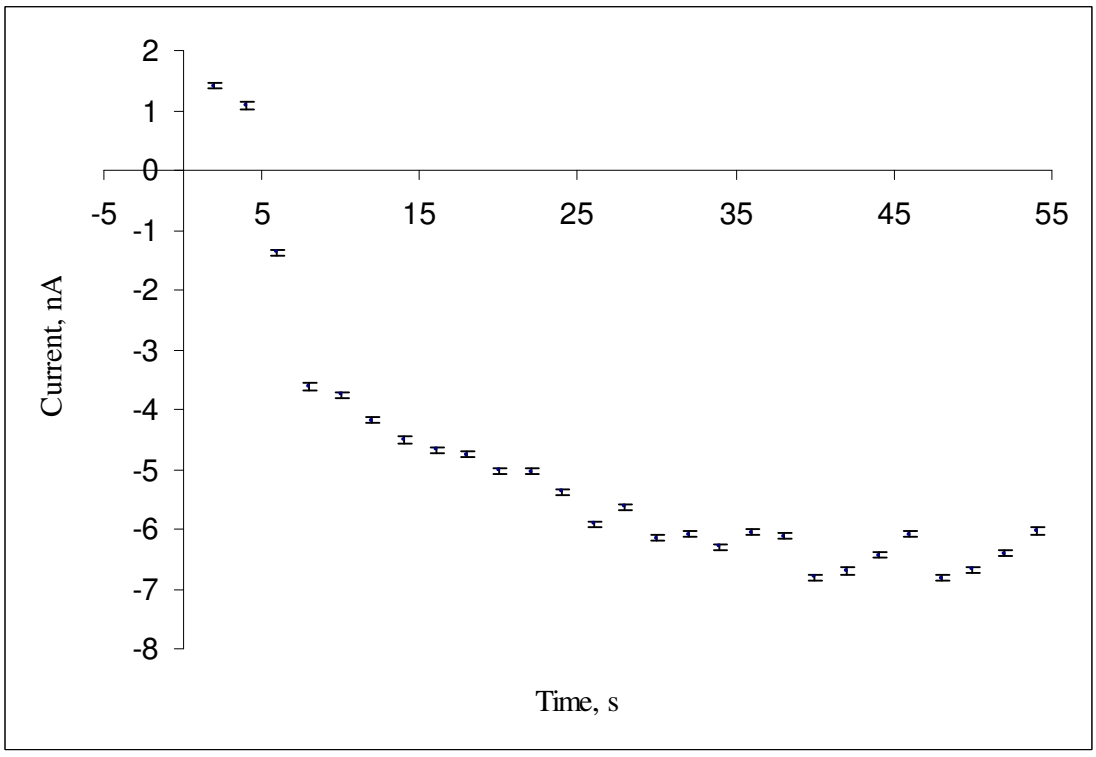

Figure 7.51: Current vs. time data for glass bubbles with pre selector plates at 8 kV.

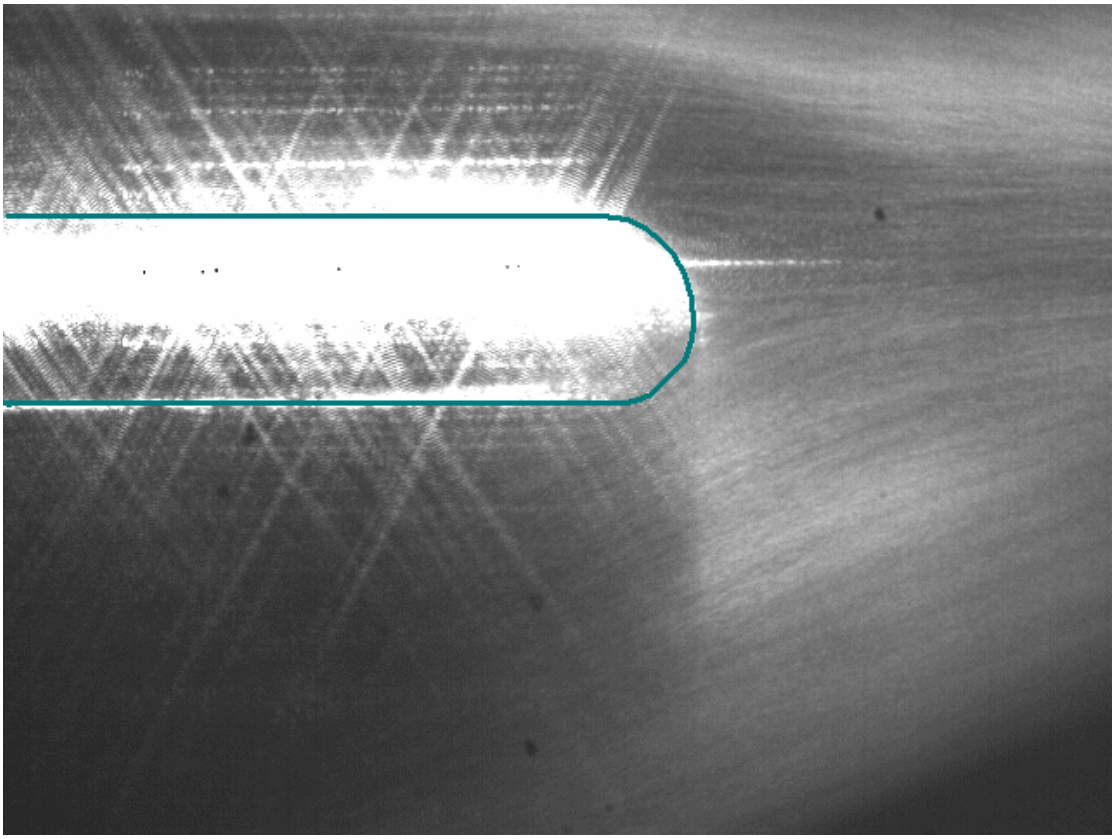

Figure 7.52: Smoke flow past the probe tip.

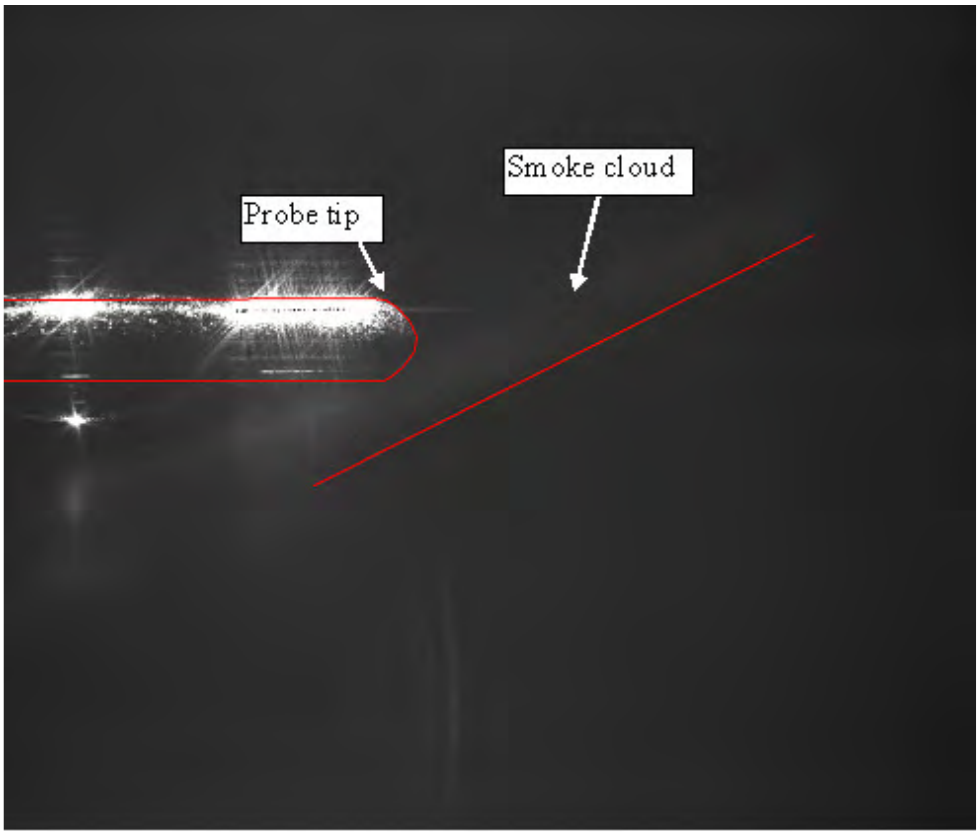

Figure 7.53: Smoke flow showing distance travelled by eddy on the frame (the length of the line plotted indicates the distance travelled during the frame time and also gives the direction of the flow).

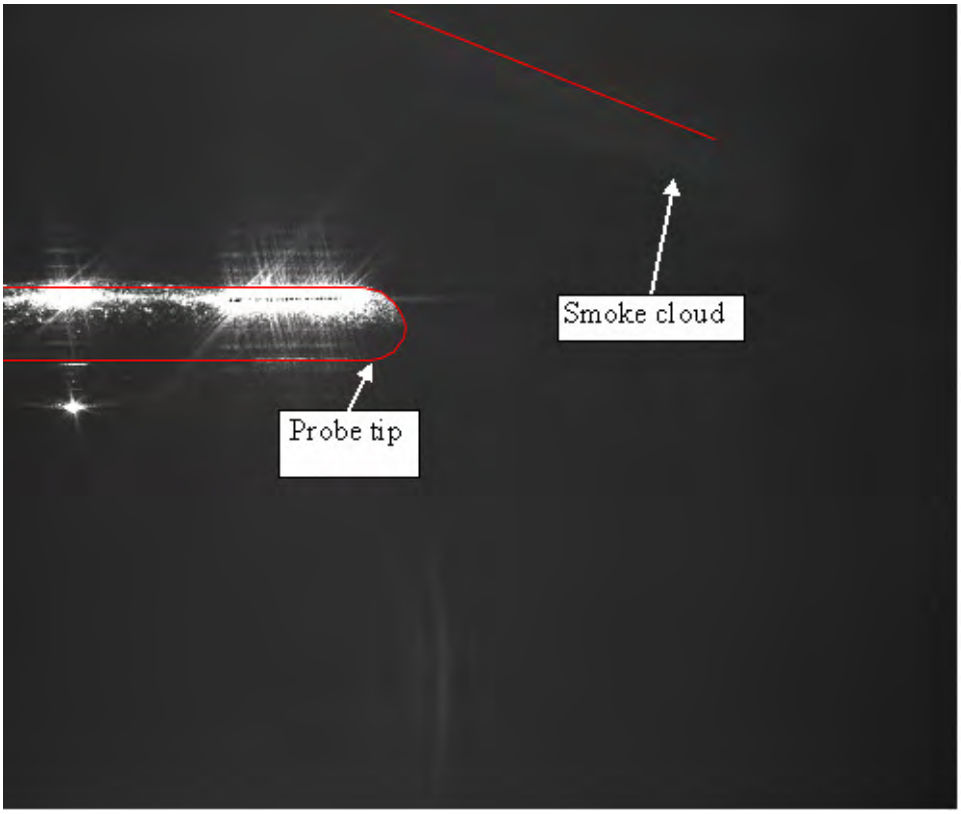

Figure 7.54: Smoke flow showing distance travelled by eddy on the frame (the length of the line plotted indicates the distance travelled during the frame time and also gives the direction of the flow).

8. Discussion

8.1 Effects of Experimental Errors and Assumptions on Net Charge and Dipole Fitting

8.1.1 Calculation Error

The position and diameter of acrylic spheres and glass bubbles was estimated from the images by tracing the upper and lower bright patches manually. For milk powder and fertiliser particles Sigma scan Pro was used to calculate the centre of mass (X and Y) for each particle position and its diameter. Both methods introduced errors in the calculated values which have been explained later in this section. Also both acrylic particles and glass bubbles were perfect spheres as can be seen from their SEM images (Figure 3.12 (a) and (b)) so there is probability of less error in the estimated diameters. There could be error in size approximation of the milk powder as it was difficult to distinguish between individual particles and small agglomerates (see Figure 3.12 (c)). For the analysis of milk particles the shape factor of a chosen area was checked by the software and only particles with shape factor close to one (which is for a circle) were analysed. Thus only spherical milk particles were analysed and reported. But the possibility of a uniform aggregate recognised as an individual particle cannot be completely ruled out. The fertiliser particles (Figure 3.12 (d)) were also not perfect spheres but rather had polygonal shapes (probably due to crystallisation).

8.1.1.1 Sigma Scan Pro Method - Applied to Milk and Fertiliser Particles

Centre of Mass

The centre of mass (CM) of a system of mass elements making a particle is defined as the average of their positions, r_i, weighted by their masses, m_i,

$$C.M. = \frac{\sum m_i r_i}{\sum m_i} \tag{8.1}$$

For a given particle the CM is a unique X, Y point that would serve to balance the particle in a body force field (e.g. gravity) on a pin point. In this study each position of the particle has been defined in a given trajectory by calculating its *CM*. The Sigma scan Pro analysis reports the centre of mass as CM_x and CM_y of the measured object in the horizontal and the vertical plane respectively. These coordinates are determined by weighting all pixels chosen for inclusion equally and then averaging the coordinates of each pixel in the object.

$$C.M._x = \frac{\sum_i x_i}{Area} = \frac{\sum_{i=0}^{N} x_i}{N} \tag{8.2}$$

$$C.M._y = \frac{\sum_i y_i}{Area} = \frac{\sum_{i=0}^{N} y_i}{N} \tag{8.3}$$

where the area is the area of the total number of *N* pixels present in the chosen surface. The sum of error squared for CM_x if all errors are independent

$$S_{CMx}^2 = \frac{S_i^2}{N} \tag{8.4}$$

Hence error in the centre of mass is given as

$$S_{CMx} = \frac{1}{\sqrt{N}} \tag{8.5}$$

8.1.1.2 Manual Method – Applied to Acrylic and Glass Particles

Initially from the selected light patches the topmost pixel of the top patch and the bottom-most pixel of the bottom patch were selected to define the extremes. Then the centre of the particle was calculated by averaging these two positions and the diameter was calculated by taking their difference. Let z_t and z_b be the top and bottom positions selected as shown in Figure 8.1 to calculate the centre of the particle and its diameter.

We have assumed $\delta z_t = \pm 1$ pixel and also $\delta z_b = \pm 1$ pixel. This assumption was made on the basis of fitting by eye by enlarging the image of a particle and then averaging the observed errors.

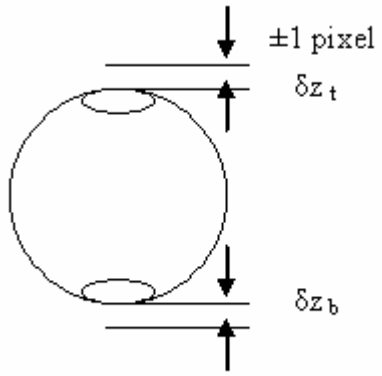

Figure 8.1: Error in selected top and bottom positions.

$$\bar{z} = \frac{z_t + z_b}{2} \tag{8.6}$$

$$\delta\bar{z}^2 = \delta z_t^2 \left(\frac{\partial \bar{z}}{\partial z_t}\right)^2 + \delta z_b^2 \left(\frac{\partial \bar{z}}{\partial z_b}\right)^2 = 2\delta_z^2 \left(\frac{1}{2}\right)^2 \tag{8.7}$$

$$\delta\bar{z} = \frac{\delta_z}{\sqrt{2}} \tag{8.8}$$

This is the error in the vertical position of the centre of the particle. The error in horizontal position of the particle may be more than this because the horizontal extremes of the particle are less clearly defined (the top and bottom reflections have rather sharp ends). For fitting purposes in this work 1 pixel was assumed for the error in both vertical and horizontal directions, but a more refined error estimate is possible.

8.1.1.3 Better Estimation of Image Errors

A simple way to approach the error of particle position and diameter is to first approximate each reflected "blob" as a rectangular patch located at the top and bottom of the particle, with the vertical dimension as shown in Figure 8.2. This figure shows the perimeter points defining the horizontal top and bottom edges with the error of each perimeter pixel again ±1 pixel.

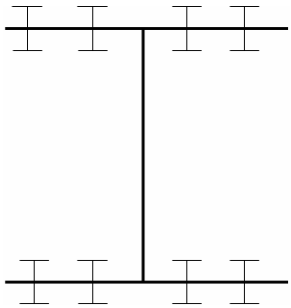

Figure 8.2: Error in position of top and bottom edges.

If there are n pixels along each edge, and the average vertical position of each is taken, then the error in the vertical position of each edge is 1 / √n pixels, and thus the error in the position of the centre of the particle, from equation 8.8, becomes

$$\delta_{\bar{z}} = \frac{\delta_z}{\sqrt{2}} = \frac{1}{\sqrt{n}\sqrt{2}} \tag{8.9}$$

So the fractional error in diameter will be

$$\frac{\Delta D}{D} = \frac{2}{n\sqrt{n}} = \frac{2}{n^{3/2}} \tag{8.10}$$

and the fractional error in area based on diameter will be

$$\frac{\Delta A}{A} = \frac{2\Delta D}{D} \tag{8.11}$$

Substituting from equation 8.10,

$$\frac{\Delta A}{A} = \frac{4}{n^{3/2}} \tag{8.12}$$

However, each (rectangular) blob has a small number of pixels vertically (say, n_v) than horizontally (n_h), so that the error in the horizontal centre position will be larger than the error vertically from equation 8.9, because n_v is smaller than n_h. If we want to go further in precision, a circle or some other curve can be fitted to the perimeter pixels with an error of 1 pixel for each point along its perimeter as shown in Figure 8.3 and then the error in the vertical position or even the diameter can be estimated. This will give a larger numerical error than the error from fitting a simple square body, but the error is likely to be more accurate.

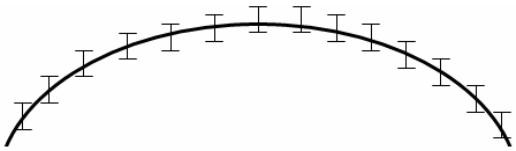

Figure 8.3: Fitting a circle to perimeter pixels of a round particle.

The errors estimated by these more refined methods can be applied by completely automated calculation methods from the images, but generally will give smaller values than the plus/minus 1 pixel assumed in this work. Thus our approach has been conservative.

8.1.2 Trajectory Fitting Error

When the assumed value of net charge was varied to extremes so that the fit drawn around each particle position just remained within the experimental errors (a sensitivity analysis) the variation corresponded to a maximum of 10% (see Figures 7.2 to Figure 7.9). The percentage error remained below 10% while the absolute error varied for different particles. Generally the absolute error increased for highly charged particles and also for larger diameter particles. In a similar analysis the fitting error for dipole charge also remained below 10%.

To check the effect of the assumption of a constant approach angle of the gas on the predicted charge values, the assumed approach angle in the theoretical analysis was varied and the predicted trajectories were compared with the best fit trajectory (Figure 7.10 to Figure 7.13). It can be observed from Figure 7.10, 7.12 and 7.13 that with large variation (~ ± 20°) in approach angle of the gas; the predicted trajectories remain within the experimental errors. Only for a few trajectories (Figure 7.11) this magnitude of angle variation resulted in trajectories exceeding the error limits.

The effect of variation in particle size was also checked for a few trajectories. For the case of a 65 μm diameter glass particle with best fitted value of q_{net} = -5.6x10^{-14} C (shown in Figure 7.19), assuming a smaller size of particle with diameter of 60 μm the fitted charge q_{net} = -4.3x10^{-14} C (- 23%) and a larger size with diameter 70 μm the fitted charge q_{net} = -6.8x10^{-14} C (+21%). Similarly in the case of a 22 μm milk particle

with fitted charge $q_{net} = 1.1x10^{-14}$ C assuming a smaller size of particle with diameter of 20 μm the fitted charge $q_{net} = 0.88x10^{-14}$ C (-20%) and a larger size with diameter 25 μm the fitted charge $q_{net} = 1.25x10^{-14}$ C (+14%). From these results it can be concluded that a variation of ± 5 μm in the diameter leads to a maximum of ~25% change in the fitted net charge for a particle.

The outcome of density change was also compared for a few trajectories particularly for the case of glass bubbles. The apparent particle density of the glass bubbles given by the manufacturer was 150 kg/m^3. This was undoubtedly a mean value over the distribution of particle sizes. With this value of density the trajectory of an 80 μm glass bubble was fitted with a net charge $q_{net} = -7.5x10^{-14}$ C and dipole charge $q_{dip} = 2.7x10^{-13}$ C (see Figure 7.23). For the same particle with density 200 kg/m^3 the fitted net charge was $q_{net} = -8.88x10^{-14}$ C and dipole charge $q_{dip} = 3.08x10^{-13}$ C. A variation of 15% in both net charge and dipole could be observed with a 33% increase in density.

8.1.3 AC Voltage Supply

It was also observed that the square waveform (Figure 3.8) was not a perfect square. The waveform initially rose to the applied voltage stated in the results and used in the calculations, but did not maintain the peak and declined to about 40% of that before the polarity change took place. The voltage could be considered constant during a single frame period which was 1/6th of the peak of a waveform but to know what the probe voltage was for each frame was a generally unresolved complicating factor as it was difficult to match up the frame position relative to the ac waveform. In the analysis the peak voltage was always used for calculating fields. Overall this is expected to have resulted in an underestimation of the net charge and the dipole charge as for a too high assumed value of voltage, too low values of charge will be fitted to explain the observed path.

8.1.4 Gravitational Force

The gravitational force was neglected in the calculations owing to low density and the small size of particles. The largest particle diameter in all the samples was 130 μm

which was for an acrylic particle. All other samples had particles with a maximum diameter close to 100 μm. To estimate the maximum discrepancy caused by neglecting gravity, the trajectory of the largest diameter particle was reanalysed including gravity. It was realised that the gravitational force experienced by the largest acrylic particle was in the range of drag and electrical forces. Even so it can be seen that there is little influence on the predicted trajectory. By including gravity for the 130 μm acrylic particle (analysed in Figure 7.14 and reanalysed in Figure 8.4) there is a slightly better fit for the last points of the trajectory within experimental errors. Without gravitational force the fit reached the extreme ends of the error bars but by including gravity the fitted positions better matched the experimental positions. There was no change in the value of the fitted net charge as the trajectory remained within the experimental error limits.

For glass bubbles the apparent density was too low to realise a significant effect of gravity. The milk powder and fertiliser particle densities were close to those of the acrylic particles and they were smaller in size. After considering the extreme effect of gravity on the largest acrylic particle it could be safely assumed that gravity had negligible effect on all the particle trajectories.

8.1.5 Probe Tip

The probe tip was examined under a microscope with 10X zoom in order to check the roundness of the tip and to estimate surface roughness. This roughness was used to define the minimum distance between the nearest dipole charge on the particle and the surface in the modelling (particularly to calculate image forces due to dipole charges). This minimum distance was that of the particle when it was sitting on the probe surface (equation 4.35). Figure 8.5 shows a closer view of the surface of the probe under the microscope with 5X zoom and with the focus on the surface. It is apparent that the tip was smoother than the shank of the probe. By looking at the round tip profile in the figure the roughness was approximated to be 5 pixels, so calculating from the scale in Figure 3.4 (b) the roughness was close to 10 μm. For calculation purposes 10 μm was the minimum distance assumed between the charge on the end of a dipole on a particle touching the probe surface and the probe tip surface itself.

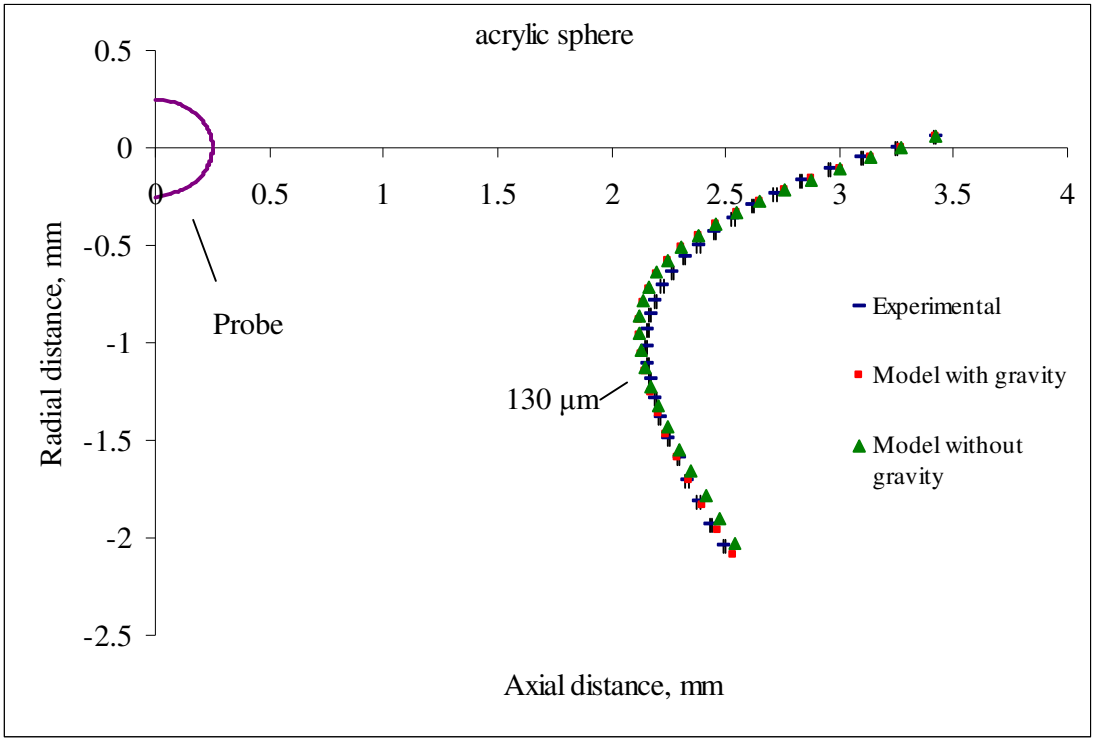

Figure 8.4: Experimental and predicted particle trajectories for a 130 µm acrylic particle with probe voltage -18 kV with fitted net charge q_{net} = -7.6x10^{-13} C with and without the effect of gravity.

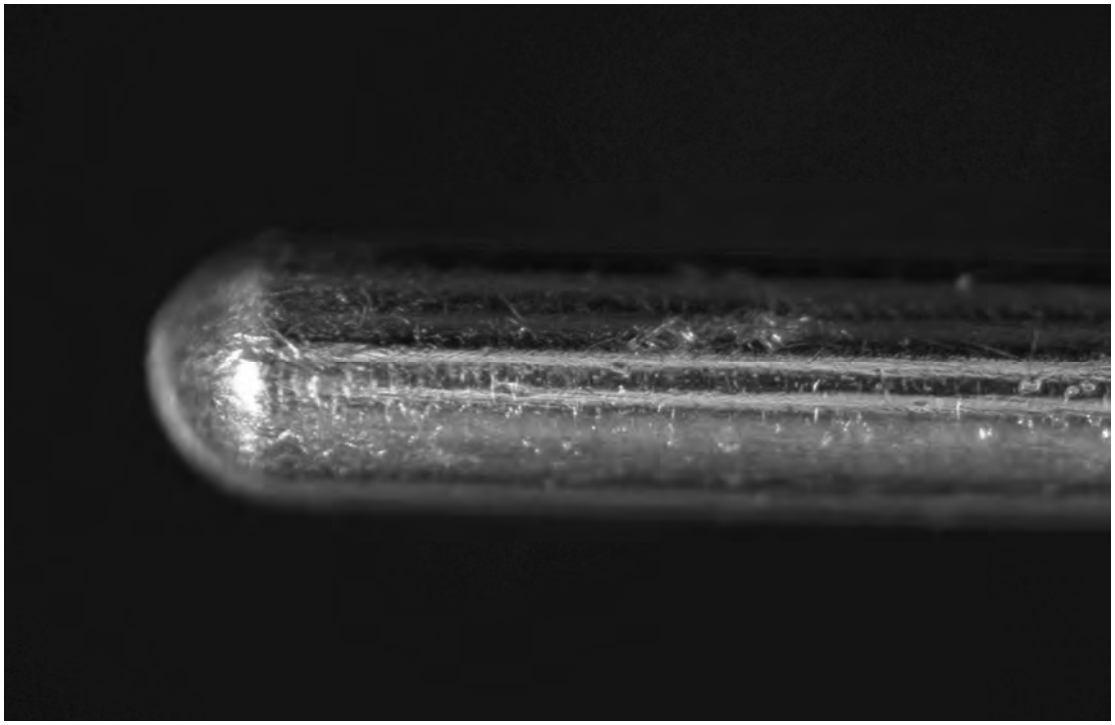

Figure 8.5: Probe tip as seen under the microscope.

8.1.6 Thickness of the Glass Bubble Shells

The mass of a hollow particle is decided by its wall thickness. The major effect of this in this study is on the effective particle density, reflecting on the inertia of the particle, influencing its trajectory. This aspect has been touched on earlier. The second effect is on the induced dipole force experienced by a particle as it closely approaches the probe. The shell thickness is used to calculate the multiplication factor U (Section 4.4.3) for estimating the induced dipole force. The thickness of the glass shells was estimated to be about 2% of the radius on the basis of their specified apparent particle density (Section 4.4.3.1).

Later to cross-check the given value, FESEM (Field emission scanning electron microscopy) of crushed glass bubbles was performed. Sticky carbon tape was fixed onto a clean FESEM stage and then crushed particles were pasted on the top of the carbon tape. The particles were gold coated and the standard procedures were followed to capture images using the FESEM. The thickness and radius of individual particles were then measured from images as shown in Figure 8.6(a). It was realised that from the given apparent particle density (150 kg/m^3), the predicted thickness for a particle of diameter 13 μm would have been 0.12 μm but experimentally it was measured to be 0.24 μm. Hence in our model the thickness assumed for this small particle was less than (approximately half) the observed thickness. The thicknesses of a few more particles were measured from SEM images. A comparison of the observed thickness from SEM images and assumed thickness values is shown in Figure 8.6 (b). It can be seen that for some cases the thickness of particle was the same as the assumed value and there were cases when the assumed thickness was greater than the observed value.

The value of U in the model was calculated to be 0.0195 (with a thickness 2% of the mean glass bubble radius) whereas according to the experimental thickness of the 13 μm particle (Figure 8.6 (a)) U should be around 0.0355 for this particle. Different values of U (according to the measured thickness for a given diameter) were used to reanalyse a few glass bubble trajectories, e.g., for the particle shown in Figure 7.23 the fit remained within experimental error limits with the new values of U.

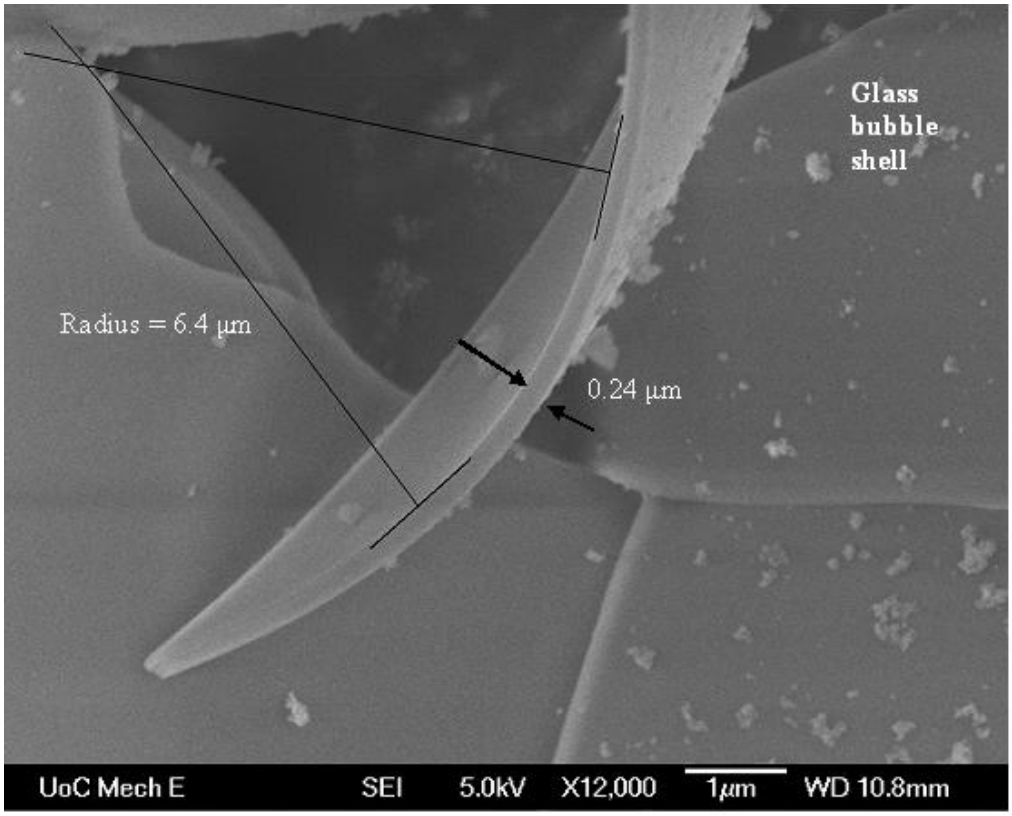

(a)

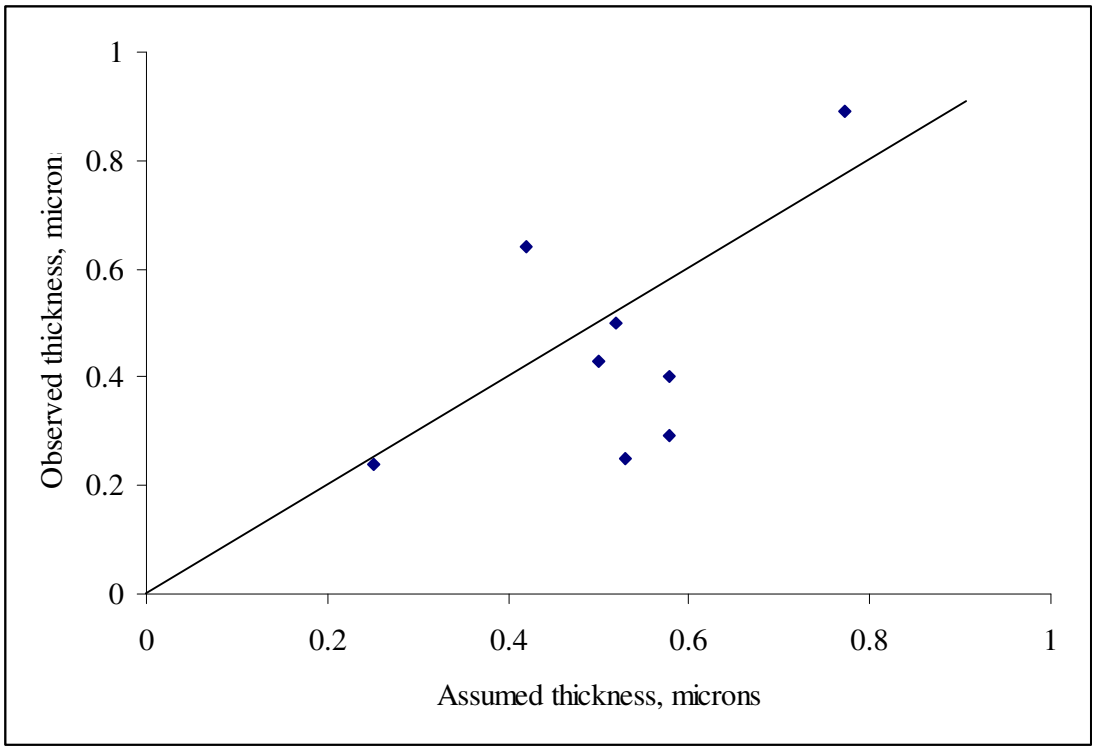

(b)

Figure 8.6: (a) Measurement of the thickness and radius of a glass bubble from its broken part (b) A comparison of the observed thickness from SEM images and assumed thickness values of glass bubbles.

A 2% reduction in fitted dipole charge for this trajectory led to a fit close to the previous fit using the assumed shell thickness. Hence it was concluded that the error introduced via induced dipole force due to assumed shell thickness can be ignored.

8.2 Assumptions made for the Modelling

8.2.1 Gas Flow Assumptions

8.2.1.1 Constant Approach Angle

A smoke study (at a nozzle exit velocity of 3 m/s) was performed to show the gas flow in the front of the probe tip photographs of the smoke streak-lines are shown in Figures 7.53 and 7.54. A measure of the eddy size of the turbulence was made by calculating the diameter of an eddy which could explain the observed velocity fluctuations. A sketch of an eddy passing in front of the probe tip is shown in Figure 8.7. If the gas approaches the probe tip at a constant velocity $\tilde{u}$ and $\tilde{v}$ is the tangential eddy velocity at its outer radius then the resultant velocity is given by the vector sum $\tilde{U}$.

The time taken by the eddy to travel a distance from point 1 to point 2 can be calculated from the number of adjacent frames over which the direction of gas flow changes from downward to upward as shown in Figure 7.53 and 7.54. From such a sequence of images U_1, U_2, θ_1 and θ_2 can be measured which correspond to the motion of the eddy passing through the field of view from its one end to the other. These values can then be used to calculate u and v. The distance travelled by the eddy is then given by

$$d = u\,t \tag{8.13}$$

where t is the period between the nearest frames showing extreme angles (gas direction from downward to upward). This is also the diameter of the eddy.

The distance travelled by the smoke on Figure 7.53 is 3.7 mm and time spent on each frame is 5.05 ms (at a video rate of 45 frames/s). The direction of flow makes an angle of 26.8° with the horizontal axis. From this information the axial velocity was

calculated to be 0.66 m/s with an eddy velocity of 0.33 m/s. The frame following that shown in Figure 7.53 gave an almost horizontal smoke streak.

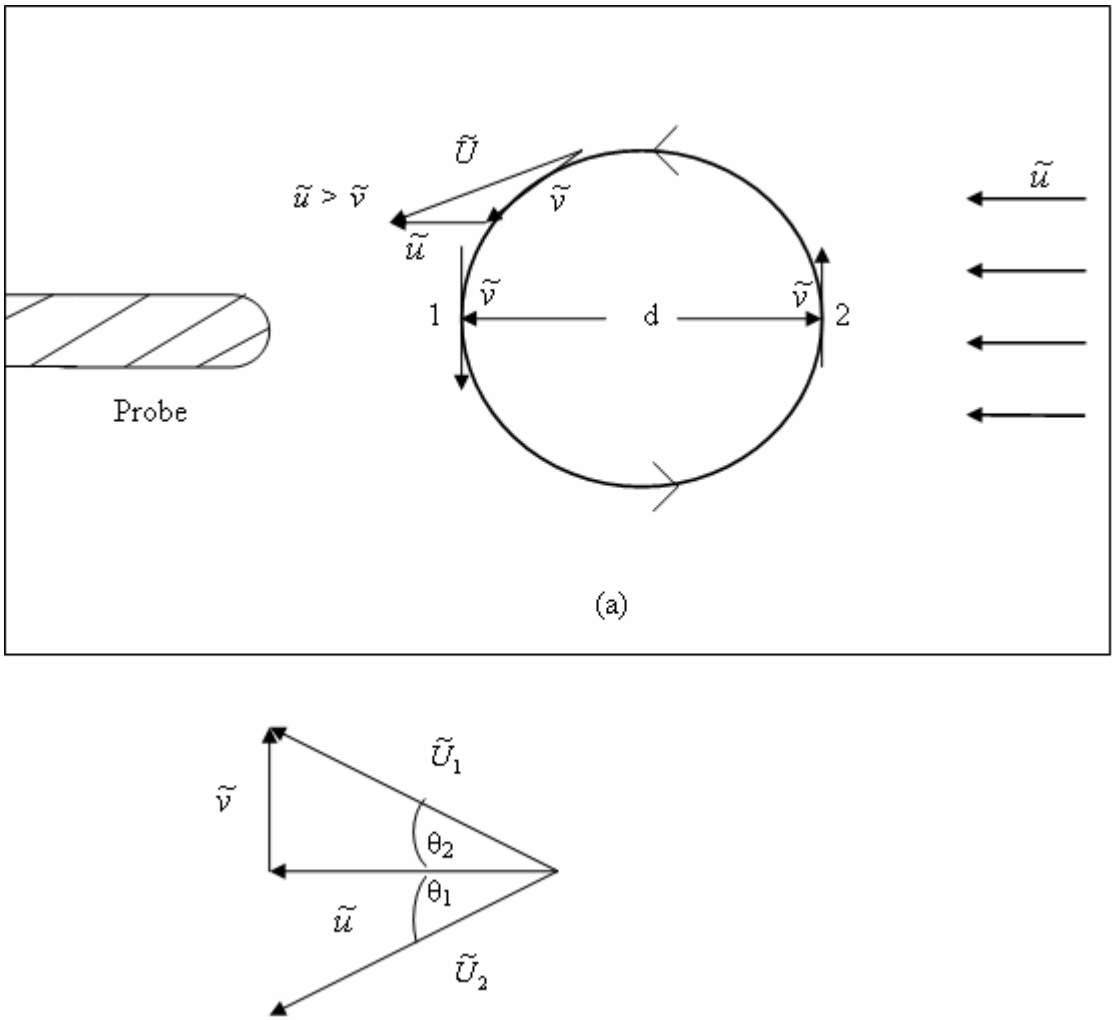

Figure 8.7: (a) The sketch of an eddy in the front of probe along with the resultant velocities (b) vector diagram of extreme $\tilde{u}$ directions.

The frame after this showed a direction of flow towards the other extreme (see Figure 7.54). Doing the same analysis on this smoke streak gave similar velocities (axial velocity 0.64 m/s, eddy velocity 0.25 m/s). As argued above, the distance travelled by the eddy between these two extreme directions based on the average axial velocity and time taken for two frames (10.1 ms) resulted in an eddy diameter of ~7 mm. The field of view covered by these smoke experiments was roughly 4 mm in front of the probe tip, being the major region of concern for trajectory analysis.

Information on the turbulence was also gathered from initial particle velocities (before the particles were affected by the probe field). These experiments were also done in the plume of the 3 m/s jet. For the flow of particles, a sequence as shown in Figure 8.8 (a), (b) and (c) is likely when the flow is as per the smoke analysis. The flow direction when the vortex is influencing a particle at position 1 (Figure 8.7) is depicted in Figure 8.8 (a) and when influencing a particle at position 2 (Figure 8.7) is depicted in Figure 8.8 (c). Trajectories within the experimental view span (3 or 4 mm) are easily within the high energy eddy size calculated from the smoke analysis. They are thus expected to have only a slowly changing gas velocity, supporting the assumption made that it is constant over the length of a trajectory.

Particle approach angle was measured for 50 consecutive frames and the variation in angle is shown in Figure 8.9. To measure the eddy diameter as explained in the smoke analysis, two frames with particle approach angles at extreme values close together in time were chosen, e.g., frame 21 with approach angle -16° and frame 26 with approach angle 20°. The axial velocity was averaged to be 0.8 m/s and eddy velocity to be 0.28 m/s from these two frames. The eddy size was calculated using the time in between the two extreme angles and it came out to be 8 mm. This appears to be the smallest eddy from the Figure 8.9 trace, as it corresponds to the most rapid change, and confirms the smoke study eddy size.

8.2.1.2 Turbulence in the Jet

In the study of a jet by Wygnanski and Fiedler (1969) the Reynolds number based on nozzle diameter was of the order of 10^5 and for the present study it was 2000. So the turbulence in the jet flow was expected to be less developed for the present study compared to that for Wygnanski's study. Nevertheless their plots of fluctuating and mean velocities in dimensionless form will be used to gauge the effect of turbulence in our system. In our present experimental setup the ratio of the distance of the probe along the length of the jet to the diameter of the nozzle (x/d) was about 20. Using this value of x/d, reading from Figure 3 in Wygnanski (1969), the ratio of the mean centreline velocity, $U_{m,}$ to the nozzle velocity U_o was

$$\frac{\overline{U}_m}{U_o} = \frac{1}{3} \tag{8.14}$$

For most of the runs of our study, the nozzle velocity was close to 3 m/s. Hence the maximum velocity at the probe is expected to be 1 m/s.

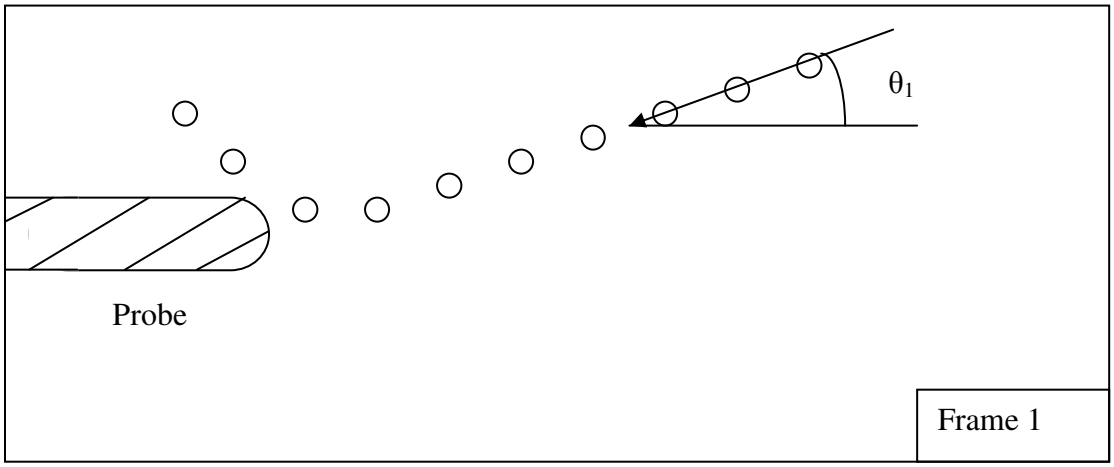

(a)

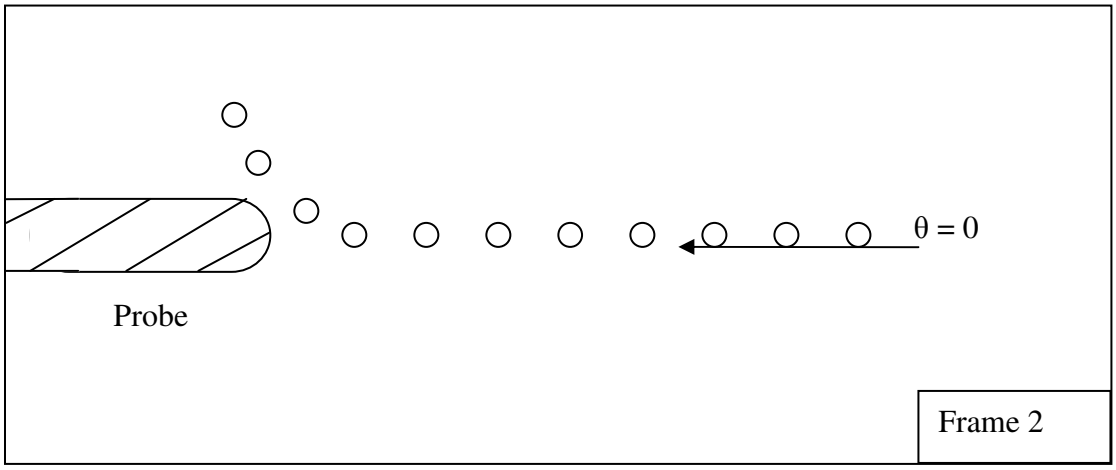

(b)

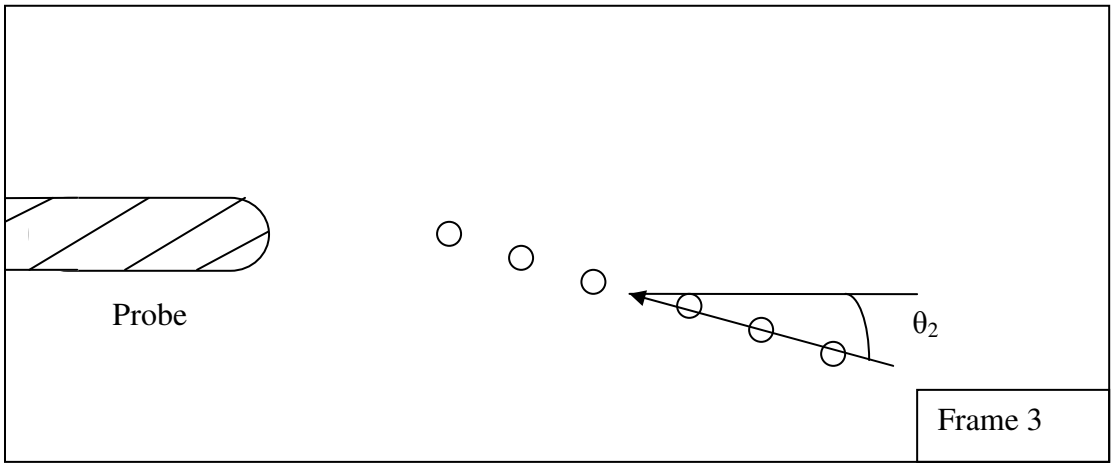

(c)

Figure 8.8: The change in direction of gas velocity on three consecutive frames at constant time interval.

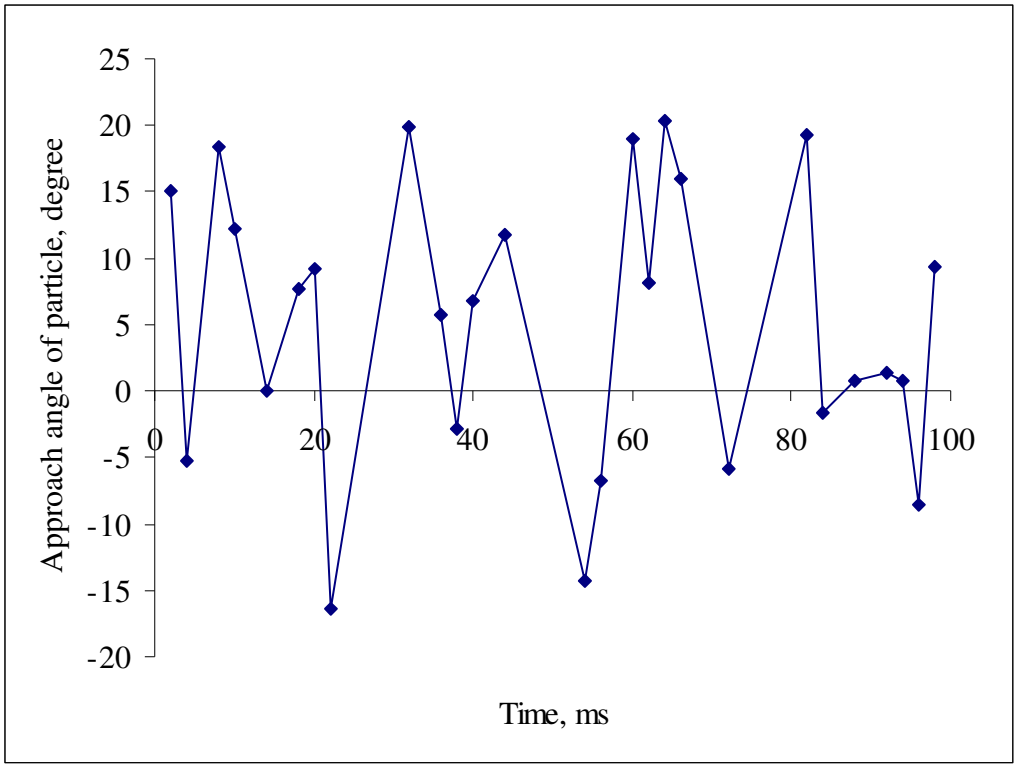

Figure 8.9: Variation in particle approach angle for 50 consecutive frames for the case of glass bubbles at 6 kV probe voltage.

Also from the same plot the variation in turbulent intensities along the jet centreline was calculated as

$$\frac{\sqrt{\overline{u'^2}}}{\overline{U}_m} = 0.175 \text{ , (axial, x-direction)} \tag{8.15}$$

$$\frac{\sqrt{\overline{v'^2}}}{\overline{U}_m} = 0.18 \text{ , (radial, y-direction)} \tag{8.16}$$

$$\frac{\sqrt{\overline{w'^2}}}{\overline{U}_m} \cong 0.26 \text{, (z-direction)} \tag{8.17}$$

Hence giving values u′= 0.175 m/s, v′= 0.18, w′= 0.26 m/s. The eddy velocity calculated in the previous section is 0.33 m/s, and is consistent with these root mean squared velocities.

Difficult to fit example

The trajectory shown in Figure 8.10 is representative of the difficult to fit cases which were about 20% of the total trajectories analysed. It was observed that for some difficult to fit trajectories the relative distance travelled by the particles with respect to the gas was greater than for the well fitted trajectories. As shown in Figure 8.12 (a) and (b) the 90 µm particle (particle trajectory in Figure 8.10) travels about 1.6 mm axially and 0.3 mm radially relative to the gas while for a good fit the relative distance travelled in axial and radial direction was smaller, perhaps half of this. However the 1.6 mm relative distance seems insufficient for a particle to transfer from one vortex to another considering that vortices in the flow smaller than the vortex analysed are not indicated by the plot of change in approach angle of particle in Figure 8.9.

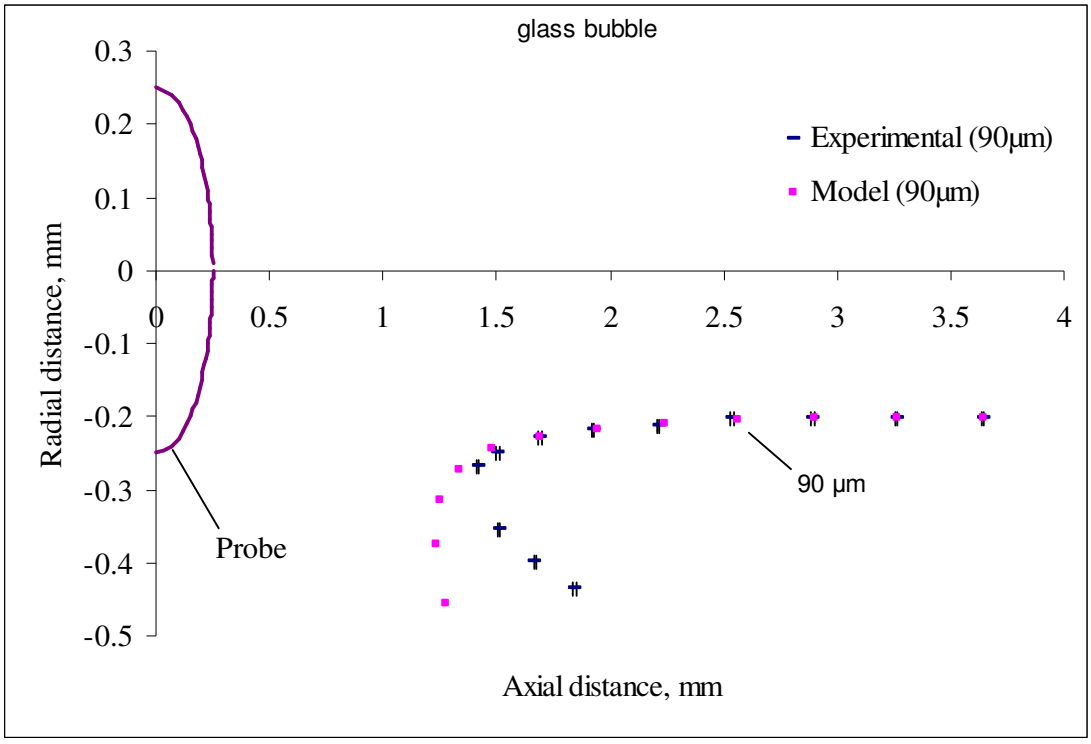

Figure 8.10: Experimental and model trajectories for a 90 µm glass particle at probe voltage -6 kV with fitted net charge q_{net}= -2.2x10^{-13} C.

In this study the focus has been on turbulence in the central area of the jet, taking it to be a high Re jet with small perturbations and eddies. There may also be large mixing eddies at the edges of the jet which can penetrate through to the central part of the jet at times and affect the trajectories. The sudden change in trajectory shown in Figure 8.10 indicates such a sudden flooding of the local forward jet stream with an influx of

gas which is almost stationary in the axial direction. It is known that jets operate either in a free-jet regime "j mode" (as in Wygnanski and Fiedler (1969)) or in a highly mixing mode "r mode". Hassel et al. (2006) outlines the differences and indicates that the r mode is found when there is a duct wall close by which generates vortices along its surface. The schematic in Figure 8.11 from their paper shows the convoluted jet form, which is influenced by large eddies external to the original jet. In our study, the plates are expected to take the place of the tube in the figure, and so eddies coming from the surfaces of the plates are expected to have disrupted the jet flow. This disruption is likely to have resulted in trajectories which cannot be fitted within the assumptions of this study.

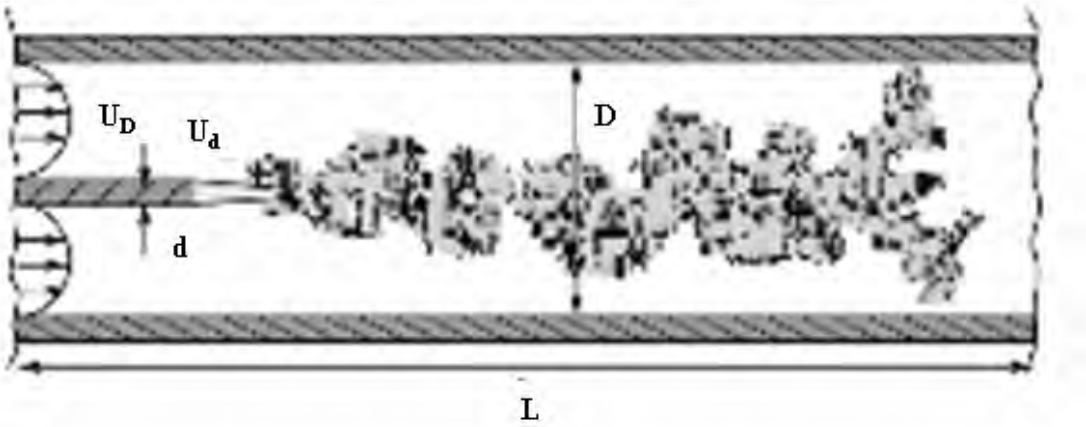

Figure 8.11: Diagram of the plume from a jet within a tube operating in the mixing mode, from Hassell et al. (2006).

Another possibility for sudden change in path can be due to heating of particle in the laser beam. The heating may vaporise some species from the surface of the particle leading to a reduced net charge. However this is unlikely for the transparent glass and acrylic particles because of their low absorption properties. This possibility has not however been fully explored in the present work.

8.2.1.3 Averaged Flow around the Probe

In the final few positions of a particle in front of the probe, it is affected by the deflection of the gas flow around the probe. Thus the details of this flow field are important and the assumed creeping flow field assumed in our calculations should be checked against other models.

As the radius of the outer cylinder was much greater than the radius of the probe, the flow behaviour of the gas only around the probe tip was considered. It was assumed that the probe tip was the only surface whose boundary layer affected the local velocity distribution of the gas. Generally the probe is not expected to affect the flow upstream of its tip unless it is within several tip radii of the tip.

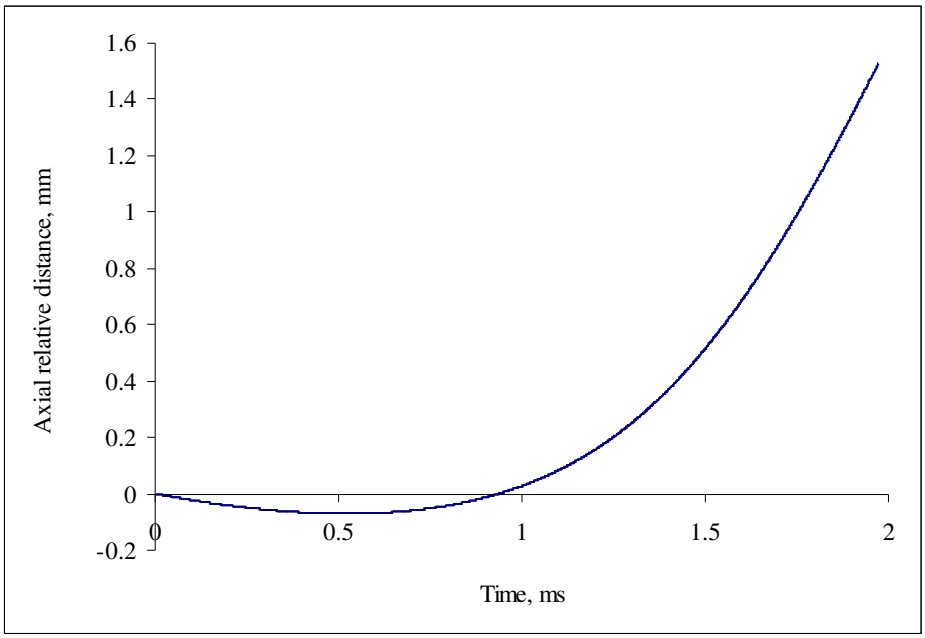

(a)

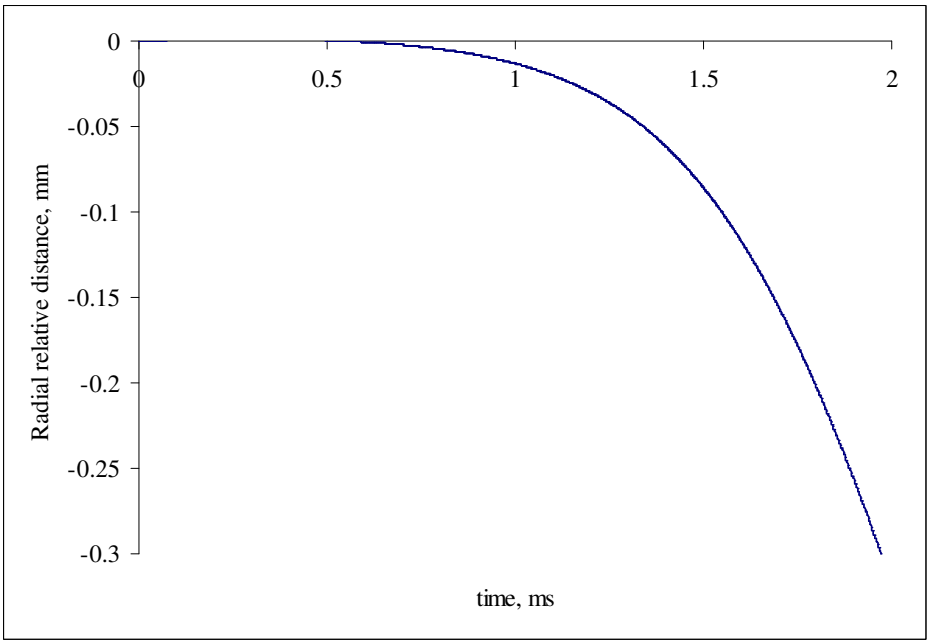

(b)

Figure 8.12: (a) Axial relative distance travelled by the 90 µm glass particle shown in Figure 8.10 in 2 ms (b) Radial relative distance travelled by the same 90 µm glass particle in 2 ms.

Therefore the gas velocity was assumed constant unless the flow was close enough to the probe to be affected by drag on the probe. This close-to-the tip region was accounted for in the particle trajectory modelling by using the Stokes equation for creeping flow around a sphere as described in Section 4.3.

A comparison was made between the gas velocities calculated by using the Stokes equations (equation 2.6 and 2.7) and those predicted by COMSOL. For modelling using COMSOL, the two extreme flow conditions with probe Reynolds numbers 1 and 1000 were chosen to define a range of velocity variations along the axis of the probe by using different inlet velocities. The actual Reynolds number of the probe according to experimental conditions most often used in this thesis was close to 70. For the simulation models a cylinder of 100 mm diameter with the probe midway along its centreline was assumed, so the affect of the outer tube walls was also considered.

Simulations were done in two domains; [I] of length of 50 mm upstream of the probe tip, with 50 mm downstream, and [II] of length 5 mm upstream of the probe tip, with 50 mm downstream. The gas was assumed to approach parallel to the axis of the probe with a uniform velocity distribution across the inlet at an axial distance of 50 mm from the probe tip, or at 5 mm, depending on the simulation domain. The inlet velocity was set at 3 m/s and a gas viscosity of 1.8×10^{-6} Pa s was used to predict the dimensionless flow field for a probe Reynolds number Re = 1000. The turbulent intensity was assumed to be 15% calculated from the conditions of the jet used in the experiments (equation 8.15). For the case of probe Re = 1, an inlet velocity of 0.05 m/s with gas viscosity of 1.8×10^{-5} Pa s was used to predict the dimensionless flow field. For all simulations the outlet boundary was set at zero gauge pressure. Figure 8.13 compares the axial velocity profile using COMSOL for the I domain and that using the analytical (Stokes) models along the axis. The rise in the Re = 1 curve taking the centreline velocity above the entry velocity may be due to the development of flow (retardation of gas near the wall yet constant flow) inside the pipe under laminar conditions.

Figure 8.14 compares Stokes-derived axial velocities with those from COMSOL for the II shorter domain. The purpose of making this comparison is related to the use of

the experimental particle velocity for the gas velocity. As described in earlier chapters, this velocity of the particle when it enters the field of view (less than 5 mm from the probe tip) underpins the analysis.

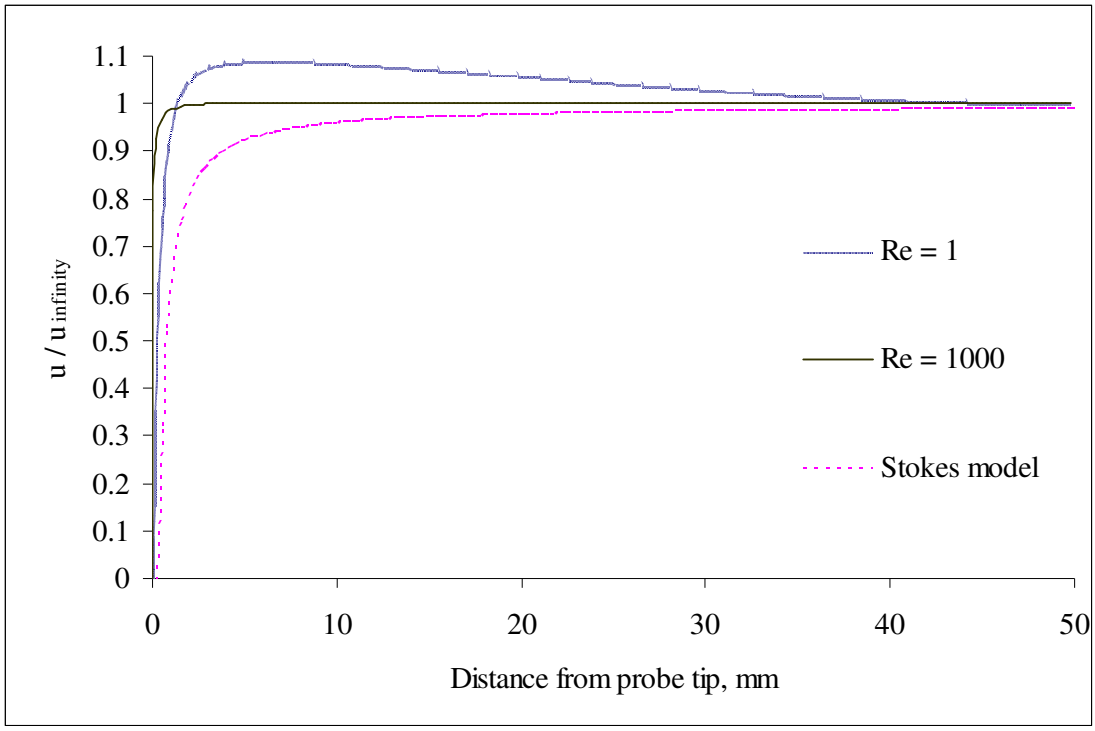

Figure 8.13: In simulation domain I: Comparison of predicted axial velocity along the axis in the sampler head at different Reynolds numbers with that of the Stokes flow.

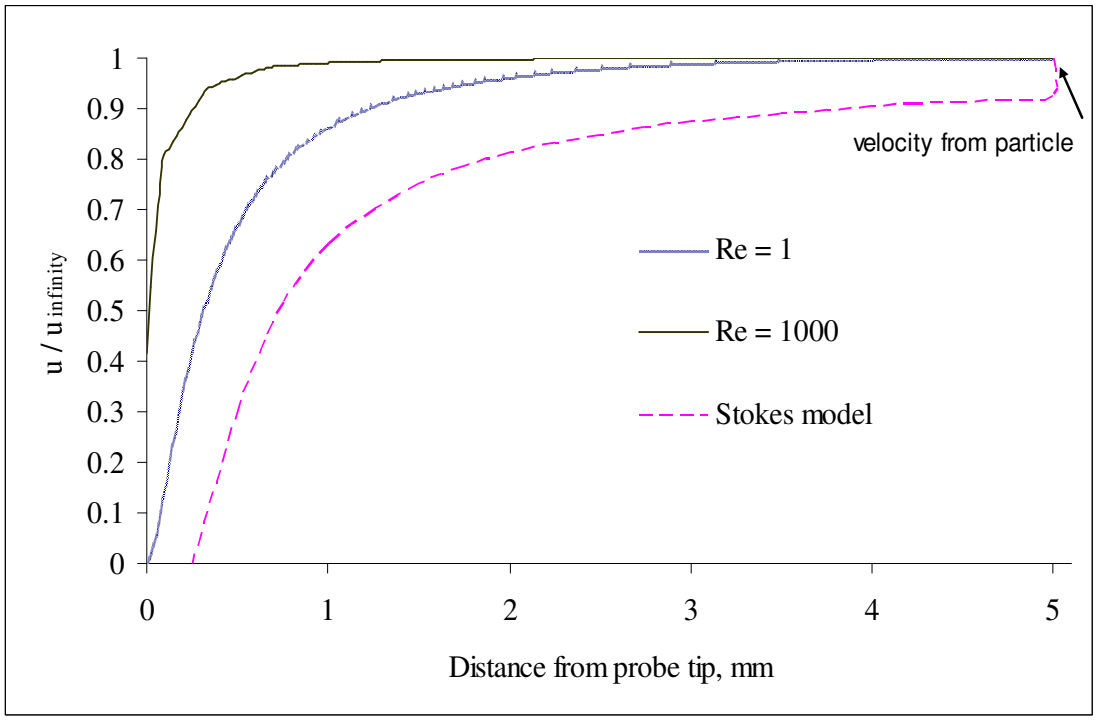

Figure 8.14: In domain II: Variation in axial velocity close to the probe tip.

For the COMSOL simulation, this velocity is assumed to be that over the inlet cross-section, whereas in the Stokes analysis it is assumed to be the approach velocity "from a distance". As one can see from the domain I analysis, this distance is close to 50 mm, and the velocity falls towards the probe becoming around 95% of the approach velocity at around 5 mm upstream. Thus in the II domain, this 95% value remains for the Stokes velocity profile because the initial particle velocity has again been put into the formulae as the approach velocity from a distance.

Very close to the probe tip at about 1 mm distance the creeping flow velocities are 20% less than the COMSOL laminar flow velocity and 40% less than the COMSOL turbulent flow velocity. To check the effect of higher gas velocity on the modelled trajectories, a 20% increased gas velocity was used in a few calculations. For the particle analysed in Figure 7.4, with such an increased gas velocity the particle position had a change of 1 micron (in either axial or radial direction) which is well within the experimental error and can be neglected.

8.2.2 Electrostatic Field inside Sampler Head

The electric field close to the tip of the probe was predicted from the equation used to calculate the electric field between concentric conducting spherical shells (equation 4.16). This assumption was based on the fact that the probe tip was hemispherical and its radius was much smaller than the radius of the outer cylinder. The form of the outer cylinder surface had negligible effect on the electric field close to the probe tip and based on this any geometry of the outer electrode could be assumed. Also only the field upstream of the tip centre was used (except in rare cases) and thus the effect of the shank was likely to be small. The pre selector plates which could be considered to have affected the field were also 30 mm (120 tip radii) away from the probe tip, indicating little influence within the field of view.

The electric field used in the trajectory model was compared with the COMSOL predicted electric field calculated for the complete sampler head geometry (see Figure 5.2). The probe and one of the preselector plates were set at 10 kV. Figure 8.15 shows the comparison of the electric field up to a distance of 5 mm from the tip, along the centreline of the wire tip, for a wire of diameter 500 μm with a hemispherical tip, to

that predicted by the concentric sphere model with an inner sphere of 250 μm in radius. Up to a distance of 1.5 mm from the tip the values are comparable and after that COMSOL predicts about 40-45% higher electric field than the concentric sphere model. If the lower values of electric field are assumed it may introduce error in the fitted charge values and higher values of charge may have been predicted in comparison to the actual ones. It is surprising that higher fields were found from the COMSOL simulation which has the influence of a shank with its lower field (cylindrical field adjacent to the hemisphere). If the COMSOL simulation was the more accurate , then the lower values used (of the spherical field) will offset the lower-than-peak potential of the probe during the later part of the square wave half-cycle.

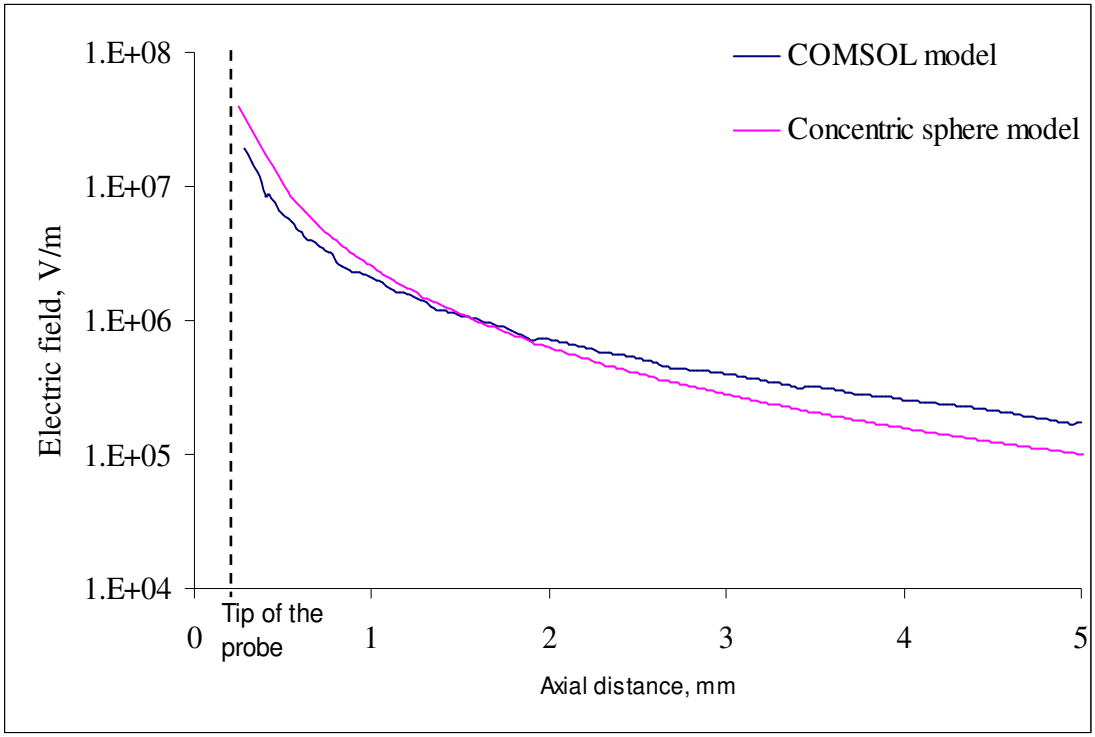

Figure 8.15: Predicted variation in electric field close to the probe tip at an applied voltage of 10 kV.

8.2.3 Rotation of Dipole

The details of the calculations for the rotation of a dipole have been discussed in Section 4.5. Consider the 80 μm glass particle described in Figure 7.23(a) with mass $4x10^{-11}$ kg and also treated in Figure 8.13. The fitted dipole strength, P = $2.16x10^{-17}$ C m .With an axial velocity of 2.75 m/s, the time taken to travel through the space

between the preselector plates is 55 ms. Assuming that before entering the plates the dipole is perpendicular to the electric field in the plates (towards negative y-axis), thus experiencing a repelling torque. Using the angular momentum equations, the time taken by the dipole to orient 180° to the electric field, i.e. towards the positive y-axis is approximately 180 µs. Hence in comparison to the time spent between the plates it is safe to assume that dipoles on particles leaving the plates had aligned with the plate field, and were perpendicular to the *r* direction pointing towards the positive y-axis.

For the trajectory simulation, this orientation is considered to remain up to the point where the dipole is affected by the field gradient; in this case where r_{sph} = 3600 µm. The time taken for this dipole from this point to rotate from 90º down to 15º misalignment with the electric field of the probe is calculated to be a further 340 µs. The predicted time was small enough for the particle to orient into complete alignment with the probe field within its first two flash positions within the field of view. Note that this happens well before the dipole force is expected to dominate over the net charge force. Considering this for the calculations, all the particles were assumed to be in full alignment with the field from the beginning of their trajectory in the field of view. On coming close enough for the dipole force to be dominant, the particles will keep rotating to stay aligned with the probe field.

The particle may overshoot its alignment with the field on entering the probe field, and continue rotating beyond alignment, due to inertia, before stopping and oscillating somewhat before coming to rest in alignment with the probe field. This final part of the orientation could not be modelled satisfactorily in this study. The model showed a jump of angle at a 12º approach to alignment which appears erroneous but could not be explained.

8.2.4 Rotation of Particles after leaving the Plate Field

During the flight of a particle between leaving the plate field and reaching significant probe field, the particle is free to rotate from two types of disturbances; (a) thermal excitation and (b) turbulent eddy torque.

(a) Thermal Excitation

The rotation of the particle due to thermal motion is considered below. The rotational diffusion coefficient for rotation of a spherical particle in a medium consisting of molecules with average thermal energy $\frac{3}{2}k_B T$ is given by (Dhont, 1996):

$$\Theta = \frac{k_B T}{8\pi\eta R_p^3} \tag{8.18}$$

where k_B is the Boltzmann constant, T is temperature, η is the shear viscosity and R_p is the radius of the sphere. For freely rotating spherical particles the mean squared angular displacement

$$\Omega(t) \equiv \frac{\left\langle \left[\Delta\theta(t)\right]^2 \right\rangle}{2} \tag{8.19}$$

where $\Delta\theta(t)$ is the one dimensional angular displacement and is given by (Reyes et al., 2005)

$$\Omega(t) = \Theta t \tag{8.20}$$

For our experimental conditions the rotational diffusion coefficient Θ for a 80 μm particle is calculated (from equation 8.18) to be $1.43\text{x}10^{-4}$ radian^2 /s. The time taken by a particle to travel the 30 mm axial gap between the plates and the probe tip with 2 m/s velocity is 15 ms. The mean squared angular displacement (equation 8.19) is then $2\text{x}10^{-6}$ radian^2 so the mean angular displacement is 0.002 radian or 0.11°. This is negligible in comparison with the rotation the particle is expected to undergo due to the dipole. It can thus be assumed that there is negligible displacement due to thermal motion.

(b) Rotation due to Eddy Torque

From the smoke analysis in Section 8.2.1.1 the eddy velocity has been calculated to be 0.33 m/s for an eddy of diameter 7 mm. For a relatively low Re number turbulence (Re = 100) it is expected that eddies will have a solid rotation tangential velocity

profile. The angular velocity of this eddy is then calculated to be $(0.33)(2)/(7x10^{-3})$ = 94 radian s^{-1} and the angular displacement of the eddy in this time frame (10.1 ms) is then close to 55°. So the rotation of a particle in the centre of vortex will be of this order while the particles on the periphery will be less affected. As mentioned in the previous section the time taken by a particle to travel the 30 mm axial gap between the plates and the probe tip is 15 ms. The particle in the centre of the eddy can thus rotate widely from its assumed orientation after leaving the plates due to the eddy torque.

A check was made for possible rotation of a particle by the vortex during the flight of the particle when field is appreciable. In the rotation calculations for the particle explained in Section 8.2.3, the angular velocity of the eddy was added to the relative angular velocity in the viscous drag expression (refer equation 4.42) and the particle orientation with time observed. It was concluded from the results that even if the strong orientation due to vortices happens, it does not affect the trajectory analysis significantly. Once the particle is inside the electrostatic field of the probe it takes just about two to three flashes for the dipole to fully align in the direction of the electric field. Following this, the prior rotation alignment does not influence the trajectory.

8.2.5 Corona Discharge

In this study a fine inner electrode (wire probe) was used and a high voltage of up to 18 kV was applied to it. The predicted electric field close to the probe surface at this voltage is expected to be up to $7x10^7$ V/m. According to equation 2.8 for calculating the field strength of the onset of corona from a perfectly smooth wire on the axis of a cylinder, for a wire of radius 250 μm in a cylinder the onset of corona is expected at electric field strength of $1x10^7$ V/m. The maximum surface charge density for a sphere of radius 250 μm estimated by equation 2.10 is $1.2x10^{-4}$ C/m^2. According to Gauss's law the electric field at the surface will the be $14x10^6$ V/m which is well above the generally quoted maximum electric field ($3x10^6$ V/m) air can sustain (from flat surfaces) before it ionises. Studies related to corona between a hemispherically capped wire and a plane by Loeb (1950) and another by Bandel (cited by Loeb, 1950) indicated the breakdown voltages (for a wire radius of 250 μm at 40 mm distance from the plane) to be close to 5 kV. This is considerably smaller than our maximum

18 kV voltage. It can be concluded that different studies indicated a probability of corona discharge close to the wire probe of this study as it was used. These are all based on DC voltages and fields.

Before the start of experiments with particles in the present study the high voltage AC supply was put to its maximum (up to 20 kV) and no visible corona could be detected though some noise could be heard close to 18 kV. It was assumed that a possible corona discharge was taking place close to this voltage. A check was again made for corona discharge around the probe tip in the experimental geometry after finishing all the experimentation. The probe had been removed just before this and handled for photography in the laboratory, and then repositioned in its normal place. A Rogowski coil was attached on the high voltage neutral return lead and connected to an oscilloscope to detect voltage spikes. In this case a "faint glow" could be detected at the probe tip at a voltage of 6.6 kV and very fast moving spikes could also be detected correspondingly on the oscilloscope. At voltages close to 14 kV a spark could be observed close to the spider support for the probe. There were lots of particles deposited all around the sampler head. So the whole of the geometry was dissembled and particles wiped away from each part. After cleaning, the assembly was again put together to check for corona. This time the initial faint glow was visible at 7 kV and no spark could be observed even at a maximum of 20 kV. Two observers did not see any faint glow at the start of the experimentation despite looking for it.

8.2.6 Two-Dimensional Particle Surface

In predicting the particle diameters and positions it was assumed that the illuminated two-dimensional area presented the surface area of a plane cut through the axis of the particle. The third dimension perpendicular to the image was completely ignored. This may have introduced some error as there may have been particles not completely inside the depth of field. In such a case only a part of the particle inside the depth of field will be illuminated and could be mistakenly assumed as a whole particle for the analysis. This error was unavoidable as it was difficult to estimate the extent of a particle inside the field. To avoid this, the general practice was to choose only frames with 6-7 consecutive clear images of a particle (if possible), i.e. with evidence that the particle remained within the laser sheet for the whole trajectory. Also it can be

difficult to identify unsymmetrical particles in a 2-dimensional image, in particular when the particle is off-centre in the third dimension.

8.3 Net Charge and Dipole Measurements

8.3.1 Quality of Particle Force Simulation

Net charge and dipole measurements were performed for four different samples; acrylic spheres, glass bubbles, whole milk powder and fertiliser particles. About 40 runs were performed for each sample of acrylic spheres and glass bubbles and 20 runs were performed for each sample of whole milk powder and fertiliser particles. After careful approximation of the forces acting on the particles inside the sampler head the particle trajectories were fitted for the presence of monopole and dipole charges. The expected errors from adequate fitting of net charge and dipole charge on individual particles indicate an acceptable precision of measurement.

The results show good agreement of the model trajectories with the experimental trajectories (Figure 7.14 to 7.22). So an adequate description of the types of forces was provided by the net charge, dipole, induced dipole and image forces terms used. All the acrylic sphere trajectories in Figure 7.14, 7.15 and 7.16 are for diameters close to or above 100 μm. As expected for larger surfaces, the fitted net charge values are also near the higher end (Hamamoto et al., 1992), in this case of the order of 10^{-13} C. In a few cases a lack of fit was observed close to the probe particularly for the last particle position which may be attributed to turbulence (eddies), adjustment of particle position after it touches the probe, particle bouncing back after touching the surface, variation in electric field due to deposition on the probe surface etc. The fitted last position in a few trajectories, e.g., the 116 μm particle in Figure 7.15 (b), the 95 μm particle in Figure 7.16 and the 60 μm particle in Figure 7.20(b) was beyond experimental error of the experimental position, even when all the forces listed in equation 4.38 were included (drag without turbulent change in gas velocity, electrical monopole, dipole, induced dipole, image). This may be due to the presence of a large eddy which passed through the region and violated the constant gas velocity assumption sufficiently to drag the particles sideways at velocities higher than predicted (as shown in Figure 8.10).

For the cases in which a particle attached to the probe surface the fitted point was out of experimental error limits, e.g., the 92 μm particle in Figure 7.16, 55 μm particle in Figure 7.18 and the 60 μm particle in Figure 7.19. This can be explained considering that when the particle comes in contact with the probe surface its surface charge will change and redistribute and it will adjust its position according to the applied field.

The fitted net charge for most of the glass bubbles and fertiliser particles was in the range of 10^{-14} C (Figure 7.17 to 7.19, 7.22). The particle sizes were also smaller (less than 100 μm) with these types and hence lower charge values were expected. The probe surface was occasionally covered with a fine layer of particles especially in the case of milk particles as they were sticky and also for the fertiliser particles which included a high fraction of fines (Figure 7.20(a), 7.21(a), 7.22(a)). When fine particles deposited, the location of the probe tip in the image was done on the basis of previous experience from the initial images of the same run. There is another possibility that for the case of the covered probe, if the particles are conducting this will affect the electric field due to an increase in probe size. On the other hand if the particles are insulating, this layer may provide a shielding effect by reducing the electric field. To simulate this effect, the COMSOL electrostatic module was used to simulate a 250 μm thick dielectric layer built around the probe tip. The comparison with a bare probe is shown in Figure 8.16. In our studies the particles were insulators with a low dielectric constant (~2.5) and layer thickness was close to 100 μm hence this shielding effect was ignored up to the contact point with the layer.

The glass bubbles were difficult to trace because of their transparency and small sizes. Some image sequences showed only the upper edge of the particle till it was close enough to the tip to be fully visible because of the light reflected from the probe surface (Figure 7.23(a)). For such images the last position with full view was used to predict the diameter of the bubble and then used to find the centre of the bubble in all the previous positions. The model indicated the spherical radius r_{sph} ranges over which net charge, dipole and image forces were dominant, as follows: 3600 μm > net charge > 600 μm > dipole > 300 μm > image charge > contact point (260 μm) as shown in Figure 8.17 for an 80 μm glass particle.

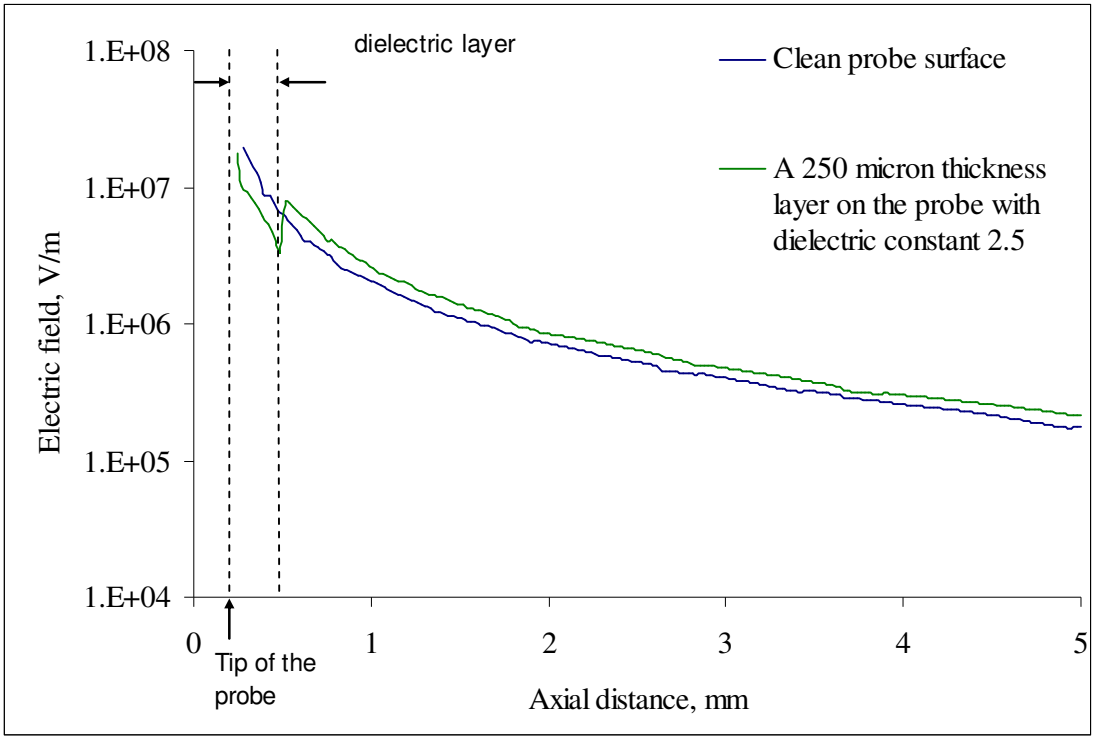

Figure 8.16: COMSOL comparison of electric field along the axis close to the probe tip at an applied voltage of 10 kV for a clean probe surface and a probe surface with 250 μm dielectric layer ($\varepsilon_r = 2.5$) on it.

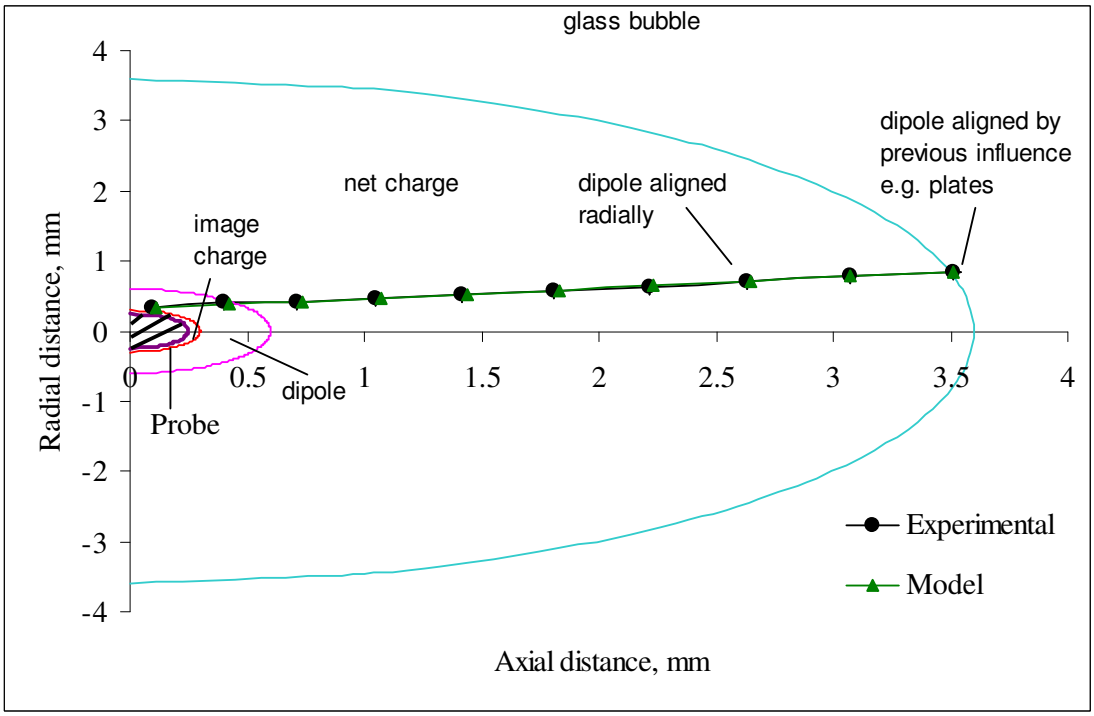

Figure 8.17: Dominating electrostatic forces for translational motion as a function of distance from the probe for an 80 μm hollow glass particle with fitted net charge and dipolar charge to be q_{net}= -7.5x10^{-14} C and q_{dip}= 2.7x10^{-13} C at probe voltage -6 kV. Also shown is the influence of the field on rotation of the particle.

8.3.2 Dipole Measurements

In particular the glass bubbles exhibited a large variation in the fitting close to the probe tip with the presence of a dipole. There were about 18 such trajectories out of the 43 glass bubble trajectories analysed (Figure 7.23, 7.24 and 7.27) when net charge alone could not fit the particle trajectory and the presence of dipolar charge was mandatory. The dipole charge value was more than twice the net charge for most of these cases (Figure 7.23 and 7.24). The model trajectory for the 82 μm glass bubble in Figure 7.27 could not be fitted close to the probe tip, even with a dipole included, within experimental error, but the closest fit required a dipole charge of about six times the net charge value. The 60 μm glass bubble trajectory in Figure 7.25 could be well explained with either net charge alone or by adding a dipole with a ten times higher dipole charge. In Figure 7.26 (b) the last particle position close to the probe tip could not be explained which might be due to the particle adjusting its position after touching the probe surface (Figure 7.26 (a)) by rotating to align with the electric field. Also there was insignificant improvement in the fitting with a dipole in this case. In a few cases there was an increase in particle approach velocity close to the probe tip as shown in Figure 7.29 (a). Close to the probe the particle experienced a strong pull towards the probe which could not be matched with an attractive net charge force; this behaviour could be nearly matched with a dipole charge only. As can be seen in the case of particles in Figure 7.27 and 7.30, assuming only net charge fails to describe the particle trajectory on approaching the probe.

8.3.2.1 Dipole Charge Fitted on Previously Fitted Trajectories with only Net Charge

Most of the particle trajectories could be explained within error on the basis of net charge alone except for the case of glass bubbles. But the presence of dipoles could not be completely ruled out even for the other three types of particles. For example, the 55 μm milk particle analysed in Figure 7.20 (b) with only a net charge of $+1.14 \times 10^{-13}$ C could also be analysed as in Figure 7.31 which results in both a net charge $+1.21 \times 10^{-13}$ C and dipole charges as high as 1.4×10^{-13} C. A similar comparison has been made in Figure 7.32 and 7.33 for a 92 μm and a 28 μm acrylic sphere. In both cases a similar kind of fitting resulted by ignoring (Figure 7.32) or considering (Figure 7.33) the presence of dipole charges. In particular for the 92 μm acrylic

particle the fitted dipole charge value of $1.5x10^{-13}$ C is significant enough not to be ignored. There were cases when the fitting of a trajectory was possible with either net charge only or dipole charge only, e.g., the 108 μm acrylic sphere in Figure 7.34, the 25 μm fertiliser particle in Figure 7.36 and 7.37. Also the trajectory of the 54 μm milk particle in Figure 7.21 (b) with a high negative charge of $-2.18x10^{-13}$ C could be well explained by assuming only the presence of a significant dipole with a charge of $4.35x10^{-12}$ C (Figure 7.38).

It can be seen from the results that individual values of both the net charge and the dipole moment values were statistically significant compared to fitting errors, and so the measurement technique appears to be successful.

8.4 Distribution of Net Charge and Dipole

The order of magnitude of the overall particle surface charge density, σ, was in the range of 10^{-7} to 10^{-5} C/m^2 in comparison with the observed values of 10^{-5} to 10^{-3} C/m^2 by Lowell and Roseinnes (1980) for different insulators after contact with a metal.

Figure 8.18 and 8.19 present the regions showing the spread of probable charge distribution (both net and dipole charges) for all negative and positive particles respectively in all the four samples. The particles whose trajectory could not be explained on the basis of net charge alone particularly in the case of glass and a few in the case of acrylic have also been mapped in their respective regions.

For acrylic particles the results shown in Figure 7.39 come from a mixed analysis of particles with and without any voltage on the preselector plates. The preselector plates were always at 8 kV for the analysis of all other samples. In case of acrylic spheres the range of estimated charge on negatively charged particles was from $-1.5x10^{-15}$ C to $-1.4x10^{-12}$ C and for positively charged particles the range was within $3x10^{-17}$ C to $5.1x10^{-13}$ C. As can be observed from Figure 7.39 there was a predominance of negative charge from the particles analysed.

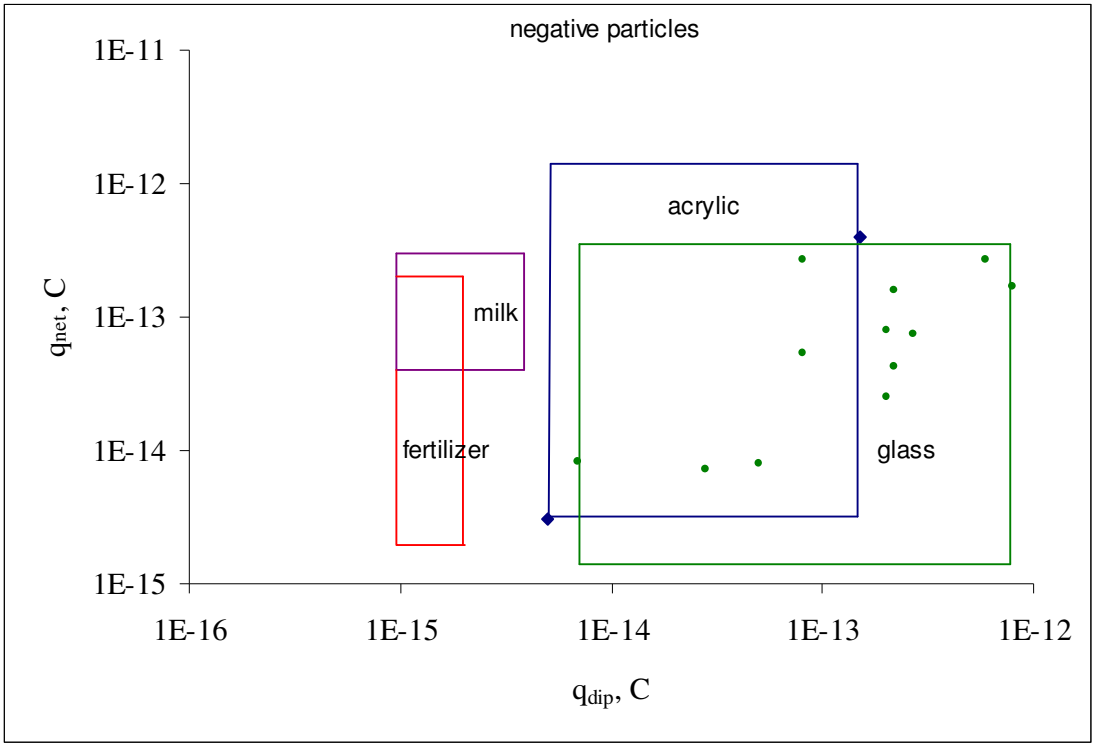

Figure 8.18: Regions presenting the spread of observed charge distribution for all negative particles in all the four samples. The dots show the particles with significant dipoles.

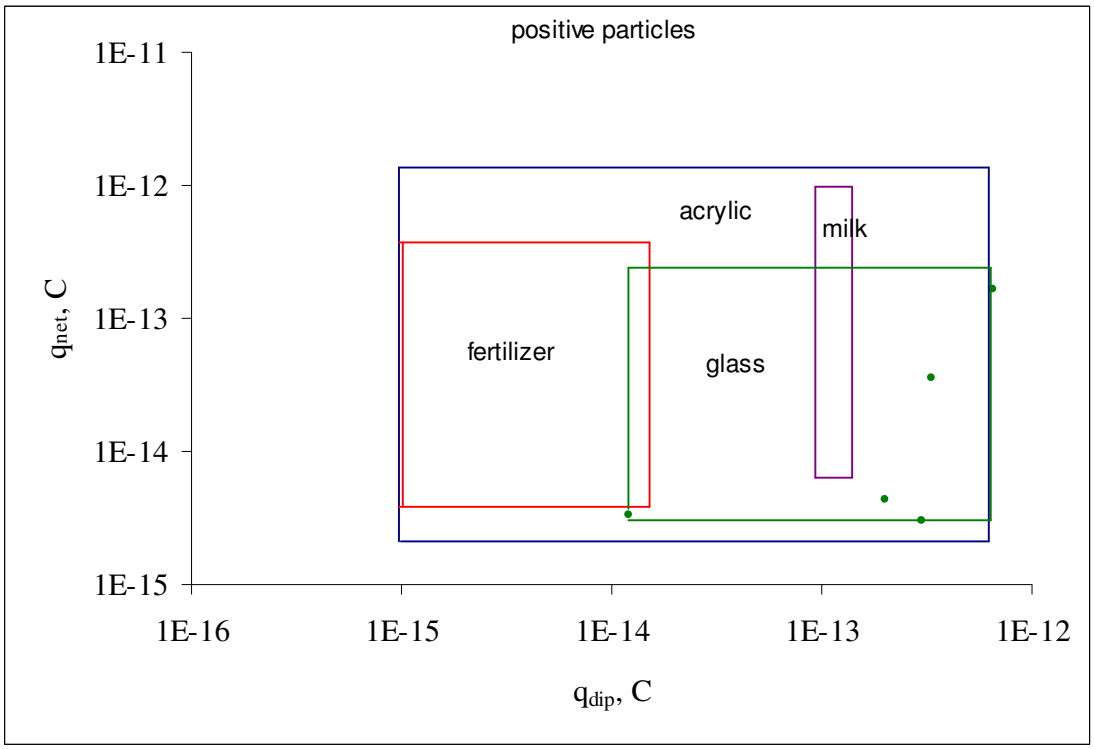

Figure 8.19: Regions presenting the spread of observed charge distribution for all positive particles in all the four samples. The dots show the particles with significant dipoles.

The glass bubbles showed an even distribution of positive and negative charges (Figure 7.41) but a dominance of positive charge could be seen at the low charge end (Figure 7.42). The range of estimated charges on negatively charged particles was from -1.5×10^{-15} C to -3.4×10^{-13} C and for positively charged particles the range was from 4×10^{-15} C to 2.5×10^{-13} C. A dipole charge of 7×10^{-15} C to 6.5×10^{-13} C was detectable (Figure 7.43) on 18 particles out of the total 44 analysed.

The charge distribution was found to be evenly spread in the case of whole milk powder (Figure 7.45). The range of estimated charge on negatively charged particles was from -4×10^{-15} C to -2.9×10^{-13} C and for positively charged particles from 1×10^{-15} C to 5.2×10^{-13} C.

In the fertiliser sample there is a dominance of negative particles and the overall charge on the particles was also low in comparison with other samples (Figure 7.47). The negative charge on the particles was estimated from -1.83×10^{-15} C to -2×10^{-13} C and the positive charge on particles was estimated from 5×10^{-16} C to 1.56×10^{-13} C.

As the number of flashes was higher in the case of negative polarity of voltage (leading to more data points), the trajectories in this case were more informative and it was easier to visualise the complete path followed by an individual particle. Most of the trajectories chosen for analysis were those which had at least 6-7 data points. So the number of analysed trajectories with negative polarity of the probe is more than for the positive polarity. This may bring about some bias in the particles selected for analysis. To clear these biases experiments can be conducted at low probe voltages and the charge distribution can be plotted as a function of probe voltage.

In the initial runs (using acrylic spheres) high voltages of 10 kV and above were applied to the probe to achieve high electrical forces for the detection of the dipoles. But later it was realised that with other samples and glass bubbles in particular the number of particles in the field of view was greatly reduced at high voltages. So for most of the later measurements a voltage close to 6 kV was applied to the probe. This is expected to be related to the inertia of the particles, and hence the sizes, as the acrylic spheres were mostly above 100 μm and hence they continued closer to the probe before being affected by the electric field close to the probe tip. The glass

bubbles had very low apparent density and the effect of the electric field was dominant at distances far away from the probe (often out of the field of view at probe voltages ~ 10 kV) and hence many could not be seen in the field of view.

Obolensky Filter Measurements Comparison

The mean charge for acrylic spheres estimated using the Obolensky filter with and without pre selector plates activated was $+2.3 \times 10^{-14}$ C (current through the filter ~ 8.2 nA) and $+2.53 \times 10^{-14}$ C (current through the filter ~ 9.00 nA) respectively (see Appendix, A6 for calculations). The charge distribution from the probe studies in Figure 7.39 shows much higher (and negative) average charge values -2×10^{-13} C and -1×10^{-13} C, with and without preselector plates. These values were calculated by averaging the charge on all the analysed particles to get a mean charge. The probe-derived mean charge value is one order higher than the value measured by the filter.

The mean charge for glass bubbles estimated using the Obolensky filter is -1.5×10^{-15} C (current through the filter ~ -6.00 nA). From the probe data in Figure 7.41 the mean charge calculated is -3.7×10^{-14} C. Also in this case the filter mean charge value is one order of magnitude lower than the probe-measured value but is of the same polarity. Uncertainties in the readings of the filter have been explored. Repeat runs showed little difference in average net charge. The metal mesh inside the filter had particles deposited on it and could not be fully cleaned with compressed air. This may have resulted in a reduced sensitivity of the mesh. The resistance to earth was checked and it was close to 40 MΩ and hence no current leak is likely. It was noticed that (see Figure 7.51) the time trace of the filter started positive (indicating a positive charge) and then went to negative values. The reason for this behaviour could not be explained.

A standard t-test was performed on the two mean currents shown in Figure 7.49 and 50 (with and without pre selector plates). The mean current values of the two traces were 8.97 nA and 8.23 nA respectively. The experimental t value using the pooled scatter standard deviation of the points was calculated to be 3.42 and the theoretical t value with a combined 60 degrees of freedom of error was 2.57 with 0.5% probability. The experimental t > theoretical t value and thus the preselector plates

made a significant impact on charge current when voltage was turned on. It is interesting that the positive current *increased* when the plate voltage was on. It is very likely that a significant fraction of the particles was collected with the voltage on. If there was no bias in collection, then the positive current would reduce. A bias in favour of collection of negative particles would explain the higher positive current in the filter.

8.5 Scope of the Probe-Trajectory Technique

In this section the range and limitations of the technique for broader use have been discussed in terms of particle size, particle density, detectable charge etc.

Minimum Particle Size

The clarity of images acquired from our camera assembly limited the lower range of particle sizes that could be detected using the technique. The size of one pixel was five μm so it was not feasible to define a particle close to this size. For particle below 10 μm it was difficult to distinguish between an actual particle and noise in the image which was also of the same range. The problem of speckle (mentioned in Section 6.1.2.1) when using the laser also limited the minimum size detectable as the speckle patch size was in the range of 1-2 pixels. Also the smaller the particle the larger will be the errors in the position resolution, resulting in larger errors in the charges from the analysis. A particle close to 10 μm may be visible if the material is opaque but in the case of transparent particles 20 μm is the safe lower limit down to which the analysis can be made with acceptable error.

To check the range of detectable particles with different diameters, charges, particle densities, gas velocities etc., a simulation of particle trajectories was done.

Effect of diameter

The effect of variation in particle diameter on the trajectory of a particle with 100 kg/m^3 density (assuming a minimum value) and net charge $q_{net} = -1x10^{-12}$ C with a probe voltage -7 kV (the maximum safe limit before corona) is shown in Figure 8.20.

A high dielectric material (refractive index =3) was assumed to keep induced dipole forces to a maximum. The gas velocity was assumed to be the minimum observed in our experiments of 1 m/s. The axial field of view in our set up can be extended to a maximum of 5 mm in front of the probe tip. It can be seen that under these conditions there is a possibility that a 20 µm particle will never enter the field of view and a high chance that even a 100 µm particle is repelled unnoticed.

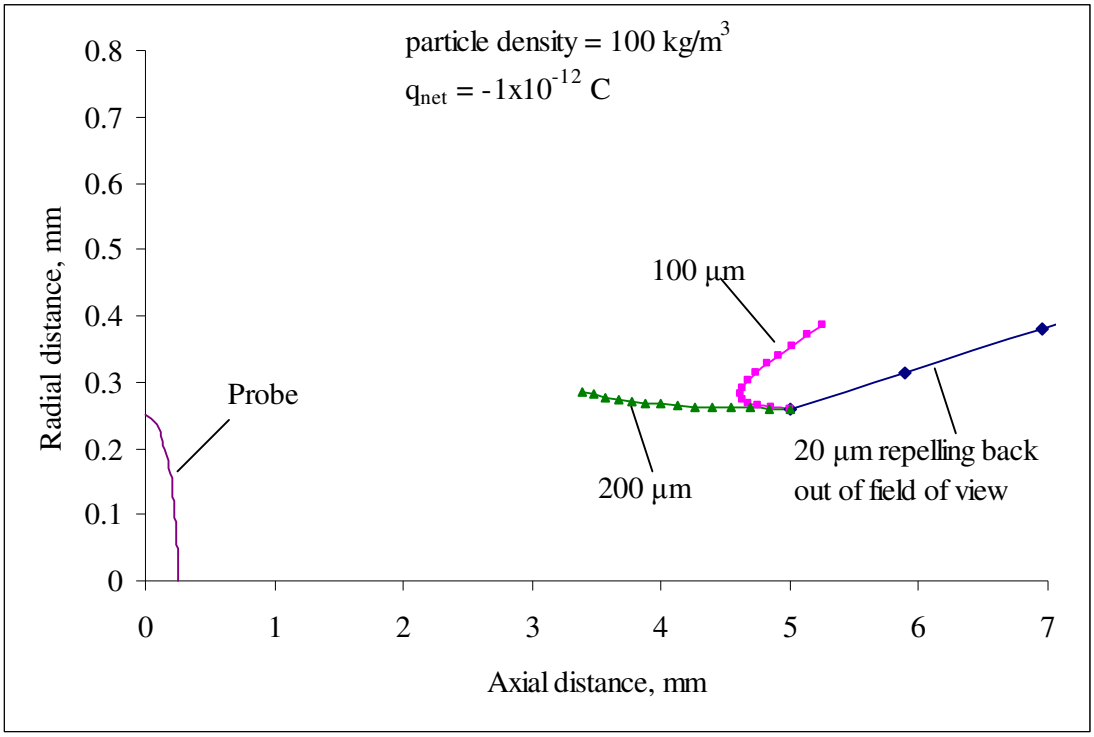

Figure 8.20: Effect of variation in particle diameter on the trajectory of a particle with 100 kg/m^3 density and net charge q_{net} = -1x10^{-12} C with probe voltage -7 kV.

Effect of Particle Density

In the present study the largest density of particles used was close to 1500 kg/m^3 and the maximum particle size was nearly 130 µm. A particle density above this may introduce considerable error in the calculations. This is due to the gravitational force which becomes significant for particles in this size range at higher densities. In such cases a correction in the equation of force balance can be easily made to account for gravity. To check the extremes, simulations of particle trajectories were performed for a particle of size 200 µm under varying densities and maximum charge of -1.6x10^{-11} C on this size (Hamamoto et al., 1992). The effect of gravity was also included and all other conditions were similar to the previous section. A particle density in the high

range of 7000 kg/m^3 (e.g. steel) was assumed and then density lowered to see the changes in the trajectory of the particle. As shown in Figure 8.21 this large diameter particle with low density of 100 kg/m^3 was repelled close to 5 mm from the probe tip so there is a high probability that a particle smaller than this under such conditions will never enter the field of view. The droop in path of the particle with density 4000 kg/m^3 and 7000 kg/m^3 can also be observed.

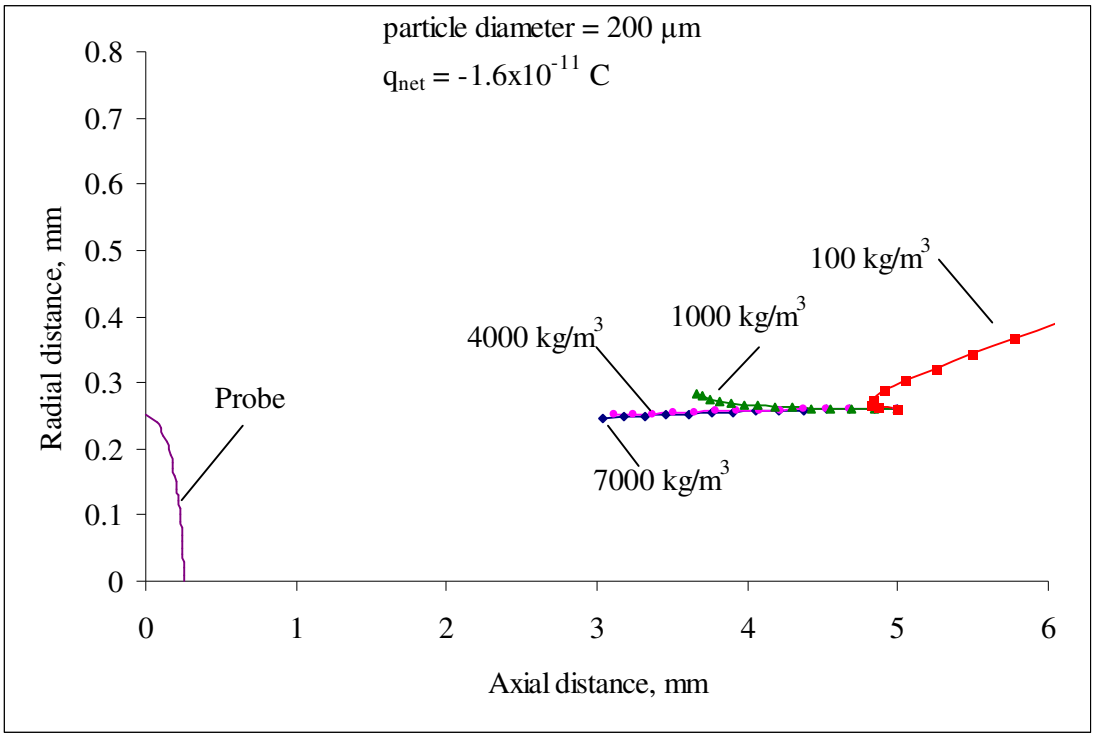

Figure 8.21: Effect of variation in particle density on the trajectory of a 200 µm particle with net charge q_{net} = -1.6x10^{-11} C at probe voltage -7 kV.

Minimum Detectable Charge

Among all the particles analysed for this study the minimum detectable charge has been 3x10^{-17} C for an acrylic particle. Another lower range charge of 5x10^{-16} C has been detected for fertiliser particles. Hence it can be considered that it is not possible to detect charges below 10^{-17} C using the technique in the present form. Another limit is placed on the measurement of net charge by the particle size and its density. These two will affect the drag force and higher diameters and particle densities could render electric forces ineffective in changing particle direction. This is shown in Figure 8.22 for a steel particle of 200 µm diameter in which case the particle trajectory has little variation between zero net charge to a high net charge of -1.6x10^{-11} C even with the

effect of gravity included. This variation is difficult to distinguish as all the trajectories lie between the assumed error limits of ±1 pixel.

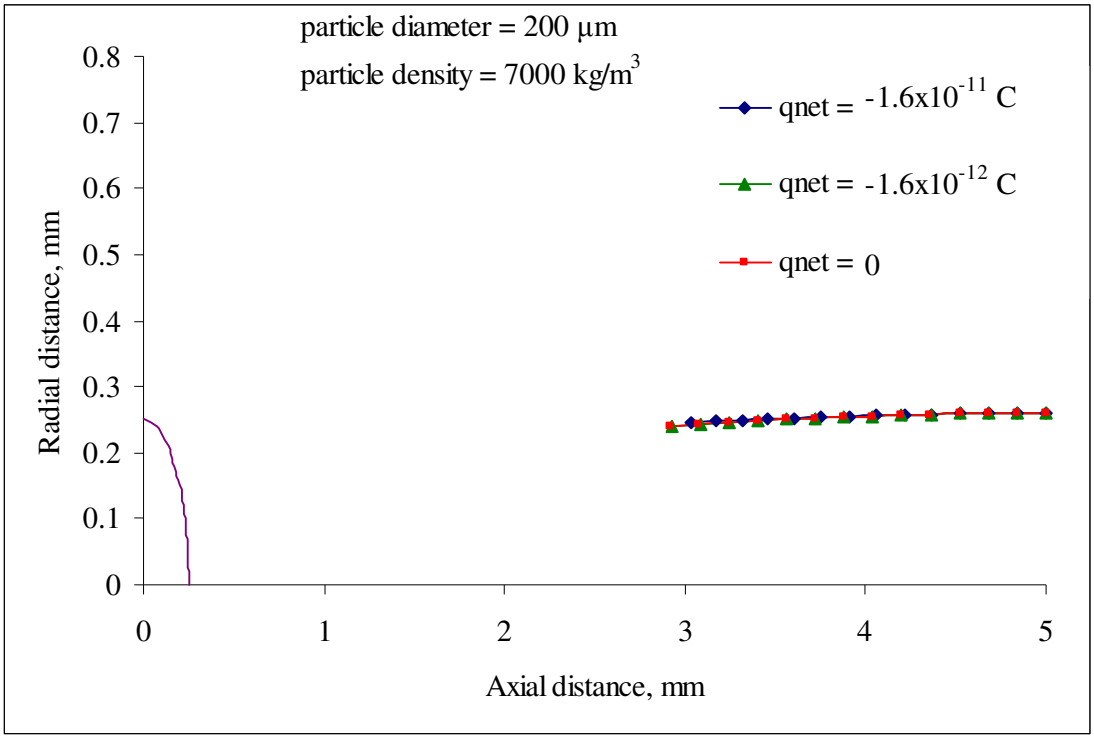

Figure 8.22: Effect of variation in net charge on the trajectory of a high inertia particle (200 µm with particle density 7000 kg/m^3 at probe voltage -7 kV).

Minimum velocity of particle due to laser flashes

A laser flash of 20 µs in a pulse period of 160 µs was used to visualise individual particle positions. If a pulse period greater than this, e.g., 320 µs was used, then the number of positions will reduce and points on the trajectory will not be sufficient to see the variations in a particle trajectory. If the pulse period was reduced, e.g., to 40 µs than only a bright streak on the image could be seen (overlapping images) instead of distinct particle positions. The pulse period of 160 µs was the optimum. For a particle to be visible distinctly at different positions it needs to travel at a minimum velocity. Consider a particle of 20 µm which will be visible in a 4x4 pixel area. To travel to the next position with a difference of at least 10 µm (2 pixels) in between images at the two positions, this particle needs to travel 30 µm (6 pixels) in 160 µs. So the minimum velocity required for the particle to travel to be seen in a distinct next position will be 0.2 m/s. Similarly for a large particle of 200 µm to be seen at a separation of 10 µm between its two positions on an image it needs to travel at a velocity of 1.3 m/s.

Masking of permanent dipoles

The induced dipole force experienced by a particle greatly depends on the multiplication factor *U* (refer equation 4.25). Higher permittivity of a material implies a greater value of *U* and such particles experience larger induced dipole forces close to the probe tip. It is expected that the induced dipole forces dominate the permanent dipole forces in the region where the two dipole forces become effective (close to the probe tip) for high permittivity particles. This masking of permanent dipole forces provides difficulty in detection of permanent dipoles. Figure 8.23 shows a comparison of masking of permanent dipole forces by the dominating induced dipole forces close to the probe tip for an 85 μm (solid) acrylic sphere and the same size glass bubble both fitted with same net charges (q_{net} = -7.2x10^{-14}C) and dipole charges (q_{dip} = 2.8x10^{-14}C) at -7 kV probe voltage. It can be observed that the effect of masking is more evident in the case of acrylic spheres. Acrylic spheres have relative permittivity close to 2.2 which means that the dipole measurement is difficult for particles with permittivities close to and higher than 2.2.

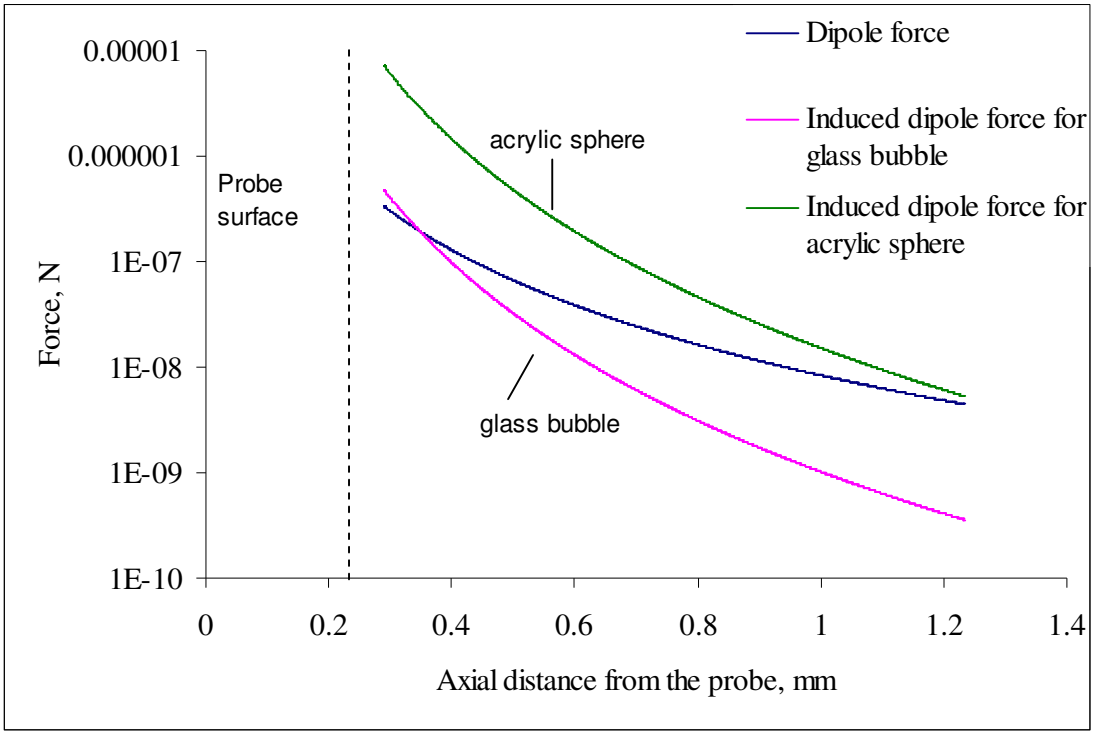

Figure 8.23: Comparison of masking of dipole forces by the dominating induced dipole forces close to the probe tip for an 85 μm acrylic sphere and the same size glass bubble both fitted with same net charge and dipole charge (q_{net} = -7.2x10^{-14}C and q_{dip} = 2.8x10^{-14}C at -7 kV probe voltage).

Glass has a lower value of relative permittivity, i.e. around 1.56, but the reduction of mass in the particle due to the shell construction, and especially that close to the high field at the surface, dramatically reduces the expected induced dipole. Also the dipole force varies proportionally with voltage and the induced dipole varies with square of voltage. If the voltage is halved the dipole force is halved but the induced dipole force reduces to a quarter. So to measure permanent dipoles low voltages and high resolution is recommended.

8.6 Method of Charging of Particles

In our experiments the particles were fed through a nozzle inside the sampler head with the help of a brush feeder. Along the way through the feeder, from the inlet to the exit point, the particles came into contact with the walls of the brass syringe and the piston which pushed them upwards towards the rotating nylon brush. The rotating brush picked up the particles which were blown off the brush into another brass tube. Particles exiting from the brass tube passed through a polyacetal nozzle and then flowed towards the sampler head. At various stages of their path the particles had opportunity to be tribocharged due to contact with various materials like brass, nylon and polyacetal along with the inter-particle contacts.

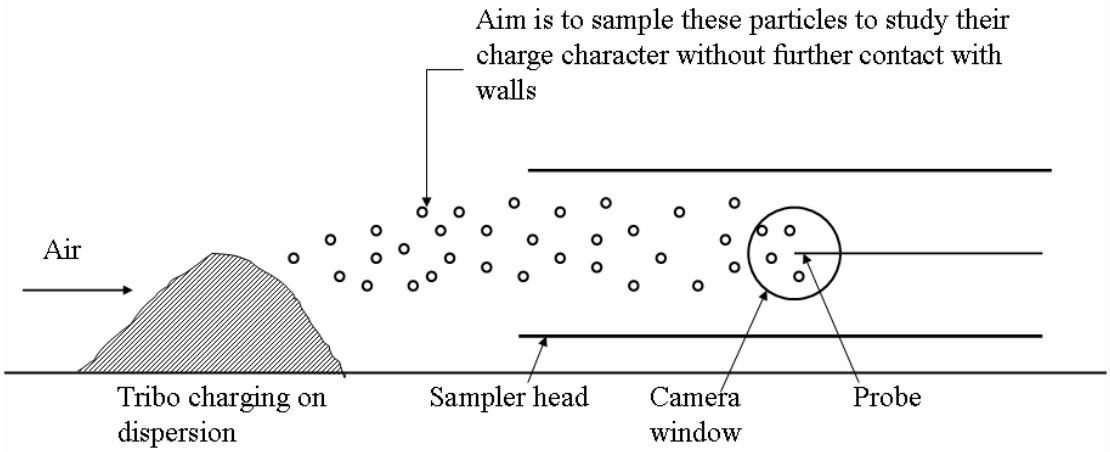

Figure 8.24: Sampling of particles after dispersion from a heap**.**

In designing a more complete experiment to investigate tribocharging on dispersion, the dispersion system can be designed to have a simpler geometry, have limited wall contacts, or to even avoid them as presented in Figure 8.24. In the simplest situation the particles can be fed directly from a heap by dispersion with the aid of an air jet.

Care then needs to be taken to avoid further wall interaction on entering the sampler head.

8.7 Observed Exceptional Behaviour of Particles

8.7.1 Aggregation

A few runs were carried out with two different samples of acrylic particles with mean diameters 90 μm and 20 μm mixed together. The mixed sample exhibited aggregation and trajectories of the aggregates are shown in Figure 8.25 and 8.26. Note the apparent rotation of the aggregate in Figure 8.24. Similar aggregation could be observed in a few cases of glass bubbles as well (Figure 8.27).

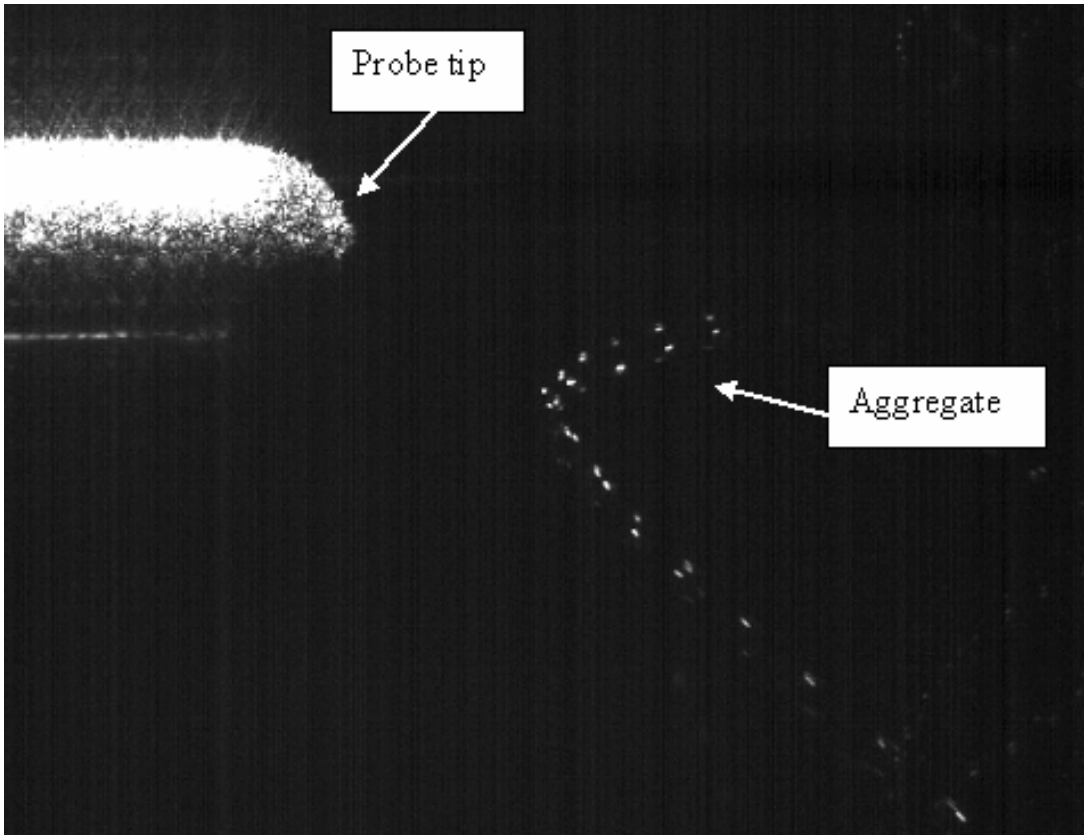

Figure 8.25: Trajectory of an aggregate of acrylic particles at probe voltage -6 kV.

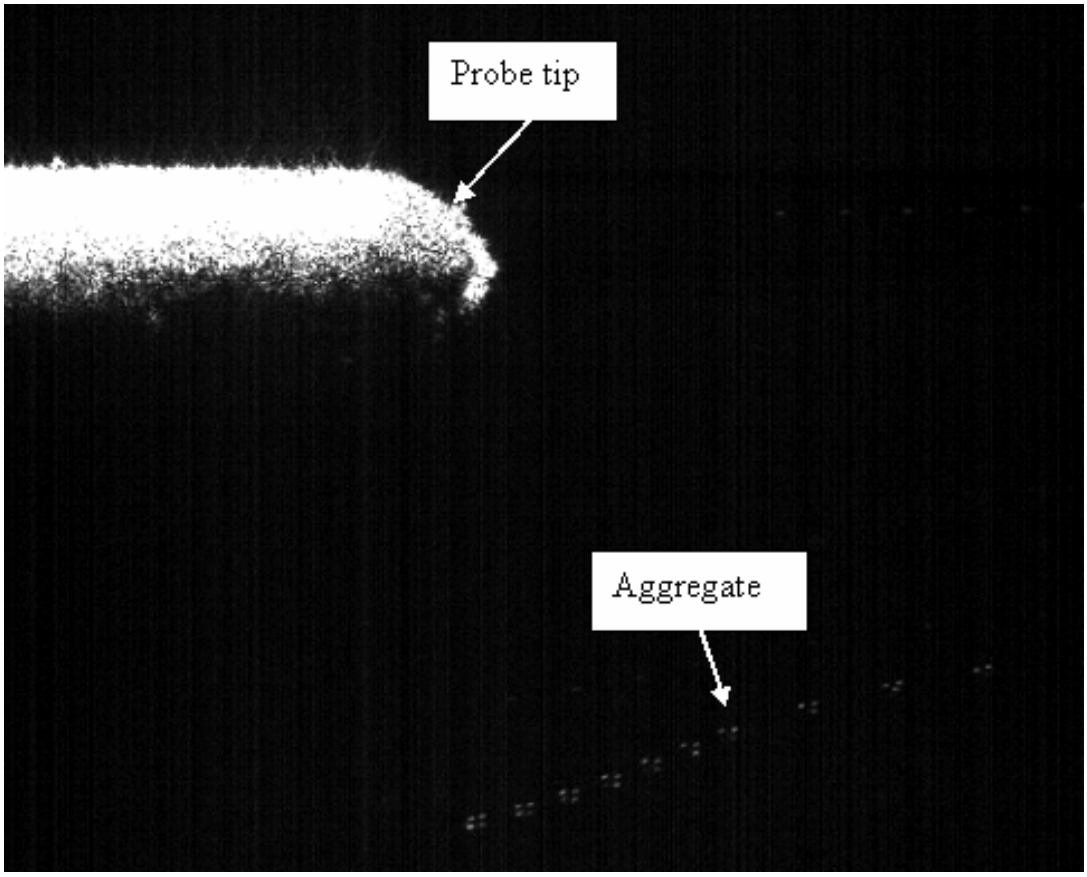

Figure 8.26: Trajectory of an aggregate of acrylic particles at probe voltage -6 kV.

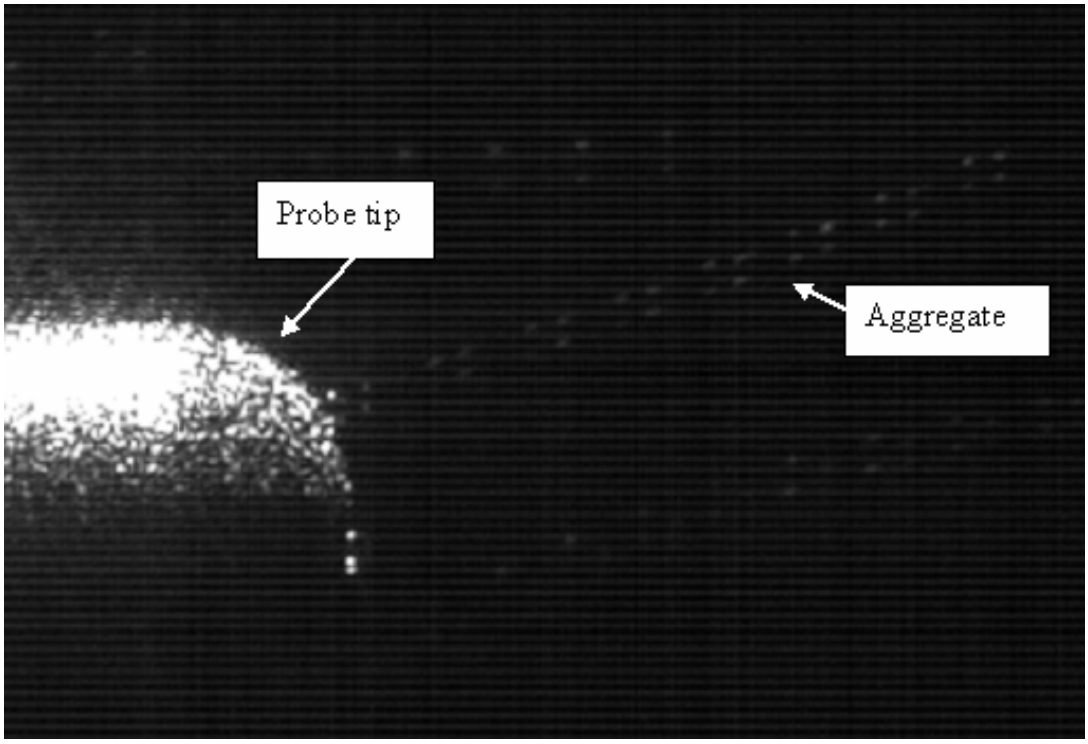

Figure 8.27: Trajectory of a binary aggregate of glass particles at probe voltage -6 kV.

8.7.2 Polarity Change

A few of the trajectories which had a change in probe polarity along the path were also analysed (Figure 8.28 (a)). It was difficult to achieve a good fit of the model trajectory in such cases when charges were confined to net charges (Figure 8.28 (b)). If a dipole was present, as the polarity changed, the dipole on the particle would be expected to reorient to adjust itself in alignment with the new electric field. This may cause a lift in the particles position. Another reason could be the time gap between the flashes during the change in polarity which may not be accurate as it was difficult to say when exactly the transition occurred (the flashes were synchronised with the waveform supply such that the number of flashes halved for a positive waveform but were not synchronised in timing with the waveform). In Figure 8.29 an aggregate of milk particles can be seen rotating with a change in the polarity of the probe from -4 kV to +4 kV. It was difficult to distinguish whether it was a single particle or an aggregate but based on the fact that SEM micrographs of milk particles showed many aggregates and the appearance of the particle was not spherical, it can be assumed to be an aggregate. The rotation which seems to be of 180° may be due to a large dipole on the aggregate which tried to orient itself in the direction of field with the change in polarity.

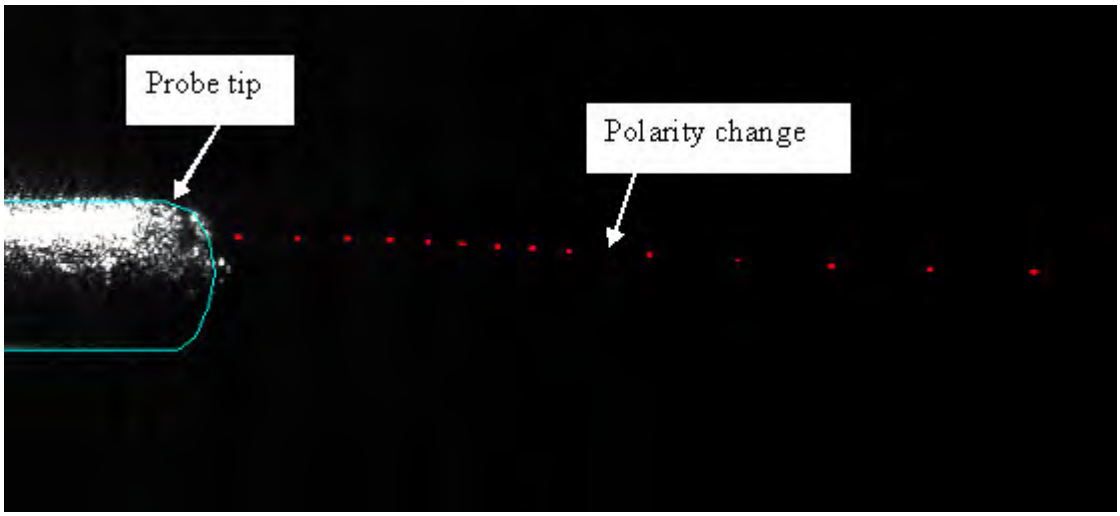

Figure 8.28: (a) Polarity change along the trajectory of an 87 µm acrylic particle at probe voltage +4 kV changing to -4 kV

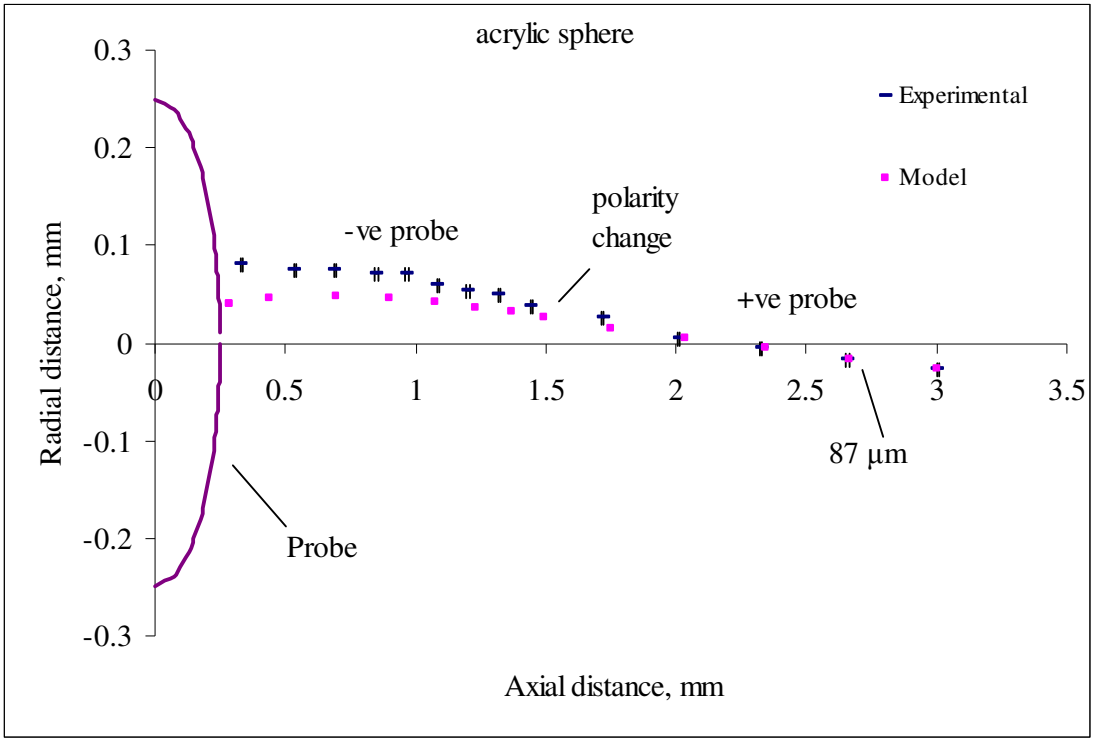

Figure 8.28: (b) Experimental and predicted particle trajectories for an 87 µm acrylic particle with fitted net charge q_{net} = -3.8x10^{-13} C. (Note the enhanced rate of flashes for negative polarity).

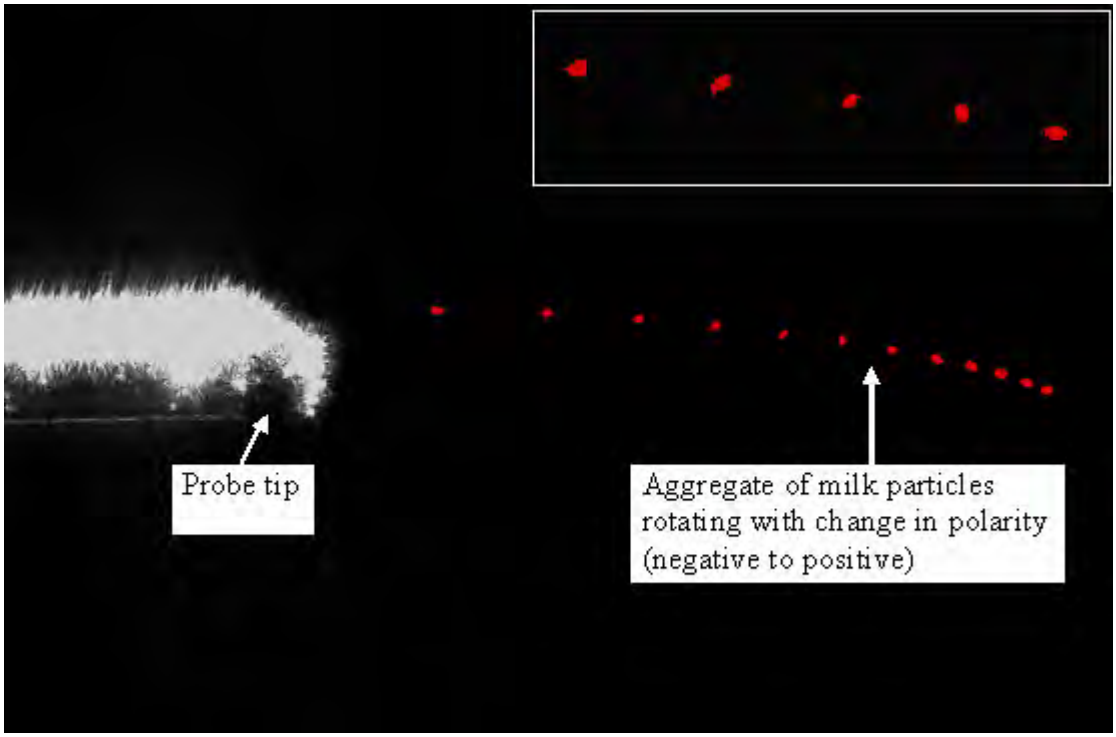

Figure 8.29: Trajectory of an aggregate of milk particles rotating with change in polarity of probe voltage from -4 kV to +4 kV. The insert at the top right end shows an enlarged view of the aggregate rotation.

8.7.3 Jumping of Particles on the Probe Surface

Some particles were observed jumping up and down on the probe surface after they initially touched it. Figure 8.30 (a) has been produced by the combination of four different sequential frames over which the jumping could be observed. The polarity change after the second frame can also be observed but due to lack in clarity it was difficult to model it on the image. During the transition of the polarities the particle seems to travel a little distance in the gas without being visible which made it difficult to follow the trajectory during that part. The particle trajectory was difficult to fit after the polarity change (see Figure 8.30 (b)). The jumping can be simply explained in this case by bouncing of the particle on the probe in the presence of an attractive force to the probe (positive particle, negative probe).

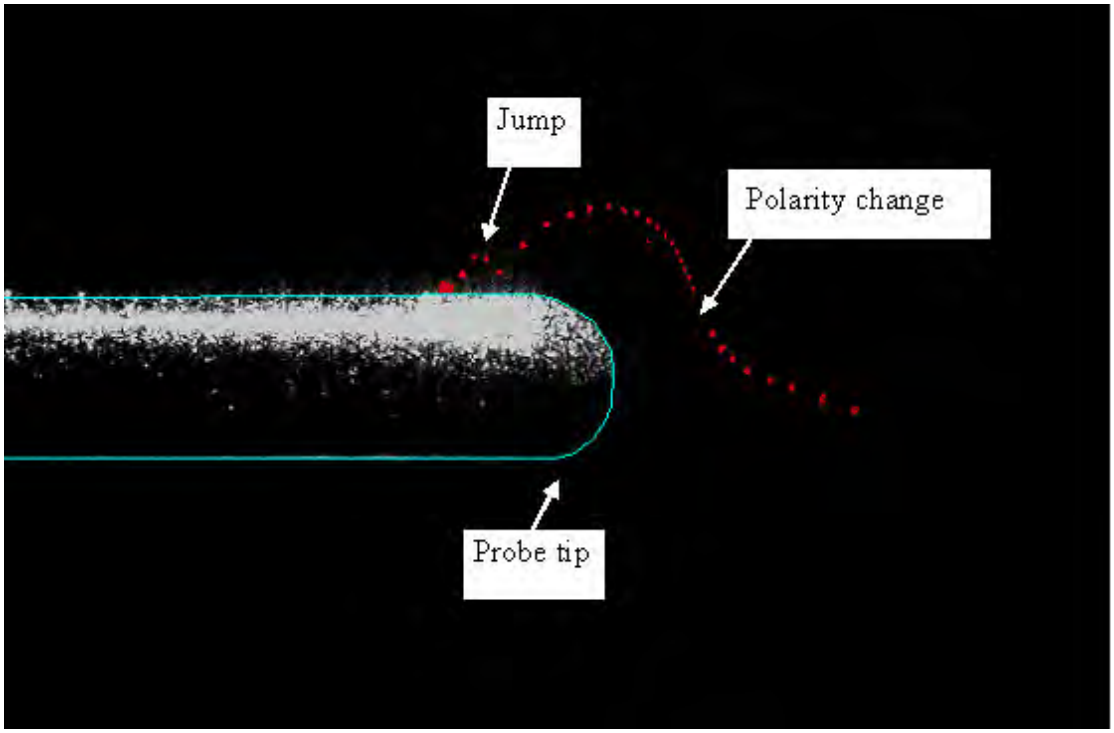

Figure 8.30: (a) A Particle 60 µm acrylic particle jumping on the probe at the probe voltage +5 kV.

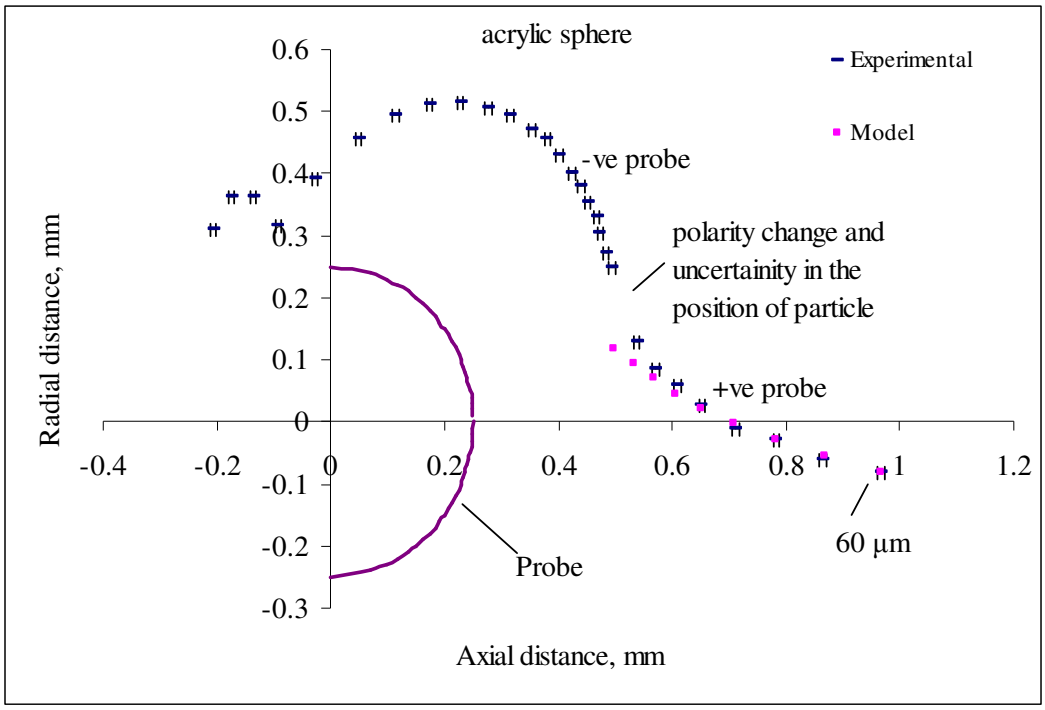

Figure 8.30: (b) Experimental and predicted particle trajectories for the 60 µm acrylic particle with fitted net charge $q_{net} = +1.32 \times 10^{-14}$ C.

8.8 Implications of Dipole Measurements

The "dipole charge" values reported here are a *minimum*, derived from the fitted dipole moment by using the maximum separation distance (particle diameter). In reality, with charge expected to be distributed randomly around each particle surface in patches (Abrahamson and Marshall 2002), most dipole charge separation distances will be smaller. It is interesting that for an appreciable fraction of the glass bubble particles sampled in this study (where permanent dipoles were easier to measure), this minimum charge for the dipole was much larger than the net charge. The particles which have suffered multiple collisions then apparently have high localised surface charges. The summation of all the local charges to get an overall net charge will result in many cases in lower values than patch charges due to mutual cancellation of positive and negative charges. Also the summation of charges over the particle population to get mean charge leads to further cancellation of charges among each other, resulting in a much lower average charge. Based on the study by Gady et al. (1999) there is a possibility that surface charge may be lost from the patches with high charge due to local discharges. Due to these factors original information about the charges on impact is lost.

9. Conclusions and Recommendations

9.1 Conclusions

The technique described in this study opens up the possibility of measurement of the distribution of net charge *and* permanent dipoles on dust and grit in both natural events and in industry. With this technique at the present state of development these distributions can be studied for samples with particle sizes above 10 μm and with minimum charges of the order of ~10^{-16} C (1000 electron charges). It appears to have adequate sensitivity to show for the first time the existence and importance of dipoles on conventionally tribocharged particles. The main conclusions drawn from this study are:

1. Given adequately fast images of particles travelling towards a high voltage probe, it is possible to separate the effects of net particle charge from the effects of a fixed or permanent dipole. This can be done by interpreting a two-dimensional trajectory within a plane central to the probe, using the integration of both translational and rotational particle momentum conservation equations. Positions of the centre of the particle were used in the trajectories. No rotational measurements were used in this study.
2. Image capture for this purpose required a specially designed pulsing laser sheet located within the trajectory plane and synchronised with a fast video camera. The technique limitations of particle size and charge appear to relate to the quality of images, in turn a function of the laser, laser driver and video/optics technology, which were state of art in 2006-2008.
3. Most of the modelled trajectories were adequately fitted to the experimental trajectories within an expected experimental error of ±5 μm (±1 pixel). There were a few cases in which the fitted positions differed more than this, explained by eddies affecting the trajectory, particle bounce back from the probe tip at its last position, adjustment of particle position on the probe surface due to redistribution of charges, and reduced electric field close to the probe tip due to deposition of a dielectric layer, depending on the situation.
4. It was easier to predict permanent dipoles on particles with low dielectric constant and with low mass near the probe as it reduces the induced dipole

force, e.g., for hollow glass bubbles. Most of the trajectories fitted on the basis of net charge alone could also be fitted with both net charge and dipole charge or in some cases alone with dipole charge. So the presence of dipoles on surfaces of such particles cannot be completely ruled out. A dipole charge in the range of $1x10^{-15}$ C to $1x10^{-12}$ C could be fitted on various particles.

5. The smoke and particle studies showed that vortices may affect the orientation of particles after leaving the plates. Hence the introduction of preselector or aligning plates with an aim to fix the particle orientation before it arrived within the influence of the probe field was not successful and they should be removed in future studies.
6. The rotation of particles was considered under dipolar forces and the time calculated for the rotation of most of the particles to come into alignment with the field was within 350 μs. Dipolar forces dominate any rotation caused by vortices and once under the influence of dipolar forces in the probe field the particles become fully aligned within the first two particle images in the trajectory. So the assumption of particles to be aligned with the field from the beginning of their trajectory, although flawed, is not necessary. Thus the simple approach without the use of alignment plates should be successful, leading to a simple, robust technique.
7. All the errors estimated in particle diameter or centre of mass position for various analysis techniques were calculated in terms of a basic uncertainty in position in the image of ±1 pixel, and were judged to be all less than this because of averaging. A conservative ±1 pixel error was applied in the trajectory fitting.
8. The AC voltage square waveform declined from its peak to about 40% of the peak. As the peak value was used in the fitting, this will have resulted in an underestimation of fitted charges.
9. Gravitational force (ignored in most of the work in this thesis) can be easily added to the momentum equation to accommodate for larger size or higher density particles, where it cannot be ignored.
10. The thickness of glass bubble shells was not a uniform fraction of the outer diameter (as assumed) but the error introduced both in the net charge and dipole strength due to this variation was within 2%.

11. Variation in gas direction with time was sensed by smoke studies and also by initial particle directions seen in the frame field of view. These two techniques provided common estimates of eddy velocity and size of eddies passing with the jet plume issuing from the 10 mm diameter nozzle (jet Re ~2000). The eddy velocities were close to that expected from literature measurements of the turbulent velocities of an unbounded jet. The smallest eddy sizes were ~ 10 mm close to the probe tip (larger than the field of view) indicating that the assumption of constant approach angle of gas during the whole trajectory was a reasonable assumption.
12. It was realised that the jet of our study was not an unbounded jet, but was influenced strongly by the boundary walls of the alignment plates. This influence appears to cause strong mixing eddies that invade the jet, causing erratic movements in the flow, sporadically causing sharp changes in direction which could not be explained by normal treatment of this thesis. Based on the jet studies, the removal of the alignment plates is therefore concluded to be essential to reduce this effect.
13. The assumption of Stokes flow around the probe tip was comparable with the COMSOL modelled flow field. The assumed spherical electric field around the probe tip also matched closely with the COMSOL modelled electric field.
14. The mean charge of the particle samples found using the Obolensky filter was an order different to the mean charge found with the probe technique.
15. No corona was observed early in the work, with probe voltages up to 18 kV. However a corona was observed starting at 6.8 kV during the checks conducted after the end of the sampling experiments. This may be due to the impurities deposited on the surface during inspection, or some rupture of the probe tip, as the checks were run after finishing the sampling of particles. Also it was hard to identify the exact position of the corona, whether it was on the tip or to the side towards the shank. The presence of corona cannot be ignored and it will be safe to run the experiments below the observed voltage limit to ensure reliable values of electric field close to the probe tip.
16. Due to the limitations of the measurement technique net charge on highly charged particles with very high density (above 4000 kg/m^3) and large diameters (above 200 μm) may not be fitted with accuracy as inertia overcomes electrostatic forces in such cases. Small particles with low

densities, on the other hand may not even reach the field of view because of electrical repulsion. For these particles, a certain minimum initial velocity is necessary to enter the field of view.

17. The distribution of net charge and dipole strength found with this technique is expected to relate to the conditions of tribocharging (collisions among particles and with walls). It is thus expected that from its further use and development, a) tribocharging of particles will be understood more deeply, and b) consequent dust behaviour may be better predicted, such as the aggregation rates of clouds of particles, their effective diffusivity and effective viscosity as an ensemble (e.g., in a fluid bed, or in a freely flowing granular bed).

9.2 Recommendations and Future Work

1. At present the analysis process is long and tedious. An automation of the whole analysis procedure, starting from image pixels to the final fitted trajectories and charge parameters will be very useful for quick estimation of charge distributions.
2. The presence of dipoles could be found more easily in the case of hollow glass bubbles as compared to other fully solid particles. Keeping this in mind it will be useful to sample more hollow dielectric particles to establish the widespread existence of permanent dipoles due to their surface charges. These hollow particles should behave exactly the same in tribocharging as their fully solid counterparts.
3. In many cases particles were observed to rebound after collision with the probe. A study of impact charging (by modelling the trajectories before and after the collision) can be conducted using the present experimental setup.
4. The preselector or alignment plates need to be removed to reduce the influence of mixing eddies. Also the fan should be used, to create an annular flow and reduce the velocity mismatch between the jet (if one is used) and the surrounding gas, and thus reduce the mixing eddies. The minimal turbulent disturbance to the particle trajectories should come when the sampler samples from a quiescent cloud of particles or from a large flow, with the fan operating.

5. The high voltage AC supply does not have a perfect square waveform and improving this waveform (making it constant at the peak value) can reduce the error in assumed voltages applied to the probe.
6. The modelling of rotation has not been fully resolved at the point close to the end of the rotation where some oscillation is expected due to the particle inertia. This should be resolved in the spreadsheet.
7. In this study the most frequent voltage supply used has been 6 kV. For some broad distributions of particles, it may be necessary to vary the voltages to include the entire charge and dipole distribution of a given sample.
8. Different sizes of probe tip can be used to achieve higher or lower electric field and particle's behaviour in the field will also be affected accordingly.
9. The present high speed camera has a maximum resolution of 1.2 megapixels at a speed of 489 frames/s. A higher resolution giving a better image quality will be useful to improve the distinction between net charge and permanent dipole effects, and between permanent dipole and induced dipole effects, espeically close to the probe. If the laser speckle becomes a limiting factor, a noncoherent light source should be used.
10. A more careful treatment of image charge effects, especially related to the presence of patch charges on the surface of particles (causing dipoles or higher order arrangements), may be beneficial.
11. A number of aggregates were observed, particularly of acrylic particles with a wide size distribution and also of milk particles. The experimental can be used to study the aggregation process by measuring the aggregate size and charge characteristics, especially combined dipole strengths, and perhaps even to see aggregation in the field itself and to explore possible reasons of aggregation.
12. A close study of trajectories captured by the apparatus during a polarity change in the probe voltage should be made, to check the technique and models further.
13. A further investigation on corona discharge close to the probe tip needs to be carried out, to find all the conditions necessary for its prevention.

References

Abraham, F.F., (1970) Functional dependence of drag coefficient of a sphere on Reynolds number. *Physics Fluids*, **13**, 2194-5.

Abrahamson, J., and Dinniss, J.,(2000) Ball lightning caused by oxidation of nanoparticle networks from normal lightning strikes on soil. *Nature*, **403**, 519.

Abrahamson, J., and Marshall, J., (2002) Permanent electric dipoles on gas-suspended particles and the production of filamentary aggregates. *J. Electrostatics*, **55**, 43-63.

Abrahamson, J., (2008) Electrical aspects of nanostructure formation. In: proceeding of *Chemcon-2008,* Chandigarh, India.

Aleksandrov, V.Y., Borodin, I.P., Kechenko, E.V., and Podmoshenskii, I.V., (1982) Rapid coagulation of submicron aerosols into filamentary three-dimensional structures. *Sov. Phys. Tech. Phys.,* **27**,527.

Arridge, R.G.C., (1967) Static electrification of nylon. *Brit. J. Appl. Phys.*, **18**, 1311-1316.

Astbury, G.R., and Harper, A. J., (1999) Large-scale chemical plants: eliminating the electrostatic hazards. In proceedings of *Electrostatics 1999: 10th International Conf.,* Cambridge, U.K., 207-210.

Bailey, A. G., (2001) The charging of insulator surfaces. *Journal of Electrostatics* **51**: 82-90.

Balachandran, W., Ahmad, C.N., and Barton, S.A., (1991) Deposition of electrically charged drug aerosols in lungs. : in proceedings of *Inst. Phys. Conf.* Ser. No.118: Section 1, 57-62.

Balachandran W., Kulon J., Koolpiruck D., Dawson M., and Burnel P., (2003). Bipolar charge measurement of pharmaceutical powders. *Powder Technology,* **135**, 156-163.

Balachandran, W., Machowski, W., Gaura, E., and Hudson, C., (1997) Control of Drug Aerosol in Human Airways Using electrostatic forces. *J. Electrostatics*, **40&41**, 579-584.

Beischer, D., and A. Winkel , (1936) Directed coagulation in aerosols. *Zeitschrift Fur Physikalische Chemie-Abteilung a-Chemische Thermodynamik Kinetik Elektrochemie Eigenschaftslehre* , **176**(1), 1-10.

Bird, R.B., Stewart W.E., and Lightfoot E.N., (1962) *Transport Phenomena,* John Wiley and Sons, New York, USA, 57-58.

Briceno, C., Vivas A. K., et al., (2001) The CIDA-QUEST large-scale survey of Orion OB1: Evidence for rapid disk dissipation in a dispersed stellar population. *Science*, **291**(5501), 93-96.

Bridges, F. G., Supulver K. D., et al., (1996) Energy loss and sticking mechanisms in particle aggregation in planetesimal formation. *Icarus*, **123**(2), 422-435.

Brown, R. C., (1997) Tutorial review: Simultaneous measurement of particle size and particle charge. *Journal of Aerosol Science*, **28**(8), 1373-1391.

Bunker, M.J., Davies M.C., James, M. B., et al., (2007) Direct observation of single particle electrostatic charging by atomic force microscopy. *Pharmaceutical Research*, **24**(6), 1165-1169.

Chan, H.K., (2005) Dry powder aerosol drug delivery- Opportunities for colloid and surface scientists. *Colloids and Surfaces A: Physiochem. Eng. Aspects* **284-285**, 50-55.

Chen, A.H., Bi, H.T., and Grace, J.R., (2003) Measurement of particle charge-to-mass ratios in a gas-solids fluidized bed by a collision probe. *Powder Technology*, **135-136**, 181-191.

Coste, J., and Pechery, P., (1981) Influence of surface profile in polymer metal contact charging. *J. Electrostatics*, **10**, 129-136.

Coury, J., and Clift, R., (1984) The distribution of electrical charge between airborne solid particles. In: *Int. Symp. on Electrical and Magnetic Separation and Filtration Techniques (Antwerp)*, 27-35.

Coury, J.R., Raper, J.A., Guang, D., and Clift, R., (1991) Measurement of electrostatic charge on gas-borne particles and the effect of charges on fabric filtration. *Trans IChemE,* **69**(B), 97-106.

Cross, J.A., (1987) *Electrostatics: principles, problems and applications*, IOP Publishing Limited, Bristol, England.

Davies, D.K., (1967) Examination of the electrical properties of insulators by surface charge measurements. *J.Sci. Instrum.*, **44**, 521-524.

Davies, D.K., (1969) Charge generation on dielectric surfaces. *J. Phys. D: Appl. Phys.*, **2**, 1533-1537.

Dhont, J.K.G., (1996) *An Introduction to Dynamics of Colloids*, Elsevier Science, Amsterdam.

Emets, E. P., V. A. Kascheev and Poluektov, P.P, (1991) Simultaneous Measurement of Aerosol-Particle Charge and Size Distributions. *Journal of Aerosol Science*, **22**(3), 389-394.

Eve, J.K., Patel, N., Luk, S.Y., Ebbens, S.J., and Roberts, C.J., (2002) A study of single drug particle adhesion interactions using atomic force microscopy. *International Journal of Pharmaceutics*, **238**, 17-27.

Fabish, T.J., and Duke, C.B., (1977) Molecular charge states and charge exchange in polymers. *J. Appl. Phys*., **48**, 4256-4266.

Fabish, T.J., Saltsburg, H.M., and Hair, M.L., (1976) Charge transfer in metal-atactic polystyrene contacts. *J.Appl. Phys*., **47**,930-939.

Farrell W.M., Desch M.D., Kaiser M.L., Houser J., Landis G.A., and Wilt D.M.. (2000) Radio and optical detection of Martian dust storm discharges. *Acta Astronautica*, **46**(1), 25-36.

Fermigier M., and Gast A.P., (1992) Structure Evolution in a Paramagnetic Latex Suspension. *Journal of Colloid and Interface Science*, **154**(2), 522-539.

Fowlkes, W.Y., and Robinson, K.S., (1998) The electrostatic force on a dielectric shere resting on a conducting substrate. Mittal K.L., Ed., *Particles on Surfaces 1,* Plenum Press, New York, USA, 143.

Francon, M., (1979) *Laser speckle and applications in optics*, Academic Press, New York, USA, 14-16.

Gady B., Reifenberger R., Rimai, D.S., and DeMejo, L.P., (1997) Contact electrification and the interaction force between a micrometer-size Polystyrene sphere and a graphite surface. *Langmuir,* **13**, 2533-2537.

Gady, B., Quesnel, D.J., Rimai, D.S., Leone, S., and Alexandrovich P., (1999) Effects of Silica additive concentration on toner adhesion, cohesion, transfer, and image quality. *Journal of Imaging Science and Technology* , **43**(3),288-294.

Gross M., Kiskamp S., (1997) New Long-Range Interaction between Dipolar Chains. *Physical Review Letters*, **79**(13), 2566-2569.

Haenen, H.T.M., (1976) Experimental investigation of the relationship between generation and decay of charges on dielectrics. *J. Electrostatics*, **2**,151-173.

Hamamoto, N., Nakajima, Y., and Sato, B., (1992) Experimental discussion on maximum surface charge density of fine particles sustainable in normal atmosphere. *Journal of Electrostatics*, **28**, 161-173.

Harper W.R., (1967) *Contact and Frictional Electrification*, Oxford University Press, London, England.

Hassel, E., Jahnke, S., Kornev, N., Tkatchenko, I., and Zhdanov V., (2006) Large eddy simulation and laser diagnostic measurements of mixing in a coaxial jet mixer. *Chemical Engineering Science*, **61**(9), 2908-2912.

Hays, D. A., and W. H. Wayman, (1989) Adhesion of a Nonuniformly Charged Dielectric Sphere. *Journal of Imaging Science,* **33**(5), 160-165.

Hays, D.A., (1978) Electric field detachment of toner. *Photogr. Sci. Eng*., **22**,232.

He J., Cutler P.H., Miskovsky, N.M., and Feuchtwang T.E.,(1991) Derivation of the image interaction for non-planar pointed emitter geometries:application to field emission I-V characteristics. *Surface Science* **246**, 348-364.

He, G., Muser, M.H., and Robbins, M.O., (1999) Adsorbed layers and the origin of static friction. *Science* **284**, 1650-1652.

Helgesen G., Skjeltorp A.T., Mors P.M., Botet R., and Jullien R.,(1988) Aggregation of Magnetic Microspheres:Experiments and Simulations. *Physical Review Letters*, **61**(15), 1736-1739.

Hogue, M.D., Mucciolo, E.R., and Calle, C.I., (2006) Insulator-insulator contact charging as a function of pressure. 5th *World Congress on Particle technology*, Orlando, Florida, USA.

Holscher, H., Schirmeisen, A., and Schwarz, D., (2008) Principles of atomic friction: from sticking atoms to superlubric sliding. *Phil. Trans. R. Soc. A*, **366**, 1383-1404.

Homewood, K. P., and A. C. Roseinnes (1982) An Investigation of Contact-Charge Accumulation on Insulators Repeatedly Touched by Metals. *Journal of Physics D-Applied Physics***, 15**(11), 2283-2296.

Homewood, K. P., (1984) An Experimental Investigation of the Depth of Penetration of Charge into Insulators Contacted by a Metal. *Journal of Physics D-Applied Physics,* **17**(6), 1255-1263.

Hull, H.H., (1949) A method for studying the distribution and sign of static charges on solid materials. *Journal of Applied physics*, **20**, 1157.

Iedema, M.J., Dresser, M.J., Doering, D.L., Rowland, J.B., Hess, W.P., Tsekouras, A.A., and Cowin, J.P., (1998) Ferroelectricity in water ice. *Journal of Physical Chemistry B*, **102**, 9203-9214.

Jeffrey, G.B., (1915) Steady rotation of a solid of revolution in a viscous fluid. *Proc. London Math. Soc.* (2)**14**, 327-338.

Johnson, K.L., Kendall, K., Roberts, A.D., (1971) Surface energy and contact of elastic solids. *Proc. Roy. Soc. London Ser. A*, **324**, 301-&.

Jones, T.B., (1995) *Electromechanics of Particles*, Cambridge University Press, New York, USA, 199-200.

Karma, A.K., (1972) Measurements of the electrical properties of dust storms. *Journal of Geophysical Research*, **77**, 585-590.

Keogh, M.K., Murray, C.A., and O'Kennedy, B.T., (2003) Effects of ultrafiltration of whole milk on some properties of spray-dried milk powders. *International dairy journal*, **13**, 995-1002.

Knutson, E.O., and Whitby, K.T. (1975) Aerosol classification by electrical mobility: apparatus, theory and applications. *J.Aerosol Sci.*, **6**, 443-451.

Ko Y.T.C., Huang J.P., and Yu K.W., (2004) The dielectric behaviour of single-shell spherical cells with a dielectric anisotropy in the shell. *J .Physics: Condens. Matter*, **16**, 499-509.

Kornfeld, M.I., (1976) Frictional Electrification. *Journal of Physics D-Applied Physics,* **9**(8), 1183-1192.

Kousaka, Y., Okuyama, K., Adachi, M., and Ebie, K., (1981) Measurement of electric charge of aerosol particles generated by various methods. *J. Chem. Eng. Japan*, **14**(1), 54-58.

Kousaka, Y., M. Adachi, Okuyama, K., Kitada, N., and Motouchi, T., (1983) Bipolar Charging of Ultrafine Aerosol-Particles. *Aerosol Science and Technology*, **2**(4), 421-427.

Krupa, A., and Jaworek, A. (1989) A method for aerosol particles charge measurement. *J. Electrostatics*, **23**, 289-292.

Kulon, J., Malyan B., and Balachandran W., (2003) Simultaneous measurement of particle size and electrostatic charge distribution in DC electric field using Phase Doppler Anemometry. *IEEE Transactions on Industry Applications***,** **39**(5), 1522-1528.

Kunkel, W. B., (1950) The Static Electrification of Dust Particles on Dispersion into a Cloud. *Journal of Applied Physics*, **21**(8), 820-832.

Lacks, D.J., and Levandovsky, A., (2007) Effect of particle size distribution on the polarity of triboelectric charging in granular insulator systems. *J. Electrostatics*, **65**, 107-112.

Lamb H., (1952) *Hydrodynamics*, Cambridge University Press, New York, USA, 588-589.

Lee, M. H. and Ayala J. (1985) Adhesion of Toner to Photoconductor. *Journal of Imaging Technology*, **11**(6), 279-284.

Lee, M. H., (1986) Toner Adhesion in Electrophotographic Printers. *Proceedings of the SID*, **27**(1), 9-14.

Lewis, B.M., David, P., and Lesqueren, A.M., (1995) Mainline OH detection rates from blue circumstellar shells. *Astronomy and Astrophysics Supplement Series*, **111**(2), 237-254.

Lim, T.T., (2000) *Flow visualisation-techniques and examples*, Imperial college press, London, England, 43-72.

Loeb, L.B., (1965) *Electrical Coronas: Their Basic Physical Mechanisms*, University of California Press, California, USA.

Loeb, L.B., Parker, J.H., Dodd, E.E., and English, W.N., (1950) The choice of suitable gaps forms for the study of corona breakdown and the field along the axis of a hemispherically capped cylindrical point-to-plane gap. *The Review of Scientific Instrument*, **21**(1), 42-27.

Lowell, J., (1976) The electrification of polymers by metals. *Journal of Physics D-Applied Physics*, **9**, 1571-85.

Lowell, J., and Rose-Innes A.C., (1980) Contact electrification. *Advances in Physics*, **29**(6), 947-1023.

Marshall J.R., Freund F., T. Sauke, and M. Freund, (1997) Catastrophic collapse of particulate clouds: Implications from aggregation experiments in the USML-1 and USML-2 glovebox. NASA TM 1998-208697, Second United States Microgravity Laboratory: One Year Report, **2**, 35/579-35/592.

Marshall, J.R. Cuzzi J.N., (2001) *in: proceedings of the 32nd Lunar and Planetary Science Conference (LPSC)*, Texas, USA, 1262.

Marshall, J.R., and Sauke T.B., (1999) Computer modelling of electrostatic aggregation of granular materials in planetary and astrophysical settings. in: *proceedings of the 30th Lunar and Planetary Science Conference (LPSC)*, Lunar and Planetary Institute(LPI), Texas, USA, 1234.

Marshall, J.R., Sauke, T.B., and Cuzzi J.N., (2005) Microgravity studies of aggregation in particulate clouds. *Geophys. Res. Lett*., **32**, 11202

Material safety datasheet, (2007) 3M^{TM} Glass bubbles K15.

Matsuyama T., and Hideo Y., (1995) Charge relaxation process dominates contact charging of a particle in atmospheric conditions. *Appied Physics*, **28**(12), 2418-2423.

Matsuyama, T., and Yamamoto, H., (2006a) Impact charging of particulate materials. *Chemical Engineering Science*, **61**, 2230-2238.

Matsuyama, T., and Yamamoto, H., (2006b) Measurement of force curves due to electrostatic charge on a particle. in: *5th World Congress on Particle technology*, Orlando, Florida USA.

Mazumder M.K., Sims R.A., et al., (2006) Twenty-first century research needs in electrostatic processes applied to industry and medicine. *Chemical Enginering Science,* **61**, 2192-2211.

Mazumder, M.K., Ware, M.E., Yokoyama, T., Rubin, B.J., and Kamp, D., (1991) Measurement of particle size and electrostatic charge distributions on toners using E-SPART analyzer. *IEEE Trans. Ind. Applicat*, **27**, 611-618.

Milikan, R. A., (1950) Autobiography of Robert A. Millikan, Prentice-Hall, USA.

Montgomery, D.J., (1959) Static electrification of solids. *Solid state Physics*, **9**, 139-196.

Mott, N.F., (1968) Electrons in disordered structures. *Advances in Physics*, **16**, 49-144.

Mueller, T.J., (1983) Smoke visualisation in wind tunnels. *Astronautics & Aeronautics*, 50-54 and 62.

Nakayama, K., (1996) Tribocharging and friction in insulators in ambient air. *Wear*, **194**, 185-189.

New England Precision Grinding, (2007) 35 Jeffrey Avenue, Holliston, MA, USA.

Nuth, J.A., and Berg O., (1994) Magnetically Enhanced Coagulation of Very Small Iron Grains: A correction to the enhancement factor due to dipole-dipole interactions. *Icarus*c, **107**, 155-163.

Nuth, J.A., and Wilkinson, G.M., (1995) Magnetically Enhanced Coagulation of Very Small Iron Grains. *Icarus*, **117**, 431-435.

Ohara, K., Nakamura I., and Kinoshita, M., (2001) Frictional electrification between flat surfaces of polymers and of Langmuir-Blodgett layers. *Journal of Electrostatics,* **51**, 351-358.

Ossenkopf, V., (1993) Dust coagulation in dense molecular clouds- the formation of fluffy aggregates. *Astronomy and Astrophysics*, **280**, 617-646.

Peek, F.W., (1929) *Dielectric phenomena in high voltage engineering,* Mcgraw Hill, New York, USA.

Penney, G.W. and Lynch, R.D., (1957) Measurements of charge imparted to fine particles by corona discharge. *AIEEE Trans.,* **76**, 294-299.

Pollock, H.M., Burnham, N.A., and Colton R.J., (1995) Attractive forces between micron-sized particles: a patch charge model. *J. Adhesion*, **51**, 71-86.

Promislow J.H.E., Gast A.P., and Fermigier M., (1995) Aggregation kinetics of paramagnetic colloidal particles. *J.Chem.Phys*., **102**(13), 5492-5498.

Reyes, E.A., Levya, P.D., and Lara, L.A., (2005) Microrheology from rotational diffusion of colloidal particles. *Physical Review Letters*, **94**, 106001.

Roth, J., and Dignam, M.J., (1973) Scattering and extinction cross sections for a spherical particle coated with an oriented molecular layer. *Journal of the Optical Society of America*, **63**, 308-311.

Russ, J.C., (2007) *The Image Processing Handbook,* CRC Press, Boca Raton.

Schein, L.B., (1999) Recent advances in our understanding of toner charging. *Journal of Electrostatics*, **46**, 29-36.

Schmeisser, D., Bohme, O., Yfantis, A., Heller, T., and Batchelor, D.R., (1999) Dipole moment of nanoparticles at interfaces *Physical Review Letters,* **83**, 380.

Schulz, H., (1998) Mechanism and factors affecting intrapulmonary particle deposition: implications for efficient inhalation therapies. *Pharmaceutical Science and Technology Today*, **1**, 336-344.

Schumann, W.O., (1923) *Elektrische Durchbruchfeldstarke von Gasen*, Springer, Berlin, Germany.

Sounilhac, S., Barthel, E., and Creuzet, F., (1999) The electrostatic contribution to the long-range interactions between tungsten and oxide surfaces under ultrahigh vacuum. *Applied Surface Science*, **140**, 411-414.

Sternovsky, Z., Robertson, S., Sickafoose, A., Colwell, J., and Horanyi, M., (2002) Contact charging of lunar and Martian dust simulants. *Journal of geophysical research*, **107**(15), 1-8.

Stokes C.G., (1850) *Trans. Cambridge Phil. Soc.*, **9**, 8.

Takeuchi, M., (2006) Adhesion force of charged particles. *Chemical Engineering Science*, **61**, 2279-2289.

Wang, H., Bell, R.C., Iedema, M.J., et al., (2005) Sticky ice grains aid planet formation: Unusual properties of cryogenic water ice. *Astrophys. J* **620**(2), 1027-1032.

Watanabe, H., Samimi A., Ding, Y., and Ghadiri, M., (2006) Measurement of charge transfer due to single particle impact. *Particle & Particle Systems Characterization*, **23**(2), 133-137.

Wilcox, D.C., (1998) *Turbulence modelling for CFD*, DCW Industries Inc.

Withey, P.A., and Nuth J.A., (1999) Formation of Single-Magnetic-Domain Iron Particles via Vapor-Phase Nucleation: Implications for the Solar Nebula. *Icarus*, **139**, 367-373.

Wygnanski, I., and Fiedler, H., (1969) Some measurements in the self-preserving jet. *J.Fluid Mech.* **38**, 577-612.

Zebel, G., Coagulation of aerosols. (1996) Davies C. N. (Ed.), *Aerosol Science,* Academic Press, New York, USA, 31.

Appendix A.1 Design of Pre Selector Plates

Terminal velocity u_t of a spherical particle in an electric field is determined by the balance of two forces:

Aerodynamic drag force on a particle given by the Stokes Law,

$$F_d = 3\pi\mu x u_t \tag{A.1}$$

Electrostatic force on a particle with charge q, in a field E_o is given by

$$F_e = q E_o \tag{A.2}$$

The particle accelerates and rapidly reaches its terminal velocity where the aerodynamic drag is balanced by the electrostatic force and hence Equation 3.1 can be equated to Equation 3.2.

$$F_d = 3\pi\mu x u_t = F_e = qE_o$$

$$u_t = \frac{qE_o}{3\pi\mu x} \tag{A.3}$$

The maximum charge on the particle is calculated from Pauthenier limit and given by equation (Cross,1987, Page 147)

$$q_{max} = 4\pi\varepsilon_0 p E_c r_p^{\,2} \tag{A.4}$$

where E_c is the electric field in which the particle is charged, ε_0=8.8 x 10^{-12} F/m,

r_p is the radius of particle and $p = \frac{3\varepsilon_r}{(\varepsilon_r + 2)}$.

p varies between 3 for a conducting particle (relative dielectric constant ∞) and 1 for an insulating particle of relative dielectric constant 1. For a material of dielectric constant 2, p = 1.5.

The following values were assumed to design the plates:

- Viscosity of air, μ = 1.8 x 10^{-5} Pa s

- Diameter of particle, x = 90 x 10^{-6} m

- Axial velocity, u_a =20 m/s

- At 10 kV voltage electric field between the plates assumed to be 10 mm apart is given by E_o = 10,000 V/ 10 x 10^{-3} m = 1 x 10^6 V m^{-1}.

Substituting the values in Equation A.3 and A.4 the terminal velocity u_t was calculated to be 22.1 m/s. The collection time for which the particle must remain in plates in order to travel distance to get collected on it, *t*, is the ratio of distance between plates and the terminal velocity. The value of *t* was calculated to be 4.5 x 10^{-4} s and based on this collection time the dimensions of each plate were assumed to be 100 x 30 mm. The effective width was assumed to be 20 x 10^{-3} m, so the effective collection area A_t was calculated to be 2 x 10^{-3} m^2 and the volume of collection cell, V to be 30 x 10^{-6} m^3.

Turbulent mixing gives an exponential efficiency equation (Deutsch equation)

$$\eta = 1 - exp\left(\frac{-u_t A_t L}{u_a V} \right) \qquad \text{(A.5)}$$

The values were substituted in Equation A.5 as below

$$\eta = 1 - exp\left(\frac{-22.135 * 2e-3 * 100e-3}{20 * 30e-6} \right)$$

which resulted in an efficiency of 0.9994.

Appendix A.2 Pulsed LASER Diode

A.2.1 Warnings

- This laser is a class 3B laser device, and the output, even when reflected off a shiny surface (glass, metal, glossy paint etc) can permanently damage eye sight.

- Never look into the laser or it's specular reflections.

- Never point the laser towards other people, or areas people may enter. Always ensure the laser beam is terminated at the end of it's useful path, by a solidly mounted barrier.

- Laser safety glasses suitable for 670nm wavelength and of optical density 2 or greater are recommended to be worn when operating the laser in any situation where exposure to the beam may occur.

- The electronic controls are not a failsafe method of preventing laser emission, so always treat the laser as on, unless the power supply is positively disconnected by removal of the supply cord.

- The wavelength is 670nm (deep red), at which the human eye is not particularly sensitive. This means that the light output is much stronger than it may appear. If the light were green, it would appear more than ten times stronger.

- Other operating procedures may be required, and the local standard should be consulted for guidance. AS/NZS in New Zealand and Australia. IEC in Europe and ANSI in the US.

A.2.2 General Description

A diode based laser light source capable of 300mW optical output.

The laser diode is temperature stabilised to 25 degrees by a thermoelectric heat pump and closed loop control. This enables stabilization of the laser diode output when it is driven by a constant current source.

A constant current drive circuit is built into the laser head, and laser output is initiated by a TTL signal on the control line. The rise and fall time is fast, allowing pulses of 500 nS to be created.

The laser diode controller controls various aspects of the laser operation such as power supply, temperature control and pulse timing. Connection between the controller and laser head is via an umbilical cable fitted with 9 pin plugs at each end. Alteration of this cable is not recommended as it contains multiple cores, some of which are coaxial. Increase in length of this cable may result in unpredictable performance, or failure of the temperature control system.

A.2.3 In Use

Ensure all cables are correctly installed before connecting power.

It is recommended to disable laser power by switching the key switch to the horizontal position, before turning on power as this will prevent unanticipated laser emission.

Switch on power, via either the wall switch or the switch on the back of the controller near the power inlet.

The power light should come on, and the temperature good light may briefly illuminate and go off. If the laser diode is already at 25 degrees, the temperature good light will remain on; otherwise temperature will take 1 or 2 minutes to stabilise. When

the temperature has stabilised, the temperature good light will remain on, and after a few seconds an internal relay will switch on power to the laser power supply circuit.

The laser key switch may now be switched on, and the laser power light will illuminate to indicate the laser circuit is energised. Depending on the front panel settings of the controller, and any trigger signals present, laser emission may now be present.

There are two inputs provided on the front panel, a trigger input and an enable input. The trigger input will initiate a pulse sequence, as programmed by the switches on the front panel, on either a positive (rising edge) or a negative (falling edge) TTL transition, as set by the toggle switch. The enable input is pulled high internally by a resistor, pulling this low externally prevents trigger pulses from initiating a pulse sequence.

The rotary switches on the front panel are used to program the pulse sequence timing. The first two switches control the interval between pulses, the third switch sets the number of pulses to be generated (this can be set for infinite, in which case the pulses will automatically start, and run continuously). The fourth switch controls the pulse duration. If the pulse duration is equal to or longer than the pulse interval, the laser will produce light continuously, with no pulses generated.

When long pulse intervals are selected, the pulses may stop for a long period of time due to the internal counter operation being interrupted by the selection process. The counter may be reset by using the reset toggle switch on the front panel, and normal operation will then resume.

The pulse output connector on the front panel allows the pulse sequence, as sent to the laser head, to be monitored.

Appendix A.3 Particle Size Distributions

Figure A.1 shows the particle size distribution for a sample of glass bubbles and Figure A.2 shows the particle size distribution for acrylic spheres (MR-90 G) when passed through the X-100 laser analyser in a wet run using water.

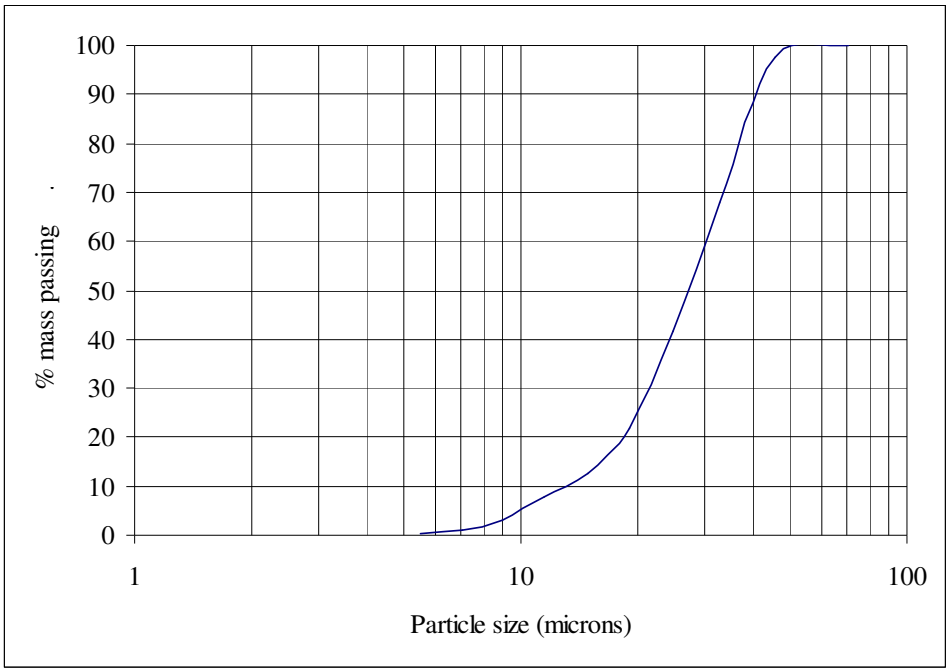

Figure A.1: Particle size distribution of glass bubbles as measured in a wet run (using water) by the X-100 laser size analyser.

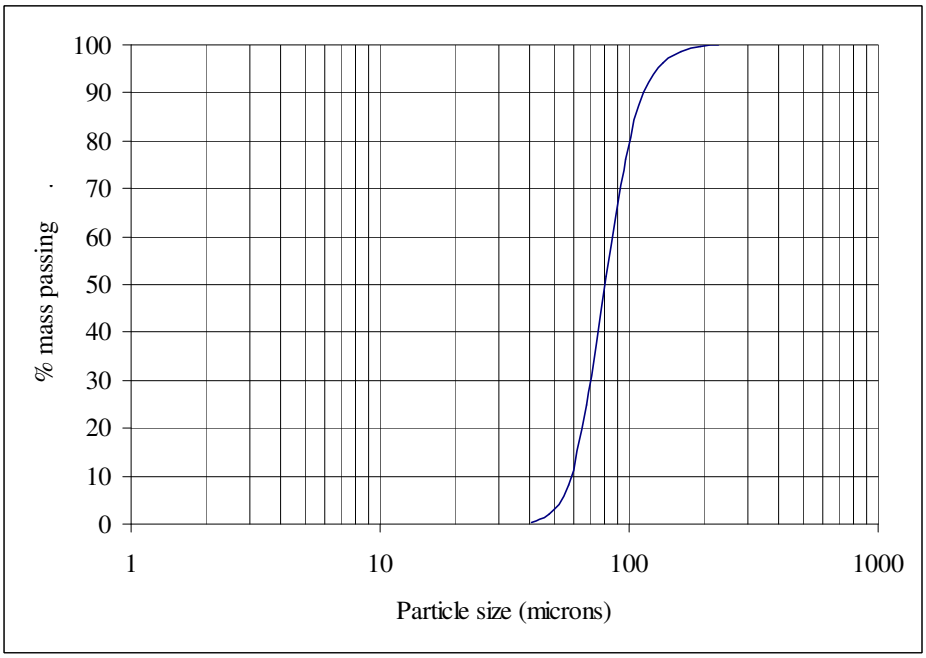

Figure A.2: Particle size distribution of acrylic spheres (MR-90G) as measured in a wet run (using water) by the X-100 laser size analyser.

Appendix A.4 Net Charge Measurements

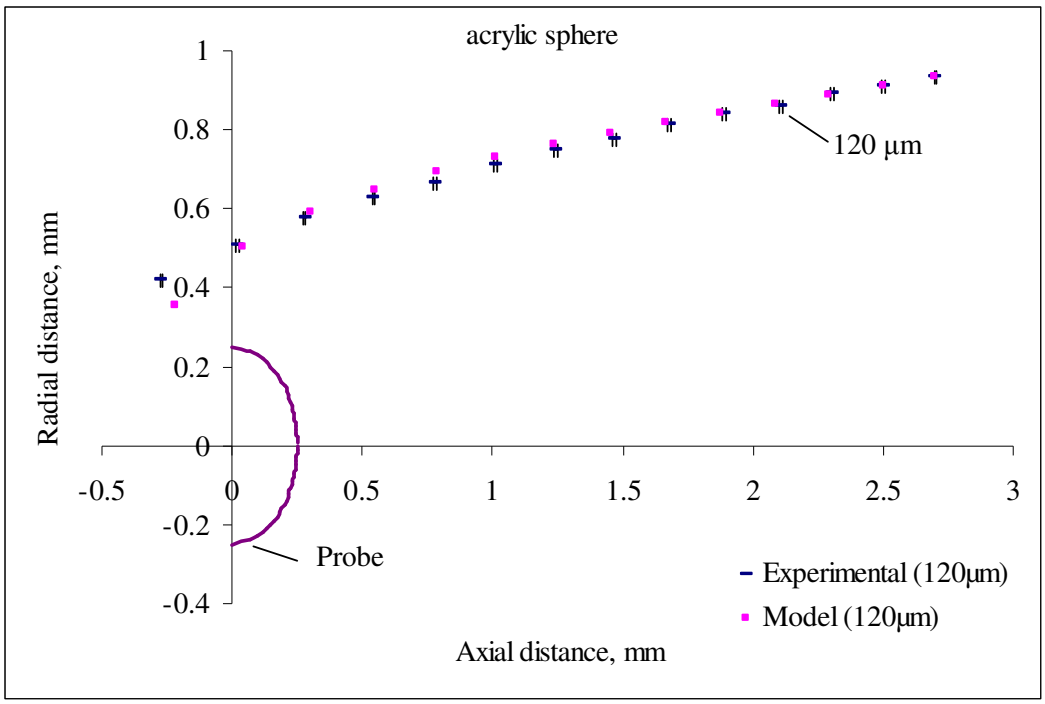

Figure A.3: Experimental and predicted particle trajectories for a 120 µm acrylic particle with probe voltage -4kV with fitted net charge q_{net} = +5.1x10^{-13} C.

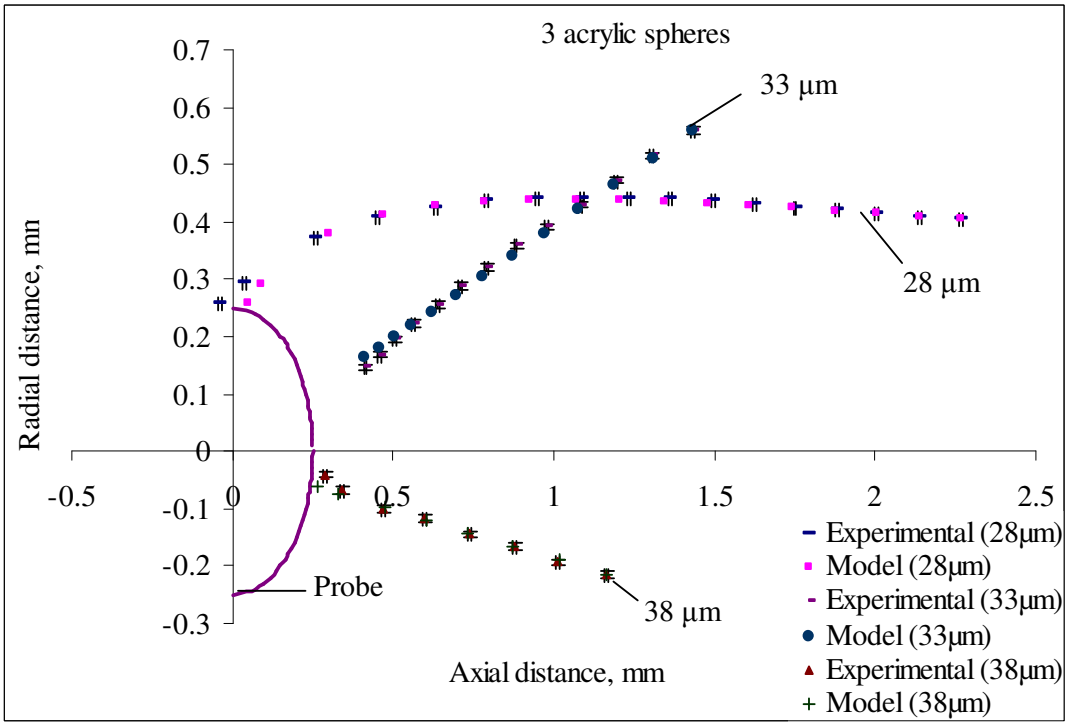

Figure A.4: Experimental and predicted particle trajectories at probe voltage -6 kV for a 28µm acrylic particle with fitted net charge q_{net} = 2.8x10^{-15} C, a 33 µm acrylic particle with fitted net charge q_{net} = -4.1x10^{-15} C and a 38 µm acrylic particle with fitted net charge q_{net} = -3.5x10^{-15} C.

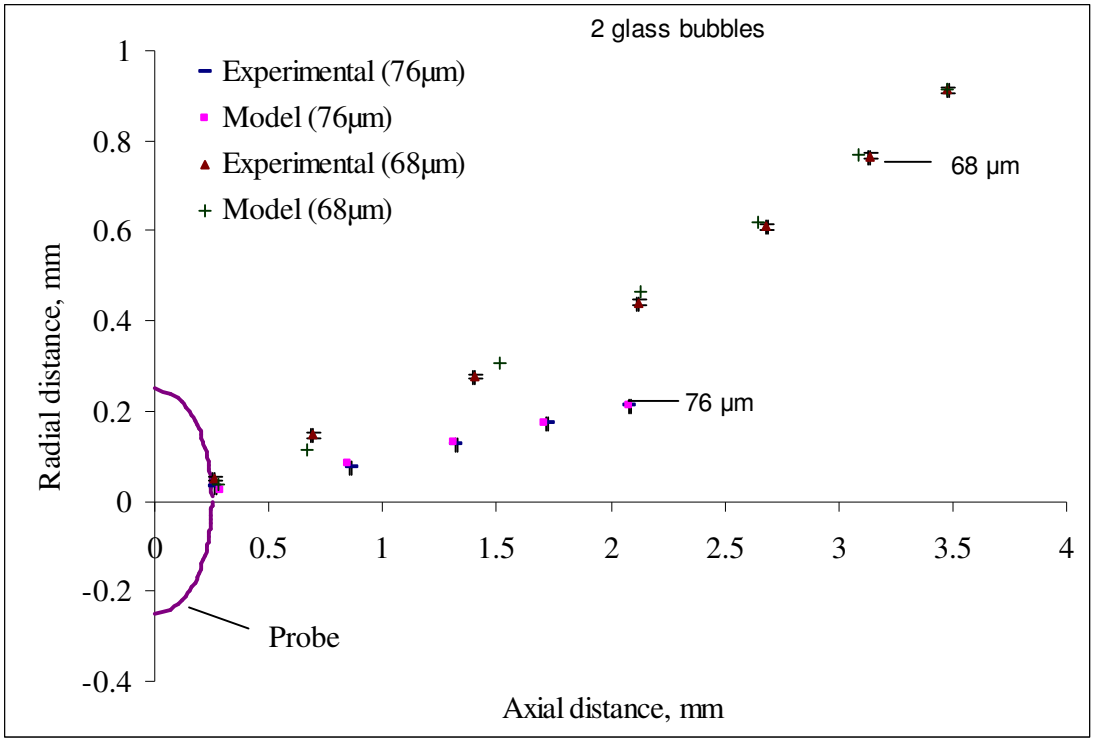

Figure A.5: Experimental and predicted particle trajectories for a 76 µm glass particle with probe voltage -10kV with fitted net charge q_{net} = +6.5x10^{-14} C and a 68 µm glass particle with probe voltage -10kV with fitted net charge q_{net} = +2.5x10^{-13} C.

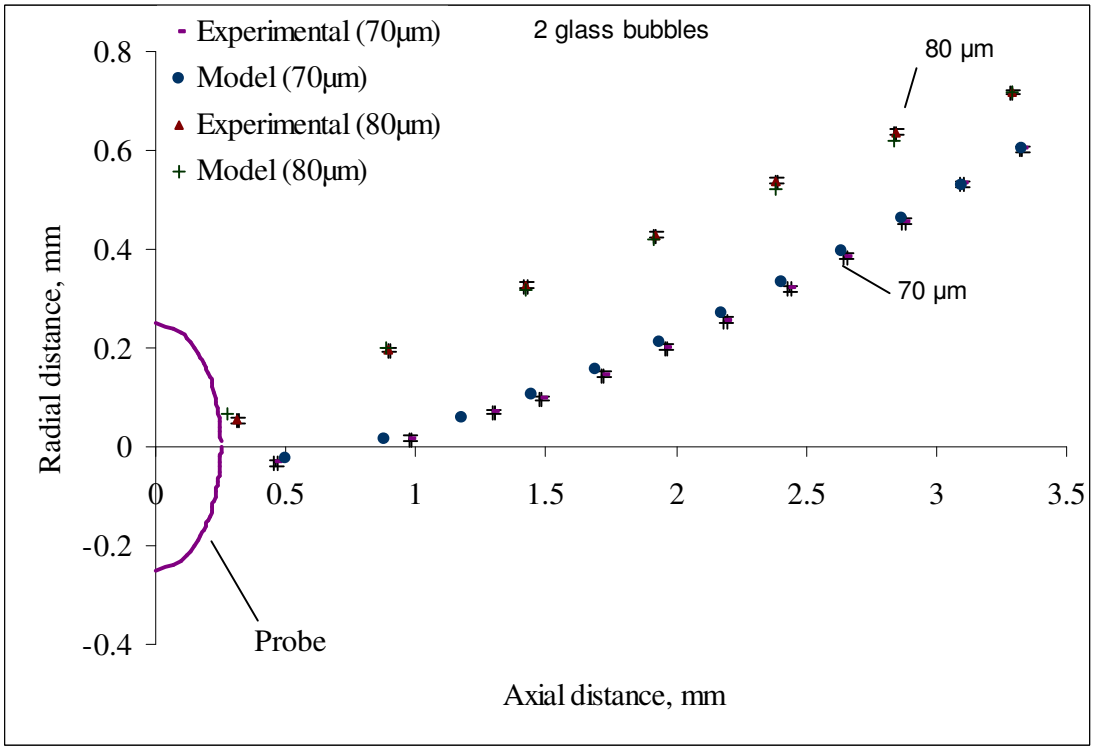

Figure A.6: Experimental and predicted particle trajectories for a 70 µm glass particle with probe voltage -6kV with fitted net charge q_{net} = +3x10^{-15} C and an 80 µm glass particle with probe voltage 6kV with fitted net charge q_{net} = -3.8x10^{-14} C.

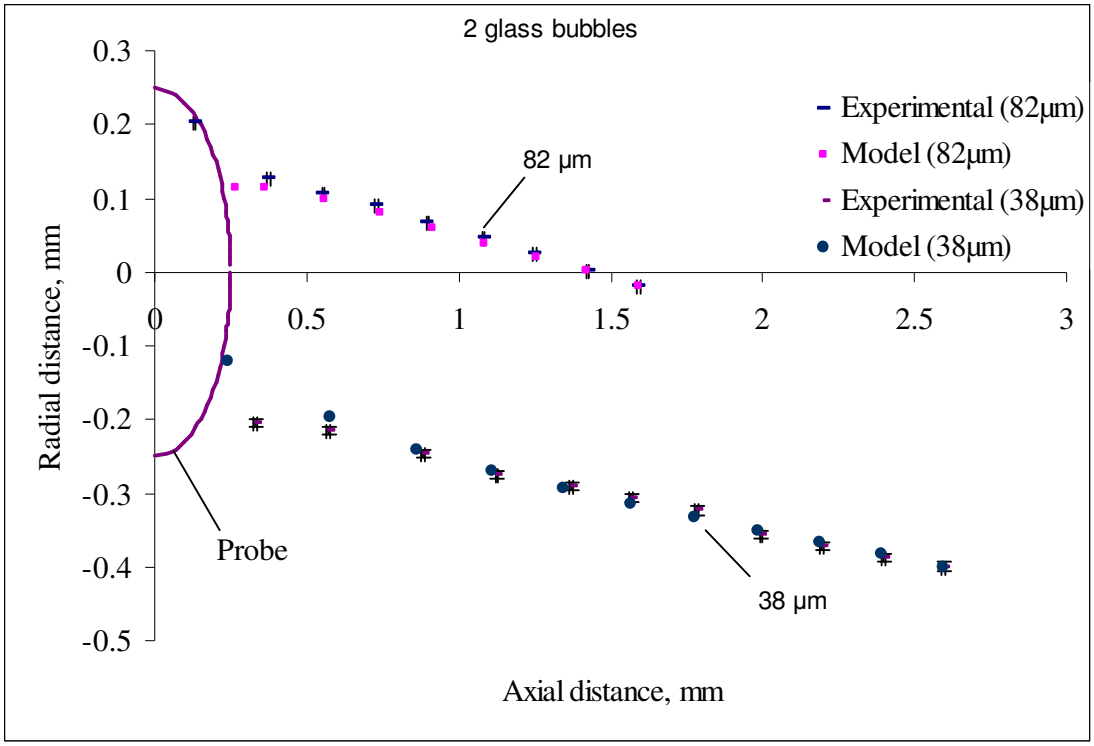

Figure A.7: Experimental and predicted particle trajectories for an 82 µm glass particle with probe voltage -6 kV with fitted net charge q_{net} = +6.5x10^{-15} C and a 38 µm glass particle with probe voltage -7 kV with fitted net charge q_{net} = +6.5x10^{-15} C.

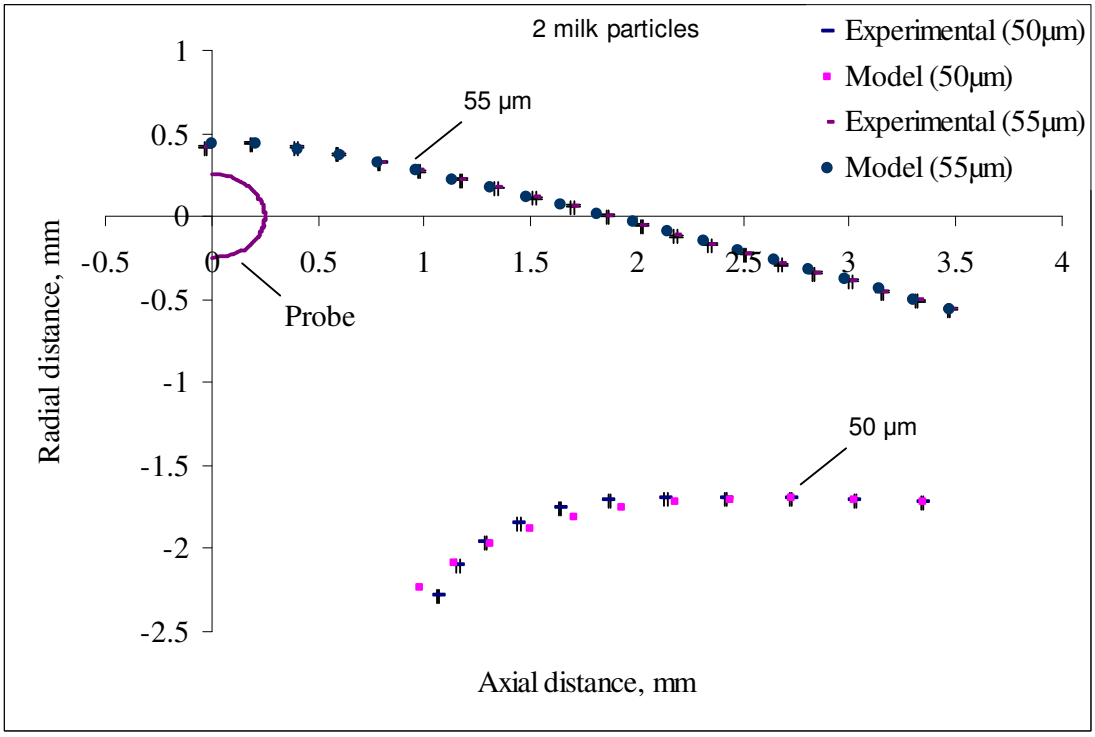

Figure A.8: Experimental and predicted particle trajectories for a 50 µm milk particle with probe voltage +6 kV with fitted net charge q_{net} = +1.07x10^{-13} C and a 55 µm milk particle with probe voltage -4 kV with fitted net charge q_{net} = +2.02x10^{-14} C.

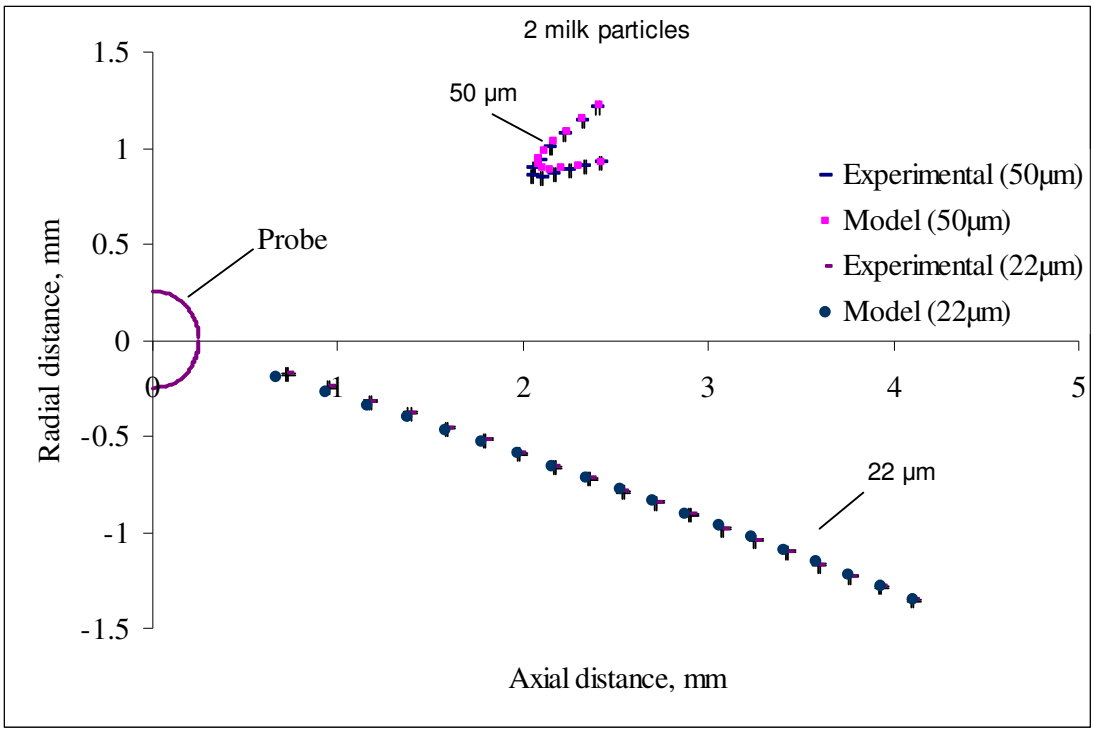

Figure A.9: Experimental and predicted particle trajectories for a 50 µm milk particle with probe voltage +6 kV with fitted net charge q_{net} = +8x10^{-14} C and a 22 µm milk particle with probe voltage -4 kV with fitted net charge q_{net} = +1.1x10^{-14} C.

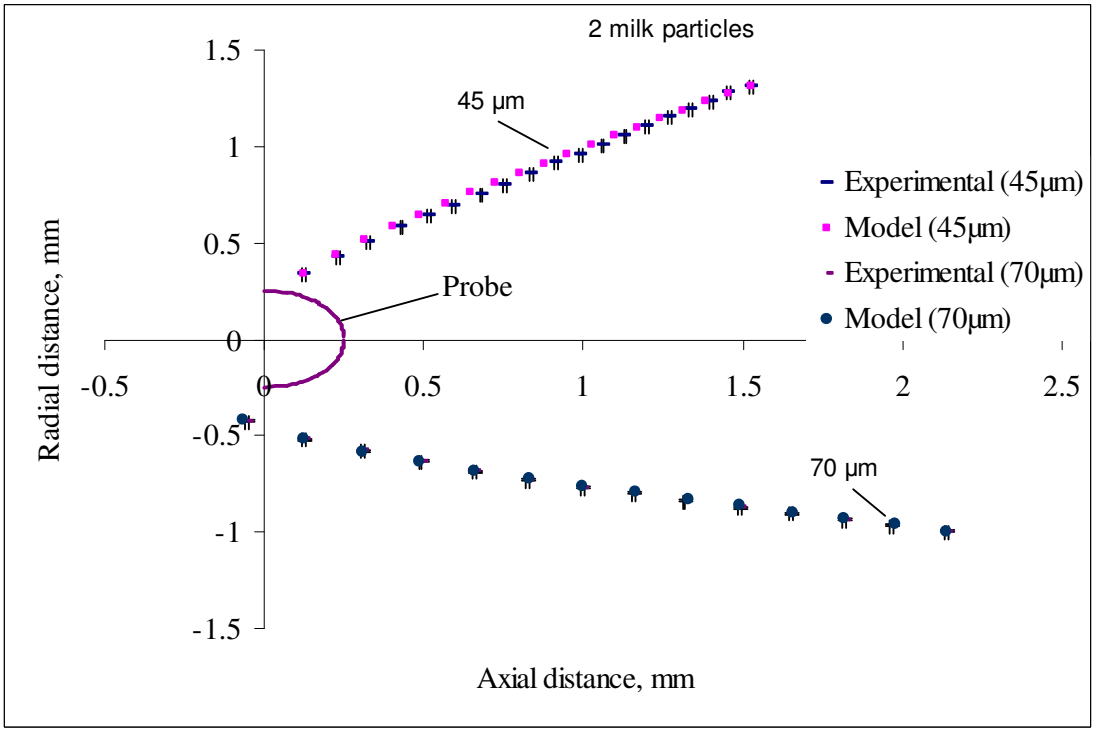

Figure A.10: Experimental and predicted particle trajectories for a 45 µm milk particle with probe voltage -5 kV with fitted net charge q_{net} = +7x10^{-15} C and a 70 µm milk particle with probe voltage +5 kV with fitted net charge q_{net} = -1x10^{-14} C.

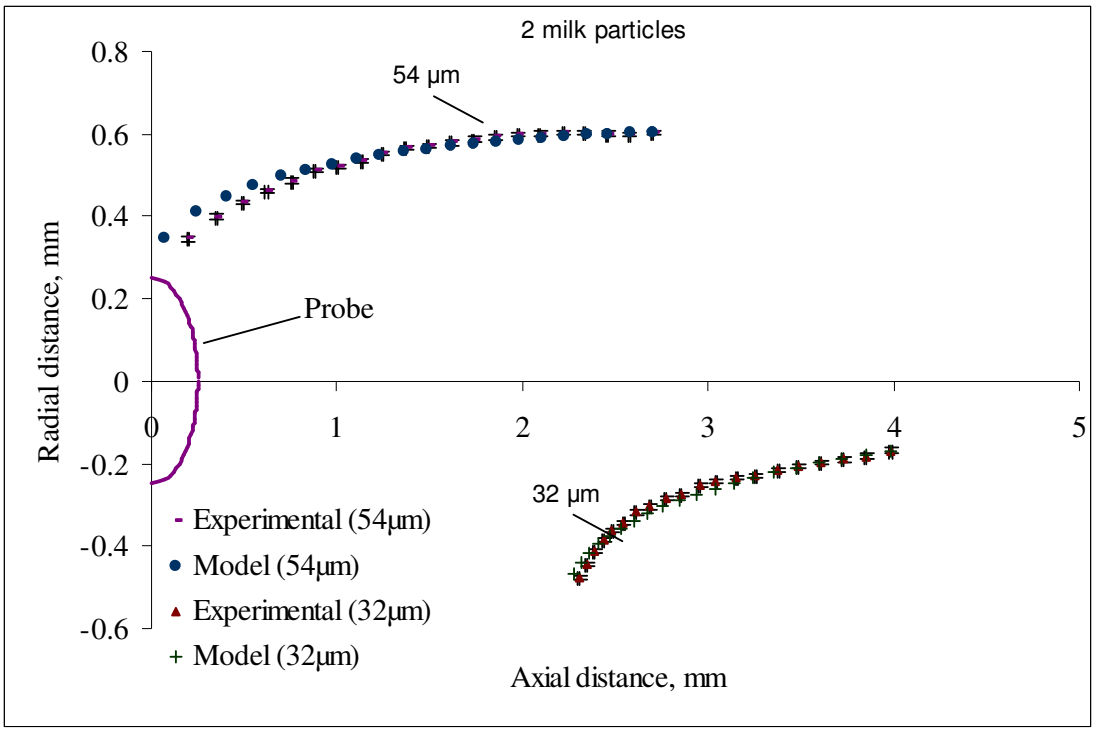

Figure A.11: Experimental and predicted particle trajectories for a 54 µm milk particle with probe voltage -5 kV with fitted net charge q_{net} = +1.7x10^{-14} C and a 32 µm milk particle with probe voltage -6 kV with fitted net charge q_{net} = -3.1x10^{-14} C.

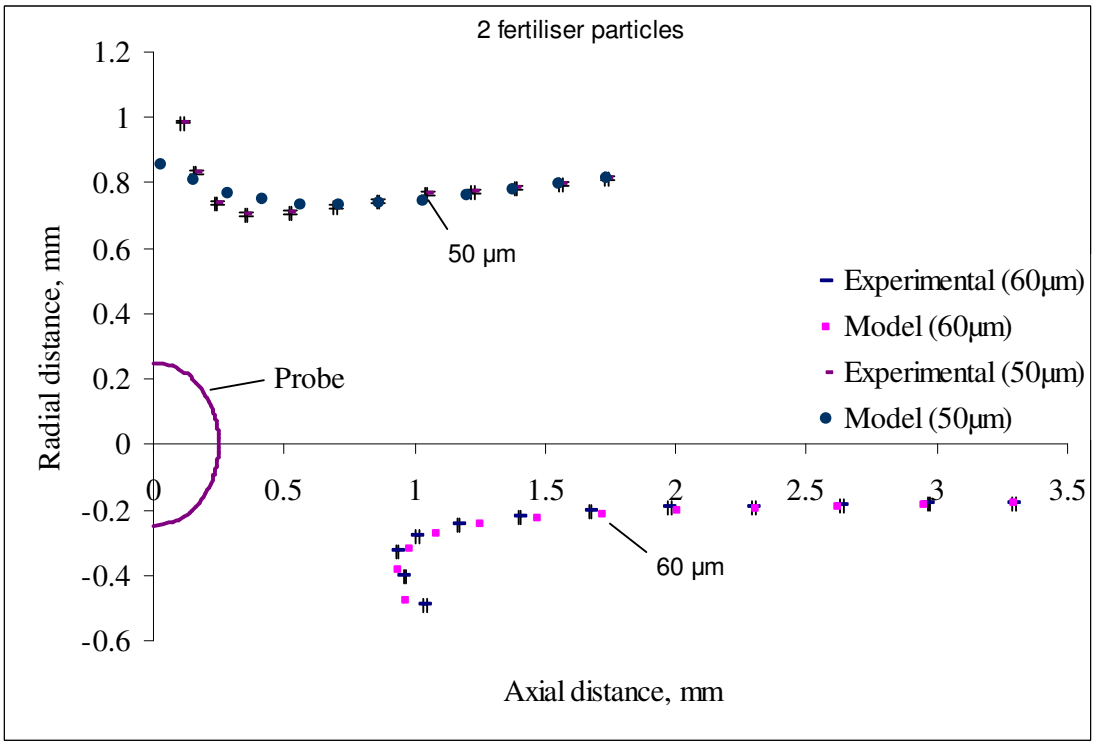

Figure A.12: Experimental and predicted particle trajectories for a 60 µm fertiliser particle with probe voltage +6 kV with fitted net charge q_{net} = +9.2x10^{-14} C and a 50 µm fertiliser particle with probe voltage -6 kV with fitted net charge q_{net} = -2.8x10^{-14} C.

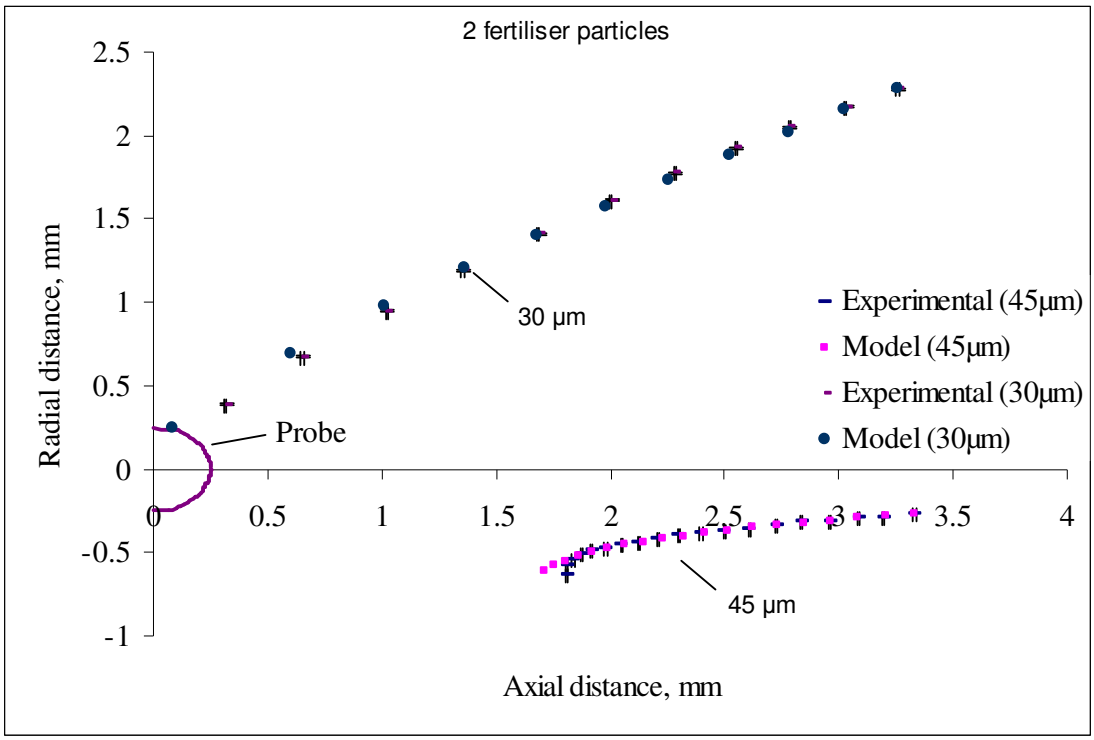

Figure A.13: Experimental and predicted particle trajectories for a 45 µm fertiliser particle with probe voltage -6 kV with fitted net charge q_{net} = -5.7x10^{-14} C and a 30 µm fertiliser particle with probe voltage -6 kV with fitted net charge q_{net} = +1x10^{-13} C.

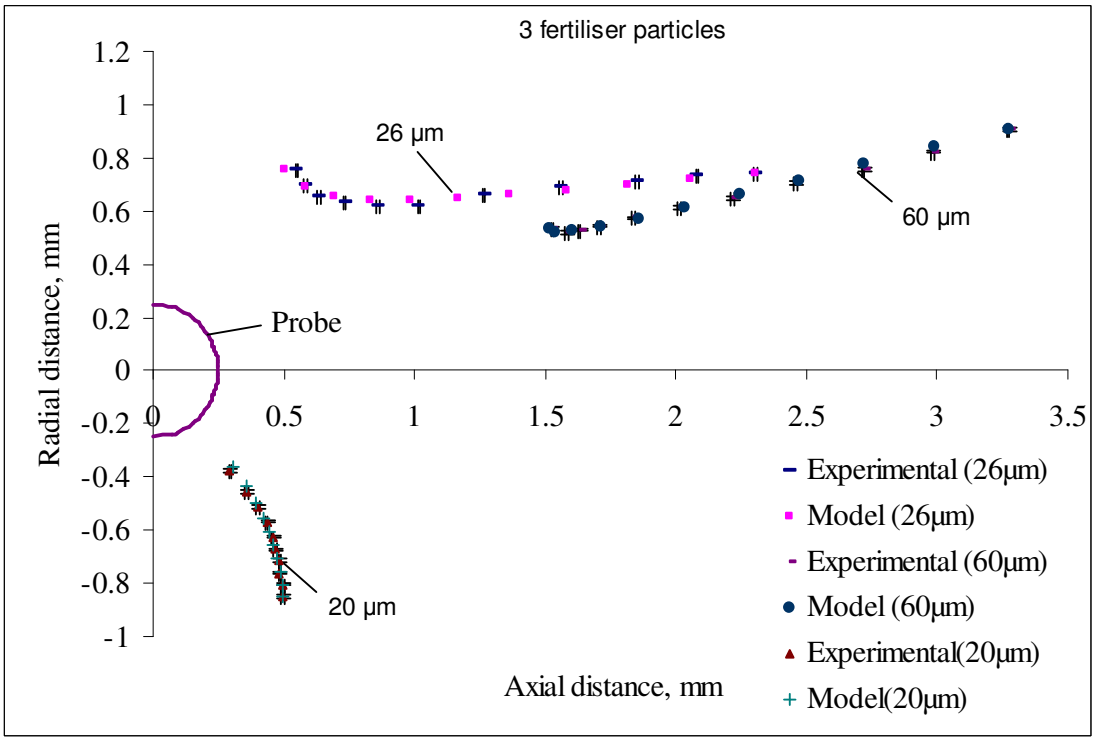

Figure A.14: Experimental and predicted particle trajectories for a 26 µm fertiliser particle with probe voltage -6 kV with fitted net charge q_{net} = -1.3x10^{-14} C, a 60 µm fertiliser particle with probe voltage +6 kV with fitted net charge q_{net} = +1.5x10^{-13} C and a 20 µm fertiliser particle with probe voltage -6 kV with fitted net charge q_{net} = +5x10^{-16} C.

Appendix A.5 Net Charge and Dipole Measurements

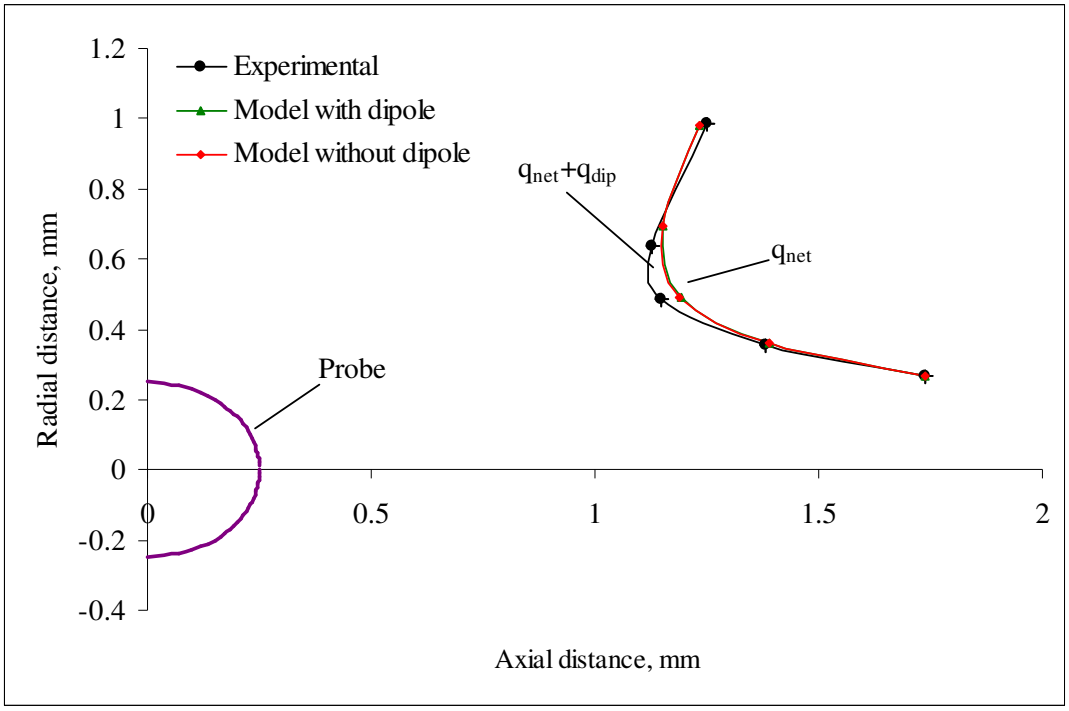

Figure A.15: Experimental and model trajectories for an 86 µm glass particle at probe voltage -10 kV. For only net charge fitted the charge is q_{net}= -2.6x10^{-13} C and for both net charge and dipolar charge fitted the values are q_{net}= -2.7x10^{-13} C and q_{dip}= 8x10^{-14} C.

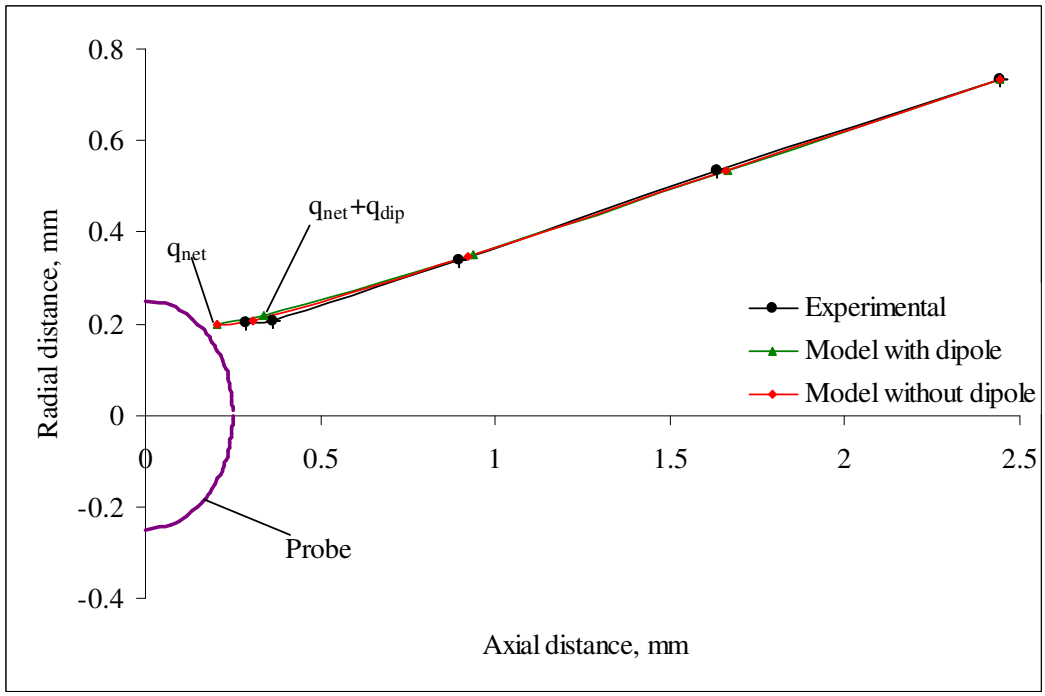

Figure A.16: Experimental and model trajectories for a 70 µm glass particle at probe voltage -10 kV. For only net charge fitted the charge is q_{net}= -3.5x10^{-14} C and for both net charge and dipolar charge fitted the values are q_{net}= -5.4x10^{-14} C and q_{dip}= 8x10^{-14} C.

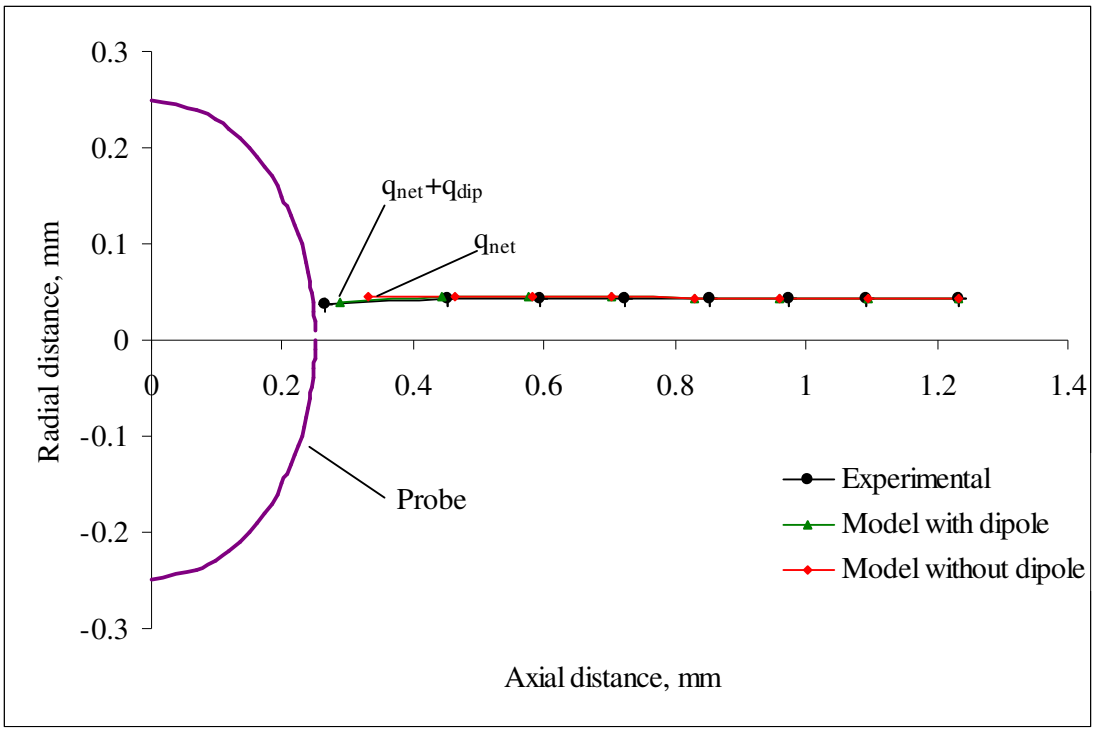

Figure A.17: Experimental and model trajectories for an 85 µm glass particle at probe voltage -7 kV. For only net charge fitted the charge is q_{net}= -2.4x10^{-15} C and for both net charge and dipolar charge fitted the values are q_{net}= -7.2x10^{-15} C and q_{dip}= 2.8x10^{-14} C.

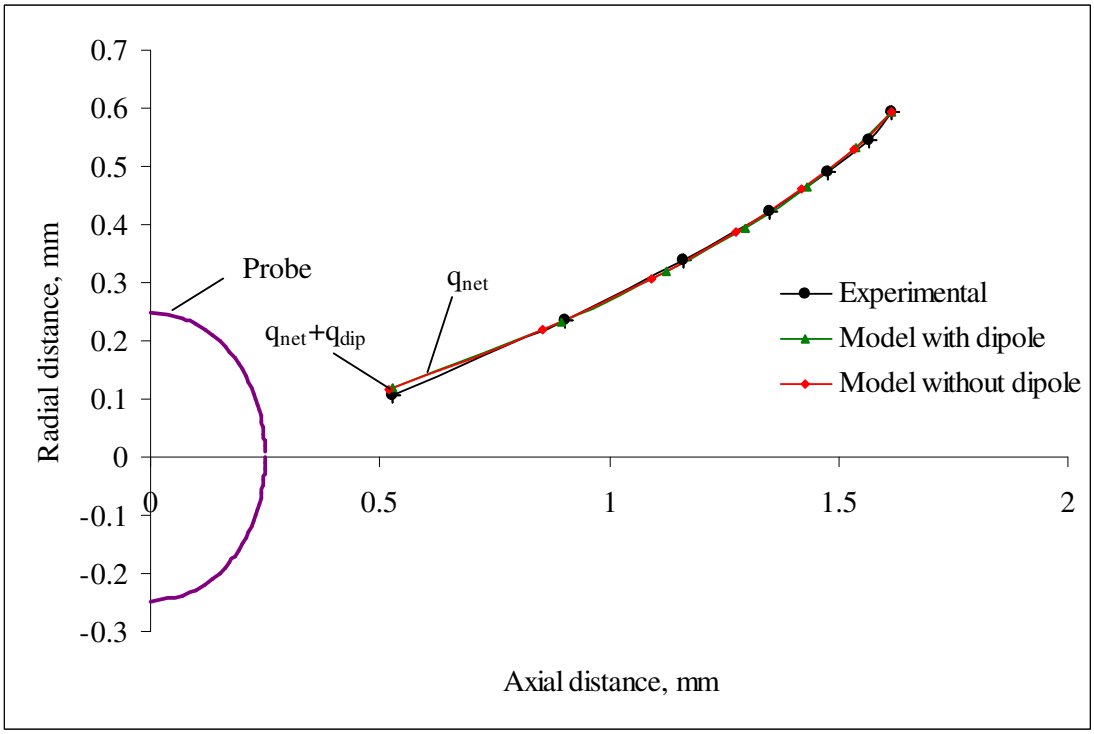

Figure A.18: Experimental and model trajectories for a 48 µm glass particle at probe voltage -8 kV. For only net charge fitted the charge is q_{net}= +1.9x10^{-14} C and for both net charge and dipolar charge fitted the values are q_{net}= +4.3x10^{-15} C and q_{dip}= 2x10^{-13} C.

Appendix A.6 Obolensky Filter Results

A.6.1 Average Charge on Glass Spheres passed through pre selector plates operating at 8kV

Charge Module: Aluminium
Piston used: Large
Cylinder diameter, ID = 13.5 mm
Time taken by piston to travel 1 cm = 10.5 s
Volume travelled by piston in 10.5 s = 1.43×10^{-6} m^3
Volume travelled by piston in 1 s = 1.36×10^{-7} m^3

Run 1

Time (s)	Current (nA)
0	2.7
2	1.84
4	-0.2
6	-1.27
8	-2.91
10	-3.38
12	-3.09
4	-3.61
16	-3.98
18	-3.83
20	-4.18
22	-4.23
24	-4.15
26	-4.21
28	-4.65
30	-4.82
32	-5.21
34	-5.38
36	-5.43
38	-5.82
40	-5.85
42	-5.97
44	-6.41
46	-6.08
48	-5.92

Run 2

Time (s)	Current (nA) (± 0.05)
0	1.4
2	1.08
4	-1.37
6	-3.62
8	-3.76
10	-4.18
12	-4.51
4	-4.67
16	-4.75
18	-5.03
20	-5.04
22	-5.37
24	-5.91
26	-5.63
28	-6.15
30	-6.08
32	-6.29
34	-6.05
36	-6.12
38	-6.80
40	-6.70
42	-6.44
44	-6.09
46	-6.81
48	-6.68
50	-6.41
52	-6.03

Apparent density of glass spheres = 150 kg/ m^3
Mass flow rate = 2×10^{-5} kg/s
Mean diameter of particle = 40 micron
Volume of a single particle = 3.4×10^{-14} m^3
Number of particles per kg = 2×10^{11}
Assuming an average current = -6nA
Average charge = -3×10^{-4} C/kg
Average charge on each particle = -1.5×10^{-15} C

A.6.2 Average Charge on Acrylic Spheres (MR-90G) without Preselector Plates

Charge Module: Aluminium
Piston used: Large

Cylinder diameter, ID = 13.5 mm
Time taken by piston to travel 1 cm = 10.5 s
Volume travelled by piston in 10.5 s = 1.43 x 10^{-6} m^3
Volume travelled by piston in 1 s = 1.36 x 10^{-7} m^3

Run 1

Time (s)	Current (nA) (± 0.05)
2	9.97
4	10.38
6	10.85
8	9.76
10	10.29
12	9.37
14	8.87
16	7.82
18	9.02
20	8.65
22	7.72
24	8.46
26	9.55
28	8.35
30	8.04
32	9.41
34	7.26
36	7.00
38	6.85
40	7.35
42	9.20
44	9.65
46	10.10
48	9.22
50	9.51
52	9.07
56	10.51
58	8.65
60	7.95
62	10.19

Run 2

Time (s)	Current (nA) (± 0.05)
4	8.80
8	10.25
12	9.80
16	9.20
20	8.40
24	8.10
28	8.90
32	7.80
36	7.10
40	7.80
44	8.00
48	9.20
52	9.50
56	8.35
60	8.04
64	9.20
68	8.56
72	8.35
76	8.65
80	7.90
84	8.55
88	7.95

Bulk density of acrylic spheres = 1190 kg/ m^3
Mass flow rate = 1.62 x 10^{-4} kg/s
Mean diameter of particle = 90 micron
Volume of a single particle = 3.8 x 10^{-13} m^3
Number of particles per kg = 2.2 x 10^9
Assuming an average current = 9 nA
Average charge = 55.6 x 10^{-6} C/kg
Average charge on each particle = 2.53 x 10^{-14} C

A.6.3 Average Charge on Acrylic Spheres (MR-90G) passed through Preselector Plates operating at 8 kV

Charge Module: Aluminium
Piston used: Large
Cylinder diameter, ID = 13.5 mm
Time taken by piston to travel 1 cm = 10.5 s
Volume travelled by piston in 10.5 s = 1.43×10^{-6} m^3
Volume travelled by piston in 1 s = 1.363×10^{-7} m^3

Run 1

Time (s)	Current (nA) (± 0.05)
2	8.11
4	7.63
6	7.86
8	8.06
10	8.10
12	7.88
14	8.03
16	7.94
18	8.01
20	8.15
22	7.82
24	8.29
26	8.03
28	8.43
30	4.85
32	8.51
34	7.95
36	8.81
38	7.89
40	8.36
42	8.55
44	8.69
46	8.90
48	9.01
50	9.07
52	8.44
56	7.96
58	8.27
60	8.02
62	7.96

Run 2

Time (s)	Current (nA) (± 0.05)
2	8.85
4	8.35
6	7.53
8	8.76
10	7.91
12	8.60
14	7.72
16	9.00
18	8.48
20	7.91
22	8.95
24	9.01
26	8.69
28	8.88
30	8.22
32	8.35
34	8.56
36	8.22
38	8.48
40	7.85
42	7.96
44	8.30
46	8.87
48	8.60
50	7.96
52	7.71
56	7.74
58	8.12
60	8.19
62	7.88
64	7.50
66	7.01
68	7.80
70	8.15

Bulk density of acrylic spheres = 1190 kg/ m^3
Mass flow rate = 1.62×10^{-4} kg/s
Mean diameter of particle = 90 micron
Volume of a single particle = 3.8×10^{-13} m^3
Number of particles per kg = 2.2×10^{9}
Assuming an average current = 8.2 nA
Average charge = 51×10^{-6} C/kg
Average charge on each particle = 2.3×10^{-14} C.

Appendix A.7

Paper published in Advanced Powder Technology, March, 2009 (also presented in Chemeca 2008, New Castle, Australia)

doi:10.1016/j.apt.2009.03.002

Original Research Paper

Measurement of electrostatic dipoles and net charge on particles suspended in air

Payel Bagga[a], **John Abrahamson**[a], and **John Marshall**[b]

[a]Chemical and Process Engineering Department, University of Canterbury, Private Bag 4800, Christchurch, New Zealand

[b]SETI Institute, 515 N Whisman Rd., Mountain View, CA, USA

Received 17 March 2009;
accepted 17 March 2009.
Available online 7 April 2009.

Abstract

Explanations of electrostatic behaviour of individual particulates have always invoked *net* electrostatic charge and neglected any fixed dipoles arising from nonuniform distribution of charge on their surface. Here for the first time, techniques are described to measure both net charge of each particle and its dipole moment by sampling, photography, and movement analysis of particles suspended in air. In this study, spherical dielectric particles were subjected to a non-uniform electric field (around a probe) and their trajectory was followed with a multi-flash high-speed video camera. These first results support the existence of fixed or “permanent” dipoles, on tribocharged particles

Appendix A.8

Paper presented in CHEMCON-2008, Chandigarh, India.

Measurement of Net Charge on Air-Dispersed Dust Particles

Payel Bagga, John Abrahamson
Chemical and Process Engineering Department, University of Canterbury,
Private Bag 4800, Christchurch, NZ

John Marshall
SETI Institute, 515 N Whisman Rd, Mountain View, California 94043, USA

ABSTRACT

This paper represents a method for charge measurement on individual spherical dielectric particles dispersed in air. The particles are subjected to a nonuniform electric field (around a probe tip) and their trajectories are followed with a multi-flash high-speed video camera. The nonuniform field in principle allows for measurement of monopoles, dipoles and higher moments. By solving the equation of particle motion under the influence of an electric field, the magnitude as well as the polarity of the particle charge can be obtained. The preliminary experimental tests were carried out on two samples of acrylic spheres with mean sizes of 20 µm and 90 µm. Techniques are described for the sampling, photography and analysis to effectively provide distributions of net charge.

Keywords*: Particle Charge measurement, Net charge*

INTRODUCTION

The presence of electric charge on particulates can be beneficial as well as hazardous. It has useful applications in the control of dust by electric precipitators, deposition of inhaled drug powders in lungs, electrostatic coating, spraying, and xerography, for example. It can also be undesirable as it causes electrical bridging of conductors in electronics, aggregation and clogging in particulate transport systems and may even leads to dust explosions etc.

The measurement of charge on a particle is necessary to understand its properties and to control its behavior; Brown (1997) reviewed methods of measurement of charge on particles and divided them into static and dynamic methods. Static methods involve direct measurement of absolute charge and dynamic methods infer charge from measuring electrical mobility. In static methods, charge is generally measured by its transfer to a capacitor and observing the voltage developed. The collection electrode may be a wire (Krupa and Jaworek, 1989) or coarse conducting grids on which particles leave charge by impact. Apart from giving up its charge the particle can also be collected in a Faraday cage in which an equal charge is induced (Penney and Lynch, 1957). The static methods of charge measurement have a drawback that only the mean charge of many particles is measured and generally only charges much higher than that of a single electron can be detected.

Measurement of net charge by dynamic methods measures the response of a particle in an electric field and has more flexibility (Brown, 1997). Millikan (1950) in his attempt to measure the charge of an electron used a one-dimensional equation of motion of the particle in an electric field with gravity opposing the motion. This method has been used by different researchers by making various modifications for essentially measuring the charge of single

particles. Rather than a single particle study, devices known as mobility analyzers have also been developed in order to provide data about a population of particles, generating diameter and charge distributions. A number of such devices were reviewed by Knutson et al (1975). Most of these devices have been designed for submicron particle sizes with flow along collection electrodes. An increase in particle size will lead to very long collection electrodes as the electromobility of particle will be smaller. Coury et al (1991) in an improved design overcame this limitation and used shorter electrodes - the gases after passing between the two parallel plates enter a battery of parallel collecting plates where they deposit according to their electromobility. The charge distribution of gas-borne particles up to 15 microns in diameter was measured. In both static and dynamic methods the problems include (a) confining the particles to be analyzed to the narrow focal plane of the system and (b) very long sampling times that involve tedious post-processing analysis.

This paper describes method ultimately aimed at measuring charge distributions over the surface of particles, described by firstly net charge and then dipole. The monopole charge and higher moments can be evaluated for each sampled particle from its motion in air through a *non-uniform* electric field. Measurements were enabled by high-speed video and synchronized illumination and image analysis techniques. Particle trajectories can be readily viewed in the focal plane with the help of a laser sheet. This paper describes the use of the method to measure monopole charge

EXPERIMENTAL RATIONALE

A simple wire probe was chosen to generate a non-uniform field. The purpose of using a non-uniform field was to make the measurement method more generalised. Such a field allows for the measurement of both monopole and dipole moments as dipoles tend to orient and move towards higher field regions which were close to probe in this case. High voltages were used to let the particles respond during their traverse over the small field of view. The voltage was reversed in polarity frequently during a run, to allow a symmetrical treatment of both positive and negative particles while flows and velocities remain constant (treating positive and negative particles equally and reducing possible distribution bias). This also provided additional checks on the trajectory analysis when a polarity switch occurred during a trajectory. One expects that the charge parameters of a particle will remain constant before and after such switches. There was no evidence of corona discharge close to the probe in optical observation which may also be due to polarity changing rapidly giving insufficient time for corona to develop.

EXPERIMENTAL SETUP

In our initial experiments a dilute flow ($5x10^{-4}$ volume fraction) of spherical dielectric particles was continuously supplied by an air jet from a brush feeder. This suspension emerged from a small tube into a much larger tube along its axis and flowed around the probe (which pointed upstream). Close to the probe, video images were taken of particle trajectories. Multiple images were possible through the use of multiple laser flashes for each video frame, leading to a sequence of particle positions along the trajectory within each frame.

The photograph of the experimental arrangement is shown in Fig. 1. The experimental apparatus consisted of a Sampler head, Laser unit, High speed camera, High voltage AC power supply, and a Brush feeder.

Sampler unit

The sampler unit was built around a cylindrical stainless steel tube of 100 mm ID and 500 mm length, aligned horizontally. This tube acted both as the outer electrode and the channel for the particle/air suspension flow. The particles were blown off a nylon brush through a brass tube 10 mm ID and 25 mm length, leading into a polyacetal tube of 3 mm ID and 90 mm length. The polyacetal tube tip was 220 mm upstream of the probe. The probe was a fine tungsten wire of 500 µm diameter with a hemispherical tip and was mounted midway along the tube on its centreline. The wire was attached to a high-voltage supply. Application of high voltage to this probe provided a nearly spherical field around and in front of the tip of the probe.

Laser unit and high voltage supply for probe

The red laser (Roithner Lasertechnik, Austria, RLT67300T, 670nm) was rated at 300 mW of continuous optical output, and was pulsed at 200 mW power level. After enlarging the cylindrical beam with a diverging-converging lens arrangement, it was expanded into a rectangular sheet of 10 x 0.8 mm cross-section. The laser driver controlled pulse duration and pulse period and the number of flashes per frame (up to 33). The laser head was mounted on the sampler tube with the sheet in line with the tip of the probe to illuminate particles close to the probe in a plane perpendicular to the axis of the video camera. The camera triggered the laser at the start of capture. The high voltage supply abruptly changed the polarity of the probe voltage after a set number of video frames and its square wave form had a maximum of 40 kV peak to peak. In order to indicate which polarity existed during the exposure of a video frame, the supply waveform was sent to the laser driver, which halved the frequency of pulsing when the output voltage was positive.

High speed camera

The CMOS high speed camera (Canadian Photonics Lab MS50K) was operated at 500 frames / s with a resolution of 1200 x 1020 pixels. A field of view of 6.5 mm by 5.5 mm could be imaged through the 55 mm lens on a 230 mm extension tube. Depth of field was 0.85 mm. The camera imaged through a flat glass window on the side of the tube.

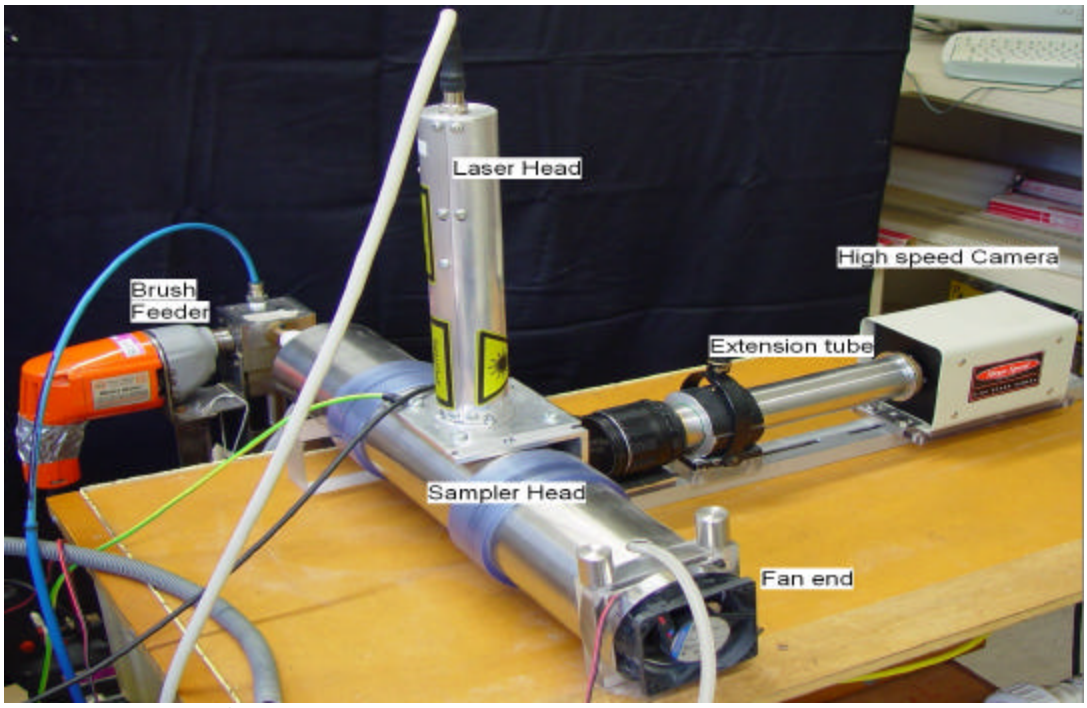

Figure1: Photograph of the sampling head, including the mounted camera, laser and electrical connections.

THEORETICAL MODEL

The rate of change of particle velocity was calculated through particle momentum conservation as in eqn. 1, using drag force, $F_{d,}$ and electrical force, $F_{el,}$ as the dominant forces acting,

$$m\frac{dU_p}{dt} = F_d + F_{el} \tag{1}$$

where m is the mass of the particle. This vector equation was used in two directions in the plane of the light sheet; both axially (z direction) and radially (r direction) neglecting gravitational force. The F_d direction opposed U_{rel} and the magnitude obtained via the drag coefficient correlation proposed by Abraham (1970). This drag force was resolved in the z and r directions and components inserted in the corresponding z and r momentum equations. It was assumed that these values fluctuated somewhat between trajectories because the flow had the turbulence of the nozzle jet. For each trajectory, the initial velocity (magnitude and direction) of the *particle* while entering the field of view was assumed to be that of the *gas* during the whole trajectory. The flow field around the hemispherical tip was taken as that approaching a sphere, using Stokes' equations (Bird et al. 1962).

All electrical forces were taken to be along the radius r_{sph} from the particle centre to the probe tip centre. The electrostatic force was taken as the sum of the monopole, induced dipole and the image forces.

$$\vec{F}_{el} = \vec{F}_{mono} + \vec{F}_{ind} + \vec{F}_{image} \tag{2}$$

All of these acts along the probe centre-to-particle centre direction, and are a function of their separation r_{sph}. Thus

$$F_{el} = \frac{Q_{net}V}{(1/a - 1/b)r_{sph}^{\ 2}} + U\frac{-8\pi e_o V^2 R_p^{\ 3}}{(1/a - 1/b)^2 r_{sph}^{\ 5}} + \frac{-Q_{net}^2}{16\pi e_o (r_{sph} - a)^2} \tag{3}$$

where a is probe tip radius, b is tube radius, V is probe voltage, R_p is particle radius, U is the permittivity multiplication factor and e_o is free space permittivity.

This suggested a sequential method of fitting parameter values for the trajectory. The first few particle positions on the frame were used to calculate the radial and axial velocities of the particle, and assumed to be those of the gas, giving the velocity and angle of gas approach to the probe. The monopole charge on the particle was varied to fit the model to points closer to the tip of the probe. Image forces were calculated by using the fitted monopole charge with minimum separation distance equal to the radius of the particle.

RESULTS AND DISCUSSION

The particles used as samples for running the experiments were acrylic particles from Esprix technologies (MR-90G and MR-20G). These are white particles with a specific gravity of 1.19 and refraction index of 1.49, with mean diameter 90µm and 20µm. The scale of the image was measured by photographing a high-precision scale positioned in the plane of the light sheet. Individual frames were examined later on the computer, and if necessary particle positions from several consecutive frames were linked together in one analysis. Probe voltage was reversed every 6 frames.

Owing to the transparency of the acrylic spheres, their images depended on being able to record side scattered light from the laser sheet. Thus, only the tops and bottoms of particles were visible in the form of small light patches. The centre of a particle was taken to be the midpoint between the farthest pixels of each pair of light patches. The parameters used in numerical calculations were tip radius a = 2.5x10^{-4} m, tube inner radius b = 0.05 m, apparent density of the glass bubbles $?_p$ = 1180 kg / m^3, permittivity of free space e_o = 8.85 x 10^{-12} F / m, multiplication factor for the glass bubbles U = 0.289, viscosity of air μ = 1.8 x 10^{-5} Pa s.

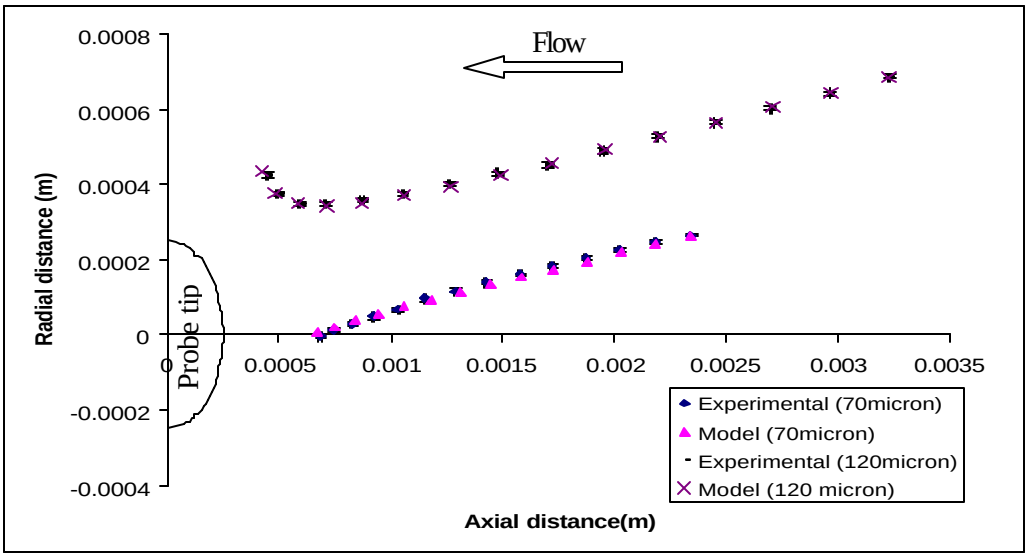

Figure 3: Experimental and predicted particle trajectories for a 70µm particle with probe voltage -6 kV with fitted net charge q_{net} = -5.5 x 10^{-14} C and a 120 µm particle with probe voltage -10 kV with fitted net charge q_{net} = -4.42 x 10^{-13} C.

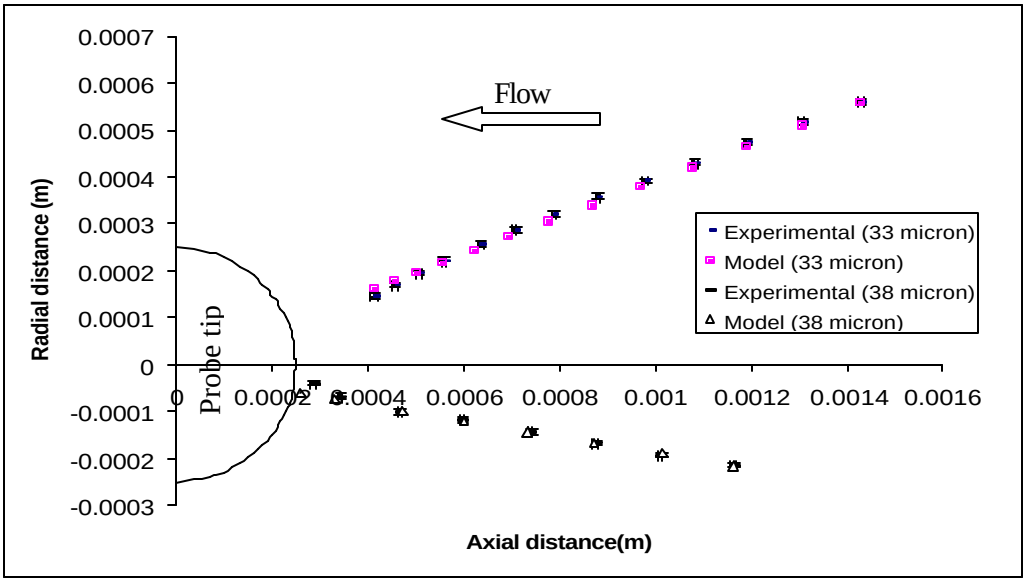

Figure 4: Experimental and predicted particle trajectories at probe voltage -6 kV for a 33µm particle with fitted net charge q_{net} = -4.1 x 10^{-15} C and a 38 µm particle with fitted net charge q_{net} = -3.5 x 10^{-15} C

Fig 3-5 show the trajectories for some individual particles analysed for charge measurements. Error bars are for 1 pixel image error in both directions. Fitting errors were determined by adjustment net charge so that the modelled trajectories just remained within the experimental error bars.

Figure 3 shows modelled and observed trajectories of a 70 µm particle which has been repelled away for negative probe voltage. The particle's net charge comes out to be -5.5 x 10^{-14} C with an error of ± 0.4 x 10^{-14} C .The120 µm particle in the same figure decelerates at negative probe voltage and its charge is measured to be -4.42 x 10^{-13} C with an error of ± 0.8 x 10^{-13} C.

Figure 4 shows modelled and observed trajectories for smaller particle sizes of 33 µm and 38 µm for which the particle's net charge comes out to be -4.1 x 10^{-15} C and -3.5 x 10^{-15} C respectively with an error of ± 0.1 x 10^{-15} C and ± 0.3 x10^{-15} C. Figure 5 shows a 28µm particle with a net positive charge of 2.8 x 10^{-15} C.

It was observed that some trajectories could not be fitted with monopole charge alone and some other force with different dependence on probe to particle separation was needed to explain the path followed by the particle. For such cases an addition of dipole force due to presence of permanent dipoles on particle surface could well fit the experimental points. This study has been reported elsewhere and further work is ongoing.

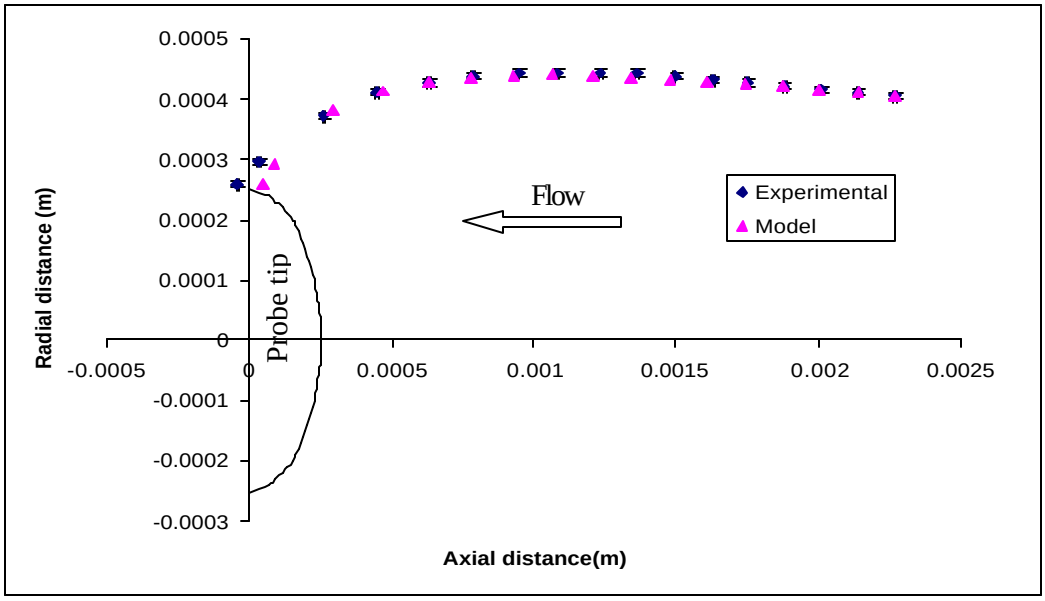

Figure 5: Experimental and predicted particle trajectories for a 28µm particle with probe voltage -6 kV with fitted net charge q_{net} = 2.8 x 10^{-15} C.

CONCLUSIONS

A technique for measurement of charge on micron sized particles has been developed. Net charge on individual particles has been successfully measured using a laser sheet and photographic analysis. The technique can potentially also measure dipole strength as well as net charge, and so can reveal the tribocharging history of a particle from two or more collisions. At this stage the work is time consuming and automation of the procedure is recommended in future work.

ACKNOWLEDGEMENTS

We are thankful to Peter Jones, Tim Moore and Trevor Berry for technical assistance and Julian Smith for building the Laser Flash Unit.

REFERENCES

1. Abraham, F.F. (1970) Functional dependence of drag coefficient of a sphere on Reynolds number. *Physics Fluids*, **13**, 2194-5
2. Brown, R. C. (1997) Tutorial review: Simultaneous measurement of particle size and particle charge. *Journal of Aerosol Science*, **28**(8),1373-1391
3. Bird R.B., Stewart W.E., Lightfoot E.N., (1962) *Transport Phenomena*, John Wiley and Sons, 57-58.
4. Coury, J.R., Raper, J.A.,Guang, D. and Clift, R.(1991) Measurement of electrostatic charge on gas-borne particles and the effect of charges on fabric filtration. *Trans IChemE*, **69**(B), 97-106
5. Knutson, E.O. and Whitby, K.T. (1975) Aerosol classification by electrical mobility: apparatus, theory and applications *J.Aerosol Sci*., **6**, 443-451
6. Krupa, A. and Jaworek, A. (1989) A method for aerosol particles charge measurement. *J. Electrostatics*, **23**, 289-292.
7. Autobiography of Robert A. Millikan, (1950), Prentice-Hall, p. 81
8. Penney, G.W. and Lynch, R.D. (1957) Measurements of charge imparted to fine particles by corona discharge. *AIEEE Trans.*, **76**, 294-299